Optimisation of multimode waveguide platforms for optical chemical sensors and biosensors

A dissertation submitted for the degree of
Doctor of Philosophy

by

Ľuboš Poleredký
M.S. (Charles University, Prague) 1998
M.Eng. (Czech Technical University, Prague) 1998

Supervisor: Prof. Brian D. MacCraith
School of Physical Sciences
Dublin City University
Dublin, Ireland

February 2002

To my parents and Irene

I hereby certify that this material, which I now submit for assessment on the programme of study leading to the award of *Doctor of Philosophy* is entirely my own work and has not been taken from the work of others save and to the extent that such work has been cited and acknowledged within the text of my work.

Signed:  ID No.: 98970720

Date: 16 April 2002

Acknowledgements

This dissertation is a result of over three years of research carried out in the Optical Sensors Laboratory, School of Physical Sciences, Dublin City University, Ireland. I would like to recognize and thank the following individuals for their helpful guidance and support in this project.

Firstly, I would like to thank my thesis supervisor, Professor Brian MacCraith, for giving me the opportunity to work in the Optical Sensors Laboratory. I wish to express my appreciation for his guidance and unwavering support over the last three years. I am grateful for his helpful suggestions, constructive criticism, comments, and, of course, financial support.

I am grateful to my good friend, Jaroslav Hamrle, for the very many fruitful discussions, which helped to formulate some of the core ideas in this work. I am also thankful to him for sharing his expertise and wisdom in the area of electronics, and for his willingness to work through the day and continue long into the night!

I would also like to express my appreciation to Des Lavelle and Cian Merne in the School workshop. Without their craftsmanship the experimental set-ups would not have worked so well.

Thanks are also due to Conor Burke and Helen McEvoy for their co-operation in the experiments that I conducted, in particular for the samples and assistance with the experiments.

Equally, I owe my thanks to Christoph von Bültzingslöwen for making some of the samples and sharing his knowledge of chemistry which helped me to interpret some of the experimental data.

I would also like to thank Dr. Thomas Glanzmann for his moral support, encouragement and friendship during my first years at DCU.

Thanks go to Dr. Claire Davis and Pierre Couratier for taking part in the experiments regarding the luminescence capture efficiency.

I am grateful also for the help and advice I received from all the other members, past and present, of the Optical Sensors Laboratory and the School of Physical Science, who are too numerous to mention individually here. Thank you!

I have reserved this final paragraph to acknowledge the people who have supported me not only during this work but throughout my life. My parents, who provided the item of greatest worth—opportunity. Thank you for standing by me through the many trials and decisions of my educational career. My family and friends, particularly those in Ireland, who have always been there for me when I needed them. And Irene, whose cheerful attitude helped me to overcome many moments of desperation, who provided me with an invaluable support and encouragement and whose presence just made things so much easier.

THANK YOU!

Contents

Optimisation of multimode waveguide platforms for optical chemical sensors and biosensors

by

Ľuboš Polerecký

Abstract

In this dissertation, a theoretical description of the operation of absorption and fluorescence-based optical chemical sensors employing planar multimode waveguides is developed. Using this theory, the design issues that should be taken into account in order to fabricate such sensor systems with an optimised performance are addressed and discussed in detail. Prototype sensor systems whose fabrication was based on these optimised design parameters are described and the experimental results of their performance are presented.

The key issues dealt with in the dissertation are:

1. Development of a rigorous electromagnetic theory of operation of absorption-based optical chemical sensors employing multimode waveguides coated with a thin absorbing layer.

2. Application of this theory to the development of sensor systems with optimised performance.

3. Fabrication and experimental testing of a compact and portable absorption-based optical chemical sensor.

4. Development and experimental verification of a theory of radiation of fluorescent molecules embedded in a planar multilayer structure.

5. Application of this theory to the design of configurations with optimised fluorescence capture efficiency. Fabrication and experimental testing of these structures.

6. Development and testing of the experimental set-up facilitating the collection of a surface-generated fluorescence excited by a direct illumination.

Chapter 1

Introduction

Devices capable of providing accurate and reliable quantitative evaluation of parameters characterising physical, chemical or biological systems are in high demand today in almost every industrial, medical or environmental application. These devices are generally called *sensors* and the act of acquiring the relevant information about the system of interest is called *sensing*. Typically, the quantity that is to be sensed is transferred to another quantity which is more convenient for further processing or evaluation (e.g., analogue or digital output signal) by a process called *transduction*.

In accordance with the diversity of applications for which sensing is required, the number of different transduction mechanisms employed in sensors is large. In the past two or three decades, triggered by the technological advances achieved in the areas of material science, mechanics, microelectronics and optics, transducers based on *optical* principles have been employed in an increasing number of sensor systems. This shift towards optical sensor systems can be attributed to two main factors. Firstly, the optical sensor systems can often achieve considerably greater sensitivity than their non-optical counterparts. Secondly, the developments in opto-electronics, which led to low-cost availability of devices such as light emitting diodes (LEDs), laser diodes (LDs), photodiodes (PDs), CCD or linear detector arrays, etc., have enabled the fabrication of optical sensor devices that are compact, portable and even hand-held.

There are various classes of optical sensors. Of particular interest to this work are optical sensors which (i) employ *waveguides* as a platform for facilitating or enhancing the interaction of light with the location where the transduction process takes place and which (ii) are used to quantify the amount of a *chemical compound*, referred to as the *analyte*, in a certain environment. Such sensors are also called *waveguide-based optical chemical sensors*.

Applications of this type of sensors are diverse. They can be used, for example, to monitor the concentration of oxygen present in a living tissue, quantify the levels of oxygen or ammonia dissolved in waste water, determine the composition of the protective atmosphere gases (N_2 and CO_2) in a food package, assess the pH, salinity or the concentration of heavy metal ions in sea water, to name a few.

Taking into account different optical phenomena which determine the principle of operation of an optical chemical sensor, the class of sensors that will be dealt with in this work is further narrowed. In particular, this dissertation deals with the optical chemical sensors

employing *absorption* and *emission* of light as the transduction mechanism. The goal is to provide a detailed theoretical insight into the operation of this class of sensors and address a number of issues related to the optimisation of their performance.

Before going into details, however, a brief overview of the types of waveguide-based optical chemical sensors that are most frequently used among the scientific community is given. This summary deals mainly with the issues related to the *instrumentation* and *optical design* of the sensor systems [1], which is closely related to the design and optimisation issues dealt with in the subsequent parts of this dissertation.

1.1 Refractometric optical chemical sensors

The working principle of the refractometric sensors is based on the fact that the *real part* of the refractive index of at least one part of the waveguide structure changes upon interaction with the analyte. The interaction is most often provided either by adsorption or simply by the presence of the (bio)chemical molecules in the close vicinity of the guiding layer. Therefore, these sensors are most often used in biomedical or pharmaceutical applications to monitor biochemical reactions.

To monitor the changes of the real part of the refractive index, various waveguide configurations have been proposed, fabricated and tested. The principle configurations are listed and briefly described below.

1.1.1 Integrated optical sensor based on grating couplers

Grating couplers are well known structures used in the area of integrated optics (IO) to couple light into or out of a waveguide. The coupling conditions (e.g., angle of incidence) and efficiency of the grating coupler are determined by matching between the effective refractive index (ERI) of the diffracted beam of the input/output light beam and the ERI of the guided mode of the waveguide.

The energy carried by the guided mode is not confined entirely within the guiding layer but penetrates into the surrounding media. The penetration depth of this so-called *evanescent field*, which depends on the optical parameters of the structure and the character of the propagating modes, is in the order of the wavelength of the light used (typically around 100 to 500 nm). Therefore, if the biomolecules or other species adsorb or bind in the region of the evanescent field, they alter the ERI of the guided mode and consequently the conditions for which efficient in/out-coupling of light occurs.

The changes in the effective refractive index can be monitored by various means. Spinke et al. [2] exploited the fact that the ERI is altered differently for the TE_0 and TM_0 modes (see Fig. 1.1(a)). After these modes are out-coupled, they overlap and interfere. The *spatial frequency* of the interference pattern is proportional to the relative phase velocity (determined by the ERI) of the two modes which is related to the mass loading at the sensor surface. By simultaneous monitoring of the *out-coupling angles* of the TE_0 and TM_0 modes, Oudshoorn et al. [4] and Clerk & Lukosz [5, 6] were able to determine both the refractive index and thickness of the layer of the molecules bound/adsorbed on the surface. Wiki & Kunz [7, 8] used a tunable laser diode to sweep the wavelength of the interrogating light over a small

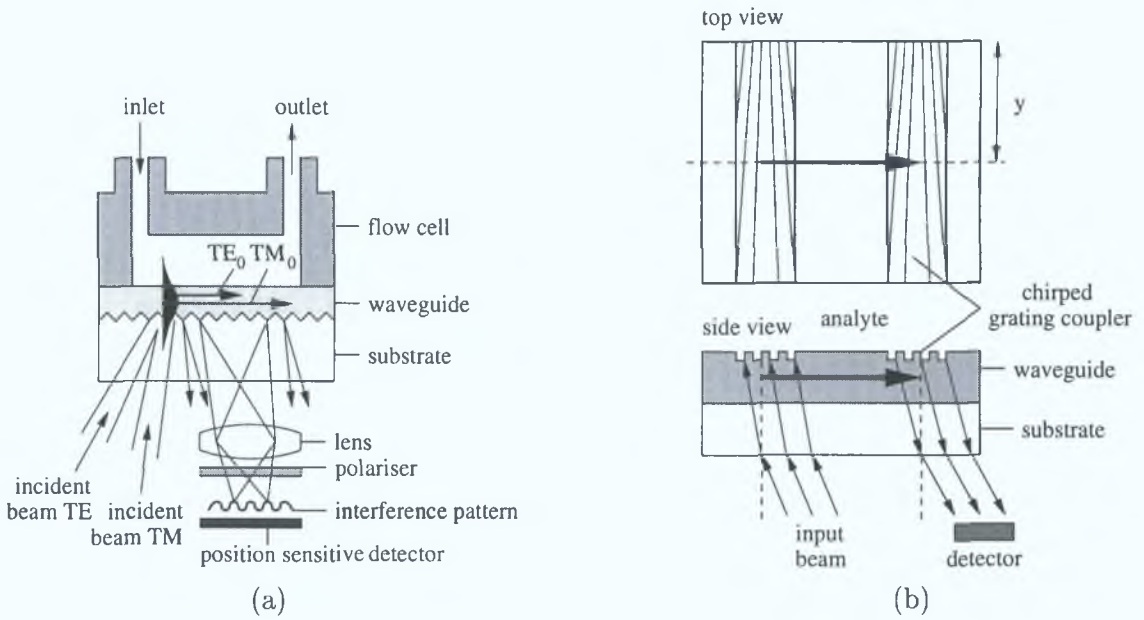

Figure 1.1: (a) A schematic diagram of the refractometric optical chemical sensor employing a grating coupler (from Spinke et al. [2]). (b) A schematic diagram of the sensor configuration employing a chirped grating coupler (from Wiki et al. [3]).

interval. Changes in the ERI were measured by monitoring the *wavelength* at which the optimum out-coupling of the guided mode occurred. An interesting configuration employing chirped grating couplers or uniform grating couplers incorporated in a tapered-thickness waveguide was developed by Dübendorfer et al. [9], Wiki et al. [3] and Kunz [8]. The optimum coupling conditions were monitored by locating the *position* y of the out-coupled laser beam with a position sensitive photo-detector, as shown in Fig. 1.1(b).

1.1.2 Integrated optical difference interferometers

The transduction mechanism of IO difference interferometers is equivalent to that of the sensors based on grating couplers (see Sec. 1.1.1). The changes of the ERI of the TE_0 and TM_0 modes are, however, determined by measuring the *position* of the interference pattern which is created as a result of the interference of the TE_0 and TM_0 modes coupled out through the waveguide's end face.

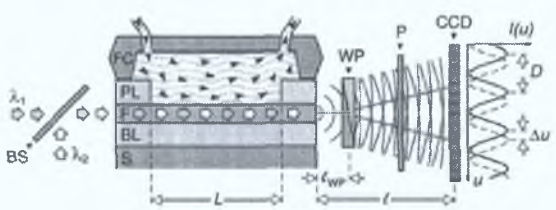

Figure 1.2: A typical configuration of the integrated optical sensor employing difference interferometer (from Stamm et al. [13]).

IO sensors based on difference interferometry were extensively studied by Lukosz and his co-workers [10, 11, 12, 13]. A typical configuration of the compact sensor unit is depicted in

Fig. 1.2. Apart from the sensitivity to adsorption or binding of molecules to the waveguide surface, this configuration is also sensitive to variations of other parameters, such as the refractive index of the solution covering the waveguide, temperature, etc. These parasite effects were successfully eliminated by extending the operation of the sensor to dual-wavelength mode, as reported by Stamm et al. [14].

1.1.3 Integrated Mach-Zehnder interferometer

Another possibility for monitoring the changes of the ERI of the guided mode is to employ an IO Mach-Zehnder interferometer (MZI). This configuration, which is depicted in Fig. 1.3, was extensively studied by Heideman et al. [15, 16], Schipper et al. [17, 18], Drapp et al. [19] and Busse et al. [20].

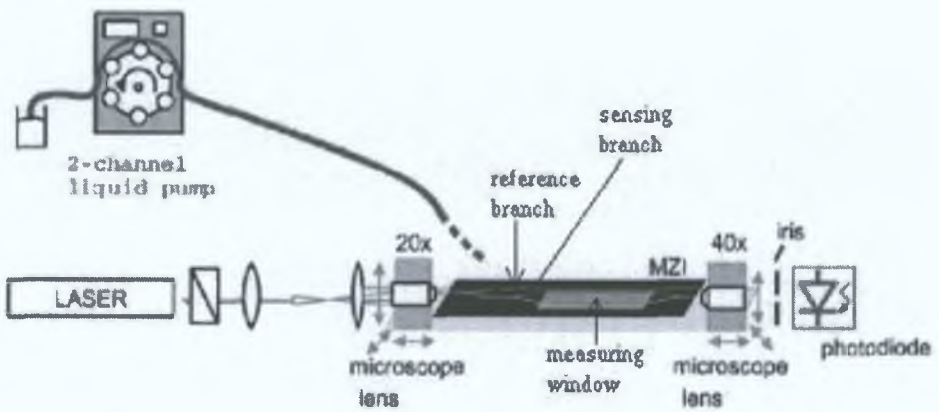

Figure 1.3: A typical configuration of the sensor system employing integrated optical Mach-Zehnder interferometer (from Busse et al. [20]).

Material covering one branch of the MZI, referred to as the sensing branch, is removed. Through this "measuring window", the analyte can interact directly with the evanescent field of the mode propagating through the sensing branch, which results in the alteration of its ERI. The resulting difference between the phases of the field propagating through the sensing and reference branches is monitored by measuring the light intensity at the output of the MZI. The sensitivity of this configuration can be dramatically increased by increasing the length of the branches. Furthermore, the geometrical character of the IO MZI allows fabrication of many independent interferometers on one chip thus opening new possibilities in multi-analyte sensing on a single IO device.

1.1.4 Reflectometric interference spectroscopy

The transduction mechanism of a sensor system employing reflectometric interference spectroscopy (RIFS) is based on the interference of white light at thin films, as shown in Fig. 1.4(a). White light illuminating an interface between two media of different refractive index is partially reflected. The reflected beams can superimpose and result in an interference pattern, depending on the angle of incidence, wavelength (λ), physical thickness of the film (d) and its refractive index (n). For perpendicular incidence, a non-absorbing layer and low reflectances, the reflectance of the thin film can be written as $R = R_1 + R_2 + 2\sqrt{R_1 R_2}\cos(4\pi nd/\lambda)$, where

R_1 and R_2 denote the Fresnel reflectances at the two interfaces. A typical interference pattern, as described by this equation, is shown in Fig. 1.4(b). The optical thickness nd can be determined from the position of the extrema of the interference pattern.

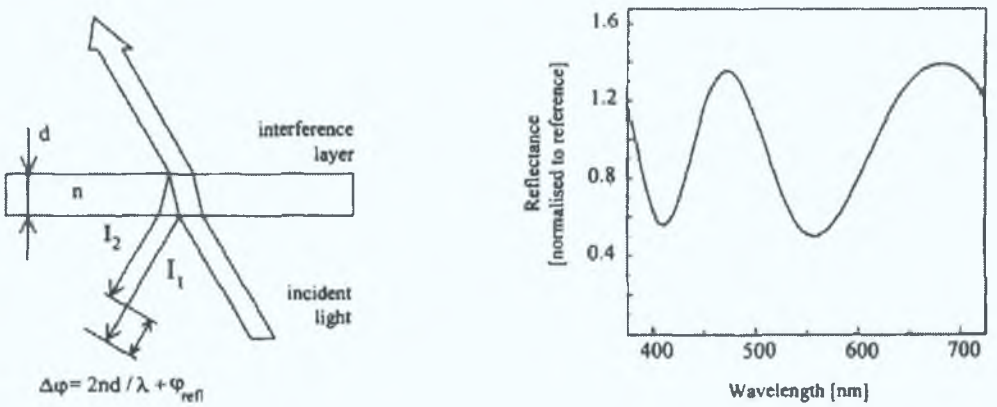

Figure 1.4: (a) A schematic diagram of the principle of reflectometric interference spectroscopy (RIFS). (b) A typical example of the interference pattern obtained from the RIFS measurement. (from Schmitt et al. [21]).

An integrated optical sensor system based on this principle was constructed and tested by Schmitt et al. [21] and Brecht et al. [22]. Illumination of the interference layer with white light and acquisition of the reflected light was performed by fibre optics and a spectrometer. From the acquired spectra, they were able to monitor the optical thickness of the layer in real time. They successfully applied this to monitoring of binding of molecules to the surface of the SiO_2 interference layer deposited on a glass slide substrate.

1.1.5 General performance issues

The configurations mentioned above represent the most popular implementations of the refractometric principle in waveguide-based optical chemical sensors. The spectrum of possible configurations is obviously broader and the interested reader is referred to the literature where these and other configurations are discussed in more detail [8, 10, 23, 24, 25, 26]. Furthermore, a considerable number of theoretical studies has been reported in order to optimise the performance of such sensor systems [11, 14, 27, 28, 29].

A typical achievable resolution of refractometric sensor systems, when expressed in terms of the minimum resolvable value of refractive index, has been reported to be in the order of 10^{-5}–10^{-7}. This resolution enabled successful application of the refractometric transduction mechanism in the area of surface-specific immunoassays which are of great importance in biotechnology, medical and pharmaceutical applications. This mechanism provides a very sensitive and *label-free* tool for *in-situ* and real-time monitoring of biochemical reactions, which is its main advantage. On the other hand, special care has to be taken during the interpretation of the experimental data. Due to its high sensitivity, this method is prone to parasite effects, such as temperature variations, non-specific binding or adsorption, etc.

1.2 Surface plasmon-based optical chemical sensors

Strictly speaking, optical chemical sensors based on surface plasmon resonance (SPR) belong to the category of refractometric sensors discussed in the previous section. However, the exploitation of the surface plasmon (SP) phenomenon in sensing applications has become so popular that it merits a separate treatment.

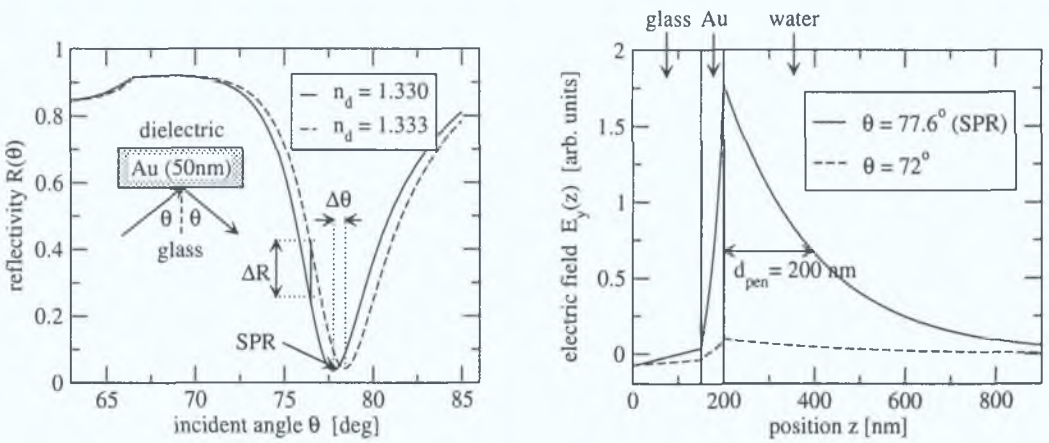

Figure 1.5: (a) The angular dependence of reflectivity of a thin gold layer deposited on a glass substrate. The calculation was performed for wavelength $\lambda = 642.8$ nm and for two values of the refractive index n_d characterising the dielectric medium covering the gold layer (see the legend). The dip in reflectivity corresponds to efficient excitation of the surface plasma wave, the so-called surface plasmon resonance (SPR). (b) An example of a distribution of the electric field intensity calculated for two values of the incident angle θ (see the schematic diagram of the configuration in the graph (a)). For $\theta = 77.6°$, which corresponds to the SPR, the field at the metal/water interface is considerably enhanced in comparison to the field corresponding to some other angle of incidence.

A surface plasmon is a charge-density oscillation that may exist at the interface of two media with dielectric constants of opposite signs, for instance, a metal and a dielectric. The charge density wave is associated with an electromagnetic wave, the field vectors of which reach their maxima at the interface and decay exponentially into both media. This surface plasma wave (SPW) is a TM-polarised wave (magnetic vector is perpendicular to the direction of propagation of the SPW and parallel to the plane of interface). The propagation constant β of the SPW propagating along the interface between a semi-infinite dielectric and metal is given by the expression $\beta = k\sqrt{\epsilon_m n_d^2/(\epsilon_m + n_d^2)}$, where k denotes the free space wave number, ϵ_m the dielectric constant of the metal ($\epsilon_m = \epsilon_m^{\mathrm{re}} + i\epsilon_m^{\mathrm{im}}$) and n_d the refractive index of the dielectric [30]. As may be concluded from this expression, the SPR may occur provided that $\epsilon_m^{\mathrm{re}} < -n_d^2$. At optical wavelengths, this condition is fulfilled by several metals of which gold and silver are the most commonly used.

The electromagnetic field of the SPW is distributed in a highly asymmetric fashion and most of the energy is concentrated in the dielectric within the penetration length in the order of approximately 200 to 400 nm, as depicted in Fig. 1.5. It is this enhanced field that makes the SPW particularly sensitive to the variations of the refractive index in the close vicinity

of the surface of the metal layer.

The propagation length of the SPW is very limited (to approximately 20–30 nm [31]) and so the sensing action is performed directly in the area where the SPW is excited by an optical wave. The optical system used to excite the SPW is simultaneously used for the interrogation of SPR. Therefore, the sensitivity of SPR sensors cannot benefit from increasing the interaction length of the sensor as is common in sensors employing guided modes of dielectric waveguides (see Sec. 1.1).

The propagation constant of the SPW is always greater than that of the optical wave propagating in the dielectric. Therefore, the SPW cannot be excited directly by an incident optical wave at a planar metal-dielectric interface. The momentum of the incident optical wave has to be increased to match that of the SPW. This is commonly achieved using (glass) prism couplers (Fig. 1.6(a)), integrated optical waveguides (Fig. 1.6(b)), or diffraction gratings (Fig. 1.6(c)).

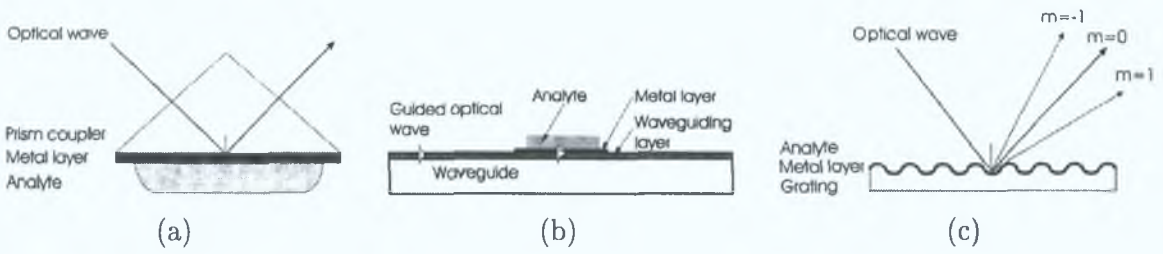

Figure 1.6: Examples of configurations commonly used in SPR-based sensors for efficient excitation of the SPW: (a) prism coupler-based SPR system (ATR method), (b) optical waveguide-based SPR system, (c) grating coupler-based SPR system. (From Homola et al. [31].)

There are two main techniques that have been commonly used in SPR-based sensors [31, 32]. The first one employs the measurement of the *intensity* of the optical wave *near* the resonance [33, 34, 35]. With reference to Figs. 1.5(a) and 1.6(a), monitoring changes in the refractive index of the dielectric above the metal layer can be achieved by measuring the changes of reflectivity ΔR at a given incident angle below or above the angular position of the SPR. An equivalent principle is used in the configuration employing an integrated optical waveguide [11, 36, 37, 38, 39, 40], as shown in Fig. 1.6(b). In this case, the attenuation of the guided mode in the region containing the metal layer is determined by the coupling of the guided wave to the SPW and the attenuation of the SPW. The coupling efficiency is strongly affected by the refractive index of the analyte above the metal layer, which provides a very sensitive transduction mechanism.

The second approach employs the measurement of the resonant condition for which the SPR occurs. This is typically done either be determining the *angular position* [41, 42] of the SPR dip (see $\Delta\theta$ in Fig. 1.5(a)) or the *wavelength* [43, 44, 45, 46, 47, 48, 49, 50] of the interrogating light at which the SPR occurs. The angular interrogation employs the Kretschmann configuration [51] depicted in Fig. 1.6(a) and a highly focused laser beam providing the interrogation in a sufficiently broad angular range. The angular profile is detected by a position sensitive detector (CCD or a linear detector array) which allows monitoring of the changes $\Delta\theta$ of the angular position of the SPR dip (see Fig. 1.5(a)) in response to changes of the analyte's refractive index.

In the wavelength interrogation of the SPR, a light source with a broad spectral range is used. Keeping the incident angle constant, the wavelength for which the SPR occurs can be monitored by a spectrometer. Recently, this approach has been successfully employed in a miniature and very compact fibre-optic based sensor by Slavík et al. [49, 50]. The schematic diagram of the sensor probe is depicted in Fig. 1.7.

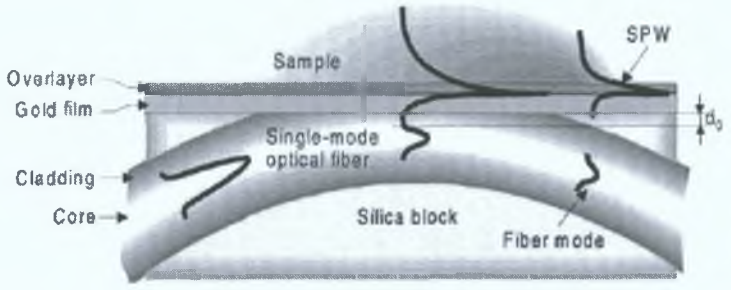

Figure 1.7: A schematic diagram of the SPR sensing structure based on a side-polished single-mode fiber (from Slavík et al. [49, 50]).

Similarly to the refractometric transduction mechanism discussed in Sec. 1.1, the SPR-based technique can achieve resolution in the changes of the refractive index of the analyte in the order of 5×10^{-7}–1×10^{-5}. Results obtained recently by Nenninger et al. [48] show that it could be decreased even further by employing long-range surface plasmon waves.

This shows that the SPR-based sensors are a very attractive class of optical chemical sensors. Their great potential in the biotechnology, medical and pharmaceutical applications has been successfully demonstrated not only under laboratory conditions but was also developed into commercially available sensor systems (BIAcore [52], Texas Instruments [53], Quantech [54], BioTuL BioInstruments [55]).

1.3 Absorption-based optical chemical sensors

Absorption-based optical chemical sensors can be divided into two main categories. Those in the first category probe the *intrinsic* absorption properties of the studied analyte. Typical gases of interest, such as CO_2, ammonia, methane, CO, H_2O and others, are characterised by specific absorption peaks in the (near) infra-red (IR) region. Using a light source whose emission spectrum overlaps with these peaks, one can quantify the gas concentration by determining the intensity of the light transmitted through the volume containing the gas. While this approach is very efficient and potentially simple, it can also be limiting in the range of applications that can be addressed. The limitations arise from two main reasons. Firstly, the analyte might not have an intrinsic spectral feature which could be accessible by the available light sources. Secondly, the spectral characteristics of the analyte might overlap with absorption spectra of some parasite species which could introduce undesirable effects of non-specific sensor response or cross-sensitivity.

In order to circumvent these problems, another approach to absorption-based optical chemical sensing is often employed. Instead of exploiting the intrinsic spectral properties of the analyte alone, a *reagent chemistry* can be physically confined in a matrix located at, near

or in a waveguide which is used for the delivery of the interrogating light. The main advantage of this approach is that the reagent is usually selected so as to facilitate an *analyte-specific* reaction. This reaction results in a change of the absorption properties of the matrix which can be directly monitored by detecting the light intensity at the output of the waveguide.

1.3.1 Direct probing of intrinsic absorption properties of the analyte

Direct probing of intrinsic absorption properties of the analyte is employed in many industrial and environmental applications. Recently reported developments in this area include, for example, sensor systems for monitoring of gas dynamics, emission of combustion gases in aeropropulsion or car engines [57], monitoring and controlling of NH_3 [58] and CO_2 levels in bio-reactors for water treatment technologies [59], measurement of the levels of CO_2 or explosive gases in room air [60], remote sensing of CO in vehicle exhaust [61], etc.

A schematic diagram of the optical arrangement, which is common in the above mentioned sensor systems, is shown in Fig. 1.8. The characteristic peaks of the (near) IR absorption spectrum of the analyte molecules can be probed by a narrow-band tunable light source (such as a tunable laser diode) and the attenuation of the light intensity monitored by a detector (such as a photodiode). Another possibility is to use a broad-band light source and a spectrometer which can detect the variations of the strength of the absorption peaks.

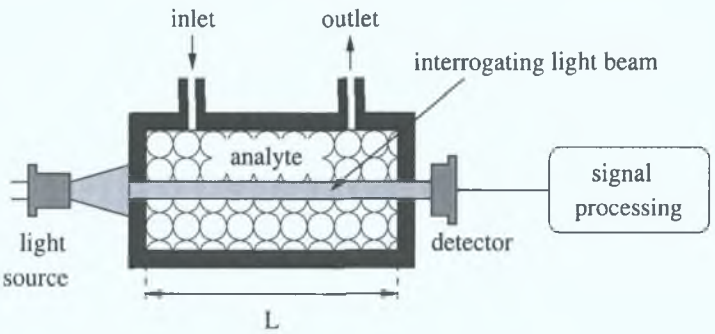

Figure 1.8: A schematic diagram of the absorption-based sensor system employing direct probing of the intrinsic absorption properties of the analyte.

The limit of detection of this technique is primarily determined by the interaction length L and the quality of the light source and detector. If the absorption of the analyte is very low, detectable levels of the light attenuation can be obtained by increasing the interaction length. However, this expansion is restricted by practical limitations (such as the dimensions of the laboratory or the size of a gas tank) and is undesirable in compact and portable sensor systems.

1.3.2 Absorption-based sensor systems employing fibre optics

Absorption-based chemical sensors were the very first type of fibre-optics chemical sensors described in the literature [62]. These sensors use the optical fibres as "pipes" to guide light to and from the region where the absorption properties of either the analyte itself or the analyte-sensitive reagent are probed. Several configurations, which are commonly used, are briefly discussed below.

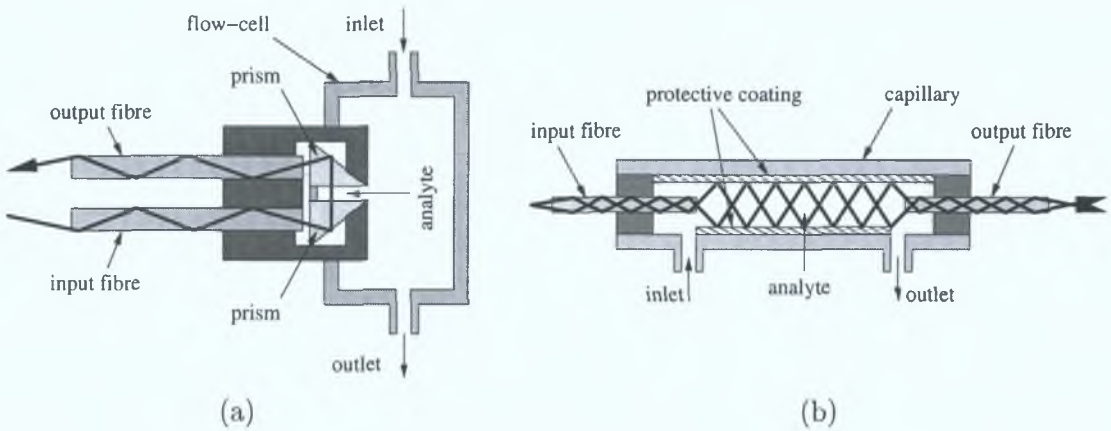

Figure 1.9: Schematic diagrams of fibre-optic absorption-based optical chemical sensors. The input and output fibres are used solely for delivery and collection of the light interrogating the analyte. (From (a) Yokota & Yoshino [63] and (b) Dress et al. [64].)

A fibre-optics version of the direct absorption measurement described in Sec. 1.3.1 was developed by Yokota & Yoshino [63] and Dress et al. [64]. They both used fibres solely for delivery/collection of the interrogating light to/from the cell containing the analyte. The sensor cell reported by Yokota & Yoshino contained two right-angle prisms separated by a gap where the analyte could flow. The light delivered by the input fibre was reflected by the first prism, partially absorbed in the gap by the analyte and reflected towards to output fibre by the second prism, as shown in Fig. 1.9(a). The configuration reported by Dress et al. used a capillary, the core of which facilitated both flow of the analyte and guiding of the interrogating light, as depicted in Fig. 1.9(b).

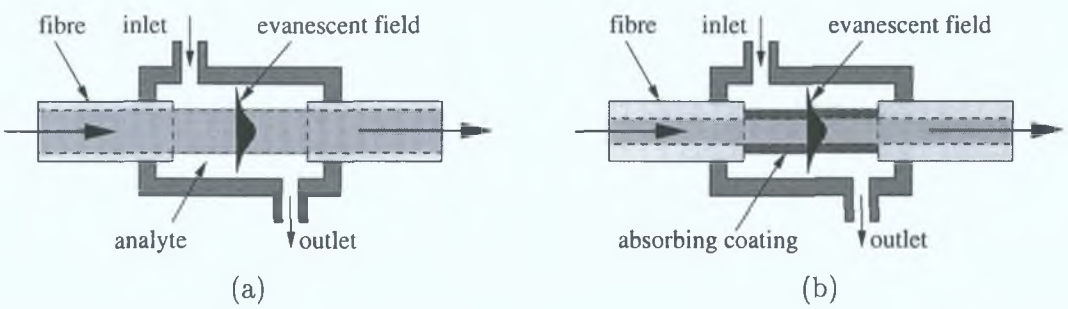

Figure 1.10: Schematic diagrams of generic configurations of absorption-based optical chemical sensors employing declad fibres. In the configuration (a), the evanescent field interrogates directly the absorbing analyte surrounding the fibre core. In the configuration (b), the evanescent field interrogates a thin film which is coated on the fibre core and contains analyte sensitive reagents.

An important advantage of optical fibres is the possibility of employing the evanescent field of the guided light to interact with the sensing environment along a specific length. Typically, in the interaction region, the cladding of the fibre is removed, which provides direct access of the evanescent field of the guided mode(s) to the analyte surrounding the fibre, as shown in Fig. 1.10(a). In this manner, Li & Meichsner [65] were able to monitor in-situ plasma polymerisation in a gas discharge. Matějec et al. [66] have shown that the sensitivity of evanescent wave absorption can be further increased by a properly designed

radial variation of the refractive index of the fibre core.

Many fibre-optic absorption-based chemical sensors use declad fibres coated with a thin film containing the sensing chemistry [67, 68, 69, 70, 71]. This configuration is schematically depicted in Fig. 1.10(b). The attenuation of the optical power propagating along the fibre is determined, among other factors, by the absorption coefficient of the coating. This is due to the fact that the field corresponding to the guided mode(s) penetrates into the absorbing film. Since the absorption properties of the coating are chosen so as to respond to a specific analyte, the analyte concentration can be quantified by measuring the optical power transmitted through the fibre.

1.3.3 Absorption-based sensors employing planar waveguides

Absorption-based optical chemical sensors employing planar waveguides use the same principle as their fibre-optics counterparts. In the work by Pandraud et al. [72] and Maims et al. [73], the guiding layer is uncovered and the evanescent wave has direct access to the analyte above the waveguide, as shown in Fig. 1.11(a). Planar waveguides, whose guiding layer is covered by a thin absorbing film (see Fig. 1.11(b)) were used, e.g., by Lavers et al. [74] and Ock et al. [75]. Kim and co-workers [76] went even further and developed a sensor system where the thin absorbing layer acted at the same time as the guiding layer, as shown in Fig. 1.11(c). In this case, the greater "concentration" of the electromagnetic field in the sensing (i.e., guiding) layer provided enhanced sensitivity. Wang et al. [77] recently reported on an absorption-based sensor system employing surface plasmon resonance (see Sec. 1.2) to enhance the absorption of the molecules adsorbed on the planar surface.

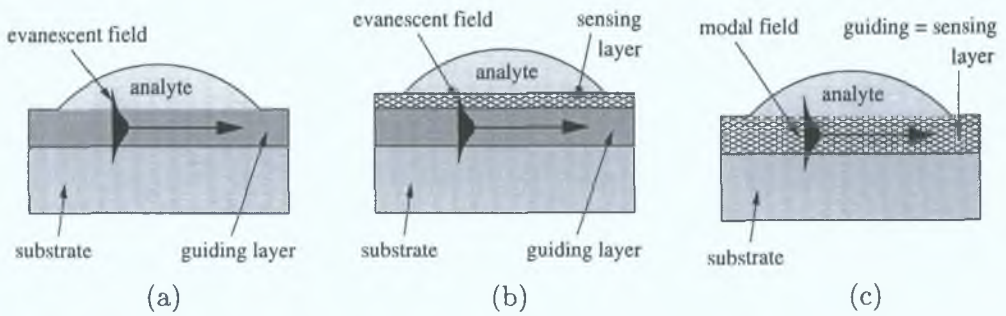

Figure 1.11: Schematic diagrams of absorption-based optical chemical sensors using planar waveguides. In the configuration (a), the evanescent field interrogates directly the absorbing analyte above the guiding layer. In the configuration (b), the evanescent field interrogates a thin film (sensing layer) which is coated on top of the guiding layer and contains analyte sensitive reagents. In the configuration (c), the analyte sensitive layer acts at the same time as the guiding layer.

The configurations employing planar waveguides provide certain advantages when compared to their fibre-optics counterparts. In particular, they can be manufactured using techniques commonly used in the fabrication of integrated optical devices. Furthermore, the geometry of the sensing platform allows for integration of more reference and signal channels sensitive to different analytes on a single chip, thus allowing the fabrication of compact, miniature and possibly disposable multi-analyte sensor devices.

1.3.4 Detector-free absorption sensor based on DOE

An interesting configuration of an absorption-based optical chemical sensor was developed by Nakajima et al. [82]. They used an array of zones containing pH indicator separated by indicator-free zones. When the pH of the surrounding medium changed, the zones containing the pH indicator became more absorbing. Since the typical lateral dimension of the zones was in the order of the wavelength of the interrogating light, this change resulted in the transformation of the beam into a diffraction pattern, as shown in Figs. 1.12(a) and (b). Thus, the analytical result (i.e., the change of pH) could be displayed without any detector, electronics or recorder. All the relevant information could be acquired by visual perception. If the zones containing the pH indicator are designed as more advanced diffractive optical element, this approach could be used as an on-site display of the analytical results using letters, figures or even diagrams, as shown in Fig. 1.12(c).

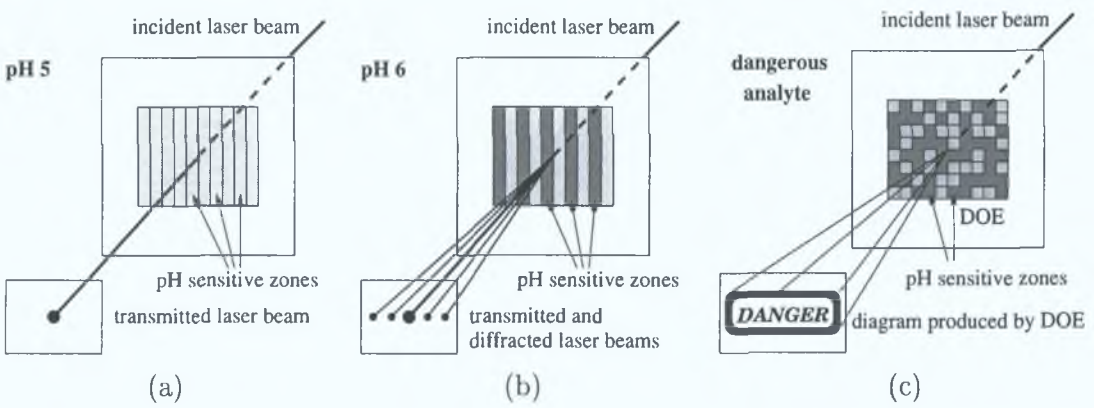

Figure 1.12: A schematic diagram of a detector-free absorption-based sensor using microscopic-size analyte sensitive zones separated by analyte insensitive zones. See text for more details. (From Nakajima et al. [82].)

1.4 Luminescence-based optical chemical sensors

Luminescence-based optical chemical sensors can be divided into three main categories. Those in the first category probe the *intrinsic* luminescence emitted by the studied analyte upon illumination by the excitation light. Although this approach can be simple and efficient, only a very few analytes of interest emit luminescence that is sufficiently bright to be practically exploited using simple and inexpensive sensor systems. This drawback limits the range of applications where this approach can be used.

A variation of this approach is based on the idea that the luminescence is provided by molecules which are labelled with a luminescent moiety and which bind specifically to the analyte of interest. This so-called *luminescently labelled technique* has been successfully implemented in biotechnology, medical and pharmaceutical applications.

Luminescence-based immunosensors [83] using a sandwich assay format are one type of sensor employing this technique. A schematic diagram of such a sensor configuration is shown in Fig. 1.13. To detect the presence of antigens in the sample solution, antigen-specific antibodies are firstly attached onto the surface of a planar waveguide. The solution

in which the presence of the antigens is to be determined is then passed over the treated waveguide surface. If the antigens are present, they bind to the surface-attached antibodies. Subsequently, a solution containing labelled antibodies, which can probe this binding, is passed over the waveguide surface.

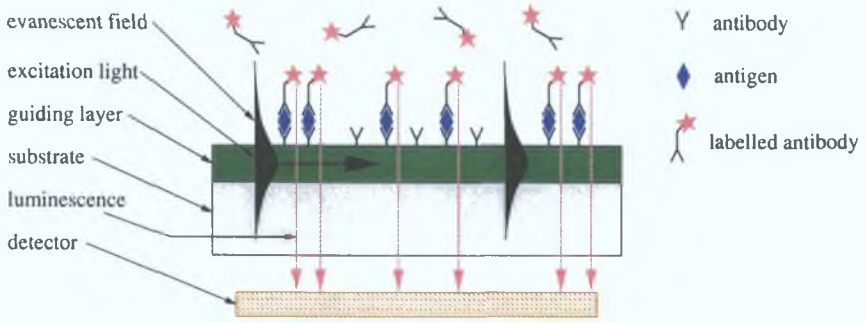

Figure 1.13: A schematic diagram of the configuration where specific antigen-antibody binding on the waveguide surface is monitored by detecting the luminescent light excited by the evanescent wave.

This method exploits the fact that the electromagnetic field of a guided mode is not confined entirely in the guiding layer but a fraction penetrates into the surrounding media in the form of an evanescent field. (A typical value of the penetration depth is in the order of wavelength, i.e., roughly 50–500 nm.) Therefore, if the luminescently labelled molecules are present in this region and the wavelength of the propagating light matches the excitation spectrum of the luminescent moiety, the emitted luminescence directly indicates the specific surface binding, i.e., the presence of the antigens in the sample solution, as shown in Fig. 1.13. On the other hand, if the antigens are not present, the specific binding does not take place and consequently there is no luminescence emitted [84, 85, 86].

It was pointed out in sections 1.1 and 1.2 that another tool for monitoring specific binding or adsorption of molecules at surfaces is provided by refractometric techniques employing surface plasmon resonance, grating couplers or integrated optical interferometers. However, the signals of these devices are directly associated with the adsorbed molecular mass. Consequently, the sensitivity of these configurations is not always sufficient for detection of small analyte molecules at small concentration levels. The advantage of the above mentioned immunoassay sensor is derived from the fact that it provides an improved sensitivity independent of the molecular size.

The immunoassay method was successfully employed and expanded to multi-analyte immunosensing by Rowe et al. [86]. They used a patterned array of recognition elements immobilised on a surface of a planar waveguide. Using laser line generator and imaging by a CCD camera, they could successfully correlate the positions of fluorescent signal with the identity of analyte present in clinical samples.

Another class of luminescence-based sensors, which is most often applied to chemical sensing, is based on the idea that the luminescence of some molecules can be *quenched* by the presence of specific analytes. The quenching is manifested as change in either the luminescence *intensity* [87, 88, 89, 90, 91, 92, 93] or *life-time* [94, 95, 96, 97, 98, 99, 100, 101, 102, 103, 104, 105, 106] or both. It is not the purpose of this brief introduction to

discuss various mechanisms involved in the luminescence quenching. Instead, the following discussion focuses on the description of different *instrumentation techniques* used to monitor these variations.

Understandably, the most important step of this monitoring process is the *detection* of luminescence, i.e., the transformation of the information carried by the light into a form suitable for further processing (such as an electrical signal). Many different approaches, which facilitate the collection of luminescence, have been reported in the literature. The most common ones are described below.

1.4.1 Collection of luminescence by fibre tip/bundle

Collection of luminescence by the tip of an optical fibre or a fibre bundle is frequently used in applications where luminescence generated in remote or unaccessible regions needs to be detected [87, 89, 90, 103, 104, 105, 106, 107, 108, 109, 110, 111, 112]. Luminescence collection by fibre optics is also popular in applications where the emission spectrum of luminescence is of importance [113, 114, 115, 116]. In these applications, portable and easy-to-handle spectrometers with fibre-optics input connectors are often used.

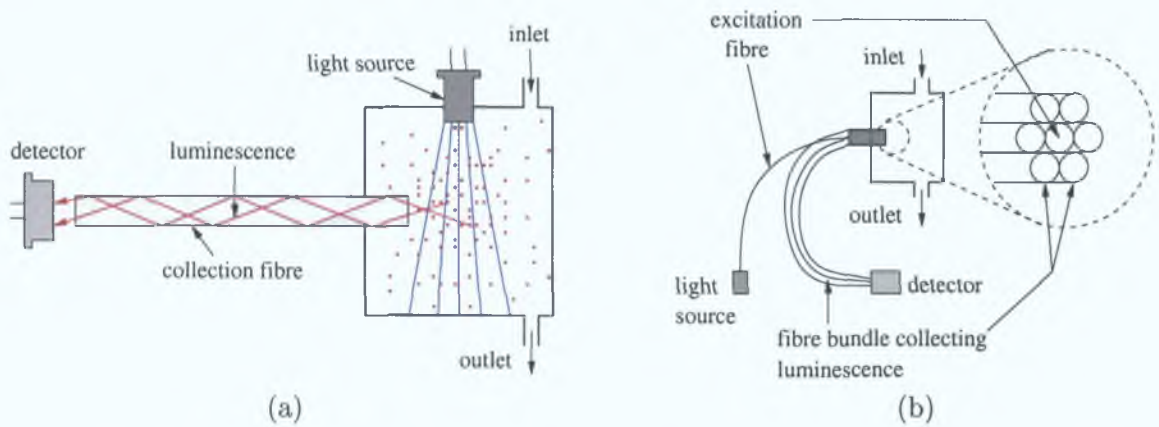

Figure 1.14: A schematic diagram of sensor configurations employing (a) fibre tip and (b) fibre bundle for collection of luminescence.

Typical configurations employing the fibre tip and fibre bundle for the luminescence collection are shown in Fig. 1.14(a) and 1.14(b), respectively. In the configuration depicted in Fig. 1.14(a), the fibre is used to access the region where the luminescence is generated. Due to the small dimensions of the fibre tip (typical core diameters do not exceed 1 mm) and limited numerical aperture, the collection efficiency is very poor. The collection efficiency can be slightly improved by using a fibre bundle, as shown in Fig. 1.14(b). A fibre bundle provides an additional advantage, namely the possibility of using one (or more) of the fibres to deliver the excitation light to the site.

1.4.2 Direct detection of luminescence emitted into free space

Many luminescence-based optical chemical sensors employ a thin luminescent film or array of luminescent spots which emit luminescence into the free space surrounding the substrate. The detection of luminescence is facilitated by a detector located directly above or below

the planar substrate containing the film/spots [85, 86, 91, 92, 96, 97, 99, 116, 117, 118]. This configuration is particularly useful if a spatial resolution of the luminescence intensity is required. In this case, a detector array (e.g., a CCD camera) is typically placed under the substrate to monitor the luminescence emitted by the array of spots. Examples of typical configurations are shown in Fig. 1.15.

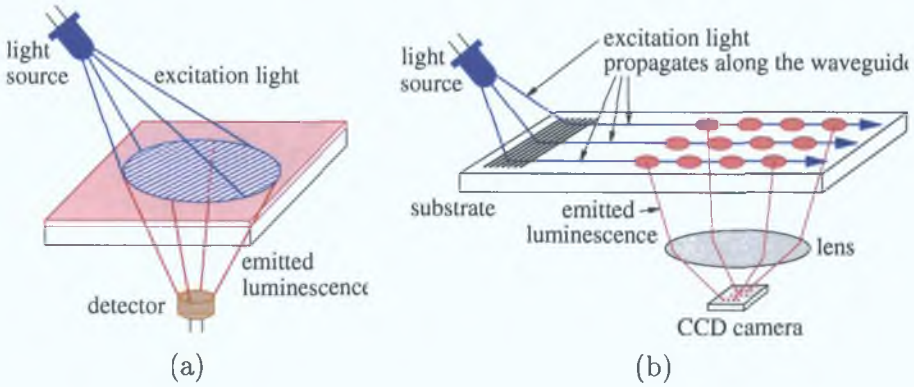

Figure 1.15: A schematic diagram of sensor configurations employing direct detection of the emitted luminescence by a detector located directly under the substrate. Configurations (a) and (b) employ a thin luminescent film and a two-dimensional array of luminescent spots, respectively.

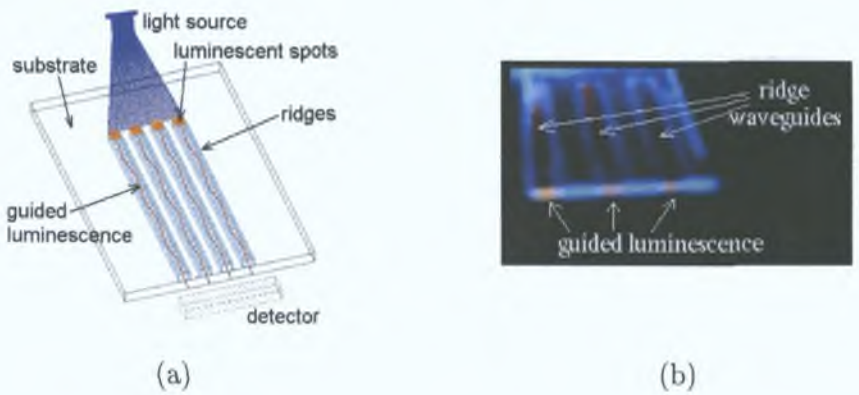

Figure 1.16: A schematic diagram (a) and image (b) of a ridge waveguide structure deposited on a Si substrate. Luminescent spots are deposited on one end of the ridges. When the luminescence is excited by a blue LED, it is coupled into the guided modes and can be observed at the other end of the ridge waveguides. The red areas corresponding to the luminescence spots out-coupled from the ridge waveguides are clearly visible in the image. (From MacCraith et al. [131, 132].)

1.4.3 Detection of luminescence entrapped in the waveguide

It has been predicted theoretically [119, 120, 121, 122, 123, 124, 125] and observed experimentally that the luminescence radiated by molecules located at or near a waveguide can be efficiently coupled into the guided modes. This was successfully exploited using both fibre-optic [124, 125, 126, 127, 128] and planar waveguide [88, 95, 122, 129, 130, 131] configurations. The planar waveguide configuration is particularly attractive, since it allows construction of a sensor chip suitable for multi-analyte sensing. If, for example, a number of ridge waveg-

uides, each containing a luminescent spot sensitive to a different analyte, is deposited on a planar substrate (see Fig. 1.16), an integrated luminescence-based optical chemical sensor can be constructed.

1.4.4 Processing of the detected luminescence

Once the luminescence is detected and successfully converted into electrical signal, the relevant information can be extracted by subsequent signal processing. In principle, there are two parameters characterising luminescence which carry valuable information—luminescence *intensity* and *life-time*.

In intensity-based sensor systems, monitoring the levels of detected luminescence intensity provides valuable information about the analyte concentration, specific antigen-antibody binding or other processes. The information obtained by the measurement of luminescence intensity is, however, not reliable for absolute quantitative analysis. This is mainly due to the fact that the detected intensity is prone to alterations by non-specific effects, such as photo-bleaching, leaching, misalignment of the source of the excitation light or detector, etc. Nevertheless, this principle is widely used in biotechnology, genomics or other medical applications.

A method, which is (to a high degree) free of the undesirable effects encountered in the intensity-based luminescence sensor systems, is based on the measurement of the luminescence life-time [94, 95, 96, 97, 98, 99, 100, 101, 102, 103, 104, 105, 106]. It follows from the physical processes involved in the act of emission of photons that the intensity of luminescence decays exponentially after the excitation light was abruptly switched off. Although this exponential decay can be monitored directly by, e.g., time-resolved spectroscopy or by a CCD camera capable of time-delayed image acquisition [134], these methods are not widely used since they are rather complicated and require expensive instrumentation.

A simpler and more cost-effective option for the luminescence life-time measurement is offered by a method called phase fluorometry. This method employs excitation of luminescence by a light source with periodically (e.g., sinusoidal or square-wave) alternating intensity. The same physical laws, which describe the luminescence decay, imply that the luminescence intensity generated by the alternating excitation light is phase-shifted with respect to the excitation light. In particular, if the intensity of the excitation light varies as $I_{\mathrm{exc}} = I_{\mathrm{exc},0}\sin(2\pi f t)$, the observed luminescence intensity varies as $I_{\mathrm{lum}} = I_{\mathrm{lum},0}\sin(2\pi f t + \Phi)$. The phase shift Φ is related to the frequency f of the variation of the excitation light intensity and the luminescence life-time τ by $\tan\Phi = 2\pi f\tau$. Therefore, the luminescence life-time can be directly monitored by measuring the phase shift between the excitation light and detected luminescence [96, 99, 100].

If the luminescence life-time is sufficiently long ($\tau \gtrsim 1$–$10\,\mu$s), relatively simple electronic circuits working at moderate frequencies ($f \approx 10$–$100\,$kHz) can be designed to obtain measurable values of the phase shift. For very short life-times, different approaches have been developed, an example of which is the dual luminophore referencing (DLR) method [135, 136, 137, 138].

Another important task in the measurement of the luminescence life-time is to efficiently avoid the detection of the excitation light. This is usually achieved by employing appropriate

optical filters. However, if the luminescence intensity is too weak, this pure optical filtering might not be sufficient. One method providing an elegant solution to this problem exploits the idea that the emitted luminescence can be efficiently guided to a different location where it can subsequently be detected even with a filter-free detection system (see Sec. 1.4.3). Recently, another approach was developed by Langer et al. [139]. They proposed a special electronic treatment of the detected signal consisting of components corresponding to both the excitation and luminescence light. After this treatment, the phase shift of the luminescence can be obtained independently of the intensity of the excitation light.

1.5 Aims of this work

In the previous sections of this chapter, the most common principles, methods and techniques employed in the area of optical chemical sensing and bio-sensing were summarised and briefly discussed. In the context of this brief account, it is now possible to outline the aims of the research programme described in this dissertation.

The main interests of the laboratory where this research was conducted involve the development and use of both absorption and luminescence-based sensor systems employing waveguide structures coated with thin sensing films. A number of such sensors has been successfully developed and tested [140]. The aim of this work was to develop a rigorous electromagnetic theory which would provide a detailed understanding of the operation of such sensor systems and which would be capable of identifying the conditions by which their performance could be optimised. The second aim was to implement these theoretical predictions in the design and fabrication of prototype sensor systems and to provide experimental verification of their improved performance.

In the following sections, these aims are described in further detail separately for the absorption and luminescence-based optical chemical sensors.

1.5.1 Absorption-based optical chemical sensors

In the case of absorption-based sensors employing analyte-sensitive reagents immobilised in a suitable matrix, the analyte has to penetrate inside the matrix in order to induce changes in its absorption properties. Typically, it is the dynamics of this diffusion process that determine the response time of the sensor system. To minimise the response time of the sensor, conditions should be provided that minimise the time required for the diffusion process to reach equilibrium. Platforms employing *thin films* coated on a waveguide structure provide one possible way of achieving this.

Understandably, thinner sensing films result in a faster response of the sensor. However, as they also contain lower amount of analyte-sensitive reagents, they could also lead to a decrease in the sensor sensitivity. It was already mentioned in Sec. 1.3 that the sensitivity can be improved by increasing the interaction length over which the light interrogates such sensing films. The interaction length can, however, be limited by some other factors dictated by the application. Therefore, it is necessary to identify different ways of improving the sensor sensitivity.

The issue of the optimisation of the sensor performance has been dealt with extensively

in the literature [80, 84, 123, 141, 142, 143, 144, 145, 146, 147]. Most of these theoretical studies focused, however, on sensor systems employing mono-mode waveguide structures and evanescent-wave (EW) absorption. These sensors can be fabricated using technology typically employed in the area of microelectronics and integrated optics. Although the manufacture process is well established, it requires several steps [72, 74] which makes it rather complicated and expensive. More difficulties are encountered when one wants to incorporate the mono-mode waveguide platform into a functional sensor system. It is well known that efficient coupling of light into mono-mode waveguides requires very precise alignment of all the elements involved and can therefore be very sensitive to vibrations, temperature variations and other factors. Last but not least, mono-mode waveguide platforms typically require high quality light sources, such as lasers or laser diodes, which are not yet suitable for the mass production of low-cost sensor systems.

In comparison with mono-mode waveguides employing EW sensing techniques, multimode waveguide platforms provide a number of advantages, such as ease of fabrication, handling and less elaborate in/out-coupling of light. However, to the author's knowledge, there is no theoretical analysis available in the literature that thoroughly describes the operation of such sensor systems, with particular emphasis to non-EW sensing techniques. Therefore, one of the aims of this dissertation is to develop a rigorous electromagnetic *theory* suitable for the description of the *operation* of absorption-based optical chemical sensors employing multimode waveguide platforms coated with thin analyte-sensitive films. Using the theory, one should be able to identify conditions for which the performance of such sensor systems could be optimised. In addition to the development of the theory itself, this work also aimed to implement the developed theoretical predictions in the design and fabrication of a compact and low-cost prototype absorption-based sensor system.

1.5.2 Luminescence-based optical chemical sensors

As mentioned in Sec. 1.4, many luminescence-based optical chemical sensors employ quenching of the luminescence intensity or life-time as the transduction mechanism for the detection of the analyte. Due to the same reasons as those mentioned in Sec. 1.5.1, sensor systems employing thin luminescent films are particularly attractive. However, the use of thin films usually means that the intensity of the emitted luminescence is low and can be a limiting factor in the performance of the sensor system. Immunosensors, which are very attractive in biotechnology, medical and pharmaceutical applications are also highly affected by the low intensity of luminescence emitted by the surface attached molecules (see Sec. 1.4).

The problems related to low values of the luminescence intensity have been addressed by several authors. Liebermann et al. [148] exploited the enhancement of the amplitude of the excitation light in the close vicinity of the surface provided by the efficient excitation of a surface plasmon wave. Blair & Chen [149] showed that luminescence of molecules can be enhanced by the use of planar cylindrical resonant optical cavities. Recently, very promising results related to the enhancement of the luminescence quantum yield have been reported by Mayer et al. [150] and Lakowicz et al. [151]. They showed that the use of metal nanoparticles can have a very positive influence on the intensity of luminescence emitted by molecules located in their close vicinity. Enhancement of the quantum yield in the order of 100-1000

was reported.

Although these new developments are certainly valuable for the improvement of the performance of luminescence-based chemical sensors and bio-sensors, they do not address the most important issue common to most of them, namely the *efficiency of the luminescence capture*. It has been shown by several authors that both the spatial distribution and lifetime of the emitted luminescence can be significantly altered if the radiating molecules are located in the vicinity of dielectric [119, 152, 153, 154, 155], metal [156, 157, 158, 159] or corrugated [160, 161] surfaces. These predictions, in particular those related to the spatial anisotropy of the emitted luminescence, were used in the design and fabrication of configurations with improved luminescence capture efficiency, such as those employing a paraboloid glass segment [153] or gratings [161].

The aim of this work was to accommodate and expand the above cited theoretical studies to the area of optical chemical sensors, in particular those employing thin films or more general planar multilayer structures as sources of the luminescent light. The purpose was to identify the main reasons why the conventional techniques do not provide efficient detection of the luminescence emitted from thin films and to design a number of configurations which would enhance the capture efficiency.

In the area of immunosensors, the luminescence generated by labelled surface-attached molecules is of primary importance. This is because it provides a *direct* indication of the specific binding between the surface-attached receptors and the analyte molecules flowing in the bulk above the surface. The detection of surface-generated luminescence is normally achieved by means of evanescent-wave excitation which provides surface-specific excitation of the luminescent molecules, as discussed in Sec. 1.4. Although this technique is widely used in the immunosensor applications [85, 86, 116, 118], it is not particularly efficient. This has two primary reasons. A typical coupling technique, such as that employing grating couplers, is not particularly efficient and only a small fraction (typically a few percent) of the optical power generated by the light source is coupled into the guided modes of the waveguide structure. Furthermore, once the light is coupled into and propagating along the waveguide, only a small fraction of its power (again typically a few percent) is contained in the evanescent field which is used for the excitation of the surface-attached molecules (see Fig. 1.13). Taking into account both of these factors, it is understandable why this technique provides only a very inefficient way of generating a surface-specific luminescence.

In this context, additional aim of this work was to propose a novel technique providing the detection of luminescence generated by molecules located specifically at or near a surface of a substrate while employing *direct illumination*, i.e., using the full power of the light source, for their excitation. The theoretical background of this technique is described using the model mentioned above. Furthermore, the experimental set-up and preliminary results demonstrating the feasibility of this method are presented.

1.5.3 Summary of the aims of the dissertation

The aims of this work, which were described in detail in the above sections, can be summarised as follows:

1. **Absorption-based optical chemical sensors:**
   (a) to develop a theory describing the operation of absorption-based optical sensors employing a multimode planar waveguide platform,
   (b) to discuss the implications of the theory for the design of such sensor systems and to identify conditions for which their performance can be optimised,
   (c) to verify the theory experimentally,
   (d) to implement the theoretical prediction in the design and fabrication of a compact and low-cost prototype absorption-based sensor system and to report on its performance.
2. **Luminescence-based optical chemical sensors:**
   (a) to develop a theory describing the radiation of molecules located near a surface or embedded within an arbitrary planar multilayer system,
   (b) to discuss the implications of the theory with regard to the efficiency of the luminescence capture and to propose configurations using which the collection efficiency could be improved,
   (c) to verify the theory experimentally,
   (d) to design and test the performance of configurations with improved efficiency of the luminescence capture,
   (e) to develop both the theoretical background and experimental set-up for a method enabling the detection of the surface-generated luminescence excited by direct illumination.

1.6 Bibliography for Chapter 1

[1] Y. Kostov and G. Rao. Low-cost optical instrumentation for biomedical measurements. *Review of Scientific Instruments*, 71(12):4361–4374, 2000.

[2] J. Spinke, N. Oranth, Ch. Fattinger, H. Koller, C. Mangold, and D. Voegelin. The bidiffractive grating coupler: application to immunosensing. *Sensors and Actuators*, B 38–39:256–260, 1997.

[3] M. Wiki, H. Gao, M. Juvet, and R. E. Kunz. Compact integrated optical sensor system. *Biosensors and Bioelectronics*, 16:37–45, 2001.

[4] R. G. C. Oudshoorn, R. P. H. Kooyman, and J. Greve. Refractive index and layer thickness of an adsorbing protein as reporters of monolayer formation. *Thin Solid Films*, 284–285:836–840, 1996.

[5] D. Clerc and W. Lukosz. Direct immunosensing with an integrated-optical output grating coupler. *Sensors and Actuators*, B 40:53–58, 1997.

[6] D. Clerc and W. Lukosz. Real-time analysis of avidin adsorption with an integrated-optical output grating coupler: adsorption kinetics and optical anisotropy of adsorped monomolecular layers. *Biosensors and Bioelectronics*, 12(3):185–194, 1997.

[7] M. Wiki and R. E. Kunz. Wavelength-interrogated optical sensor for biochemical applications. *Optics Letters*, 25(7):463–465, April 2000.

[8] R. E. Kunz. *Integrated optical circuits and components.* Marcel Dekker, Inc., New York, Basel, 1999. `http://www.dekker.com`.

[9] J. Dübendorfer, R. E. Kunz, G. Jobst, I. Moser, and G. Urban. Integrated optical pH sensor using replicated chirped grating coupler sensor chips. *Sensors and Actuators*, B 50:210–219, 1998.

[10] W. Lukosz. Integrated optical chemical and direct biochemical sensors. *Sensors and Actuators*, B 29:37–50, 1995.

[11] W. Lukosz, Ch. Stamm, H. R. Moser, R. Ryf, and J. Dübendorfer. Difference interferometer with new phase-measurement method as integrated-optical refractometer, humidity sensor and biosensor. *Sensors and Actuators*, B 38–39:316–323, 1997.

[12] W. Lukosz. Integrated-optical and surface-plasmon sensors for direct afinity sensing. part II: Anisotropy of adsorbed or bound protein adlayers. *Biosensors and Bioelectronics*, 12(3):175–184, 1997.

[13] Ch. Stamm and W. Lukosz. Integrated optical difference interferometer as immunosensor. *Sensors and Actuators*, B 31:203–207, 1996.

[14] Ch. Stamm, R. Dangel, and W. Lukosz. Biosensing with the integrated-optical difference interferometer: dual-wavelength operation. *Optics Communications*, 153:347–359, August 1998.

[15] R. G. Heideman, G. J. Veldhuis, E. W. H. Jager, and P. V. Lambeck. Fabrication and packaging of integrated chemi-optical sensors. *Sensors and Actuators*, B 35–36:234–240, 1996.

[16] R. G. Heideman and P. V. Lambeck. Remote opto-chemical sensing with extreme

sensitivity: design, fabrication and performance of a pigtailed integrated optical phase-modulated mach-zehnder interferometer system. *Sensors and Actuators*, B 61:100–127, 1999.

[17] E. F. Schipper, A. J. H. Bergevoet, R. P. H. Kooyman, and J. Greve. New detection method for atrazine pesticides with the optical waveguide mach-zehnder immunosensor. *Analytica Chimica Acta*, 341:171–176, 1997.

[18] E. F. Schipper, A. M. Brugman, C. Dominguez, L. M. Lechuga, R. P. H. Kooyman, and J. Greve. The realisation of an integrated mach-zehnder waveguide immunosensor in silicon technology. *Sensors and Actuators*, B 40:147–153, 1997.

[19] B. Drapp, J. Piehler, A. Brecht, G. Gauglitz, B. J. Luff, J. S. Wilkinson, and J. Ingenhoff. Integrated optical mach-zehnder interferometers as simazine immunoprobes. *Sensors and Actuators*, B 38–39:277–282, 1997.

[20] S. Busse, M. DePaoli, G. Wenz, and S. Mittler. An integrated optical Mach-Zehnder interferometer functionalized by β-cyclodextrin to monitor binding reactions. *Sensors and Actuators*, B 80:116–124, 2001.

[21] H.-M. Schmitt, A. Brecht, J. Piehler, and G. Gauglitz. An integrated system for optical biomolecular integration analysis. *Biosensors and Bioelectronics*, 12(8):809–816, 1997.

[22] A. Brecht, J. Piehler, G. Lang, and G. Gauglitz. A direct optical immunosensor for atrazine detection. *Analytica Chimica Acta*, 311:289–299, 1995.

[23] V. Kochergin, I. Avrutsky, and Y. Zhao. High sensitivity waveguide grating sensor based on radiative losses. *Biosensors and Bioelectronics*, 15:283–289, 2000.

[24] J. P. Lenney, N. J. Goddard, J. C. Morey, R. D. Snook, and P. R. Fielden. An electro-osmotic flow system with integrated planar optical waveguide sensing. *Sensors and Actuators*, B 38–39:212–217, 1997.

[25] Y. Ren, P. Mormile, L. Petti, and G. H. Cross. Optical waveguide humidity sensor with symmetric multilayer configuration. *Sensors and Actuators*, B 75:76–82, 2001.

[26] E. F. Schipper, R. P. H. Kooyman, A. Borreman, and J. Greve. The critical sensor: a new type of evanescent wave immunosensor. *Biosensors and Bioelectronics*, 11(3):295–304, 1996.

[27] O. Parriaux and P. Sixt. Sensitivity optimisation of a grating coupled evanescent wave immunosensor. *Sensors and Actuators*, B 29:289–292, 1995.

[28] V. A. Sychugov, A. V. Tishchenko, N. M. Lyndin, and O. Parriaux. Waveguide coupling gratings for high-sensitivity biochemical sensors. *Sensors and Actuators*, B 38–39:360–364, 1997.

[29] R. Polzius, Th. Schneider, F. F. Bier, U. Bilitewski, and W. Koschinski. Optimisation of biosensing using grating couplers: immobilisation on tantalum oxide waveguides. *Biosensors and Bioelectronics*, 11(5):503–514, 1996.

[30] H. Raether. *Surface plasmons on smooth and rough surfaces and on gratings*. Springer-Verlag, Berlin, 1988.

[31] J. Homola, S. S. Yee, and G. Gauglitz. Surface plasmon resonance sensors: review. *Sensors and Actuators*, B 54:3–15, 1999.

[32] Dev K. Kambhampati and W. Knoll. Surface-plasmon optical techniques. *Current Opinion in Colloid and Interface Science*, 4:273–280, 1999.

[33] C. Nylander, B. Liedberg, and T. Lind. Gas detection by means of surface plasmons resonance. *Sensors and Actuators*, 3:79–88, 1982.

[34] B. Liedberg, C. Nylander, and I. Lundström. Surface plasmons resonance for gas detection and biosensing. *Sensors and Actuators*, 4:299–304, 1983.

[35] M. M. B. Vidal, R. Lopez, S. Aleggret, J. Alonso-Chamarro, I. Garces, and J. Mateo. Determination of probable alcohol yield in musts by means of an spr optical sensor. *Sensors and Actuators*, B 11:455–459, 1993.

[36] R. D. Harris, B. J. Luff, J. S. Wilkinson, J. Piehler, A. Brecht, G. Gauglitz, and R. A. Abuknesha. Integrated optical surface plasmon resonance immunoprobe for simazine detection. *Biosensors & Bioelectronics*, 14:377–386, 1999.

[37] O. Hugon, P. Benech, and H. Gagnaire. Surface plasmon chemical/biological sensor in integrated optics. *Sensors and Actuators*, B 51:316–320, 1998.

[38] M. Weisser, B. Menges, and S. Mittler-Neher. Refractive index and thickness determination of monolayers by multi mode waveguide coupled surface plasmons. *Sensors and Actuators*, B 56:189–187, 1999.

[39] J. L. Elkind, D. I. Stimpson, A. A. Strong, and D. U. Bartholomew andJ. L. Melendez. Integrated analytical sensors: the use of the TISPR-1 as a biosensor. *Sensors and Actuators*, B 54:182–190, 1999.

[40] P. Tobiška, O. Hugon, A. Trouillet, and H. Gagnaire. An integrated optic hydrogen sensor based on SPR on palladium. *Sensors and Actuators*, B 74:168–172, 2001.

[41] K. Matsubara, S. Kawata, and S. Minami. Optical chemical sensor based on surface plasmon measurement. *Applied Optics*, 27:1160–1163, 1988.

[42] B. Liedberg, I. Lundstrom, and E. Stenberg. Principles of biosensing with an extended coupling matrix and surface plasmon resonance. *Sensors and Actuators*, B 11:63–72, 1993.

[43] L. M. Zhang and D. Uttamchandani. Optical chemical sensing employing surface plasmon resonance. *Electronic Letters*, 23:1469–1470, 1988.

[44] R. C. Jorgenson and S. S. Yee. A fiber-optic chemical sensor based on surface plasmon resonance. *Sensors and Actuators*, B 12:213–220, 1993.

[45] P. S. Vukusic, G. P. Bryan-Brown, and J. R. Sambles. Surface plasmon resonance on grating as novel means for gas sensing. *Sensors and Actuators*, B 8:155–160, 1992.

[46] H. P. Ho, S. Y. Wu, M. Yang, and A. C. Cheung. Application of white light-emitting diode to surface plasmon resonance sensors. *Sensors and Actuators*, B 80:89–94, 2001.

[47] G. G. Nenninger, J. B. Clendenning, C. E. Furlong, and S. S. Yee. Reference-compensated biosensing using a dual-channel surface plasmon resonance sensor system based on a planar lightpipe configuration. *Sensors and Actuators*, B 51:38–45, 1998.

[48] G. G. Nenninger, P. Tobiška, J. Homola, and S. S. Yee. Long-range surface plasmons for high-resolution surface plasmon resonance sensors. *Sensors and Actuators*, B 74:145–151, 2001.

[49] R. Slavík, J. Homola, and J. Čtyroký. Single-mode optical fiber surface plasmon resonance sensor. *Sensors and Actuators*, B 54:74–79, 1999.

[50] R. Slavík, J. Homola, J. Čtyroký, and E. Brynda. Novel spectral fiber optic sensor based on surface plasmon resonance. *Sensors and Actuators*, B 74:106–111, 2001.

[51] E. Kretschmann and H. Raether. Radiative decay of non-radiative surface plasmons excited by light. *Z. Naturforsch*, 23 A:2135–2136, 1968.

[52] BIAcore. *http://www.biacore.com/*.

[53] Texas Instruments. *http://www.ti.com/spr/*.

[54] Quantech. *http://www.biosensor.com/*.

[55] BioTuL BioInstruments. *http://www.biotul.com/*.

[56] F. Mariaudeau, T. Downey, A. Wig, A. Passian, M. Buncick, and T. L. Ferrell. Fibre optic sensor based on gold island plasmon resonance. *Sensors and Actuators*, B 54:106–117, 1999.

[57] M. G. Allen. Diode laser absorption sensors for gas-dynamic and combustion flows. *Meas. Sci. Technol.*, 9(4):545–562, 1998.

[58] Z. Jin, Y. Su, and Y. Duan. Development of a polyaniline-based optical ammonia sensor. *Sensors and Actuators*, B 72:75–79, 2001.

[59] R. Claps, F. V. Englich, D. P. Leleux, D. Richter, F. K. Tittel, and R. F. Curl. Ammonia detection by use of near-infrared diode-laser-based overtone spectroscopy. *Applied Optics*, 40(24):4387–4403, 2001.

[60] J. Frank and H. Meixner. Sensor system for indoor air monitoring using semiconducting metal oxides and IR-absorption. *Sensors and Actuators*, B 78:298–302, 2001.

[61] J. Wang, M. Maiorov, J. B. Jeffries, D. Z. Garbuzov, J. C. Connolly, and R. K. Hanson. A potential remote sensor of CO in vehicle exhaust using 2.3 μm diode lasers. *Meas. Sci. Technol.*, 11:1576–1584, 2000.

[62] L. W. Burgess. Absorption-based sensors. *Sensors and Actuators*, B 29:10–15, 1995.

[63] M. Yokota and T. Yoshino. An optical-fibre water-concentration sensor using Tm^{3+}:YAG fluorescent light. *Meas. Sci. Technol.*, 11:152–156, 2000.

[64] P. Dress, M. Belz, K.-F. Klein, K. T. V. Grattan, and H. Franke. Physical analysis of teflon coated capillary waveguides. *Sensors and Actuators*, B 51:278–284, 1998.

[65] K. Li and J. Meichsner. In situ infrared fibre evanescent wave spectroscopy as a diagnostic tool for plasma polymerization in a gas discharge. *J. Phys. D: Appl. Phys.*, 34:1318–1325, 2001.

[66] V. Matějec, M. Chomát, I. Kašík, J. Čtyroký, D. Berková, and M. Hayer. Inverted-graded index fiber structures for evanescent-wave chemical sensing. *Sensors and Actuators*, B 51:340–347, 1998.

[67] B. D. Gupta and D. K. Sharma. Evanescent wave absorption based fiber optic pH sensor prepared by dye doped sol-gel immobilization technique. *Optics Communications*, 140:32–35, 1997.

[68] B. D. Gupta and Ratnanjali. A novel probe for a fiber optic humidity sensor. *Sensors*

and Actuators, B 80:132–135, 2001.

[69] H. Lehmann, G. Schwotzer, P. Czerney, and G. J. Mohr. Fiber-optic pH meter using NIR dye. *Sensors and Actuators*, B 29:392–400, 1995.

[70] C. Malins, M. Landl, P. Šimon, , and Brian D. MacCraith. Fibre optic ammonia sensing employing novel near infrared dyes. *Sensors and Actuators*, B 51:359–367, 1998.

[71] P. A. Wallace, N. Elliott, M. Uttamlal, A. S. Holmes-Smith, and M. Campbell. Development of a quasi-distributed optical fibre pH sensor using a covalently bound indicator. *Meas. Sci. Technol.*, 12:882–886, 2001.

[72] G. Pandraud, T. M. Koster, C. Gui, M. Dijkstra, A. van den Berg, and P. V. Lambeck. Evanescent wave sensing: new features for detection in small volumes. *Sensors and Actuators*, A 85:158–162, 2000.

[73] C. Maims, J. Hulme, P. R. Fielden, and N. J. Goddard. Grating coupled leaky waveguide micro channel sensor chips for optical analysis. *Sensors and Actuators*, B 77:671–678, 2001.

[74] C. R. Lavers, K. Itoh, S. C. Wu, M. Murabayashi, I. Mauchline, G. Stewart, and T. Stout. Planar optical waveguides for sensing applications. *Sensors and Actuators*, B 69:85–95, 2000.

[75] K. Ock, N. Jo, J. Kim, S. Kim, and K. Koh. Thin film optical waveguide type UV sensor using a photochromic molecular device, spirooxazine. *Synthetic Metals*, 117:131–133, 2001.

[76] K. Kim, H. Minamitani, H. Hisamoto, K. Suzuki, and S. Kang. Active optical thin-film waveguide sensor for ion sensing. *Analytica Chimica Acta*, 343:199–208, 1997.

[77] S. Wang, S. Boussaad, and N. J. Tao. Surface plasmon resonance enhanced optical absorption spectroscopy for studying molecular adsorbates. *Review of Scientific Instruments*, 72(7):3055–3060, 2001.

[78] J. P. Silveira and F. Grasdepot. New signal processing for absorption-based gas sensing. *Sensors and Actuators*, B 29:363–367, 1995.

[79] J. H. Correia, G. de Graaf, S. H. Kong, M. Bartek, and R. F. Wolffenbuttel. Single-chip CMOS optical microspectrometer. *Sensors and Actuators*, 82:191–197, 2000.

[80] Y. Xu, N. B. Jones, J. C. Fothergill, and C. D. Hanning. Error analysis of two-wavelength absorption-based fibre-optic sensors. *Optics and Lasers in Engineering*, 36:607–615, 2001.

[81] A. Lobnik, N. Majcen, K. Niederreiter, and G. Uray. Optical pH sensor based on the absorption of antenna generated europium luminescence by bromothymolblue in a sol-gel membrane. *Sensors and Actuators*, B 74:200–206, 2001.

[82] F. Nakajima, Y. Hirakawa, T. Kaneta, and T. Imasaka. Diffractive optical chemical sensor based on light absorption. *Anal. Chem.*, 71:2262–2265, 1999.

[83] S. Y. Rabbany, B. L. Donner, and F. S. Ligler. Optical immunosensors. *Critical Reviews in Biomedical Engineering*, 22(5/6):307–346, 1994.

[84] T. E. Plowman, S. S. Saavedra, and W. M. Reichert. Planar integrated optical methods for examining thin films and their surface adlayres. *Biomaterials*, 19:341–355, 1998.

[85] T. E. Plowman, J. D. Durstchi, H. K. Wang, D. A. Christensen, J. N. Herron, and W. M. Reichert. Multiple-analyte fluoroimmunoassay using an integrated optical waveguide sensor. *Analytical Chemistry*, 71(19):4344–4352, 1999.

[86] C. A. Rowe, S. B. Scruggs, M. J. Feldstein, J. P. Golden, and F. S. Ligler. An array immunosensor for simultaneous detection of clinical analytes. *Analytical Chemistry*, 71(2):433–439, 1999.

[87] P. C. Hauser, C. L. C. Liang, and B. Müller. A solid-state instrument for fluorescence chemical sensors using a blue light-emitting diode of high intensity. *Meas. Sci. Technol*, 6:1081–1985, 1995.

[88] C. D. Geddes, P. Douglas, C. P. Moore, T. J. Wear, and P. L. Egerton. A compact optical flow cell for use in acqueous halide determination. *Meas. Sci. Technol*, 10:N34–N37, 1999.

[89] J. G. Kornet, H. Griffioen, and K. Schurer. An improved sensor for the measurement of chlorophyll fluorescence. *Meas. Sci. Technol*, 3:196–199, 1992.

[90] D. W. Lübbers. How to measure pO_2 of tissue sealed in a transparent chamber? Development and construction of the first optrodes/optodes. *Sensors and Actuators*, B 51:5–11, 1998.

[91] C. Malins, M. Niggemann, and B. D. MacCraith. Multi-analyte optical chemical sensor employing a plastic substrate. *Meas. Sci. Technol*, 11:1105–1110, 2000.

[92] I. Murkovic and O. S. Wolfbeis. Fluorescence-based sensor membrane for mercury(II) detection. *Sensors and Actuators*, B 38–39:246–251, 2997.

[93] C. G. Cooney, B. C. Towe, and C. R. Eyster. Optical pH, oxygen and carbon dioxide monitoring using a microdialysis approach. *Sensors and Actuators*, B 69:183–188, 2000.

[94] I. Koronczi, J. Reichert, H-J. Ache, Ch. Krause, T. Werner, and O. S. Wolfbeis. Submicron sensors for ion detection based on measurement of luminescence decay time. *Sensors and Actuators*, B 74:47–53, 2001.

[95] M. E. Lippitsch, S. Draxler, and D. Kieslinger. Luminiscence life-time based sensing: new materials, new devices. *Sensors and Actuators*, B 38–39(1–3):96–102, 1997.

[96] C. McDonagh, C. Kolle, A.K. McEvoy, D. Dowling, A. A. Cafolla, S. J. Cullen, and B. D. MacCraith. Phase fluorometric oxygen sensor. *Sensors and Actuators B-Chem*, 74(1–3):123–129, April 2001.

[97] G. Neurauter, I. Klimant, and O. S. Wolfbeis. Microsecond lifetime-based optical carbon dioxide sensor using luminescence resonance energy transfer. *Analytica Chimica Acta*, 382:67–75, 1999.

[98] O. J. Rolinski and D. J. S. Birch. A fluorescence lifetime sensor for Cu(I) ions. *Meas. Sci. Technol.*, 10:127–136, 1999.

[99] W. Trettnak, C. Kolle, F. Reininger, C. Dolezal, P. O'Leary, and R. A. Binot. Optical oxygen sensor instrumentation based on the detection of luminescence lifetime. *Adv. Space Res.*, 22(10):1465–1474, 1998.

[100] E. Rabinovich, M. J. O'Brien, S. R. J. Brueck, and G. P. Lopez. Phase-sensitive multichannel detection system for chemical and biosensor arrays and fluorescence lifetime-

based imaging. *Rev. Sci. Instrum.*, 71(2):522–529, 2000.

[101] T. Sun, Z. Y. Zhang, and K. T. V. Grattan. Frequency-domain fluorescence based fiber optic fire alarm system. *Rev. Sci. Instrum.*, 72(4):2191–2196, 2001.

[102] V. Vadde and V. Srinivas. A closed loop scheme for phase-sensitive fluorometry. *Rev. Sci. Instrum.*, 66(7):3750–3754, 1995.

[103] F. Anghel, C. Illiescu, K. T. V. Grattan, A. W. Palmer, and Z. Y. Zhang. Fluorescent-based lifetime measurement thermometer for use at subroom temperatures (200–300 k). *Rev. Sci. Instrum.*, 66(3):2611–2614, 1995.

[104] H. S. Voraberger, H. Kreimaier, K. Biebernik, and W. Kern. Novel oxygen optrode withstanding autoclavation: technical solutions and performance. *Sensors and Actuators*, B 74:179–185, 2001.

[105] H. Hecht and M. Kölling. A low-cost optode-array measuring system based on 1 mm plastic optical fibres—new technique for in situ detection and quantification of pyrite weathering process. *Sensors and Actuators*, B 4082:1–7, 2001.

[106] J. F. Gouin, F. Baros, D. Birot, and J. C. André. A fibre-optic oxygen sensor for oceanography. *Sensors and Actuators*, B 38–39:401–406, 1997.

[107] A. Elamari, N. Gisin, J. L. Munoz, S. Poitry, M. Tsacopoulos, and H. Zbinden. Photon-counting optical fiber sensor for the detection of ammonia in neurochemical applications. *Sensors and Actuators*, B38–39:183–188, 1997.

[108] A. Klotz, A. Brecht, C. Barzen, G. Gauglitz, R. D. Harris, G. R. Quigley, J. S. Wilkinson, and R. A. Abuknesha. Immunofluorescence sensor for water analysis. *Sensors and Actuators*, B 51:181–187, 1998.

[109] A. Babnik, A. Kobe, D. Kuzman, I. Bajsič, and J. Možina. Improved probe geometry for fluorescence-based fibre-optic temperature sensor. *Sensors and Actuators*, A 57:203–207, 1996.

[110] D. Merchant, P. J. Scully, R. Edwards, and J. Grabowski. Optical fibre fluorescence and toxicity sensor. *Sensors and Actuators*, B 48:476–484, 1998.

[111] A. C. Jones, M. Millington, J. Muhl, J. M. De Freitas, J. S. Barton, and G. Gregory. Calibration of an optical fluorescence method for film thickness measurement. *Meas. Sci. Technol.*, 12:N23–N27, 2001.

[112] R. T. Ramos, A. Holmes, X. Wu, and E. Dussan. A local optical probe using fluorescence and reflectance for measurement of volume fractions in multi-phase flows. *Meas. Sci. Technol.*, 12:871–876, 2001.

[113] M. Ahmad and R. Narayanaswamy. Optical fibre Al(III) sensor based on solid surface fluorescence measurement. *Sensors and Actuators*, B 4108:1–8, 2001.

[114] Y. Gu, Z. Qian, B. Tao, and G. Wang. A new fibre optic sensor for detecting in situ the concentration of pharmaceuticals in blood. *Sensors and Actuators*, B 66:197–199, 2000.

[115] V. M. Starodub, L. L. Fedorenko, and N. F. Starodub. Optical immune sensors for the monitoring protein substances in the air. *Sensors and Actuators*, B 68:40–47, 2000.

[116] D. Kelly, K. Grace, X. Song, B. I. Swanson, D. Frayer, B. Mendes, and N. Peyghambar-

ian. Integrated optical biosensors for detection of multivalent proteins. *Optics Letters*, 24(23):1723–1725, 1999.

[117] G. L. Duveneck, M. Pawlak, D. Neuschäfer, E. Bär, W. Budach, U. Pieles, and M. Ehrat. Novel bioaffinity sensors for trace analysis based on luminescence excitation by planar waveguides. *Sensors and Actuators*, B 38–39:88–95, 1997.

[118] A. Donval, D. Josse, G. Kranzelbinder, R. Hierle, E. Toussaere, J. Zyss, G. Perpelitsa, O. Levi, D. Davidov, I. Bar-Nahum, and R. Neumann. Photo-luminescence in a conjugated polymer/glass composite film. *Synthetic Metals*, 124:59–61, 2001.

[119] V.L. Ratner. Calculation of the angular distribution and waveguide capture efficiency of the light emitted by a fluorophore situated at or adsorbed to the waveguide side wall. *Sensors and Actuators B*, 17:113–119, 1994.

[120] W.R. Holland and D.G. Hall. Waveguide mode enhancement of molecular fluorescence. *Optics Letter*, 10(8):414–416, August 1985.

[121] T. R. Glass, S. Lackie, and T. Hirschfeld. Effect of numerical aperture on signal level in cylindrical waveguide evanescent fluorosensors. *Applied Optics*, 26(11):2181–2186, 1987.

[122] Y. Zhou, P. J. Laybourn, J. V. Magill, and R. M. De La Rue. An evanescent fluorescence biosensor using ion-exchanged buried waveguides and the enhancement of peak fluorescence. *Biosensors and Bioelectronics*, 6(7):595–607, 1991.

[123] R. Srivastava, C. Bao, and C. Gómez-Reino. Planar-surface-waveguide evanescent-wave chemical sensors. *Sensors and Actuators*, A 51:165–171, 1996.

[124] H. Pin Kao and J. S. Schoeniger. Hollow cylindrical waveguides for use as evanescent fluorescence-based sensors: efect of numerical aperture on collected signal. *Applied Optics*, 36(31):8199–8205, 1997.

[125] H. Pin Kao and J. S. Schoeniger. Elliptical through reflector for the collection of light from linear sources. *Applied Optics*, 37(19):4194–4199, 1998.

[126] H. M. Shapiro and M. Hercher. Flow cytometers using optical waveguides in place of lenses for specimen illumination and light collection. *Cytometry: the Journal of the Society for Analytical Cytology*, 7(2):221–223, 1986.

[127] K. R. Rogers, J. J. Valdes, and M. E. Eldefrawi. Acetylcholine receptor fibre-optic evanescent fluorosensor. *Analytical Biochemistry*, 182(2):353–359, 1989.

[128] D. Kieslinger, S. Draxler, K. Trznadel, and M. E. Lippitsch. Lifetime-based capillary waveguide sensor instrumentation. *Sensors and Actuators*, B 38–39:300–3004, 1997.

[129] M. Pawlak, E. Grell, E. Schick, D. Anselmetti, and M. Ehrat. Functional immobilization of biomembrane fragments on planar waveguides for the investigation of side-directed ligand binding by surface-confined fluorescence. *Faraday Discussions*, 111:273–288, 1998. discussion 331–343.

[130] Y. Zhao, I. Avruthsky, and B. Li. Optical coupling between monocrystalline colloidal crystals and a planar waveguide. *Applied Physics Letters*, 75(23):3596–3598, 1999.

[131] B. D. MacCraith, S. Aubonnet, H. Barry, C. von Bültzingslöwen, J. M. Sabattié, and C. S. Burke. Optical chemical sensor systems based on photosensitive hybrid sol-gel

waveguides. In *Poster presentation at 11th International workshop on glasses, ceramics, hybrids and nano-composites from gels*, Padova, Italy, September 16–21 2001.

[132] M. J. Feldstein, B. D. MacCraith, and F. S. Ligler. Integrating multi-waveguide sensor. US Patent No. 6,137,117, Oct. 14 2000.

[133] T. Wakamatsu, T. Nakano, K. Shinbo, K. Kato, and F. Kaneko. Detection of surface-plasmon evanescent fields using a metallic probe tip covered with fluorescence. *Review of Scientific Instruments*, 70(10):3962–3966, 1999.

[134] J. Hradil, C. Davis, B. D. MacCraith, and C. McDonagh. Dual lifetime temperature-corrected PSP measurements using a single camera. Manuscript in preparation.

[135] I. Klimant, Ch. Huber, G. Liebsch, G. Neurauter, A. Stangelmayer, and O. S. Wolfbeis. *Fluorescence Spectroscopy: New Methods and Applications*, chapter Dual Lifetime Referencing (DLR)—a new scheme for converting fluorescence intensity into a frequency-domain or time-domain information. Springer Series on Fluorescence. Springer-Verlag, Berlin, 2000.

[136] G. J. Mohr, I. Klimant, U. E. Spichifger-Keller, and O. S. Wolfbeis. Fluoro reactands and dual luminophore referencing: A technique to optically measure amines. *Anal. Chem.*, 73(5):1053–1056, 2001.

[137] Ch. Huber, I. Klimant, Ch. Krause, and O. S. Wolfbeis. Dual lifetime referencing as applied to a chloride optical sensor. *Anal. Chem.*, 73(9):2097–2103, 2001.

[138] G. Liebsch, I. Klimant, Ch. Krause, and O. S. Wolfbeis. Fluorescent imaging of ph with optical sensors using time domain dual lifetime referencing (t-dlr). *Anal. Chem.*, 73(17):4354–4363, 2001.

[139] P. Langer, R. Müller, S. Drost, and T. Werner. A new method for filter-free fluorescence measurements. *Sensors and Actuators*, B 4057:1–6, 2001.

[140] `http://www.physics.dcu.ie/OSL/`. Webpage of the Optical Sensors Laboratory, Dublin City University.

[141] R. E. Jonas and M. S. Braiman. Efficient source-to-fibre coupling method using a diamond rod—theory and application to multimode evanescent-wave IR absorption spectroscopy. *Applied Spectroscopy*, 47(11):1751–1759, 1993.

[142] De-Kui Qing. A theoretical evaluation of the absorption coefficient of the optical waveguide chemical or biological sensors by group index method. *Journal of Lightwave Technology*, 14(8):1907–1916, August 1996.

[143] A. Messica, A. Greenstein, and A. Katzir. Theory of fibre-optic, evanescent-wave spectroscopy and sensors. *Applied Optics*, 35(13):2274–2284, 1996.

[144] P. G. H. Kosters and R. P. H. Kooyman. Optimum IR measurement conditions for thin layers on dielectric surfaces. *Thin Solid Films*, 327–329:283–286, 1998.

[145] V. Brioude and O. Parriaux. Normalised analysis for the design of evanescent-wave sensors and its use for tolerance evaluation. *Optical and Quantum Electronics*, 32(6–8):899–908, August 2000.

[146] G. Stewart, J. Norris, D. F. Clark, and B. Culshaw. Evanescent-wave chemical sensors—a theoretical evaluation. *Int. J. Optoelectron.*, 6:227–238, 1991.

[147] G. Stewart and B. Culshaw. Optical waveguide modeling and design for evanescent field chemical sensor. *Opt. Quantum. Electron.*, 26:S249–S259, 1994.

[148] T. Liebermann and W. Knoll. Surface-plasmon field-enhanced fluorescence spectroscopy. *Colloids and Surfaces*, A: Physicochemical and Engineering Aspects 171:115–130, 2000.

[149] S. Blair and Y. Chen. Resonant-enhanced evanescent-wave fluorescence biosensing with cylindrical optical cavities. *Applied Optics*, 40(4):570–581, 2001.

[150] C. Mayer, R. Verheijen, N. Stich, and T. G. M. Schalkhammer. Food-allergen assays on chip based on metal nano-cluster resonance. In Raymond P. Mariella and Dan V. Nicolau, editors, *Proceedings of SPIE*, volume 4265, pages 134–141, 2001.

[151] J. R. Lakowicz, I. Gryczynski, Y. Shen, J. Malicka, and Z. Gryczynski. Intensified fluorescence. *Photonics Spectra*, pages 96–104, October 2001.

[152] El-Hang Lee, R.E. Benner, J.B. Fenn, and R.K. Chang. Angular distribution of fluorescence from liquids and monodispersed spheres by evanescent wave excitation. *Applied Optics*, 18(6):862–868, March 1979.

[153] Jörg Enderlein, Thomas Ruckstuhl, and Stefan Seeger. Highly efficient optical detection of surface-generated fluorescence. *Applied Optics*, 38(4):724–732, February 1999.

[154] W.Lukosz and R. E. Kunz. New method for determining refractive index and thickness of fluorescent thin films. *Optics Communications*, 31(3):251–256, December 1979.

[155] R. E. Kunz and W. Lukosz. Changes in fluorescence lifetimes induced by variable optical environments. *Physical Review B*, 21(10):4814–4828, 1980.

[156] R.R. Chance, A. Prock, and R. Silbey. Molecular fluorescence and energy transfer near interfaces. *Adv. Chem. Phys.*, 37:1–65, 1978.

[157] E. H. Hellen and D. Axelrod. Fluorescence emission at dielectric and metal-film interfaces. *JOSA B*, 4(3):337–350, 1987.

[158] J. Enderlein. Single-molecule fluorescence near a metal layer. *Chemical Physics*, 247(1):1–9, 1999.

[159] J. Enderlein. Fluorescence detection of single molecules near a solution/glass interface—an electrodynamic analysis. *Chemical Physics Letters*, 308(3–4):263–266, 1999.

[160] R. H. Jordan and D. G. Hall. Highly directional surface emission from concentric-circle gratings on planar optical waveguides: the field expansion method. *JOSA A*, 12(1):84, 1995.

[161] P. N. Zeller, G. Voirin, and R. E. Kunz. Single-pad scheme for integrated optical fluorescence sensing. *Biosensors and Bioelectronics*, 15:591–595, 2000.

Chapter 2

Absorption-based optical chemical sensors—theory and simulation

This chapter presents detailed theoretical analysis of a particular class of absorption-based optical chemical sensors. The sensors under consideration employ a *thin film* which is doped with analyte-sensitive reagents and deposited on top of a planar waveguide structure. Owing to the presence of the reagents, the *absorption properties* of the thin film change upon exposure to a specific analyte.

The chapter starts with an explanation and formal description of the fundamental principles involved in the operation of absorption-based optical chemical sensors. Subsequently, a theoretical model describing the operation of such sensors, with a particular emphasis on the sensor systems employing multimode waveguide platforms, is developed and discussed in detail. The predictions of the model are used to identify the conditions for which an optimised performance of the sensor system can be achieved. Numerical simulations of the performance of a specific sensor configuration consisting of a thin sensing layer deposited on a multimode planar waveguide are also presented. The purpose of these simulations is to provide clearer explanations of the most important theoretical predictions using simple but illustrative examples.

In this chapter, any reference made to an absorption-based optical chemical sensor is a reference to the class of absorption-based chemical sensors employing thin films doped with analyte sensitive reagents and deposited on a multimode waveguide structure.

2.1 Principle of operation

The fundamental principle of operation of an absorption-based optical chemical sensor relies on the fact that the absorption properties of the analyte-sensitive reagent, which is immobilised in the matrix comprising the sensing film, depend on the analyte concentration. In the following analysis, the actual chemical processes involved in this type of transduction mechanism are not of concern. Instead, this property is considered as an intrinsic characteristic of the sensing film.

The absorption coefficient[1] of every absorbing material depends on the wavelength of

[1] Note that the absorption coefficient, α, in this analysis refers to the quantity characterising the dissipation

light used. A typical absorption spectrum consists of significant absorption bands or peaks in either the visible (VIS) or infra-red (IR) region. These regions are interesting from the application point of view as they overlap with the spectral regions for which high-quality light sources and detectors are available.

The following analysis does not focus on any particular material. Instead, a hypothetical medium is considered whose absorption spectrum is described by a hypothetical function, $\alpha(\lambda, c_A)$, as shown in Fig. 2.1. This function must fulfill one important requirement, namely that it varies monotonically with the analyte concentration, c_A, at least in the region where it is to be used for sensing.

The light, which is interrogating the absorbing medium, is produced by a source whose spectrum is either broad-band, such as that produced by a commercially available LED, or quasi-monochromatic, such as that from a laser. In addition to cost and size of the source, its choice is determined by the position of its emission spectrum. In particular, the absorption and emission spectra must exhibit a sufficiently large overlap (see Fig. 2.1) in order to provide efficient transduction.

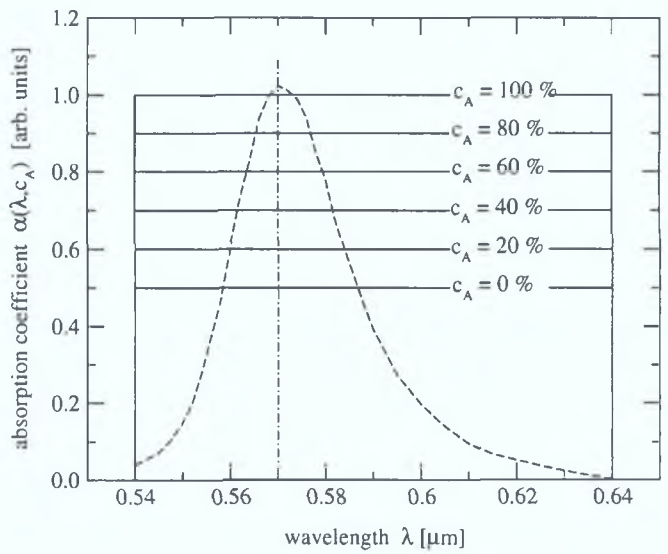

Figure 2.1: Absorption spectrum $\alpha(\lambda, c_A)$ of a hypothetical medium and its variation with the analyte concentration. The spectra are plotted for several values of the analyte concentration c_A, as indicated by the legend. The emission spectra of sources suitable for absorption-based sensing using this hypothetical medium are also shown. The dashed line corresponds to a broad band source, such as an LED, and the dash-dotted line corresponds to a quasi-monochromatic source, such as a laser.

In practical situations, the analyte concentration is measured in a range of concentrations, i.e., $c_A \in \langle c_{A,\min}, c_{A,\max} \rangle$. Within this range, the absorption coefficient varies between $\alpha_{\min} \equiv \alpha(\lambda, c_{A,\min})$ and $\alpha_{\max} \equiv \alpha(\lambda, c_{A,\max})$[2]. This reasoning is useful when one wants to quantify the sensitivity of the medium response to the changes in analyte concentration. This sensitivity

of energy carried by the electromagnetic wave propagating through a medium of length L by the well-known Beer-Lambert law, i.e., $I = I_0 \exp[-\alpha L]$.

[2]Note that the relation $\alpha_{\min} < \alpha_{\max}$ does not necessarily have to be satisfied, namely if the function $\alpha(\lambda, c_A)$ is decreasing with increasing analyte concentration c_A.

can be defined as the ratio of the total response of the medium and the total change in the analyte concentration, i.e.,

$$S_{\alpha,\mathrm{tot}} \equiv \frac{\Delta\alpha}{\Delta c_A} = \frac{\alpha_{\max} - \alpha_{\min}}{c_{A,\max} - c_{A,\min}}. \tag{2.1}$$

This expression can be generalised considering infinitesimal changes rather than the total differences, which results in a more general definition

$$S_\alpha \equiv S_\alpha\big|_{c_A} = \frac{\partial\alpha}{\partial c_A}. \tag{2.2}$$

Furthermore, from the practical point of view, it is useful to consider the *relative* change of the absorption coefficient with respect to the concentration change, i.e., $\partial\alpha/\alpha$. This leads to the definition of the quantity

$$\tilde{S}_\alpha \equiv \tilde{S}_\alpha\big|_{c_A} = \frac{1}{\alpha}\frac{\partial\alpha}{\partial c_A}, \tag{2.3}$$

which will be referred to as the relative sensitivity of the medium absorption coefficient to the changes in the analyte concentration.

2.2 Theory of absorption-based optical chemical sensors

To describe the operation of an absorption-based optical chemical sensor, it is necessary to know how light, i.e., electromagnetic field, propagates along the waveguide structure. Previous theoretical studies showed that the light propagation can be characterised by a parameter called *confinement factor* [1, 2, 3, 4], which is defined as the ratio between the amount of energy of the electromagnetic field confined in the sensing layer and the total energy carried by the guided mode. To identify the parameters that one needs to tailor in order to optimise the sensor performance, it is desirable to know how the confinement factor depends on the optical, geometrical and other parameters of the waveguide-based sensor system.

This is obviously a rather complicated task, particularly when complex waveguide structures, such as those used in the integrated optical sensor systems [5, 6, 7], are considered. It is mainly due to the fact that the analysis requires relatively complex calculations of the electromagnetic field distribution in the structure.

The aim of this section is to develop a model that would be both simple and powerful enough to provide sufficient insight into the phenomena involved in the operation of an absorption-based optical sensor system. The analysis will focus on a sensor system consisting of a multimode waveguide structure coated with a thin sensing film, as shown in Fig. 2.2.

The configuration depicted in Fig. 2.2 is only a model structure. The particular details characterising its performance will, in principle, be different from those characterising other, more complicated structures. However, the analysis of this structure will provide physical insight into the processes involved in the operation of such a structure that can be subsequently applied to other structures.

The development of the theory will proceed as follows. Firstly, expressions describing the distribution of electromagnetic field in a general multilayer system will be derived. Then, conditions for which guided modes of such a structure are supported will be identified. These

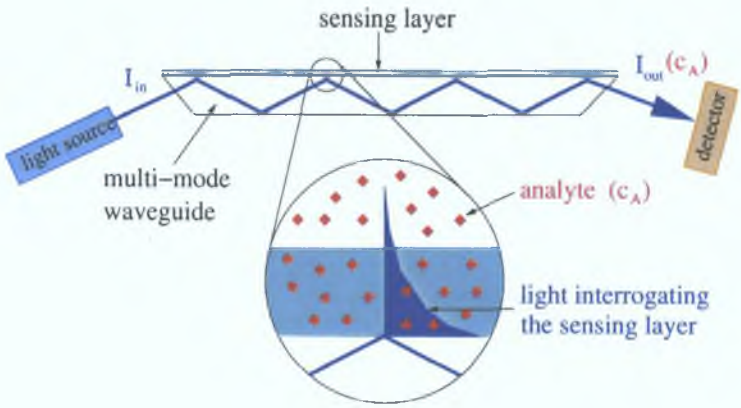

Figure 2.2: A schematic diagram of a generic configuration of an absorption-based optical chemical sensor employing a planar multimode waveguide platform coated with a thin sensing layer.

steps are based on a well established matrix formalism which is commonly used in the analysis of multilayer systems and was extensively reported in the literature [9, 10, 11, 12]. The general electromagnetic theory will subsequently be applied to a more specific task, namely to the description of operation of the sensor system depicted in Fig. 2.2. Expressions for the sensor output and sensitivity will be derived and analysed in detail. Finally, conditions for the optimum sensor performance will be identified and analysed in terms of the variable parameters of the sensor configuration. These latter steps are original to this work.

2.2.1 Field distribution in a multilayer system

In this section, rigorous electromagnetic theory is used to derive the expressions for the electromagnetic field in a multilayer structure consisting of arbitrary isotropic, non-magnetic and lossless media. The derived expressions are used in further analysis of operation of the absorption-based sensor system.

Multilayer system

The schematic diagram of a generic multilayer structure is shown in Fig. 2.3. The structure consists of M layers separated by planar interfaces parallel to the x–y plane. The position of the interface between the j^{th} and $(j+1)^{\text{th}}$ layers is characterised by the coordinate z_j, where $z_j = z_0 + t_1 + t_2 + \cdots + t_j$. In this expression, t_j denotes the thickness of the j^{th} layer.

The optical properties of the j^{th} layer are characterised by refractive index denoted by n_j, $j = 1, \ldots, M$. The multilayer system is surrounded by the superstrate ($z < 0$) and the substrate ($z > z_M$) whose refractive indices are denoted by n_0 and n_{M+1}, respectively. Because all the media comprising the multilayer system are assumed to be isotropic, non-magnetic and lossless, the values of n_j are considered to be real numbers for every $j = 0, \ldots, M+1$.

Electromagnetic field expressions

At the beginning, it is assumed that the multilayer system is interrogated by a monochromatic electromagnetic wave oscillating at the angular frequency ω, which is related to the vacuum wavelength λ by $\omega = 2\pi c/\lambda$, c being the speed of light in vacuum. The complex amplitude

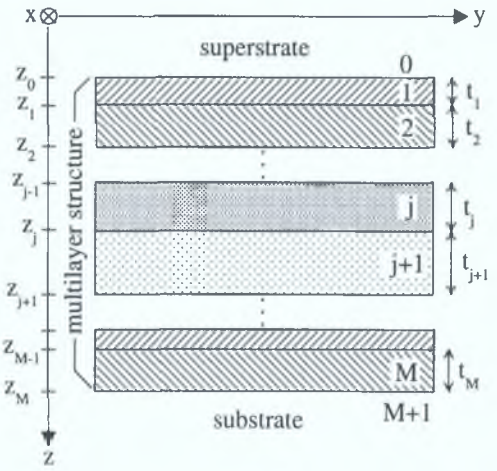

Figure 2.3: A schematic diagram of a general multilayer system consisting of M homogeneous layers surrounded by the substrate and superstrate.

of the electromagnetic field is described by the vector functions $\boldsymbol{E}(\boldsymbol{r})$ and $\boldsymbol{H}(\boldsymbol{r})$, which have to satisfy Helmholtz (wave) equation [8]

$$(\Delta + k_0^2 n^2(\boldsymbol{r}))\boldsymbol{E}(\boldsymbol{r}) = 0, \tag{2.4}$$

and similarly for $\boldsymbol{H}(\boldsymbol{r})$. In this equation, Δ stands for the Laplace operator which in the Cartesian system of co-ordinates takes the form $\Delta = \partial^2/\partial x^2 + \partial^2/\partial y^2 + \partial^2/\partial z^2$. Furthermore, k_0 denotes the vacuum wave vector and is calculated as $k_0 = \omega/c = 2\pi/\lambda$. The function $n(\boldsymbol{r})$ represents the distribution of the refractive index across the multilayer system, i.e.,

$$n(\boldsymbol{r}) = n_j \quad \text{for } \boldsymbol{r} \in j^{\text{th}} \text{ medium}. \tag{2.5}$$

The function $\boldsymbol{E}(\boldsymbol{r})$ represents the distribution of the electric field across the multilayer system. It can be written in the form

$$\boldsymbol{E}(\boldsymbol{r}) = \boldsymbol{E}_j(\boldsymbol{r}) \quad \text{for } \boldsymbol{r} \in j^{\text{th}} \text{ medium}, \tag{2.6}$$

where the function $\boldsymbol{E}_j(\boldsymbol{r})$ describes the distribution of the field in the j^{th} medium.

Due to the fact that each layer is considered to be homogeneous, the field in each layer can be analysed separately and the boundary conditions at each interface can be subsequently applied to obtain the expressions for the field in the entire multilayer system. The form of the wave equation (2.4) suggests that the electromagnetic field in each layer as well as in the surrounding media, i.e., for all $j = 0, \ldots, M+1$, can be decomposed into the sum of plane waves characterised by the wave vector $\boldsymbol{k}_j$ and the vector amplitude $\boldsymbol{\mathcal{E}}_j(\boldsymbol{k}_j)$. This decomposition takes the form of the Fourier transform

$$\boldsymbol{E}_j(\boldsymbol{r}) = \frac{1}{k_0^3} \int \mathrm{d}^3\boldsymbol{k}_j \, \boldsymbol{\mathcal{E}}_j(\boldsymbol{k}_j) \exp[i\boldsymbol{k}_j \cdot \boldsymbol{r}]. \tag{2.7}$$

The factor $1/k_0^3$ ensures that the units of the plane wave amplitudes $\boldsymbol{\mathcal{E}}_j(\boldsymbol{k}_j)$ are the same as the units of the total field. In expression (2.7), the integration is generally carried out over the entire three dimensional $\boldsymbol{k}$-space. However, in practical situations, the integration space

can be substantially reduced. In particular, it is sufficient to consider only such vectors $\boldsymbol{k}_j$ that lie in the y–z plane and their magnitude is equal to $|\boldsymbol{k}_j| = n_j k_0$, which corresponds to monochromatic light-waves propagating in the plane parallel to the y–z plane. Although this introduces substantial restrictions in the description of the field, it is sufficient for the purpose of this derivation.

When the electric field in the form (2.7) is considered and substituted into (2.4), the Helmholtz equation for the function $\boldsymbol{E}_j(\boldsymbol{r})$ can be rewritten in the form

$$\left(\boldsymbol{N}_j \boldsymbol{N}_j + n_j^2\right) \boldsymbol{\mathcal{E}}_j = N_j^2 \, \boldsymbol{\mathcal{E}}_j, \tag{2.8}$$

which is an eigenvector-eigennumber equation for the vector amplitudes $\boldsymbol{\mathcal{E}}_j$. For simplicity, the explicit dependence of $\boldsymbol{\mathcal{E}}_j$ on the wave vector $\boldsymbol{k}_j$ was omitted from this equation. The quantity $\boldsymbol{N}_j$ in (2.8) represents the normalised wave vector, i.e., $\boldsymbol{N}_j = \boldsymbol{k}_j / k_0$. Taking into account the above mentioned restrictions, this vector can be written as

$$\boldsymbol{N}_j = [0, N_{y,j}, N_{z,j}]. \tag{2.9}$$

The y and z components of this vector are related by

$$N_{y,j}^2 + N_{z,j}^2 = N_j^2, \tag{2.10}$$

where the vector magnitude N_j is calculated as

$$N_j \equiv |\boldsymbol{N}_j| = n_j. \tag{2.11}$$

To find the modes of the electromagnetic field in the j^{th} layer, one has to find the eigenvector $\boldsymbol{\mathcal{E}}_j$ and the corresponding eigennumber N_j^2 to the operator $(\boldsymbol{N}_j \boldsymbol{N}_j + n_j^2)$ in (2.8). In this equation, $\boldsymbol{N}_j \boldsymbol{N}_j$ represents the dyadic product of vectors $\boldsymbol{N}_j$. This can be done by using a well-known algebraic treatment.

Detailed analysis of this problem reveals that, for a given value of $N_{y,j}$, four independent solutions to the wave equation (2.8) exist. The choice of the solutions is to some extend arbitrary. In the following analysis, solutions corresponding to the s (TE) and p (TM) polarised waves propagating both in the positive (+) and negative (−) z-directions are chosen. The vectors of the electric field of the s and p polarised modes are perpendicular and parallel to the y–z plane, respectively.

Taking into account this choice, the eigen vectors $\boldsymbol{\mathcal{E}}_j$ of the wave equation (2.8) can be written as

$$\boldsymbol{\mathcal{E}}_{j,b} = \mathcal{E}_{j,b} \, \hat{\boldsymbol{e}}_{j,b}. \tag{2.12}$$

In this equation, the subscript b takes the values $b = s+, s-, p+, p-$, which characterise the four eigen-solutions. Furthermore, $\mathcal{E}_{j,b}$ denotes the magnitude of the mode b and $\hat{\boldsymbol{e}}_{j,b}$, where $|\hat{\boldsymbol{e}}_{j,b}| = 1$, characterises its polarisation state.

Following this analysis, electric field in the j^{th} layer, $j = 0, \ldots, M+1$, corresponding to the mode characterised by $N_{y,j}$ can be written as a sum of the four plane waves, i.e.,

$$\boldsymbol{E}_j(\boldsymbol{r}, N_{y,j}) = \sum_{b=s\pm,p\pm} \mathcal{E}_{j,b} \, \hat{\boldsymbol{e}}_{j,b} \exp\left[ik_0 (N_{z,j,b}(z - z_{j-1}) + N_{y,j} y)\right]. \tag{2.13}$$

Here, $z_{-1} = 0$ needs to be considered to describe the distribution of the field in the superstrate ($j = 0$) correctly. When the expressions (2.11) and (2.10) are used, the z components of the normalised wave vector for both s and p polarisations can be written as

$$N_{z,j,s\pm} = N_{z,j,p\pm} \equiv N_{z,j,\pm} = \pm\sqrt{n_j^2 - N_{y,j}^2}. \tag{2.14}$$

Furthermore, the unity vectors characterising the s and p polarisation states are given by

$$\begin{aligned} \hat{\boldsymbol{e}}_{j,s\pm} &= [1, 0, 0], \\ \hat{\boldsymbol{e}}_{j,p\pm} &= [0, N_{z,j,p\pm}, -N_{y,j}]/n_j. \end{aligned} \tag{2.15}$$

When the electric intensity in the form (2.13) is substituted into Maxwell's equations, the expression for the magnetic intensity in the j^{th} layer corresponding to the mode characterised by $N_{y,j}$ can be obtained. After some simple algebraic manipulation, the expression is found to be

$$\boldsymbol{H}_j(\boldsymbol{r}, N_{y,j}) = \sum_{b=s\pm,p\pm} \mathcal{H}_{j,b}\,\hat{\boldsymbol{h}}_{j,b} \exp\left[ik_0(N_{z,j,b}(z - z_{j-1}) + N_{y,j}y)\right]. \tag{2.16}$$

In this equation, the magnitudes $\mathcal{H}_{j,b}$ and the unity vectors $\hat{\boldsymbol{h}}_{j,b}$ are related to $\mathcal{E}_{j,b}$ and $\hat{\boldsymbol{e}}_{j,b}$ by

$$\mathcal{H}_{j,b} = \frac{n_j}{\eta_0}\,\mathcal{E}_{j,b} \tag{2.17}$$

and

$$\hat{\boldsymbol{h}}_{j,b} = \frac{1}{n_j}\left(\boldsymbol{N}_{j,b} \times \hat{\boldsymbol{e}}_{j,b}\right) \tag{2.18}$$

for each $b = s\pm, p\pm$. In equation (2.17), $\eta_0 = \sqrt{\mu_0/\epsilon_0}$ denotes the vacuum impedance.

To obtain the profile of the electromagnetic field throughout the entire multilayer system, the well-known boundary conditions have to be applied. They require that, in the absence of surface charges and currents, the tangential, i.e., x and y components of the electric and magnetic intensities be continuous at each interface. When both the equations (2.13) and (2.16) are considered, the boundary conditions at the j^{th} interface can be written in a compact matrix form [9, 10, 11, 12]

$$D_j P_j \boldsymbol{A}_j = D_{j+1} \boldsymbol{A}_{j+1}, \tag{2.19}$$

where the vector $\boldsymbol{A}_j$ is defined as

$$\boldsymbol{A}_j \equiv [\mathcal{E}_{j,s+}, \mathcal{E}_{j,s-}, \mathcal{E}_{j,p+}, \mathcal{E}_{j,p-}]^{\mathrm{T}}. \tag{2.20}$$

In equation (2.19), the matrices D_j and P_j are given by

$$D_j = \begin{pmatrix} 1 & 1 & 0 & 0 \\ N_{z,j,+} & N_{z,j,-} & 0 & 0 \\ 0 & 0 & N_{z,j,+}/n_j & N_{z,j,-}/n_j \\ 0 & 0 & -n_j & -n_j \end{pmatrix} \tag{2.21}$$

and

$$P_j = \begin{pmatrix} \exp[ik_0 N_{z,j,+} t_j] & 0 & 0 & 0 \\ 0 & \exp[ik_0 N_{z,j,-} t_j] & 0 & 0 \\ 0 & 0 & \exp[ik_0 N_{z,j,+} t_j] & 0 \\ 0 & 0 & 0 & \exp[ik_0 N_{z,j,-} t_j] \end{pmatrix}, \quad (2.22)$$

where the values of $N_{z,j,\pm}$ are obtained from (2.14).

In the derivation of (2.19), the equation

$$N_{y,0} = N_{y,1} = \cdots = N_{y,M} = N_{y,M+1} \quad (2.23)$$

was assumed. This corresponds to the well-known Snell's law on conservation of the tangential component of the wave vector across the multilayer system. Because of this relation, all $N_{y,j}$'s will be denoted by a single variable N_y. This step is important as it provides binding between the modes of the different layers of the multilayer structure into a single mode of the entire multilayer system, which is characterised by a single parameter N_y.

As follows from equations (2.13), (2.16) and (2.17), the distribution of the electromagnetic field across the entire multilayer system can be calculated if the magnitudes $\mathcal{E}_{j,b}$ comprising the vector $\boldsymbol{A}_j$ in (2.20) are known for each $j = 0, 1, \ldots, M+1$. This can be done by solving the complete set of equations given in (2.19). The solution depends on the particular optical configuration. For example, it is different if one is interested in finding the guided modes of the multilayer structure or if the reflectivity of the multilayer system is of interest. Further details are provided in the following section.

2.2.2 Guided modes of the planar waveguide structure

After the necessary expressions for the electromagnetic field in the multilayer structure have been derived, the distributions of electromagnetic field corresponding to guided modes can be found. At the very beginning, the term *guided modes* has to be specified precisely.

In this work, the commonly used definition of the term 'guided mode' is adopted. The distribution of the electromagnetic field is said to correspond to a guided mode of a multilayer system if (i) its modulus does not vary along the multilayer system, i.e., in the y direction, and (ii) the electromagnetic energy is confined in the multilayer structure in such a way that it is not radiated from the multilayer structure into the surrounding media or vice versa.

The first condition is formally represented by the fact that the modulus of expressions (2.13) and (2.16) does not depend on y. This is equivalent to the requirement that the quantities $\mathcal{E}_{j,b}$, $\hat{\boldsymbol{e}}_{j,b}$ and $N_{z,j,b}$ do not depend on y.

The fact that there is no field radiated from the multilayer structure into the surrounding media or vice versa can be formally satisfied by requiring that the z component of the normalised wave vector be a pure imaginary number for both $j = 0$ and $j = M+1$. According to Eq. (2.14), this implies some restrictions that have to be applied to the substrate and superstrate refractive indices, namely $n_0 < N_y$ and $n_{M+1} < N_y$. It will be shown later in this section that the self-consistent solution to equations (2.19) cannot be found unless $N_y < \max\{n_1, n_2, \ldots, n_M\}$. When these two relations are combined, the second part

of the definition of a guided mode implies that there must exist at least one layer in the multilayer system whose refractive index is greater than both the refractive indices of the substrate and superstrate. This layer is usually called the *guiding layer.*

According to (2.13) and (2.16), the fact that inequalities $n_0 < N_y$ and $n_{M+1} < N_y$ are required implies that the field in the substrate and superstrate is described either by an exponentially increasing or exponentially decreasing function. The former is not acceptable from the physical point of view, as it would result in the electromagnetic field carrying an infinite amount of energy. The latter is acceptable and it is commonly referred to as the *evanescent field.* To guarantee that the exponentially increasing terms in (2.13) and (2.16) are identically zero, the corresponding vectors $\boldsymbol{A}_0$ and $\boldsymbol{A}_{M+1}$ must be written as

$$\begin{aligned} \boldsymbol{A}_0 &= [0, \mathcal{E}_{0,s-}, 0, \mathcal{E}_{0,p-}]^{\mathrm{T}}, \\ \boldsymbol{A}_{M+1} &= [\mathcal{E}_{M+1,s+}, 0, \mathcal{E}_{M+1,p+}, 0]^{\mathrm{T}}. \end{aligned} \tag{2.24}$$

When the equations (2.19) are applied recursively, one can derive the following relation between the vectors $\boldsymbol{A}_0$ and $\boldsymbol{A}_{M+1}$:

$$\boldsymbol{A}_0 = L_{M+1} \boldsymbol{A}_{M+1}, \tag{2.25}$$

where the matrix L_{M+1} can be calculated from the definition

$$L_j \equiv D_0^{-1} D_1 P_1^{-1} \ldots D_{j-1} P_{j-1}^{-1} D_{j-1}^{-1} D_j \tag{2.26}$$

upon the substitution $j = M + 1$. In this definition, $L_0 \equiv 1$ is considered.

As can be seen from (2.21) and (2.22), the matrices D_j and P_j have a block form. This form is also taken by the matrix L_j. When Eqs. (2.24) and (2.25) are combined and the block form of the matrix L_{M+1} is taken into account, the following set of equations is obtained:

$$\begin{aligned} 0 &= L_{11,M+1}\, \mathcal{E}_{M+1,s+}, \\ \mathcal{E}_{0,s-} &= L_{21,M+1}\, \mathcal{E}_{M+1,s+}, \\ 0 &= L_{33,M+1}\, \mathcal{E}_{M+1,p+}, \\ \mathcal{E}_{0,p-} &= L_{43,M+1}\, \mathcal{E}_{M+1,p+}. \end{aligned} \tag{2.27}$$

This is a set of four equations from which four unknowns, namely the magnitudes of the field in the substrate ($\mathcal{E}_{M+1,s+}$, $\mathcal{E}_{M+1,p+}$) and the superstrate ($\mathcal{E}_{0,s-}$, $\mathcal{E}_{0,p-}$), can be found. Once they are known, they can be substituted into (2.24) and used in the evaluation of all remaining complex amplitudes comprising the vectors $\boldsymbol{A}_j$ defined in (2.20). This is done by recursively applying (2.19), which leads to equation

$$\boldsymbol{A}_j = L_j^{-1} L_{M+1} \boldsymbol{A}_{M+1}. \tag{2.28}$$

As follows from the definition (2.26), the matrix L_{M+1} depends on N_y, the optical (n_0, $\ldots$, n_{M+1}) and geometrical (t_1, $\ldots$, t_M) parameters characterising the multilayer system and the wavelength λ of the electromagnetic wave. As follows from simple algebra, a non-trivial solution to the set of equations (2.27) can be found only when

$$\begin{aligned} L_{11,M+1}(N_y^s; \lambda; n_0, \ldots, n_{M+1}; t_1, \ldots, t_M) &= 0, \\ L_{33,M+1}(N_y^p; \lambda; n_0, \ldots, n_{M+1}; t_1, \ldots, t_M) &= 0 \end{aligned} \tag{2.29}$$

is satisfied. Subsequently, the values of $\mathcal{E}_{M+1,s+}$ and $\mathcal{E}_{M+1,p+}$ can be chosen arbitrarily and the values of $\mathcal{E}_{0,s-}$ and $\mathcal{E}_{0,p-}$ can be obtained from the second and fourth equations in (2.27), respectively.

Equations (2.29) represent the conditions for which the guided modes exist. They provide implicit equations from which the y component of the normalised wave vector, called the *propagation constant*, can be calculated for given values of λ and the optical and geometrical parameters of the multilayer structure. As follows from (2.27), the first and second equations in (2.29) provide the propagation constants for the s and p polarised guided modes, which are denoted by N_y^s and N_y^p, respectively.

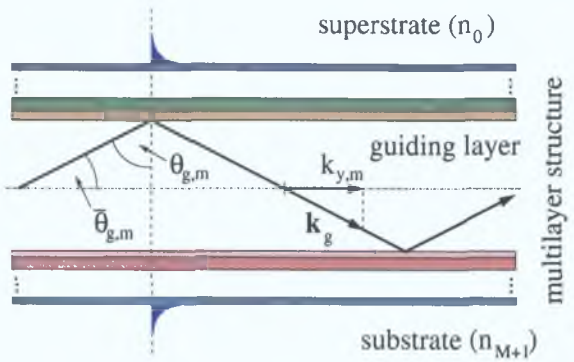

Figure 2.4: An example of a guided mode supported by the multilayer structure. The guided mode represented by a ray propagating along the waveguide structure in a "zig-zag" manner. The angle $\bar{\theta}_{g,m}$ denotes the propagation angle of the guided mode characterised by the order m.

In the description of the guided modes, it is convenient to consider a geometrical representation. Namely, the guided modes can be represented by a ray of light (or a light beam) which propagates along the guiding layer[3] in a "zig-zag" manner, as shown in Fig. 2.4. The rays can be characterised by two complementary angles. The first one is called the *propagation angle* $\bar{\theta}_g$, which is the angle between the ray and the axis of the waveguide structure. The second angle, which will be referred to as the *incident angle* θ_g, is the angle at which the light beam impinges onto the interface of the guiding layer and the neighbouring layer. The incident angle is related to the propagation angle by $\theta_g = 90° - \bar{\theta}_g$, as shown in Fig. 2.4.

The relations between the propagating or the incident angles and the propagation constant can be written as

$$\sin\theta_g = \frac{N_y}{n_g}, \quad \cos\bar{\theta}_g = \frac{N_y}{n_g}, \tag{2.30}$$

where the subscript g refers to the guiding layer, i.e., $n_g = \max\{n_1, \ldots, n_M\}$. These equations provide a relation between the two interpretations of the guided modes, namely between the wave interpretation, which is characterised by the propagation constant N_y, and the geometrical interpretation characterised by the propagation ($\bar{\theta}_g$) or incident (θ_g) angle.

2.2.3 Numerical examples

In this section, numerical examples are provided to demonstrate the theory developed in Secs. 2.2.1 and 2.2.2. In the model structure used in the numerical analysis (see Fig. 2.2),

[3]The reason why the guiding layer is chosen will become clear from the analysis below.

parameters that are common in the laboratory where this research was conducted are considered. The numerical values were obtained from a self-developed code written in Maple and Matlab.

The multilayer structure under consideration consists of two layers, i.e., $M = 2$. It comprises a glass guiding layer of refractive index $n_g = 1.515$ coated with a thin sol-gel layer of refractive index $n_s = 1.43$. Due to the fact that the sol-gel layer is assumed to be doped with the analyte sensitive reagents, which will be taken into account later in this chapter, it will be referred to as the sensing layer. The structure is surrounded by air ($n_a = 1.0$) on one side and by air or water ($n_w = 1.33$) on the other side (above the sensing layer).

The thickness of the sensing layer used in the following calculations is $t_s = 0.8\,\mu$m, which is a typical value for a sensing layer deposited by the dip-coating technique. For demonstration purposes, the thickness of the guiding layer is considered to be $t_g = 3\,\mu$m. The wavelength of the interrogating light is $\lambda = 543.5\,$nm, which corresponds to the green He-Ne laser. The parameters are summarised in Table 2.1.

parameter	value
n_0	$\boldsymbol{n_a = 1.0}$
n_1	$n_s = 1.43$
n_2	$n_g = 1.515$
n_3	$n_a = 1.0$
t_1	$t_s = 0.8\,\mu$m
t_2	$t_g = 3\,\mu$m
λ	$\lambda = 543.5\,$nm

(a)

parameter	value
n_0	$\boldsymbol{n_w = 1.33}$
n_1	$n_s = 1.43$
n_2	$n_g = 1.515$
n_3	$n_a = 1.0$
t_1	$t_s = 0.8\,\mu$m
t_2	$t_g = 3\,\mu$m
λ	$\lambda = 543.5\,$nm

(b)

Table 2.1: Parameters used in the numerical examples. Tables (a) and (b) correspond to the situations where the sensing layer is covered by air and water, respectively.

Guided modes

Firstly, the process of finding the guided modes is demonstrated. In this case, the process involves locating such values of the propagation constants N_y^s and N_y^p that the equations (2.29) are satisfied. In this example, the geometrical interpretation of the guided modes is used and so the matrix elements[4] $L_{11,3}$ and $L_{33,3}$ are plotted as a function of the propagation angle $\bar{\theta}_g$. The graphs corresponding to the sets of parameters in Table 2.1 are shown in Fig. 2.5.

It can be seen from the graphs that the lines intersect the x axis only at angles within the angular range $\bar{\theta}_g \in (0°, \bar{\theta}_c^{eg})$. Here, $\bar{\theta}_c^{eg}$ is the critical angle corresponding to the interface of the guiding layer and the higher refractive index medium surrounding the waveguide structure, referred to as the environment, i.e.,

$$\bar{\theta}_c^{eg} = 90° - \theta_c^{eg} = \arccos(n_e/n_g), \tag{2.31}$$

[4]Note that $M = 2$ and thus $M + 1 = 3$ in this analysis.

where

$$n_e = \max\{n_0, n_{M+1}\},$$
$$n_g = \max\{n_1, n_2, \ldots, n_M\}. \tag{2.32}$$

Considering (2.30), this angular restriction on the propagation angle $\bar{\theta}_g$ is equivalent to the restrictions applicable to the propagation constant N_y, which can be written as

$$n_e < N_y < n_g. \tag{2.33}$$

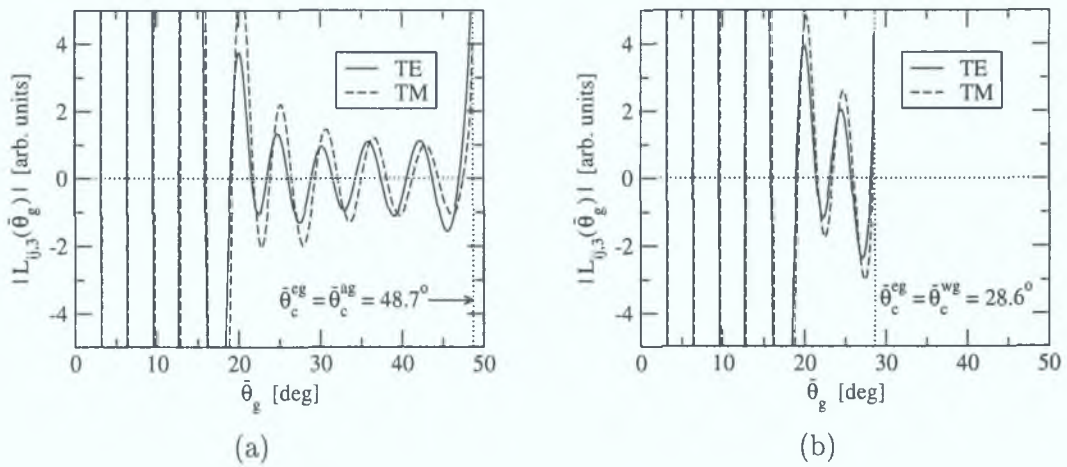

Figure 2.5: Examples of the matrix elements $L_{11,3}$ (solid line) and $L_{33,3}$ (dashed line) as a function of the propagation angle $\bar{\theta}_g$. The graphs (a) and (b) correspond to the set of parameters (a) and (b) in Table 2.1, respectively.

(a)

mode	$\bar{\theta}^s_{g,m}$	$\bar{\theta}^p_{g,m}$	mode	$\bar{\theta}^s_{g,m}$	$\bar{\theta}^p_{g,m}$
0	3.1640	3.225	10	31.506	32.133
1	6.3324	6.453	11	34.298	35.029
2	9.5080	9.685	12	37.410	38.119
3	12.689	12.917	13	40.573	41.273
4	15.864	16.127	14	43.708	44.444
5	18.965	19.230	15	46.991	47.493
6	21.607	21.838			
7	23.456	23.865			
8	26.054	26.511			
9	28.886	29.363			

(b)

mode	$\bar{\theta}^s_{g,m}$	$\bar{\theta}^p_{g,m}$
0	3.1640	3.2251
1	6.3324	6.4532
2	9.5080	9.6853
3	12.689	12.916
4	15.863	16.125
5	18.954	19.209
6	21.448	21.609
7	23.138	23.444
8	25.742	26.038
9	28.139	28.356

Table 2.2: Values of the propagation angles of the guided modes supported by the waveguide structures characterised by parameters in Table 2.1. The values are found by numerically solving equations (2.29). The tables (a) and (b) correspond to the waveguide structures characterised by parameters listed in Table 2.1(a) and (b), respectively.

This is also equivalent to the fact that the incident angle θ_g has to lie within the angular range

$$\theta_g \in (\theta_c^{eg}, 90°). \tag{2.34}$$

For the particular values used in this example, $\theta_c^{eg} \equiv \theta_c^{ag} \approx 41.3°$ ($\bar{\theta}_c^{eg} \equiv \bar{\theta}_c^{ag} \approx 48.7°$) and $\theta_c^{eg} \equiv \theta_c^{wg} \approx 61.4°$ ($\bar{\theta}_c^{eg} \equiv \bar{\theta}_c^{wg} \approx 28.6°$) for the structures characterised by the parameters listed in Table 2.1(a) and 2.1(b), respectively. The propagation angles corresponding to the guided modes of these structures are listed in Table 2.2.

Field distribution

After the propagation constants (angles) of the guided modes have been found, the corresponding electromagnetic field can be calculated. In the following analysis, the distribution of the quantity $|\boldsymbol{E}(\boldsymbol{r})|^2$ is of more interest than the profile of the components of the vectors $\boldsymbol{E}(\boldsymbol{r})$ or $\boldsymbol{H}(\boldsymbol{r})$. The reason will become clear in the next section where the waveguide structure with absorbing materials will be analysed.

Figure 2.6(a) shows the field profiles $|\boldsymbol{E}(z)|^2$ corresponding to three particular guided modes ($m = 2, 6, 13$) supported by the waveguide structure characterised by parameters in Table 2.1(a). The values of the corresponding propagation angles $\bar{\theta}_{g,m}$ are given in Table 2.2(a). Similar graphs are plotted in Fig. 2.6(b) for the structure described in Table 2.1(b) and the modes $m = 1, 6, 8$. In the graphs, SL and GL denote the sensing and guiding layers, respectively.

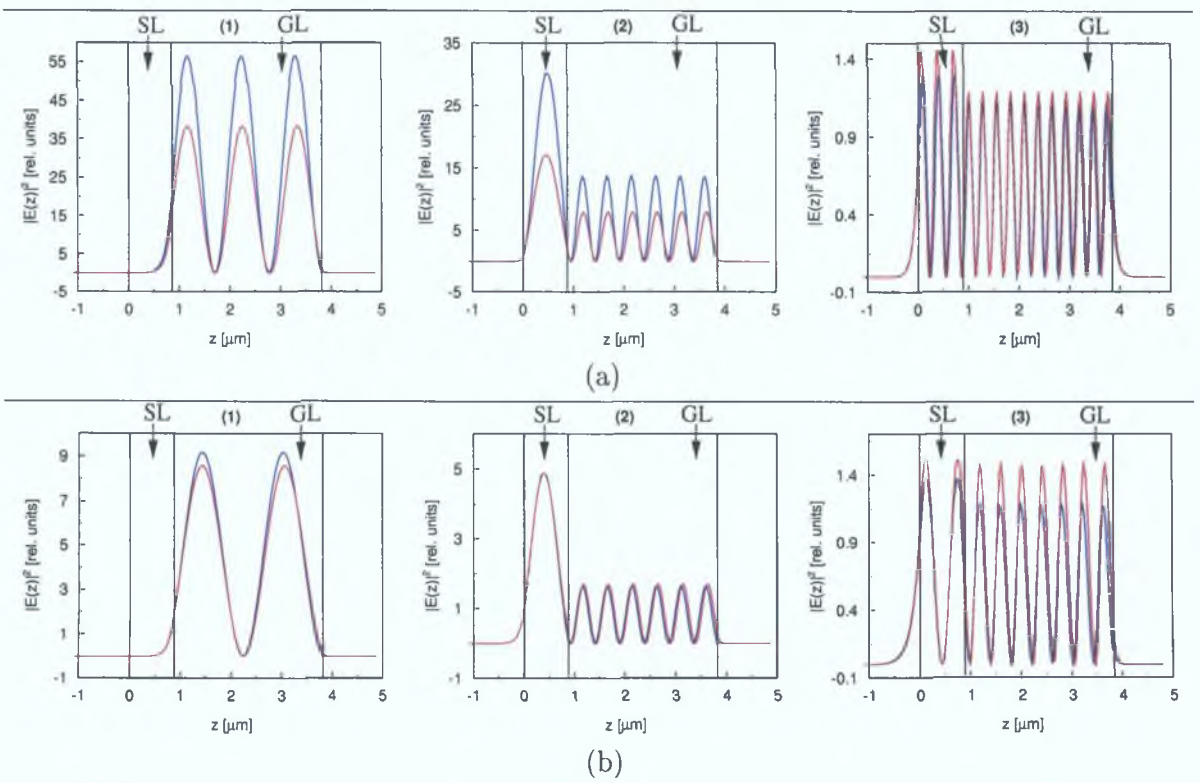

Figure 2.6: (a) Profiles of $|\boldsymbol{E}|^2$ corresponding to the guided modes supported by the waveguide structure characterised in Table 2.1(a). The graphs (1), (2) and (3) correspond to the modes characterised by $m = 2$, $m = 6$ and $m = 13$, respectively. (b) Profiles of $|\boldsymbol{E}|^2$ corresponding to the guided modes supported by the waveguide structure characterised in Table 2.1(b). The graphs (1), (2) and (3) correspond to the modes characterised by $m = 1$, $m = 6$ and $m = 8$, respectively. In all graphs, the blue and red lines correspond to the s and p polarised modes, respectively.

As can be seen from the graphs in Fig. 2.6, the electromagnetic field of the guided mode is described by a periodic function within the guiding layer (GL) and by an exponentially decreasing function in the surrounding media. This is in agreement with the definition of the guided modes discussed in Sec. 2.2.2.

The behaviour of the electromagnetic field in the sensing layer (SL) varies when different values of m characterising the guided modes are considered. For the modes with sufficiently low values of the propagation angle $\bar{\theta}_{g,m}$, the field in the sensing layer is exponentially decreasing with increasing distance from the SL/GL interface, as shown in graphs (1) in Fig. 2.6. This is due to the fact that the corresponding incident angle $\theta_{g,m} = 90° - \bar{\theta}_{g,m}$ is greater than the critical angle of the SL/GL interface, which is given by $\theta_c^{sg} = \arcsin(n_s/n_g)$. This corresponds to the so-called *evanescent-wave sensing* mode of the sensor operation [2, 3, 4, 5, 6, 13, 14, 15, 16, 17, 18]. This name originates from the fact that the field in the sensing layer is described by an evanescent wave. As can be seen from the graphs (1), the values of the field in the medium above the sensing layer are negligible compared to other regions of the waveguide structure in this sensing mode.

The field in the sensing layer has a different character when the propagation angle of the guided mode is slightly greater than $90° - \theta_c^{sg}$, or, equivalently, when the incident angle is slightly lower than the critical angle θ_c^{sg}. This is valid for example for the mode characterised by $m = 6$, whose field profile is plotted in the graphs (2) in Fig. 2.6(a). It can be seen that the field in the sensing layer exhibits a peak whose magnitude is somewhat greater than the magnitude of the field distribution in the guiding layer. This enhancement of the field within the sensing layer will be of particular interest in the next section where the sensitivity of the absorption-based optical sensor is analysed.

The number of peaks of the field distribution in the sensing layer is increased when the values of the propagating angle of the guided modes are sufficiently greater than $90° - \theta_c^{sg}$. This corresponds to greater values of m, such as $m = 13$ or $m = 8$, for which the field profiles are shown in graphs (3) in Fig. 2.6. As can be seen, the magnitude of the field distribution in the sensing layer is approximately the same as in the guiding layer. Furthermore, the magnitude of the evanescent field in the medium covering the sensing layer is increased for these modes.

2.2.4 Analysis of the output of the absorption-based sensor

As mentioned in Sec. 2.1, the operation of the absorption-based optical sensor is based on the principle that the sensing layer is absorbing and its absorption coefficient is a function of the analyte concentration c_A. Up until now, all the media comprising the waveguide system were considered to be lossless. From now on, some of the layers comprising the waveguide structure are considered to be absorbing. A typical example could be the two-layer system analysed in the previous section, where the absorption coefficient of the sensing layer (SL) depends on the analyte concentration. In the following analysis, only one absorbing, i.e., sensing layer is considered, since the generalisation to more absorbing (sensing) layers is rather straightforward. The quantities related to this layer will be denoted by a subscript s.

Based on the general electromagnetic theory, it follows that the absorbing properties of a medium can be formally represented in such a way that the refractive index, describing

its optical properties, is changed to a complex number [8]. In the case of the sensing layer, this is represented by changing its refractive index from n_s to $n_s + i\kappa_s$, where κ_s denotes the so-called *extinction coefficient*, which is related to the absorption coefficient α_s introduced in Sec. 2.1 by

$$\alpha_s = \frac{4\pi\kappa_s}{\lambda}. \tag{2.35}$$

The extinction coefficient depends, via the absorption coefficient, on both the wavelength and the analyte concentration, i.e., $\kappa_s = \kappa_s(\lambda, c_A)$. Due to Kramers-Krönig relations, the variation of κ_s with c_A implies that the real part of refractive index of the sensing layer, n_s, varies with the analyte concentration as well. In the following analysis, however, only the so-called weak absorption case will be considered. This approximation is valid when the relation $\kappa_s \ll n_s$ is true. Furthermore, the real part of the refractive index of the sensing layer will be considered to be constant, since its variation due to the analyte concentration can be neglected in the weak absorption approximation.

Due to the refractive index of the sensing layer being complex, the situation in the waveguide structure considered previously (see Sec. 2.2.1 and 2.2.2) is changed. In particular, the distribution of the electromagnetic field across the waveguide structure is modified, and the energy carried by the guided mode decreases as the guided mode propagates along the waveguide. The following analysis focuses on how these phenomena establish the functionality of the absorption-based optical sensor.

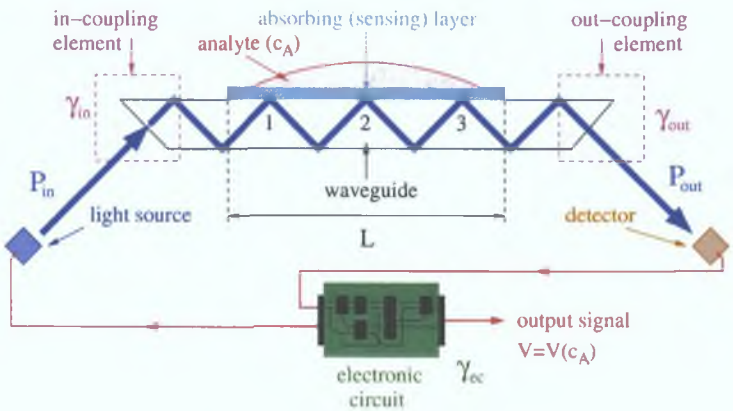

Figure 2.7: A detailed schematic diagram of a general absorption-based optical sensor employing planar multimode waveguide platform. See text for further details.

The detailed schematic diagram of a general configuration of the absorption-based optical sensor is shown in Fig. 2.7. Light from the light source is coupled into the guided modes of the waveguide structure. While propagating along the structure, the light interrogates the sensing layer resulting in attenuation of the energy carried by the guided modes. Subsequently, the light is out-coupled and detected by a photodetector. The signal from the photodetector is transformed by the electronic circuit to a form which is suitable for acquisition and further processing.

To establish an expression for the output signal $V(c_A)$ of the sensor system, the following quantities describing the function of the parts comprising the sensor system are defined. The optical power of the electromagnetic wave generated by the light source is denoted by P_{in}. A fraction of this energy, characterised by the in-coupling efficiency γ_{in}, is coupled into

a particular guided mode. The attenuation of the energy carried by this mode is described by the attenuation factor $\mathcal{T}$, which depends on the length L along which the light interrogates the sensing layer (see Fig. 2.7). The light is out-coupled from the waveguide structure with an efficiency characterised by γ_{out}. The photodetector together with the electronic circuit converts the output energy denoted by P_{out} into the final output signal. This step can be characterised by the conversion factor γ_{ec} and by an additional off-set introduced by the electronics circuit, denoted by V_0. Consequently, the output signal of the sensor system can be written as

$$V(c_A) = P_{\text{in}}\gamma_{\text{in}}\mathcal{T}(c_A, L)\,\gamma_{\text{out}}\gamma_{\text{ec}} + V_0. \tag{2.36}$$

In this expression, it is already assumed that the only quantity that depends on the analyte concentration c_A is the attenuation factor $\mathcal{T}$. This is a rather strong assumption, as it might not necessarily be satisfied in some practical situations. For example, when the variation of the real part of the sensing layer refractive index is considered, the in and out-coupling efficiencies could vary with the analyte concentration if they are based on elements such as grating couplers [19, 20, 21, 22, 23, 24, 25]. However, these effects are not considered as they would go beyond the scope of this analysis.

2.2.5 Sensor resolution, sensitivity and limit of detection

The general expression for the sensor output as a function of the analyte concentration is described by Eq. (2.36). In the area of chemical sensing, the performance of a sensor system is often quantified by the so-called sensor *resolution* ρ, *sensitivity* S and *limit of detection* LOD [26].

In every real sensor system, the output signal is limited by a level of uncertainty, which can be characterised by the signal standard deviation ΔV, i.e., $V(c_A) = \bar{V}(c_A) \pm \Delta V$. In this expression, $\bar{V}(c_A)$ denotes the mean value of the output signal at a given value of the analyte concentration. This uncertainty is due to the electric noise introduced by the light source, photodetector and the electronic circuit. Consequently, by measuring the output signal, the analyte concentration can also be determined only with a certain level of uncertainty. If this uncertainty is characterised by the standard deviation Δc_A, the concentration of the analyte can be expressed as $c_A = \bar{c}_A \pm \Delta c_A$. The sensor resolution is defined as three times the level of uncertainty with which the analyte concentration is determined, i.e., $\rho = 3\Delta c_A$.

The mean values of the sensor signal and the analyte concentration are related by $\bar{V}(c_A) = V(\bar{c}_A)$. Furthermore, the relation between the deviations of the signal and the concentration can be approximated by $\mathrm{d}V/\mathrm{d}c_A = \Delta V/\Delta c_A$, provided that the signal standard deviation is much smaller than the signal mean value.[5] Consequently, the standard deviation Δc_A and thus the resolution $\rho(c_A)$ can be calculated as

$$\rho(c_A) \equiv 3\Delta c_A = 3\frac{\Delta V}{S(c_A)}. \tag{2.37}$$

In this equation, $S(c_A)$ denotes the sensor sensitivity which is defined as the rate at which

[5] The condition $\Delta V \ll \bar{V}$ is the primary requirement on a *well-working* sensor system and therefore can be assumed to be always fulfilled.

the sensor output varies with the analyte concentration, i.e.,

$$S(c_A) = \frac{\mathrm{d}V(c_A)}{\mathrm{d}c_A}. \tag{2.38}$$

As indicated by c_A in its argument, the sensitivity can, in general, depend on the analyte concentration. This is obviously a consequence of the fact that the output signal $V(c_A)$ can be described, in general, by a non-linear function of c_A.

The limit of detection, which is another widely used parameter characterising the performance of the sensor system, is defined as

$$\mathrm{LOD} \equiv \rho(c_A = 0). \tag{2.39}$$

This parameter is relevant only in applications where the range of interest of the analyte concentration starts at $c_A = 0$. In applications where the minimum analyte concentration is non-zero, the sensor resolution defined in (2.37) is used instead.

As follows from equations (2.37) and (2.39), the sensor resolution and the limit of detection are indirectly proportional to the sensor sensitivity S. Therefore, to maximise the sensor performance, it is necessary to maximise the sensitivity and minimise the noise levels represented by the signal standard deviation ΔV.

Using the expression (2.36) for the output signal, the sensitivity can be calculated as

$$S(c_A) = P_{\mathrm{in}}\gamma_{\mathrm{in}}\gamma_{\mathrm{out}}\gamma_{\mathrm{ec}}\frac{\partial\mathcal{T}(c_A, L)}{\partial c_A}. \tag{2.40}$$

This expression implies that the optimum sensing performance is obtained when the partial derivative of the attenuation factor $\mathcal{T}$ reaches maximum. In the following section, the expression for the attenuation factor is derived and the conditions for which the sensor performance is optimised are identified.

2.2.6 Weak attenuation of the guided modes

The attenuation factor of a guided mode is derived by adopting the perturbation theory. The refractive index of the sensing layer (SL) is considered in the complex form $n_s + i\kappa_s$. The approximation of weak absorption is equivalent to the assumption that $\kappa_s \ll n_s$. Consequently, the function $n^2(\boldsymbol{r})$ in the Helmholtz equation (2.4) has to be changed to $n^2(\boldsymbol{r}) + \delta n^2(\boldsymbol{r})$, where the perturbation $\delta n^2(\boldsymbol{r})$ is given by

$$\delta n^2(\boldsymbol{r}) = \begin{cases} 2in_s\kappa_s & \text{for } \boldsymbol{r} \in \mathrm{SL}, \\ 0 & \text{elsewhere.} \end{cases} \tag{2.41}$$

Due to this perturbation of the profile of the refractive index, the distribution of the electromagnetic field in the waveguide structure is modified. If the modified vector of the electric intensity is denoted by $\tilde{\boldsymbol{E}}(\boldsymbol{r})$, it can be found by solving the modified Helmholtz equation

$$(\mathcal{H}_0(\boldsymbol{r}) + \delta\mathcal{H}(\boldsymbol{r}))\tilde{\boldsymbol{E}}(\boldsymbol{r}) = 0. \tag{2.42}$$

In this equation, $\mathcal{H}_0(\boldsymbol{r}) = \Delta + k_0^2 n^2(\boldsymbol{r})$ is the original (non-perturbed) Helmholtz operator and $\delta\mathcal{H}(\boldsymbol{r}) \equiv k_0^2\delta n^2(\boldsymbol{r})$ represents its small perturbation.

As follows from the expression (2.13) for the electric field in the j^{th} layer and from Snell's law (2.23), the distribution of the original field in the waveguide structure can be written in a factorised form

$$\boldsymbol{E}(\boldsymbol{r}) = \boldsymbol{E}(z)\ \exp[ik_0 N_y y]. \tag{2.43}$$

In this expression, $\boldsymbol{E}(z)$ denotes the field profile across the waveguide structure (see for example Fig. 2.6) and the exponential term represents the propagation of the field along the waveguide with the propagation constant N_y. It is assumed that due to the attenuation in the sensing layer, the propagation of the guided mode along the waveguide is attenuated. This attenuation can be formally represented by the propagation constant being a complex number. Furthermore, only the first order perturbation is assumed in the following derivation. This is equivalent to the assumption that the *profile* of the electromagnetic field is not altered by the small perturbation of the refractive index given by (2.41). Consequently, the modified electric intensity of the guided mode can be written as

$$\tilde{\boldsymbol{E}}(\boldsymbol{r}) = \boldsymbol{E}(z)\ \exp[ik_0 \tilde{N}_y y], \tag{2.44}$$

where $\tilde{N}_y$ denotes the modified propagation constant. If this expression is substituted into (2.42), the modified Helmholtz equation can be rewritten in the form

$$(\tilde{\mathcal{H}}_0(z) + \delta\tilde{\mathcal{H}}(z))\boldsymbol{E}(z) = \tilde{N}_y^2 \boldsymbol{E}(z), \tag{2.45}$$

where

$$\tilde{\mathcal{H}}_0(z) = \frac{1}{k_0^2}\frac{\mathrm{d}^2}{\mathrm{d}z^2} + n^2(z)$$

and

$$\delta\tilde{\mathcal{H}}(z) = \delta n^2(z).$$

The value of the modified propagation constant $\tilde{N}_y$ can now be calculated from (2.45). As follows from (2.4), the vector $\boldsymbol{E}(z)$ is the eigenvector of the operator $\tilde{\mathcal{H}}_0(z)$, i.e., $\tilde{\mathcal{H}}_0(z)\boldsymbol{E}(z) = N_y^2\boldsymbol{E}(z)$. Multiplying equation (2.45) by $\boldsymbol{E}^\star(z)$ and integrating over the entire waveguide structure results in the following expression for the modified propagation constant:

$$\tilde{N}_y^2 = N_y^2 + 2in_s\kappa_s\mathcal{F}_s, \tag{2.46}$$

where the *confinement factor* $\mathcal{F}_s$ is defined as

$$\mathcal{F}_s = \frac{\displaystyle\int_{z_{s-1}}^{z_s} |\boldsymbol{E}(z)|^2\,\mathrm{d}z}{\displaystyle\int_{-\infty}^{\infty} |\boldsymbol{E}(z)|^2\,\mathrm{d}z}. \tag{2.47}$$

This factor represents the fraction of the total power of the electromagnetic field propagated along the (non-absorbing) waveguide that is *confined in the absorbing (sensing) layer.*

It is assumed that the propagation constant is modified in such a way that it can be written in the form

$$\tilde{N}_y = N_y + iN_y^i, \tag{2.48}$$

i.e., that the introduction of non-zero absorption in the sensing layer results in such a shift of the original value N_y in the complex plane that the real part remains unchanged. This

assumption is valid in the weak absorption approximation. Comparing the equations (2.46) and (2.48) and neglecting higher-order terms, the imaginary part of the modified propagation constant can be written as

$$N_y^i \approx \frac{n_s}{N_y} \kappa_s \mathcal{F}_s. \tag{2.49}$$

Taking into account equation (2.44) and considering that the power carried by the guided mode is calculated as [1, 8, 27]

$$P(y) \propto \iiint |\tilde{\boldsymbol{E}}(\boldsymbol{r})|^2 \mathrm{d}^3\boldsymbol{r},$$

the attenuation factor $\mathcal{T}$, which is defined as the ratio between the power at a distance $y = L$ and that at $y = 0$, can be written as

$$\mathcal{T}(c_A, L) \equiv P(L)/P(0) = \exp[-\gamma(c_A)\, L]. \tag{2.50}$$

In this equation, the attenuation coefficient $\gamma(c_A)$ is given by

$$\gamma(c_A) = 2k_0 N_y^i. \tag{2.51}$$

As mentioned in Sec. 2.2.4, the generalisation of the above formalism to more than one absorbing layer is rather straightforward. In principle, the derivation would proceed in the same manner as described above. The difference would occur in the form of the perturbation $\delta\tilde{\mathcal{H}}(z)$, which would be written in a more general form:

$$\delta\tilde{\mathcal{H}}(z) = \delta n^2(z) = \begin{cases} 2i\, n_{s1}\kappa_{s1} & \text{for } z \in \mathrm{SL}_1, \\ 2i\, n_{s2}\kappa_{s2} & \text{for } z \in \mathrm{SL}_2, \\ \cdots & \\ 2i\, n_{sN}\kappa_{sN} & \text{for } z \in \mathrm{SL}_N, \\ 0 & \text{elsewhere,} \end{cases} \tag{2.52}$$

where N denotes the total number of sensing layers. Consequently, the imaginary part of the propagation constant would take a more general form (cf. (2.49))

$$N_y^i = \frac{1}{N_y} \sum_{j=1}^{N} n_{sj}\kappa_{sj}\mathcal{F}_{sj}, \tag{2.53}$$

where the confinement factor of the j^{th} sensing layer is defined as

$$\mathcal{F}_{sj} = \frac{\displaystyle\int_{z\in\mathrm{SL}_j} |\boldsymbol{E}(z)|^2 \,\mathrm{d}z}{\displaystyle\int_{-\infty}^{\infty} |\boldsymbol{E}(z)|^2 \,\mathrm{d}z}. \tag{2.54}$$

The expressions (2.50) for the attenuation factor and (2.51) for the attenuation coefficient would remain unchanged.

This approach of multiple sensing layers is useful when either the real or imaginary part of the refractive index of the sensing layer is inhomogeneous. This is relevant in situations where,

for example, the diffusion of the analyte into the sensing layer is of concern. In that case, the sensing layer could be divided into N sublayers, each being homogeneous and characterised by the appropriate complex refractive index $n_{sj} + i\kappa_{sj}$ (see (2.52)). If the number of sublayers is sufficiently large, the formalism developed above (see Eqs. (2.50–2.54)) would produce results that would appropriately describe the attenuation of the electromagnetic energy in such a waveguide structure.

Having the expression (2.50) for the attenuation factor $\mathcal{T}$, the sensitivity defined in (2.40) can be analysed in more detail. Firstly, equations (2.49–2.51) are substituted into the expression (2.40). After some simple manipulations, the sensor sensitivity can be rewritten in the form

$$S(c_A) = -P_{\text{in}}\gamma_{\text{in}}\gamma_{\text{out}}\gamma_{\text{ec}}\,\tilde{S}_{\alpha_s}\,\xi L\,\frac{\mathcal{F}_s}{N_y}\,\exp\left[-\xi L\,\frac{\mathcal{F}_s}{N_y}\right], \tag{2.55}$$

where the parameter ξ takes the form

$$\xi = n_s\alpha_s \tag{2.56}$$

and the relative sensitivity $\tilde{S}_{\alpha_s}$ of the medium comprising the sensing layer is given by (2.3). Equation (2.55) is the fundamental expression derived in this section. It provides a formal expression for the sensitivity of the absorption-based sensor employing a thin sensing film deposited on a planar waveguide structure (see Fig. 2.7). It contains all quantities relevant to the description of the sensor unit. In the following section, a number of aspects of this formula will be discussed.

2.2.7 Numerical analysis of sensor sensitivity

Expression (2.55) implies that the sensitivity of the absorption-based sensor has a number of contributions, each originating from different parts of the sensor system. The influence of the particular geometrical configuration of the sensor system is represented by the factor $P_{\text{in}}\gamma_{\text{in}}\gamma_{\text{out}}$. The geometrical configuration also determines the value of the propagation constant N_y, i.e., it dictates which mode (or a set of modes) is excited in the waveguide structure to facilitate the interrogation of light with the sensing layer. The "quality" of the interrogation provided by this mode is quantified by the confinement factor $\mathcal{F}_s$.

The location of the parameter L in the expression for $S(c_A)$ suggests that when the argument of the exponential factor is sufficiently small, the sensitivity is proportional to L. This means that the sensitivity of the absorption-based sensor can be increased by providing longer interaction length, which is commonly used in absorption-based sensors employing fibre optics and the evanescent-wave absorption [3, 13, 15, 28]. However, this increase in sensitivity is not unlimited. In particular, due to the exponential factor, the sensitivity starts to decrease after some critical interaction length has been reached. This length can be easily calculated from (2.55), provided that all the particular values of the involved parameters are known.

The sensitivity of the sensor system is proportional to the relative sensitivity $\tilde{S}_{\alpha_a}$ of the medium comprising the sensing layer to the changes in the analyte concentration. This is reasonable because a greater response of the sensor system is expected if the sensing medium itself responds to the concentration changes with greater magnitude.

Formula (2.55) also suggests that when the product ξL is small, e.g., for a very weak absorption α_s or a very short interaction length L, the sensitivity is proportional to the ratio between the confinement factor $\mathcal{F}_s$ and the propagation constant N_y of the mode providing the interrogation [1]. This is also understandable, since greater sensitivity can be expected if the amount of interrogating light confined in the sensing layer is larger. To provide a better understanding of the properties of the confinement factor, the following discussion focuses on the analysis of a number of numerical examples. The results were obtained from a self-developed code written in Matlab.

Confinement factor

Since the multimode waveguide platforms are of main interest in this work, the thickness of the guiding layer is chosen sufficiently large to fulfill this requirement. The following analysis focuses on the distribution of the confinement factor among the guided modes of the multimode waveguide structure. The structures under consideration are the same as those analysed in Sec. 2.2.3. Their optical and geometrical parameters are summarised in Table 2.1.

Firstly, it is shown that the distribution of the values of the confinement factor among the guided modes does not significantly depend on the thickness t_g of the guiding layer. To demonstrate this important property of $\mathcal{F}_s$, two values of t_g are considered in this example, namely $t_g = 5\,\mu$m and $t_g = 25\,\mu$m.

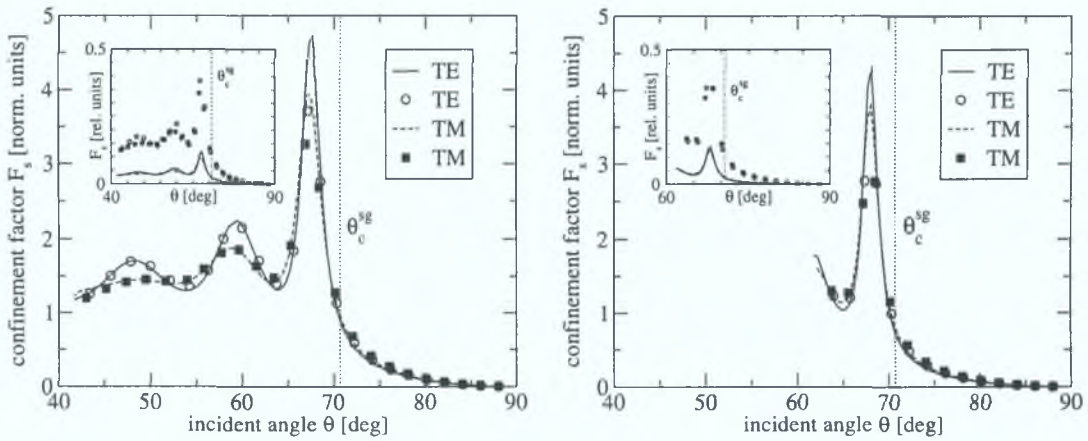

Figure 2.8: Distributions of the values of the confinement factor $\mathcal{F}_s$ among the guided modes of the waveguide structure. Lines correspond to the waveguide structure whose thickness of the guiding layer is $t_g = 25\,\mu$m, while symbols correspond to the situation where $t_g = 5\,\mu$m. Graphs (a) and (b) correspond to the waveguide structures whose parameters are listed in Table 2.1(a) and (b), respectively.

Figure 2.8 shows the distributions of the values of the confinement factor $\mathcal{F}_s$ among the guided modes of the waveguide structure characterised in Table 2.1. Rather than using the propagation constant N_y as the parameter characterising the particular guided mode, the incident angle θ, which is related to N_y by (2.30), is considered. The lines correspond to the waveguide structure with $t_g = 25\,\mu$m and represent the distribution of $\mathcal{F}_s$ across the quasi-continuous spectrum of the guided modes. The symbols correspond to $t_g = 5\,\mu$m and show how the confinement factor is distributed among the discrete modes.

The insets of the graphs in Fig. 2.8 show that the confinement of the field inside the sensing layer is generally greater when the thickness of the guiding layer is smaller. This is understandable, since the thinner guiding layer provides less "space" to store the energy of the electromagnetic field. This implies that a greater proportion of the optical energy can be confined in the sensing layer.

Although the absolute values of the confinement factor depend significantly on the thickness of the guiding layer, this is not true for its *profile*, i.e., for the normalised values $\mathcal{F}_s$. A very good agreement between the distributions depicted by lines ($t_g = 25\,\mu$m) and symbols ($t_g = 5\,\mu$m) demonstrates that the profile of the distribution of $\mathcal{F}_s$ among the guided modes does *not* change with the thickness of the guiding layer.

The graphs in Fig. 2.8 also suggest that particular modes exist whose confinement factor is significantly greater than that for the rest of the modes. It is found that the incident angle associated with these modes is slightly *below* the critical angle θ_c^{sg} of the SL/GL interface, which is equal to $\theta_c^{sg} \approx 70.7°$ for the particular parameters used in this calculation. These modes were already mentioned in Sec. 2.2.3. It was pointed out that the field corresponding to these modes (see Fig. 2.6, graphs (2)) has an enhanced magnitude in the sensing layer. Due to this enhancement, these modes should exhibit greater values of the confinement factor, which is clearly demonstrated in Fig. 2.8.

Sensitivity

The distributions of the sensitivity among the guided modes are shown in Figs. 2.9 and 2.10 for the structures characterised by the parameters listed in Tables 2.1(a) and 2.1(b), respectively. The distributions were calculated using equation (2.55). Similarly to the confinement factor, the *profile* of the sensitivity does *not* significantly change with the guiding layer thickness. This is demonstrated by a very good agreement between the profiles depicted by lines ($t_g = 25\,\mu$m) and symbols ($t_g = 5\,\mu$m).

As follows from Eq. (2.55), the parameter ξL plays a significant role in the evaluation of the sensitivity. For example, for a very short interaction length L or a very weak absorption of the sensing layer, the exponential factor in (2.55) can be approximated by unity and so the sensitivity is proportional to the ratio $\mathcal{F}_s/N_y$. This ratio is plotted in Figs. 2.9 and 2.10 by the solid line. It can be again concluded that those modes, whose incident angle θ_{opt} is slightly below the critical angle θ_c^{sg}, exhibit significantly greater sensitivity than the rest of the modes.

The situation changes when a non-zero value of the parameter ξL is chosen. This is demonstrated by the dotted ($\xi L = 0.2$), dashed ($\xi L = 0.5$) and dash-dotted ($\xi L = 1$) lines in Figs. 2.9–2.10. These lines show that the enhanced sensitivity provided by these "more sensitive" modes diminishes as the value of the product ξL increases. This can be understood from the point of view that the energy stored in these "more sensitive" modes is attenuated faster than that for the rest of the modes (because there is mode energy confined in the absorbing layer). After a certain critical propagation distance L_c is reached, the total amount of energy carried by these modes becomes less than that of the other modes. Consequently, the modes characterised by the incident angle $\theta \approx \theta_{\text{opt}}$ (see Figs. 2.9–2.10) become less sensitive for $L \geq L_c$. The critical distance L_c can be deduced from the analysis of Eq. (2.55), provided

that all the remaining parameters are known. For the set of parameters used in this analysis, L_c can be taken to be such that the critical parameter ξL_c is equal to approximately 0.5, as indicated by the dashed line in Figs. 2.9–2.10.

It is important to emphasize that the value of the critical parameter ξL_c depends on the thickness of the guiding layer. This is due to the fact that the magnitude of the ratio $\mathcal{F}_s/N_y$ depends on the guiding layer thickness, as discussed above. As the thickness of the guiding layer increases, the absolute values of the ratio $\mathcal{F}_s/N_y$ decrease (but not the profile, as mentioned earlier), and so the critical value of the parameter ξL_c increases. For these reasons, the values of ξL_c considered in the calculations leading to the graphs in Figs. 2.9 and 2.10 are not to be understood as absolute measures but only as parameters suitable for the numerical demonstration of the features discussed above.

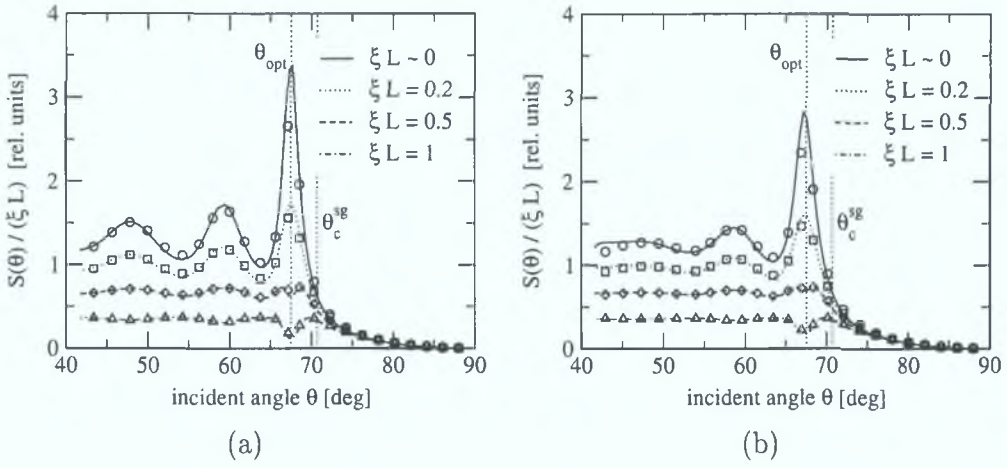

Figure 2.9: Distributions of the values of sensitivity S among the guided modes of the waveguide structure. Lines correspond to the waveguide structure whose thickness of the guiding layer is $t_g = 25\,\mu$m, while the symbols correspond to the situation where $t_g = 5\,\mu$m. Graphs (a) and (b) correspond to TE and TM polarisations of the interrogating light, respectively. The parameters characterising the structure are listed in Table 2.1(a). Different types of lines correspond to different values of the parameter ξL, as shown in the legend.

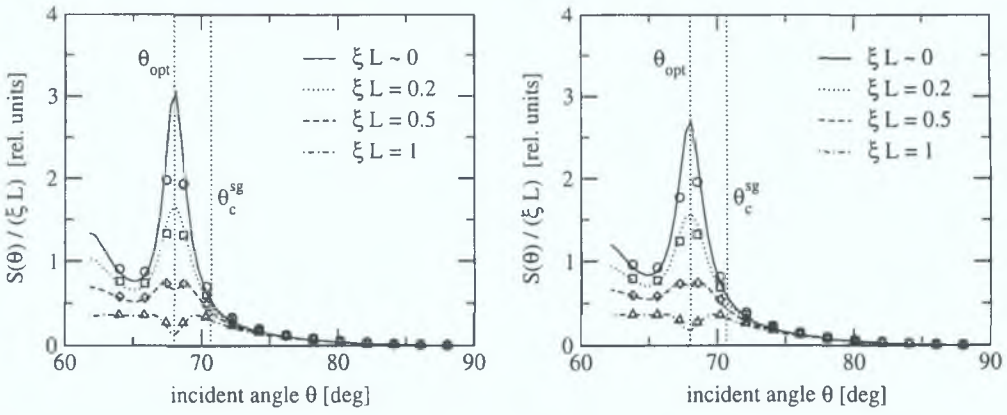

Figure 2.10: The same as in Fig. 2.9, except the parameters characterising the structure are listed in Table 2.1(b).

2.2.8 Sensitivity of the sensor system based on ray optics

In the previous sections, the sensitivity of the waveguide system under consideration was analysed using a rigorous electromagnetic theory. The analysis was built on the description based on electromagnetic *waves*. It was shown that the confinement factor, which describes the fraction of the electromagnetic energy stored within the sensing layer, played a fundamental role in the quantitative description of the sensitivity of the absorption-based sensor system.

The procedure which enables one to calculate the confinement factor for an arbitrary waveguide structure is rather complicated and requires several steps. Specifically, the complete set of guided modes has to be found and the field distribution for each mode has to be evaluated. Subsequently, the integration of the field across the waveguide structure has to be performed which provides the quantities necessary for the evaluation of the confinement factor. If this procedure was to be kept rigorous for every waveguide structure, it would become more elaborate and time consuming, especially for the structures with thicker guiding layers, i.e., those with greater number of guided modes.

It was shown that the *profile* of the confinement factor across the guided modes does *not* vary significantly with the thickness of the guiding layer. This is rather fortunate as it enables one to evaluate the profile for a structure with a relatively low number of modes, e.g., 50–100, and then to use the characteristic features of the profile for structures with a much greater number of modes. This section shows that there is another, much simpler and faster way of obtaining the profile of the sensitivity among the guided modes, which is especially useful for highly multimode waveguide structures. It is based on the analysis of reflectivity of the part of the waveguide structure containing the absorbing (sensing) layer. This approach is closely related to the *ray* model of the electromagnetic field propagation along the waveguide structure.

As shown in Fig. 2.7, the propagation of the electromagnetic field along the waveguide structure can be depicted by a ray of light propagating in a "zig-zag" manner. A detailed diagram illustrating the reflection of the beam from the part of the structure containing the absorbing (sensing) layer is shown in Fig. 2.11. The original multilayer system consisting of M layers is divided into three parts—the guiding layer itself, i.e., the layer with the largest refractive index, the multilayer system I containing the absorbing layer, and the multilayer system II. The light beam of intensity I_{in} interrogates the multilayer system I at the incident angle θ and is reflected. If the reflectivity of the multilayer system I is denoted by $R(\theta)$, the output intensity of the reflected beam can be written as $I_{\text{out}} = R(\theta) I_{\text{in}}$.

Reflectivity

The reflectivity $R(\theta)$ of the multilayer system I can be obtained using the same matrix formalism that was used for finding the guided modes (see Secs. 2.2.1–2.2.2). The field in the guiding layer is decomposed into the s and p polarised waves propagating both up and down, i.e., in the negative $(-)$ and positive $(+)$ z directions, respectively. If their corresponding magnitudes are denoted by $\mathcal{E}_{g,s\pm}$ and $\mathcal{E}_{g,p\pm}$, where the subscript g refers to the guiding layer, the vector $\boldsymbol{A}_g$ (see Eq. (2.20)) can be written as

$$\boldsymbol{A}_g = [\mathcal{E}_{g,s+}, \mathcal{E}_{g,s-}, \mathcal{E}_{g,p+}, \mathcal{E}_{g,p-}]^{\mathrm{T}}. \tag{2.57}$$

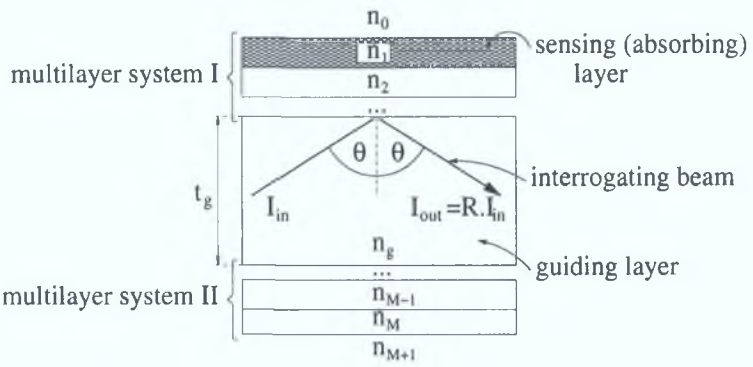

Figure 2.11: A detailed diagram of the beam interrogating the part of the waveguide structure (multilayer system I) containing the absorbing (sensing) layer.

The field in the surrounding medium is described by an exponentially decreasing function, and so the vector $\boldsymbol{A}_0$ can be written in the same way as in (2.24), i.e.,

$$\boldsymbol{A}_0 = [0, \mathcal{E}_{0,s-}, 0, \mathcal{E}_{0,p-}]^{\mathrm{T}}. \tag{2.58}$$

These vectors are related by an equation similar to (2.25), i.e.,

$$\boldsymbol{A}_0 = L_g \boldsymbol{A}_g, \tag{2.59}$$

where the matrix L_g is obtained from Eq. (2.26). When the matrices D_j and P_j, which are respectively defined in (2.21) and (2.22), are evaluated for the absorbing layer, i.e., for $j = s$, the complex refractive index of the absorbing layer, i.e., $n_s + i\kappa_s$ has to be taken into account.

The reflectivity of the multilayer system I can be easily obtained from Eqs. (2.57–2.59). After some simple manipulation, the reflection coefficients for the s and p polarised waves can be written as

$$\begin{aligned} r_s &\equiv \frac{\mathcal{E}_{g,s+}}{\mathcal{E}_{g,s-}} = -\frac{L_{g,12}}{L_{g,11}}, \\ r_p &\equiv \frac{\mathcal{E}_{g,p+}}{\mathcal{E}_{g,p-}} = -\frac{L_{g,34}}{L_{g,33}}. \end{aligned} \tag{2.60}$$

Consequently, the reflectivities of the s and p polarised waves/rays, which are defined as the square of the modulus of the reflection coefficients, can be calculated from

$$R_s = |r_s|^2, \quad R_p = |r_p|^2. \tag{2.61}$$

Sensor sensitivity

With reference to Fig. 2.7, the light beam interrogates the sensing layer ν times along the interaction length L. Using simple geometry, the number ν of reflections can be approximated by

$$\nu \approx \left[\frac{L}{2t_g \tan\theta}\right]^{\uparrow}, \tag{2.62}$$

where θ is the incident angle of the light beam, t_g is the thickness of the guiding layer (see Fig. 2.11) and $[x]^{\uparrow}$ represents the value of x rounded up to the nearest integer number.

Due to the fact that after each reflection the power carried by the beam is attenuated by the factor R, the attenuation factor $\mathcal{T}$ considered in Eq. (2.36) can be written as

$$\mathcal{T}_{\text{ray}} = R^{\nu}. \tag{2.63}$$

The subscript 'ray' is associated with the fact that the expression for the attenuation factor is based on ray optics. Substituting this expression into (2.40), the sensitivity of the sensor system based on ray optics can be written as

$$S_{\text{ray}}(c_A) \propto -\tilde{S}_{\alpha_s} L \mathcal{T}_{\text{ray}} \frac{1}{R} \left| \frac{\partial R}{\partial \kappa_s} \right| \frac{1}{\tan\theta}. \tag{2.64}$$

The negative sign originates from the fact that the derivative $\partial R/\partial \kappa_s$ is always negative. Equation (2.64) represents the ray-optics equivalent to Eq. (2.55).

Equations (2.55) and (2.64) provide formal expressions for the sensitivity of the absorption-based sensor which are based on the wave and ray descriptions of the sensor operation, respectively. In order to compare these two expressions directly, equation (2.55) needs to be rewritten. Considering that the attenuation factor $\mathcal{T}$ is given by (2.50), $S(c_A)$ based on the wave approach can be written as

$$S_{\text{wave}}(c_A) \propto -\tilde{S}_{\alpha_s} L \mathcal{T}_{\text{wave}} \frac{\mathcal{F}_s}{N_y}. \tag{2.65}$$

Consequently, the sensitivity of the sensor system can be formally written as

$$S_{\text{app}}(c_A) \propto -\tilde{S}_{\alpha_s} L \mathcal{T}_{\text{app}} Q_{\text{app}}, \tag{2.66}$$

where the subscript "app" is equal either to "ray" or "wave", depending on which approach to the description of the sensor operation is opted for. The quantities Q_{app} in (2.66), are defined as

$$Q_{\text{ray}} \equiv \frac{1}{R} \left| \frac{\partial R}{\partial \kappa_s} \right| \frac{1}{\tan\theta} \quad \text{and} \quad Q_{\text{wave}} \equiv \frac{\mathcal{F}_s}{N_y}, \tag{2.67}$$

as follows from the comparison of Eqs. (2.66), (2.64) and (2.65). The attenuation factors $\mathcal{T}_{\text{ray}}$ and $\mathcal{T}_{\text{wave}}$ are given by (2.63) and (2.50), respectively.

A comparison of expressions (2.55), (2.64), (2.65) and (2.67) implies that the sensitivity of the sensor is proportional to the quantities Q_{ray} and Q_{wave} when the ray and wave-based approaches to the sensor operation are considered, respectively. When a short interaction length L and weak attenuation in the sensing layer are considered, the value of the parameter ξL in (2.55) is small and consequently the exponential factor can be approximated by unity. Similarly, a short interaction length implies that ν can be considered to be equal to unity and weak absorption guarantees that $\mathcal{T}_{\text{ray}} \approx 1$ holds very well. Combining both of these assumptions, the sensor sensitivity is found to be proportional to the quantity Q_{app}. In particular, the angular dependence of the sensitivity is determined directly by the angular dependence of the quantity Q_{app}.

To check this conclusion, the angular distributions of Q_{ray} and Q_{wave} are plotted for the structure characterised in Table 2.1(a). The results are shown in Fig. 2.12. It can be seen that the angular distributions of Q_{ray} and Q_{wave} are in excellent agreement. This agreement

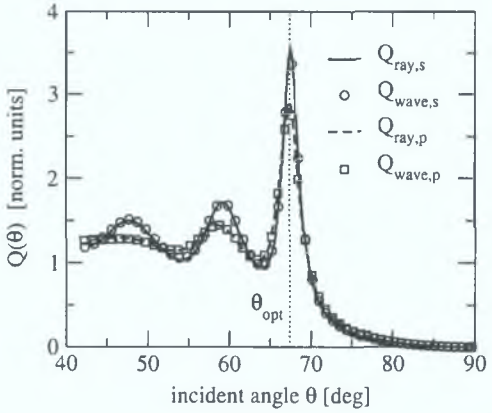

Figure 2.12: An example of the angular distributions of the quantities Q_{ray} and Q_{wave} defined in (2.67), both for s and p polarised light. The distributions were calculated for the waveguide structure characterised in Table 2.1(a). In the evaluation of Q_{ray}, the reflectivity R and its derivative $\partial R/\partial \kappa_s$ were calculated using the value $\kappa_s = 0.001$.

justifies the consistency between the ray and wave approaches to the analysis of the sensor performance in the approximation of short interaction length and weak absorption.

The quantitative results provided by (2.66) and (2.67) differ when longer interaction lengths or greater absorption in the sensing layer is considered. This is demonstrated in Fig. 2.13, where the angular distributions of the sensitivity based on the ray and wave approaches are plotted. The sensitivity calculated using the wave-based approach (Eq. (2.65)) is plotted by symbols. Different symbols correspond to different values of the parameter ξL, which is the product of the interaction length and the parameter ξ characterising the absorption properties of the sensing layer (see (2.56)). The sensitivity calculated using the ray-based approach (Eq. (2.64)) is plotted by lines. Different lines correspond to different values of the parameter ν characterising the number of reflections of the interrogating light ray.

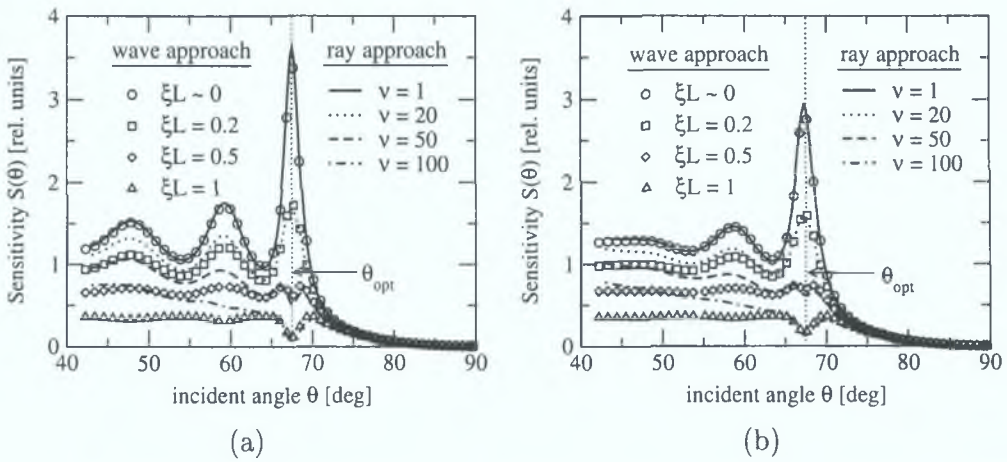

Figure 2.13: A comparison of the angular distributions of sensitivity obtained either by the ray approach (based on Eq. (2.64)) or the wave approach (based on Eq. (2.55)). The calculation was performed using the parameters specified in Table 2.1(a). Graphs (a) and (b) correspond to s (TE) and p (TM) polarisations of the interrogating light, respectively. In the evaluation of S_{ray}, the reflectivity R and its derivative $\partial R/\partial \kappa_s$ were calculated using the value $\kappa_s = 0.001$.

It can be seen that the ray-based sensitivity S_{ray} matches the wave-based sensitivity very well if a small number of reflections and a small value of the parameter ξL are considered, as concluded above. However, for a greater number of reflections and greater values of ξL, the discrepancies between the attenuation factors $\mathcal{T}_{\text{ray}}$ and $\mathcal{T}_{\text{wave}}$ become more pronounced, which is reflected in the differences between S_{ray} and S_{wave}. This is evident from the graphs in Fig. 2.13, where the lines do not follow the patterns given by the symbols very well, especially for smaller incident angles.

Despite the discrepancies discussed above, the ray model provides a very good approximation for the sensitivity of the sensor system, especially when a small number of reflections and weak attenuation of the sensing layer are considered. In the highly multimode waveguide platforms, which are of main interest in this work, the number of reflections approximated by (2.62) is always small and so the sensitivity of the sensor can be analysed by looking at the properties of the quantity Q_{ray} defined in (2.67). This will be the focus of the following section.

2.2.9 Numerical analysis of sensitivity based on ray optics

This section focuses on the numerical analysis of the quantity Q_{ray} for structures typically used in the laboratory where this research was conducted (see Sec. 2.2.3).

A typical structure consists of a glass slide of refractive index $n_g = 1.515$, which functions as a thick waveguide platform. The slide is coated with a thin sol-gel layer of refractive index $n_s = 1.43 + i\kappa_s$, which forms the sensing layer. By a standard dip/spin-coating deposition technique, thickness values of the sol-gel layer in the interval 200–900 nm can be easily achieved. In the numerical examples, two values, namely $t_s = 0.3\,\mu$m and $t_s = 0.8\,\mu$m are considered, the former representing a thin sensing layer, the latter a thick sensing layer. The sensing layer is covered by air ($n_a = 1.0$) or water ($n_w = 1.33$). The interrogating light is firstly assumed to be monochromatic with wavelength $\lambda = 543.5$ nm. The light originating from a broader band source, such as an LED, will be considered later in this section. The parameters characterising the structure under consideration are summarised in Table 2.3.

parameter	value
n_0	$\boldsymbol{n_a = 1.0}$
n_1	$n_s = 1.43 + i\kappa_s$
n_2	$n_g = 1.515$
t_1	$\boldsymbol{t_s = 0.3}$ or $\boldsymbol{0.8}\,\mu$m
λ	$\lambda = 543.5$ nm

(a)

parameter	value
n_0	$\boldsymbol{n_a = 1.33}$
n_1	$n_s = 1.43 + i\kappa_s$
n_2	$n_g = 1.515$
t_1	$\boldsymbol{t_s = 0.3}$ or $\boldsymbol{0.8}\,\mu$m
λ	$\lambda = 543.5$ nm

(b)

Table 2.3: Parameters used in the numerical example. Tables (a) and (b) correspond to the situations where the sensing layer is covered by air and water, respectively.

Monochromatic light source

The angular distribution of the quantity Q_{ray} is shown in Fig. 2.14. To provide a better comparison of the distributions for the different thicknesses of the sensing layer, the normalised

quantity Q_{ray}/t_s has been plotted. As can be seen from the graphs, the quantity Q_{ray} exhibits a distinct peak at an optimum angle of incidence, which is denoted by $\theta_{\text{opt,I}}$. This peak is

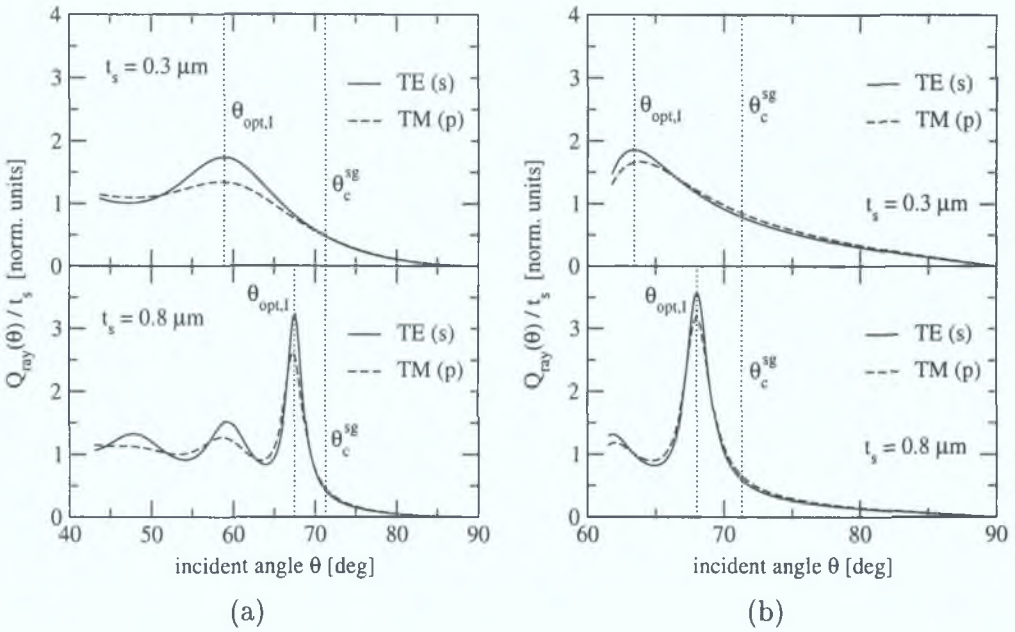

Figure 2.14: Angular distributions of the quantity Q_{ray} defined in (2.67) for two different thicknesses t_s of the sensing layer. The graphs (a) and (b) correspond to situations where the sensing layer is covered by air and water, respectively. The detailed description of the structure under consideration is summarised in Table 2.3.

more pronounced and shifted closer towards the critical angle θ_c^{sg} for thicker sensing layers. The comparison of the solid and dashed lines suggests that the optimum sensitivity of the s (TE) polarised waves is slightly greater than that of the p (TM) polarised waves. The graphs also demonstrate that the quantity Q_{ray} at the optimum angle $\theta_{\text{opt,I}}$ is significantly greater than at angles greater than the critical angle θ_c^{sg}, especially for thicker sensing layers. This suggests that in the sensor systems with a fewer reflections, the sensitivity can be reasonably enhanced by adjusting the incident angle of the interrogating light to this optimum value rather than employing the evanescent-wave sensing scheme.

Broad band light source

Until now, the light interrogating the sensing layer was considered to be monochromatic. Although this is a good approximation for applications employing lasers as the light sources, light emitting diodes (LEDs) are preferable sources in the sensor systems where the cost and the overall dimensions are of concern [29]. LEDs are characterised by a broader emission spectrum, with a typical bandwidth in the range of 50–100 nm. To demonstrate the influence of the spectral width on the angular profile of the quantity Q_{ray}, sources with different spectral characteristics are considered, as shown in Fig. 2.15.

The first source is an LED whose emission spectrum falls in the range of 540–640 nm and reaches the maximum at 570 nm, as shown by the solid line. This spectrum corresponds to a commercially available yellow-green LED. The second source has a hypothetical emission spectrum ranging from 540 to 640 nm with uniformly distributed intensity, as shown by the

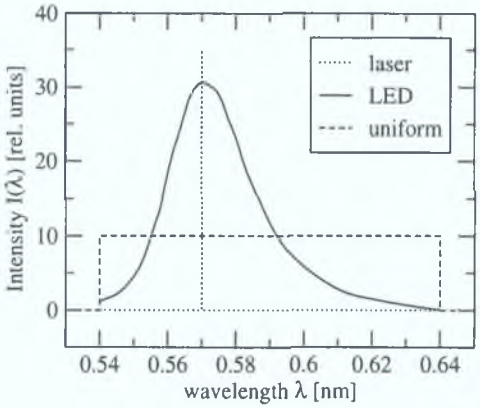

Figure 2.15: Spectral characteristics of different light sources considered in the numerical analysis. The dotted and solid lines correspond to the laser and yellow-green LED, respectively. The dashed line corresponds to a hypothetical source with uniform spectrum in the range from 540 nm to 640 nm.

dashed line. For comparison, the monochromatic light of wavelength $\lambda = 570\,\text{nm}$ (dotted line) is also considered in the following analysis.

The evaluation of the quantity Q_{ray} for the broad band spectrum light source is performed according to the following steps. Firstly, the distribution $Q_{\text{ray}}(\theta, \lambda)$ is evaluated for every wavelength within the range of the source spectrum.[6] Because the light originating from the broad-band sources like the LED can be assumed to be incoherent, the total value of the quantity $Q_{\text{ray}}(\theta)$ at the particular angle can be calculated as the weighted average of all values $Q_{\text{ray}}(\theta, \lambda)$, with the weighting function being directly proportional to the spectrum of the source, i.e., $Q_{\text{ray}}(\theta) \propto \int \mathrm{d}\lambda\, I(\lambda) Q_{\text{ray}}(\theta, \lambda)$, where $I(\lambda)$ denotes the spectrum of the broad band source.

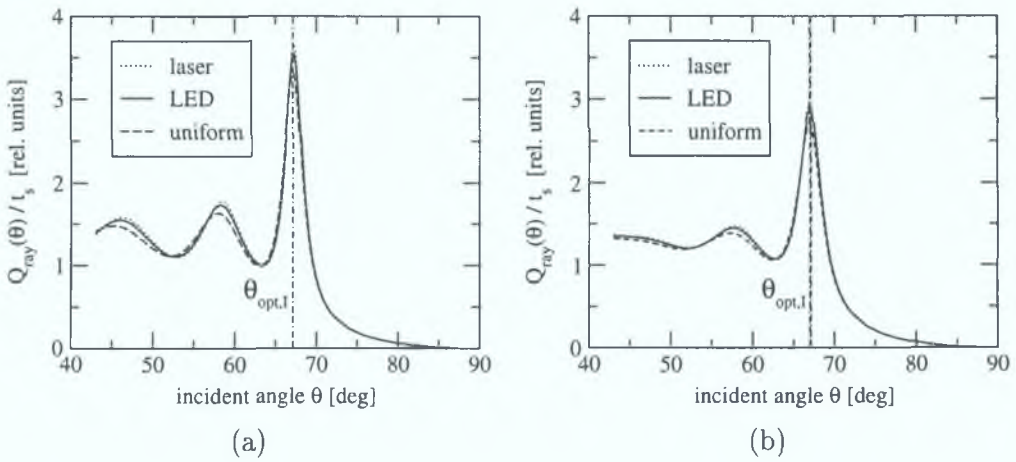

Figure 2.16: Examples of angular profiles $Q_{\text{ray}}(\theta)$ calculated for the sources whose spectral characteristics are depicted in Fig. 2.15. The graphs (a) and (b) correspond to the s and p polarisations, respectively. The refractive indices characterising the structure are listed in Table 2.3(a). See text for further details.

Figure 2.16 shows the comparison of the profiles of the quantity $Q_{\text{ray}}(\theta)$ calculated for the

[6] In practice, the spectral range is divided into a large number of discrete wavelengths.

sources whose spectral characteristics are depicted in Fig. 2.15. The graphs were calculated for the structure whose refractive indices are summarised in Table 2.3(a). It is important to note that the dispersion of the material refractive indices over the spectral range of wavelengths was neglected in the calculation. This was assumed both for the real and imaginary parts of the refractive indices. Although the latter case corresponds to a rather unrealistic situation where the medium comprising the sensing layer has uniform absorption over the spectral range of the source, the assumption is adequate to demonstrate the feature that will be highlighted below. The thickness of the sensing layer used in the calculation was $t_s = 0.8\,\mu$m.

As can be seen from the graphs, the angular dependence of Q_{ray} does *not* vary significantly if the light interrogating the sensing layer is monochromatic or that with the broader spectral range, such as those shown in Fig. 2.15. In principle, the change introduced by the broad spectrum is manifested as a slight decrease of the peaks' height. For example, when the source with the LED spectrum is considered, the peak in $Q_{\text{ray}}(\theta)$ corresponding to the most sensitive angular range is only slightly reduced in comparison with the peak corresponding to the monochromatic source. This change, along with a small angular displacement of the peaks, is more evident if the spectrum of the source is broadened further. However, practically speaking, the *spectral width* of the light interrogating the sensing layer does *not* play a significant role in the angular distribution of the quantity Q_{ray} and hence in the angular profile of the sensitivity of the sensor system with a short interaction length L.

This conclusion can have important implications in the design of a low-cost and portable sensor system. Obviously, using an LED as the source of the light interrogating the sensing layer would be beneficial, as the power consumption, size and overall cost could be kept very low.

2.3 Optimisation strategy

In section 2.2, formal description of the operation of the absorption-based sensor system employing a planar waveguide structure was developed and analysed in detail. General formulæ were derived which describe the sensor sensitivity as a function of the parameters characterising the waveguide structure. Several numerical examples were examined and typical features provided by the formulæ were described. In this section, these observations are compiled into a set of rules that should be considered in order to design a sensor system with optimised sensitivity.

The following discussion focuses on multimode planar waveguides as they are of primary interest to the laboratory where this research was conducted. This platform provides certain advantages which are discussed below.

Firstly, the preparation of a multimode waveguide structure, such as that depicted in Fig. 2.2, is relatively simple. It does not require any complicated technological procedures, such as complicated deposition techniques which require vacuum chambers and extreme temperatures, or rather expensive technology for creating buried or ridge waveguide channels which employ photolithography, etching, UV curing, etc. An example of a simple planar waveguide platform comprises a glass slide which is, indeed, readily available in high volumes and at a very low price. Another, more advanced platforms could be manufactured by means of injection molding or hot embossing into plastic which are easily applicable for mass

production.

The second advantage is related to the deposition of the sensing layer itself. When using waveguide structures such as a glass slide or a planar waveguide obtained by injection molding, the spin or dip-coating deposition techniques are very convenient for producing high quality (optical and mechanical) sensing layers at very low cost [30].

Another advantage lies in the ease of implementation of the multimode sensor element in a compact optical sensor system. The requirements on the precision, stability and reproducibility of the alignment are very large for sensor systems employing platforms with one or a very low number of modes. Difficulties related to the efficient coupling of the light into the guided mode(s) are inherent in such structures. Moreover, such platforms are very sensitive to the environment, e.g., to the variations of the ambient temperature.

Last but not least, multimode waveguide platforms are attractive when the overall size and cost of the sensor system are taken into account. Firstly, a platform with a low number of modes is expensive to manufacture. Secondly, lasers or laser diodes need to be employed as such a platform requires high quality light sources (low divergence of the beam, narrow spectral bandwidth). Although laser diodes are small, compact and already available at high volumes, they are still relatively expensive and their operation is prone to various factors, such as temperature variations, power supply stability, etc.

Considering these reasons, a sensor system based on an LED and a multimode planar waveguide structure could be an attractive candidate for a compact, cost effective and portable absorption-based optical sensor system.

It was found that by using a sensing layer whose refractive index is lower than that of the guiding layer and whose thickness is in the order of the interrogating light wavelength, significant enhancement in the sensor sensitivity can be achieved for a particular range of incident angles, or, in other words, by using a certain range of guided modes of the waveguide structure for interrogating the sensing layer. The word 'range' is important here as it allows for some tolerances in the mechanical adjustment of the optical configuration without a serious impact on the sensor performance. The enhancement in sensitivity is more pronounced for thicker sensing layers. However, using a thicker layer might imply some negative drawbacks when the sensor response time, which is usually determined by the speed of the analyte diffusion into the sensing layer, is of concern. Therefore, the thickness of the sensing layer should be tailored with care. Furthermore, as highlighted in Sec. 2.2.9, a light source with a broad band emission spectrum (up to approximately 100 nm) does not introduce any significant drawbacks in the optimum sensor performance, which makes the use of the LEDs in the absorption-based optical chemical sensor systems feasible.

2.3.1 Ideal sensing element

In this section, a strategy is proposed that could be applied in the design of an absorption-based optical sensor system employing an ideal multimode planar waveguide structure as the sensing element and an LED as the source of the interrogating light. In this context, the word *'ideal'* refers to the assumption that the parameters characterising the sensing element, such as the refractive index or thickness of the sensing layer, are known or can be tailored with *absolute accuracy*. The discussion concerning the *'real'* sensing element, i.e., a sensing

element whose parameters can be tailored only with a *limited accuracy,* will be presented in the next section.

The primary considerations in the design of the sensing element are, of course, determined by the analyte that is to be sensed. This dictates the particular chemistry involved in the preparation of the material comprising the sensing layer. This is, however, beyond the scope of this work and will not be discussed in detail here. The only implication, which is relevant to the further considerations and provided by this "chemistry step", is given by the absorption spectrum of the sensing layer, as it determines the choice of the source of the interrogating light.

A typical situation in absorption-based sensing is that a part of the absorption spectrum of the sensing layer undergoes significant changes upon interaction with the analyte. These can be, for example, in the form of an absorption peak decreasing or increasing in intensity with the change of the analyte concentration. It is therefore desirable that the emission spectrum of the LED overlaps well with this absorption peak. Understandably, the optimum overlap cannot always be achieved, but the range of LEDs available on the market is wide enough to meet the requirements of most of the sensing materials.

Once, the sensing material and the light source are selected, the refractive indices of all involved materials have to be determined. To achieve the effect of enhanced sensitivity, it is desirable that the refractive index of the sensing material be *lower* than that of the guiding layer, and, of course, greater than that of the environment containing the analyte, such as air, water, etc.

After all the above mentioned parameters are determined, the optimisation procedure is left with two free parameters that can be varied in order to optimise the sensor sensitivity, namely the thickness t_s of the sensing layer and the incident angle θ at which the light interrogates the layer.

As mentioned previously, due to response time considerations, it is desirable that the sensing layer would be as thin as possible. This is determined by the fact that the analyte is required to diffuse into the sensing layer in order to induce the changes in its absorption coefficient. However, as found in the theoretical analysis in Sec. 2.2, the enhancement of sensitivity at the optimum incident angle is more pronounced when the sensing layer is thicker. Consequently, a trade-off between these two opposite requirements has to be found. This requires that the diffusion properties of the sensing material are known and that the thickness of the sensing layer can be tailored within a reasonable range, typically 0.2–1 μm.

Once the thickness of the sensing layer is determined, the optimum angle of incidence $\theta_{\mathrm{opt,I}}$ can be found by simply plotting the function $Q_{\mathrm{ray}}(\theta)$ for the given set of parameters and taking its maximum, as shown for example in Fig. 2.16. By configuring the optical set-up of the sensor system in such a way that the light interrogates the sensing layer at this optimum angle, the sensor performance with highest sensitivity can be achieved.

As mentioned in Secs. 2.2.7 and 2.2.9, this is true only if the number of reflections is sufficiently small (refer to Eqs. (2.62–2.64)) or, more specifically, if the quantity $\xi L(\mathcal{F}_s/N_y)$ in Eq. (2.55) is sufficiently small so that the attenuation factor $\mathcal{T}$ is close to unity. If this is not the case, the function $S(\theta)$ given by (2.55) has to be calculated rigorously. This rigorous analysis is necessary because it has been shown that the enhancement of sensitivity at the optimum angle $\theta_{\mathrm{opt,I}}$ is reduced for longer interaction lengths, i.e., for greater values of the

parameter ξL (see, for example, Fig. 2.9). However, in many practical situations, one will not come across this issue very often.

In some situations, the adjustment of the incident angle θ might not be completely free. For example, due to some mechanical limitations or other restrictions, the incident angle might have to be fixed, or variable only within a small range. In this case, the optimisation procedure would be the reverse of that previously proposed. Firstly, the incident angle would be taken as the fixed parameter (desirably lying in the region $\theta_c^{cg} < \theta < \theta_c^{sg}$!), and then the numerical analysis based on either (2.64) or (2.55) would reveal the optimum value of the sensing layer thickness.

In both cases, each value of the sensing layer thickness t_s has its corresponding value of the optimum incident angle $\theta_{\mathrm{opt,I}}$, and vice versa. An example of the dependence of $\theta_{\mathrm{opt,I}}$ on t_s for the waveguide structures characterised in Table 2.1 is shown in Fig. 2.17. Similar curves can be found for any other parameter selection.

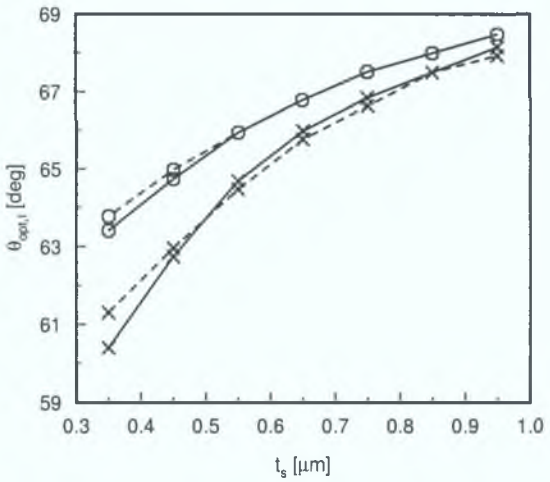

Figure 2.17: An example of the dependence of the optimum incident angle $\theta_{\mathrm{opt,I}}$ on the thickness of the sensing layer t_s calculated for the waveguide structure characterised in Table 2.1. The solid and dashed lines correspond to the s (TE) and p (TM) polarised light, while the crosses (×) and circles (○) correspond to the situation where the sensing layer is covered by air ($n_a = 1.0$) and water ($n_w = 1.33$), respectively.

As can be seen from the graph, the values of the optimum angle are practically the same for both s and p polarisations. This is convenient from the point of view that there is no need to include a polariser in the design of the sensor system based on LEDs, which produce unpolarised light. As it was shown in Secs. 2.2.7 and 2.2.9, the optimum sensitivity for the s polarised light is slightly greater than that for the p polarised light. However, the difference is not so large as to suggest that the use of the s polarised light should be preferable in comparison with the unpolarised light.

Another interesting feature demonstrated by the graph in Fig. 2.17 is that the difference between the optimum angles corresponding to the situations where the sensing layer is covered by air ($\theta_{\mathrm{opt}}^{\mathrm{a}}$), or water ($\theta_{\mathrm{opt}}^{\mathrm{w}}$), is only about 1–3 degrees for a rather large range of the sensing layer thicknesses. This means that if one specifies a tolerance on the divergence of the light beam produced by an LED to approximately 1–3 degrees, adjusting the incident angle of the interrogating light to the value $(\theta_{\mathrm{opt}}^{\mathrm{a}} + \theta_{\mathrm{opt}}^{\mathrm{w}})/2$ would result in a system whose sensitivity

would be enhanced for both the gaseous and liquid environments covering the sensing layer. Understandably, the enhancement would not be as large as possible. However, the fact that the sensor performance would be close to optimised for both environments could make the sensor system very attractive in various applications.

2.3.2 Real sensing element

In the previous section, the optimisation strategy for an ideal sensing element was described. In practical situations, however, the parameters characterising the sensing elements, i.e., the waveguide structure with the sensing layer, are only ever known with some limited level of accuracy. For example, due to various chemical procedures involved in the preparation of the sensing layer, the value of its refractive index might be prone to slight variations. Moreover, even if the best of care is taken during the deposition process, the thickness of the sensing layer can vary even among the sensing elements prepared in one technological step. As follows from the theoretical analysis of the sensor sensitivity, both of these variations can influence the overall performance of the sensor system.

Another problem arises from the fact that the output signal V of the sensor system is determined by the light *intensity*. Understandably, the intensity of the light entering the photodetector is not only determined by the attenuation inside the waveguide system, but is also prone to any minor discrepancies in the alignment of the sensing element. This is probably one of the major problems in the sensor systems based on the measurement of the light intensity.

To better explain what is meant by the 'discrepancies in the alignment of the sensing element', it is necessary to give an example which is based on practical experience. In the example, two identical sensor systems and two identical sensing elements are considered, denoted by 1 and 2, respectively. The following question arises: if the sensing element 1 is incorporated into the sensor system 1 and the same for the sensing element and sensor system 2, how likely is it to obtain identical output signal readings for identical analyte concentrations? The answer is that the likelihood depends on how identical the positioning of the sensing elements in the sensor systems is. In other words, the output signals from the two sensor systems will most likely be different, as it is almost impossible to align both sensing elements exactly in the same way.

This section provides a detailed discussion of the influence of the above mentioned misalignments and uncertainties on the stability and, more importantly, the reproducibility of the output signal. Furthermore, a solution to overcome these drawbacks is proposed. Due to the nature of the difficulties, the solution is based on redefining the criterion for the optimisation of the sensing element.

Firstly, the above mentioned factors influencing the output signal are formally identified with the quantities in the equation (2.36). The discrepancies in the alignment of the sensing element influence the values of the quantities γ_{in} and γ_{out}. This is understandable, since these quantities determine the amount of light that is coupled into and coupled out of the sensing element, which is sensitive to the positioning of the sensing element. The variations of the parameters characterising the sensing element are reflected in the variation of the attenuation factor $\mathcal{T}$. This follows from the theoretical analysis in Sec. 2.2.

Similarly, as in the previous section, it is considered that the thickness of the sensing layer t_s and the incident angle θ are the only variable parameters which can be used in the optimisation of the sensor sensitivity. The reasons for this are the same as those discussed in Sec. 2.3.2. The criterion for the optimum sensing conditions can therefore be redefined as follows: the purpose of the optimisation process is to find such sensing conditions that would result in large sensitivity to the changes of the analyte concentration, but would be insensitive or at least have very low sensitivity to small variations of the variable parameters of the sensing element, i.e., t_s and θ. Furthermore, the optimisation process should also provide a solution to the problem of the dependence of the output signal reading on minor misalignments of the sensing element.

In the following analysis, a sensor system employing a small number of reflections is considered. Consequently, the quantity Q_{ray} can be used as the approximation of the sensor sensitivity S. To achieve the first goal, the derivate $\partial Q_{\text{ray}}/\partial t_s$ and its dependence on the incident angle is analysed.

Figure 2.18 shows a typical example of this dependence calculated for a sensing element characterised in Table 2.3(a). The value of the sensing layer thickness considered in the calculation was $t_s = 0.6\,\mu$m. The derivative $\partial Q_{\text{ray}}/\partial t_s$ was calculated for the s (TE) and p (TM) polarised light as well as for the unpolarised light.

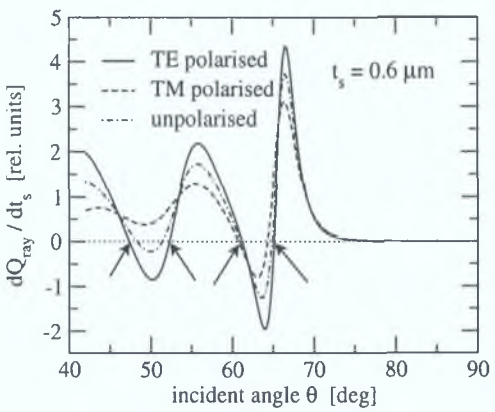

Figure 2.18: An example of the derivative $\partial Q_{\text{ray}}/\partial t_s$ as a function of the incident angle. The arrows indicate the angular positions at which the derivative $\partial Q_{\text{ray}}/\partial t_s$ is zero. See text for further details.

As can be seen from the graph, there are several values of the incident angle (indicated by arrows) at which the equation

$$\partial Q_{\text{ray}}/\partial t_s = 0 \tag{2.68}$$

is fulfilled. This means that at these angles the sensitivity of the output signal reading to small variations of the sensing layer thickness is very small. Although this might seem satisfactory, it does not yet fulfill the second part of the criterion. In particular, the graph in Fig. 2.18 indicates that fulfilling the condition (2.68) is very sensitive to the incident angle. This means that to minimise the sensitivity of the output signal to the variations of t_s, one would have to adjust the incident angle with great precision. Any misadjustment of the incident angle θ would increase this sensitivity substantially.

The graph in Fig. 2.19 is similar to that in Fig. 2.18, but in this case three well selected

values of the sensing layer thickness t_s are examined. It can be seen from this graph that the equation (2.68) is fulfilled for certain values of the incident angle, which are denoted by $\theta_{\mathrm{opt,II}}$ and indicated by arrows. However, in contrast to the previous case, the sensitivity of the condition (2.68) to the adjustment of the incident angle is eliminated, since the additional condition, namely

$$\partial^2 Q_{\mathrm{ray}}/\partial t_s \partial\theta = 0, \tag{2.69}$$

holds at these angles at the same time. This suggests that Eqs. (2.68) and (2.69) represent the formal representation of the new optimisation criterion dealt with in this section.

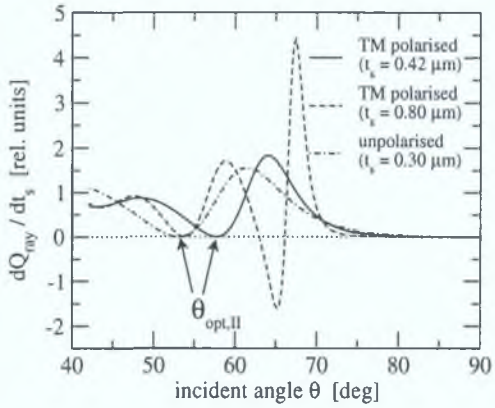

Figure 2.19: Examples of the derivative $\partial Q_{\mathrm{ray}}/\partial t_s$ as a function of the incident angle for a number of well selected values of the sensing layer thickness t_s and polarisations of the interrogating light.

As demonstrated by Figs. 2.18 and 2.19 and by the above discussion, it is not straightforward to fulfill both equations (2.68) and (2.69) simultaneously. In fact, for a given set of remaining parameters characterising the sensing element, these two equations can be satisfied only at *particular* values of the sensing layer thickness and their corresponding values of the incident angle. For example, for the refractive indices and the wavelength summarised in Table 2.3(a), equations (2.68) and (2.69) are fulfilled only for $t_s = 0.42\,\mu$m and $t_s = 0.80\,\mu$m for p (TM) polarised light, and for $t_s = 0.3\,\mu$m for unpolarised light. Furthermore, they cannot be satisfied simultaneously for the s (TE) polarised light.

Although this conclusion might seem to be restricting the design of the sensor system, it provides clear advantages. Specifically, if the sensing layer thickness and the incident angle are selected so as to fulfill Eqs. (2.68) and (2.69), the output signal reading of the sensor system will be very insensitive to small variations of t_s and misadjustments of θ, which are inherent in the processes of the layer deposition and the sensor system assembly, respectively.

For the optical parameters summarised in Table 2.3(a), these "optimum" values of t_s and $\theta_{\mathrm{opt,II}}$ are evident from Fig. 2.19. For illustration purposes, the variation of these values with the refractive index of the sensing layer is shown in Fig. 2.20. The graph (a) suggests that the value of the optimum thickness, denoted by $t_{s,\mathrm{opt,II}}$, does not vary significantly with the sensing layer refractive index around the typical value of 1.43. Furthermore, it lies well within the typical interval of precision of the sensing layer thickness achievable by the dip/spin-coating deposition technique. On the other hand, changes in the optimum angle $\theta_{\mathrm{opt,II}}$ are approximately 5° over the range $n_s = 1.40$–1.45.

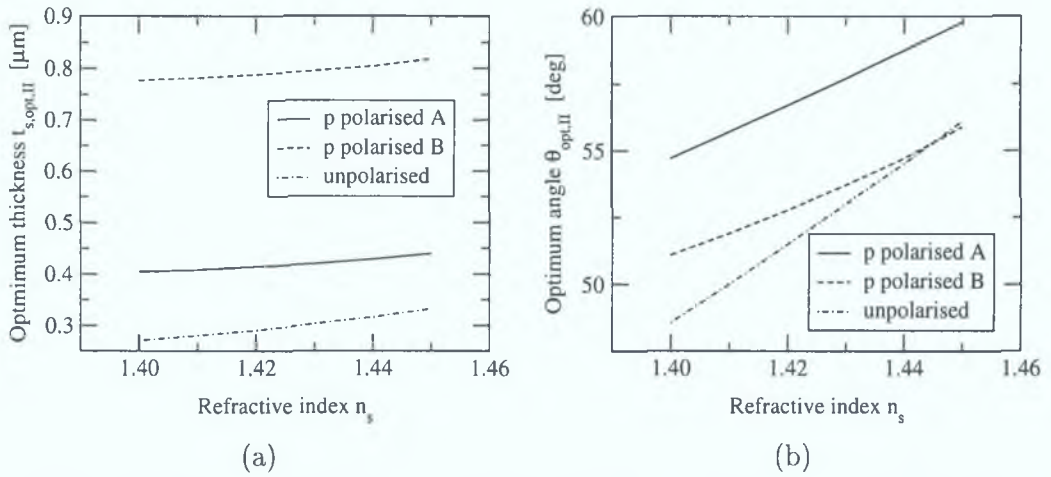

Figure 2.20: An example of $t_{s,\mathrm{opt,II}}$ (graph a) and $\theta_{\mathrm{opt,II}}$ (graph b) for which Eqs. (2.68) and (2.69) are satisfied, as a function of the sensing layer refractive index. The remaining parameters characterising the sensor system are summarised in Table 2.3(a).

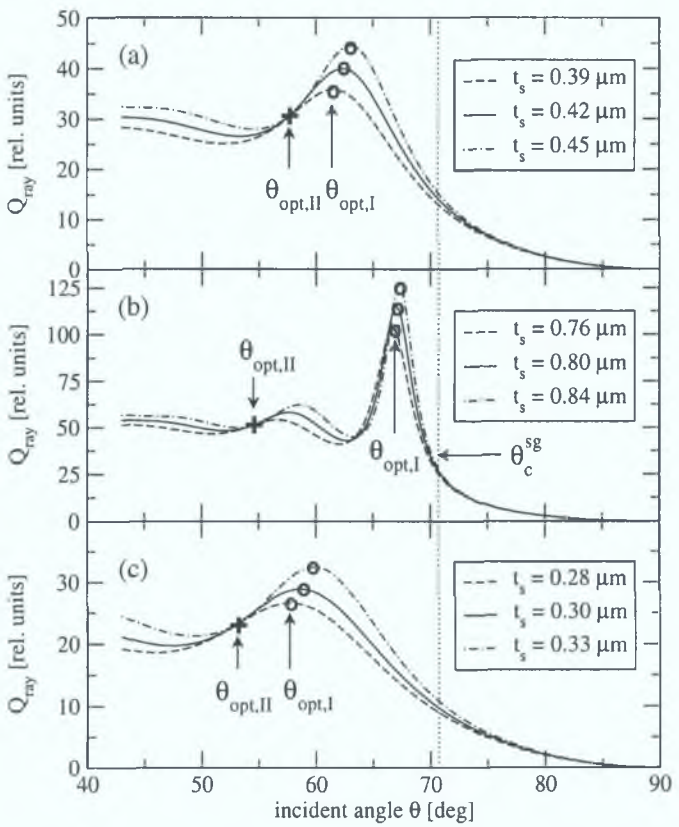

Figure 2.21: A comparison of the angular distributions of the quantity Q_{ray} for three different sets of the sensing layer thicknesses. The solid lines correspond to the distributions plotted for values at which Eqs. (2.68) and (2.69) are satisfied. The dashed and dash-dotted lines correspond to the values of the sensing layer thickness which differ slightly from the optimum value. The graphs (a), and (b) correspond to p (TM) polarised light, the graph (c) corresponds to unpolarised light. The remaining parameters characterising the sensor system are summarised in Table 2.3(a).

To explain the advantages provided by the above analysis, the angular distribution of the sensor sensitivity is plotted for three different values of the sensing layer thickness around the optimum value for which Eqs. (2.68) and (2.69) are satisfied. The sensitivity is approximated by the quantity Q_{ray}. The situation is illustrated by the graphs in Fig 2.21. These graphs demonstrate that the maximum sensitivity (depicted by bold circles), which is considered as the optimum sensitivity for the ideal sensing element, varies significantly even for such small changes of the sensing layer thickness as $\Delta t_s = \pm(20\text{–}30)$ nm. Furthermore, the angular position $\theta_{\text{opt,I}}$ of this sensing configuration is slightly affected. On the other hand, when the sensor operation is shifted towards the angle $\theta_{\text{opt,II}}$ (indicated by bold crosses), small discrepancies in the sensing layer thickness do not significantly affect the sensitivity of the sensor system. Furthermore, the difference in the absolute sensitivity induced by moving from the optimum angle $\theta_{\text{opt,I}}$ to $\theta_{\text{opt,II}}$ is relatively large, especially for the thicker sensing layer (compare the values indicated by the circles and the cross in Fig. 2.21(b)). Therefore, the decision between the two choices has to be a trade-off between the maximisation of the sensor sensitivity and its acceptable variations due to the discrepancies in the sensing layer thickness.

The solution to the problem related to the influence of the small misalignments of the sensing element on the output signal reading is relatively straightforward. It is suggested immediately by the formal expression for the output signal given by Eq. (2.36). As mentioned above, the discrepancies in the alignment of the sensing element affect the values of the coupling efficiencies γ_{in} and γ_{out}. If the values of these parameters for the (slightly) misaligned sensing element are denoted by $\tilde{\gamma}_{\text{in}}$ and $\tilde{\gamma}_{\text{out}}$, respectively, it is possible to represent the misalignment by a factor μ, which relates the two situations by $\tilde{\gamma}_{\text{in}}\tilde{\gamma}_{\text{out}} = \mu\gamma_{\text{in}}\gamma_{\text{out}}$. This means that the factor μ is the measure of the difference between the light intensity levels that reach the photodetector in both situations. As can be seen from (2.36), these differences can be eliminated by *adjusting the gain factor* γ_{el} of the electronics circuit to the value $\tilde{\gamma}_{\text{el}} = \gamma_{\text{el}}/\mu$ so as to satisfy the equation

$$\tilde{\gamma}_{\text{in}}\tilde{\gamma}_{\text{out}}\tilde{\gamma}_{\text{el}} = \gamma_{\text{in}}\gamma_{\text{out}}\gamma_{\text{el}}. \tag{2.70}$$

This means that either manual or automatic adjustment of the gain factor of the electronic circuit at a *certain* analyte concentration should result in the same output signal reading for the *entire* range of analyte concentrations.

It needs to be pointed out that this conclusion is slightly modified in real sensor systems in which the noise introduced by the electronic circuit is always present. In practice, the level of noise of the output signal is proportional to the total amplification of the circuit, which is represented by γ_{el}. Consequently, as concluded above, modification of the amplification factor γ_{el} not only helps adjust the output signal reading, but also influences its level of noise and consequently the sensor resolution. For example, the greater is the value of the amplification factor, the smaller the resolution of the sensor system that can be expected.

This conclusion along with the results obtained earlier in this section will become clearer in Sec. 2.4, where the performance of the sensor system in various configurations is numerically simulated.

2.4 Simulation of sensor performance

In this section, simulations of the sensor performance in various configurations are presented. The purpose is to illustrate the theoretical predictions and main conclusions drawn in Secs. 2.2 and 2.3.

2.4.1 Definition of medium for absorption-based sensing

Before proceeding with the simulations of the sensor performance, it is necessary to define the parameters characterising the sensing medium. The medium under consideration is assumed to be hypothetical, i.e., the absorption spectrum of the medium and its variation with the analyte concentration is assumed to be described by a hypothetical function. Although this function does not represent any particular material used in practical applications, it is realistic enough to be considered in the calculations of the performance of a real absorption-based optical sensor.

The spectral variations of the extinction coefficient κ_s of the hypothetical medium are shown in Fig. 2.22. The values of κ_s are non-zero only within the region corresponding to the emission peak of the light source. The value of the extinction coefficient varies linearly with the analyte concentration according to the formula

$$\kappa_s = \kappa_{s0} + \kappa'_s c_A \,[\%], \tag{2.71}$$

where

$$\begin{aligned} \kappa_{s0} &= 0.5 \times 10^{-3}, \\ \kappa'_s &= 0.5 \times 10^{-5}\ [\%^{-1}]. \end{aligned} \tag{2.72}$$

In other words, the extinction coefficient of the sensing layer varies linearly between 0.0005 and 0.001 for the analyte concentrations changing from 0 % to 100 %.

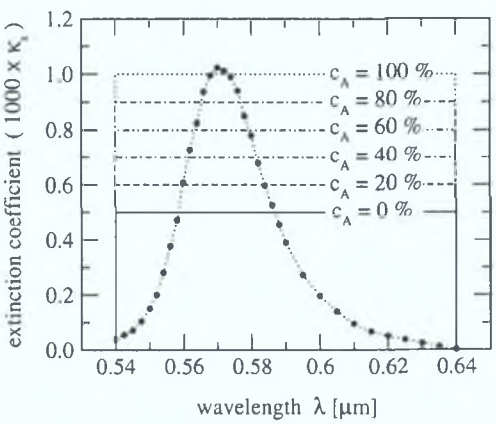

Figure 2.22: Spectral variations of the extinction coefficient κ_s of the hypothetical medium comprising the sensing layer considered in the simulation. The spectra are plotted for several values of the analyte concentration c_A, as shown by the legend. The emission spectrum of the source (dotted line with points), which corresponds to an LED with peak intensity at 570 nm, is also plotted.

2.4.2 Diffusion of analyte into the sensing layer

In the majority of sensor systems based on absorption change of a doped sensing layer in response to changes in analyte concentration, the analyte is required to diffuse into the sensing layer. The diffusion of the analyte is described by the diffusion coefficient D_s. Once the analyte is in the sensing layer, it reacts with the analyte sensitive reagent immobilised inside the layer. The rate of this chemical reaction can be characterised by the parameter D_r. When these two processes are combined, the extinction coefficient of the sensing layer changes at a rate which can be characterised by the coefficient D_κ, which is related to D_s and D_r as $1/D_\kappa = 1/D_s + 1/D_r$. In the following, it is assumed that the reactions leading to the modification of the extinction coefficient happen instantaneously, i.e., it is the diffusion rate that limits the response time of the sensing element. Formally, this can be represented by $D_s \ll D_r$, i.e.,

$$D_\kappa \approx D_s. \tag{2.73}$$

The diffusion of the analyte into the sensing layer can be described by a one-dimensional diffusion equation

$$\frac{\partial c_A(z,t)}{\partial t} = D_s \frac{\partial^2 c_A(z,t)}{\partial z^2}. \tag{2.74}$$

In this equation, $c_A(z,t)$ denotes the distribution of the analyte concentration across the sensing element containing the sensing layer in time t. To find the solution to (2.74), boundary and initial conditions have to be supplied. The solution is subsequently found by applying well known techniques of higher level calculus.

In this analysis, two processes are of interest, namely the diffusion of the analyte *into* the layer and the diffusion of the analyte *out* of the layer into the environment above it. Formally, these two processes are characterised by two sets of boundary and initial conditions.

Firstly, the analyte concentration above the sensing layer, which is denoted by c_{A0}, is assumed to be constant for a sufficiently long period of time, i.e., until the equilibrium of the distribution of the analyte molecules in the sensing layer has been reached. Then, the concentration above the sensing layer abruptly changes to its new value, which will be denoted by c_{A1}. This can be formally represented by the condition at the boundary of the sensing layer and the medium containing the analyte (i.e., the environment) as

$$c_A(z=0,t) = \begin{cases} c_{A0}, & \text{for } t < 0, \\ c_{A1}, & \text{for } t \geq 0, \end{cases} \tag{2.75}$$

where $z = 0$ represents the position of the boundary. Furthermore, the guiding layer, which is below the sensing layer, is assumed to be impermeable to the analyte. This means that there is no diffusion of the analyte occurring at the boundary of the sensing and guiding layers. Because this boundary is characterised by[7] $z = t_s$, this condition can be formally represented by

$$\left.\frac{\partial c_A(z,t)}{\partial z}\right|_{z=t_s} = 0, \quad \text{for all } t. \tag{2.76}$$

Prior to the abrupt change of the analyte concentration above the sensing layer, the profile of the analyte concentration in the sensing layer was in an equilibrium. In this representation,

[7] Please avoid confusion between t denoting time and t_s denoting the thickness of the sensing layer.

the initial condition can be written as

$$\begin{aligned} c_A(z, t = 0) &= c_{A0}, \quad \text{for } z \in (0, t_s\rangle, \\ c_A(z = 0, t = 0) &= c_{A1}. \end{aligned} \tag{2.77}$$

The process of the diffusion of the analyte into the sensing layer is represented by $c_{A0} < c_{A1}$, while the reverse process is characterised by $c_{A0} > c_{A1}$.

The solution to the diffusion equation (2.74) obeying the boundary and initial conditions (2.75–2.77) can be found as follows. Due to the separable form of the partial differential equation (2.74), the function $c_A(z, t)$ can be written in a factorised form

$$c_A(z, t) = Z(z)T(t). \tag{2.78}$$

Upon substitution of this function into (2.74) and after some rearrangements, Eq. (2.74) can be rewritten in the form

$$\frac{1}{D_s}\frac{1}{T}\frac{\mathrm{d}T}{\mathrm{d}t} = \frac{1}{Z}\frac{\mathrm{d}^2 Z}{\mathrm{d}z^2}. \tag{2.79}$$

Because the left-hand side of this equation is a function of t and the right-hand side is a function of z, the only chance that they are equal to each other is if they are both equal to a constant. If this constant is denoted by $-\xi^2$, the solution to (2.74) can be found by finding the solution to the following two differential equations:

$$\begin{aligned} \frac{\mathrm{d}T}{\mathrm{d}t} &= -\xi^2 D_s T, \\ \frac{\mathrm{d}^2 Z}{\mathrm{d}z^2} &= -\xi^2 Z. \end{aligned} \tag{2.80}$$

The solutions to the differential equations (2.80) can be found easily. Its general form is

$$\begin{aligned} T(t) &= T_0(\xi)\exp(-\xi^2 D_s t), \\ Z(z) &= Z_c(\xi)\cos(\xi z) + Z_s(\xi)\sin(\xi z), \end{aligned} \tag{2.81}$$

where $T_0(\xi)$, $Z_c(\xi)$ and $Z_s(\xi)$ are functions of ξ which need to be found from the initial and boundary conditions applicable to the function $c_A(z, t)$.

In the preceding derivations, no assumptions were made about the constant $-\xi^2$. The function $c_A(z, t)$ in the form (2.78), where $Z(z)$ and $T(z)$ are taken from (2.81), fulfills the differential equation (2.74) for any value of ξ. Consequently, the most general form of the function $c_A(z, t)$ must be written as

$$c_A(z, t) = c_0 + \int \mathrm{d}\xi\, T_0(\xi)\exp(-\xi^2 D_s t)\,[Z_c(\xi)\cos(\xi z) + Z_s(\xi)\sin(\xi z)]. \tag{2.82}$$

The form of the functions $T_0(\xi)$, $Z_c(\xi)$ and $Z_s(\xi)$ is found by the analysis of the initial condition.

To find the initial condition in a more convenient form, the function $c_A(z, t = 0)$ is expanded beyond the interval $z \in \langle 0, t_s\rangle$, which corresponds to the sensing layer. The expansion, which is represented by the function $\tilde{c}_A(z)$, is in the form

$$\begin{aligned} \tilde{c}_A(z) &= c_{A1} && \text{for } z = 2mt_s, \\ \tilde{c}_A(z) &= c_{A0} && \text{for } z \in (0, 2t_s) + 4mt_s, \\ \tilde{c}_A(z) &= 2c_{A1} - c_{A0} && \text{for } z \in (2t_s, 4t_s) + 4mt_s, \end{aligned} \tag{2.83}$$

where $m = 0, \pm 1, \pm 2, \ldots$, and $4t_s$ is its periodicity. It is important to note the open intervals in the second and third lines of the definition (2.83). For better visualisation of this function, its graphical representation is shown in Fig. 2.23. This function is equivalent to the initial condition (2.77) at $z \in (0, t_s\rangle$, and also agrees with the boundary condition (2.75) at $z = 0$. Furthermore, it fulfills the condition (2.76), which justifies that the choice of this expansion is appropriate.

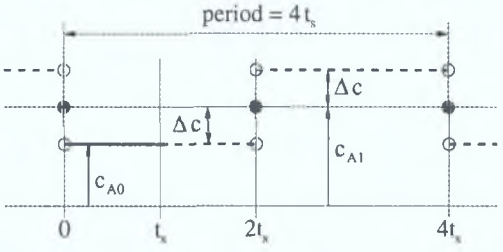

Figure 2.23: Graphical representation of the function $\tilde{c}_A(z)$ (bold dashed line), which is a periodic expansion of the function $c_A(z, 0)$ (bold solid line) representing the initial analyte distribution across the sensing layer. The open points represent those points that do not belong to the lines (see the open intervals in Eq. (2.83)). The difference Δc is given by $\Delta c = c_{A1} - c_{A0}$.

Employing Fourier analysis, it follows that the function $\tilde{c}_A(z)$ defined in (2.83) can be written in the form of the Fourier series

$$\tilde{c}_A(z) = a_0 + \sum_{n=1}^{\infty} \left[a_n \cos\left(2\pi n \frac{z}{4t_s}\right) + b_n \sin\left(2\pi n \frac{z}{4t_s}\right) \right]. \tag{2.84}$$

Using a well known procedure, the coefficients a_n and b_n can be found as

$$\begin{aligned} a_0 &= c_{A1}, \\ a_n &= -\frac{2}{\pi}\left[1 - (-1)^n\right](c_{A1} - c_{A0}) \quad n = 1, 2, \ldots, \\ b_n &\equiv 0, \quad n = 1, 2, \ldots. \end{aligned} \tag{2.85}$$

By comparing the expressions (2.82) and (2.84), the distribution of the analyte concentration in the sensing layer, as a function of time, can be written as

$$c_A(z,t) = c_{A1} - (c_{A1} - c_{A0}) \frac{4}{\pi} \sum_{n=1}^{\infty} \frac{1}{2n-1} \sin\left[(2n-1)\frac{\pi}{2t_s} z\right] \exp\left[-\left((2n-1)\frac{\pi}{2t_s}\right)^2 D_s t\right]. \tag{2.86}$$

Figure 2.24 shows an example of the time evolution of the analyte concentration profile based on Eq. (2.86). In the calculation, the values of $D_s = 10^{-12}\,\mathrm{m^2 s^{-1}}$ and $t_s = 1\,\mu\mathrm{m}$ were considered. The graph in Fig. 2.24(a) shows the process of the diffusion of the analyte into the sensing layer. At the beginning of the process, i.e., at $t = 0\,\mathrm{s}$, the concentration in the sensing layer is constant and equal to $c_{A0} = 10\,\%$. As the time passes, the layer becomes filled by the analyte from the left-hand side. Note that the derivative $\partial c_A(z,t)/\partial z$ is zero at $z = t_s$ for every time t, as it should according to Eq. (2.76). After a sufficiently long time ($t \gtrsim 2\,\mathrm{s}$), the distribution of the analyte concentration does not change and remains equal to the equilibrium value of $c_{A1} = 90\,\%$ across the entire sensing layer.

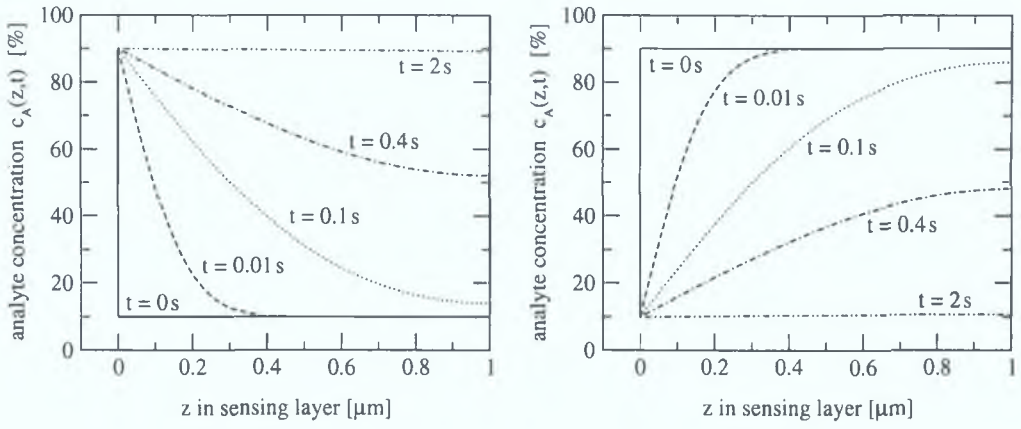

Figure 2.24: Examples of the time evolution of the analyte concentration profile across the sensing layer. In the calculations, which are based on Eq. (2.86), the values $D_s = 10^{-12}\,\mathrm{m^2 s^{-1}}$ and $t_s = 1\,\mu\mathrm{m}$ were used. The graphs (a) and (b) correspond to the process of diffusion into and out of the sensing layer, respectively.

The reverse diffusion process for the same parameters $D_s = 10^{-12}\,\mathrm{m^2 s^{-1}}$ and $t_s = 1\,\mu\mathrm{m}$ is shown in Fig. 2.24(b). In this case, the initial analyte concentration is equal to the equilibrium value $c_{A0} = 90\,\%$. When the concentration outside the sensing layer changes abruptly to $c_{A1} = 10\,\%$ at $t = 0\,\mathrm{s}$, the analyte starts leaving the layer from the left-hand side. Again, the condition $\partial c_A(z,t)/\partial z = 0$ is satisfied for every time t. After a sufficiently long time ($t \gtrsim 2\,\mathrm{s}$), the distribution of the analyte concentration does not change and remains equal to the equilibrium value of $c_{A1} = 10\,\%$ across the entire sensing layer.

2.4.3 Time evolution of the output signal

This section presents numerical examples of the time evolution of the output signal of the sensor system. The examples are based on Eq. (2.36) and the dynamics of the analyte diffusion discussed in the previous section. Combining equations (2.71) and (2.86), it is evident that due to the diffusion of the analyte into the sensing layer, the distribution of the extinction coefficient κ_s varies across the sensing layer in time, i.e., $\kappa_s(z,t) = \kappa_{s0} + \kappa'_s c_A(z,t)$. Due to the linearity of the relation, the profile $\kappa_s(z,t)$ looks similar to that of $c_A(z,t)$ already analysed in Sec. 2.4.2 (see Fig. 2.24), and will not therefore be discussed any further.

The feature of $\kappa_s(z,t)$ relevant to the evaluation of the sensor output signal is that it is non-homogeneously distributed across the sensing layer. The matrix formalism developed in Sec. 2.2, which is suitable for the analysis of multilayer systems consisting of an arbitrary number of layers (see equations (2.52–2.54)), can now be advantageously applied. Firstly, the single sensing layer with the extinction coefficient profile $\kappa_s(z,t)$ is approximated by a stack of N layers, each having a uniform distribution of the extinction coefficient. Depending on the precision required from the calculation, the division of the sensing layer into the stack of N layers can vary. In the simulations presented below, the layer is divided into layers of *equal* thicknesses denoted by $\bar{t}_s = t_s/N$. The extinction coefficient of each of these layers is

calculated as the value of $\kappa_s(z,t)$ in the center of the particular layer, i.e.,

$$\begin{aligned} &\text{layer } j\text{: expands from } z_{j-1} = (j-1)\bar{t}_s \text{ to } z_j = j\bar{t}_s, \\ &\kappa_{sj} = \kappa_s((z_{j-1}+z_j)/2), \end{aligned} \tag{2.87}$$

where $j = 1, 2, \ldots, N$. The real part of the refractive index of each layer in the stack is assumed to be the same and equal to that of the sensing layer, i.e., $\Re\{n_{sj}\} = \Re\{n_s\}$.

To find the time evolution of the output signal V in (2.36), it is necessary to evaluate the time variations of the attenuation factor $\mathcal{T}$. In the following analysis, a ray-optics approach is employed, i.e., $\mathcal{T}$ is approximated by $\mathcal{T}_{\text{ray}}$ in Eq. (2.63). Furthermore, for simplicity reasons, only a sensor system based on one reflection, i.e., $\nu = 1$, is considered.

The parameters characterising the sensing element are summarised in Table 2.3(a), i.e., it consists of a guiding layer ($n_g = 1.515$) and a sensing layer ($n_s = 1.43 + i\kappa_s$) surrounded by air ($n_a = 1.0$). The spectral characteristics of the interrogating light, which is assumed to be s-polarised, are shown in Fig. 2.22. The sensing layer is divided into $N = 50$ layers. The relation between the analyte concentration inside the sensing layer and the extinction coefficient is given by (2.71) and (2.72). The diffusion coefficient is assumed to be $D_s = 10^{-12}\,\text{m}^2\text{s}^{-1}$.

The examples of the response of the sensor system, which employs the above described sensing element, to the variations of the analyte concentration between 0 % and 100 % are shown in Fig. 2.25. The curves in the graph (a) and (b) correspond to the values of the sensing layer thickness $t_s = 0.3\,\mu\text{m}$ and $t_s = 0.8\,\mu\text{m}$, respectively. The output signals were calculated for several values of the incident angle θ (see the legend of the graphs) in order to compare the corresponding sensor performances.

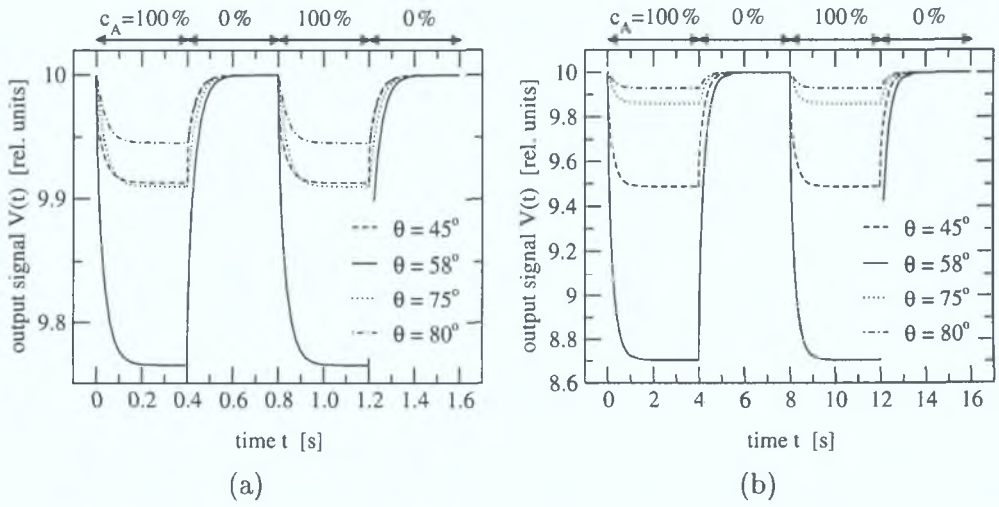

Figure 2.25: Numerical simulations of the time evolution of the output signal of the sensor system employing a sensing element characterised in Table 2.3(a). The sensing layer, with thickness of either $t_s = 0.3\,\mu\text{m}$ (a) or $t_s = 0.8\,\mu\text{m}$ (b), is assumed to be interrogated by an s-polarised light with spectral characteristics shown in Fig. 2.22. The concentration above the sensing layer changes abruptly between 0 % and 100 %. See text for more details.

As can be seen from the graphs, the thicker layer results in a greater dynamic range of the sensor output but longer response time (compare the scales of the x and y axes), as expected from the sensitivity curves in Fig. 2.14(a) and from the analysis of the analyte diffusion. The

graphs also demonstrate the variations of the dynamic range of the output signal with the incident angle θ. As expected from the analysis in Secs. 2.2.7 and 2.2.9, the sensitivity of the sensor to the variations of the analyte concentration is lower when the evanescent mode of the sensor operation is chosen (see the curves plotted for $\theta = 75°$ and $\theta = 80°$). On the other hand, by adjusting the incident angle to the optimum value $\theta_{\text{opt,I}}$ (see the solid lines), the dynamic range of the sensor can be increased significantly, especially for a thicker sensing layer. This demonstrates that the sensing configuration employing the optimum angle of incidence $\theta_{\text{opt,I}}$ provides enhanced sensitivity in comparison with the sensitivity achieved by the evanescent-wave sensing.

2.4.4 Response of the sensor system—ideal vs real sensing element

In this section, the performance of the sensor systems employing the ideal and real sensing elements is compared. The purpose is to provide better understanding of the conclusions drawn in Sec. 2.3.1 and 2.3.2. It was found that the maximum sensitivity of the sensor system employing an ideal sensing element is achieved when the interrogating light impinges on the sensing layer at the incident angle of $\theta = \theta_{\text{opt,I}}$, as shown in Figs. 2.14 and 2.16. On the other hand, following a different criterion for the optimum sensor performance, the optimum sensitivity of the sensor system employing a real sensing element is achieved when the incident angle is equal to $\theta = \theta_{\text{opt,II}}$, as shown in Fig. 2.21.

The conditions for which the numerical simulations are carried out are very similar to those in the previous section. The sensing element consists of a glass substrate ($n_g = 1.515$) and a sensing layer ($n_s = 1.43 + i\kappa_s$) covered by air ($n_a = 1.0$). It is interrogated by the broad-band light whose spectrum is shown in Fig. 2.22. The light is assumed to be p polarised, as opposed to the s polarisation considered previously. Only the single-reflection interrogation is considered.

The thickness of the sensing layer is considered to be *around* the optimum value $t_{s,\text{opt,II}} = 0.80\,\mu\text{m}$, as discussed in Sec. 2.3.2 and shown in Fig. 2.20(b). This thickness corresponds to the situation where one can achieve such a sensing configuration that the sensor response is very *insensitive* to the variations of the sensing layer thickness or the incident angle (see Fig. 2.21).

For the purpose of comparison, two values of the incident angle θ, namely $\theta = \theta_{\text{opt,II}} = 54°$ and $\theta = \theta_{\text{opt,I}} = 67°$, are considered in the numerical simulations. As follows from Fig. 2.21, the sensitivity at the incident angle $\theta_{\text{opt,I}}$ is approximately twice as large as that at the angle $\theta_{\text{opt,II}}$. On the other hand, this sensitivity also exhibits much greater dependence on the thickness of the sensing layer, which is almost negligible when $\theta = \theta_{\text{opt,II}}$ is used.

Instead of analysing the time evolution of the output signal, which was done in the previous section, the focus here is on the calibration function of the sensor system. The calibration function provides a relation between the response of the sensor (output signal) and the analyte concentration.

The response of the sensing medium, in terms of the variation of the extinction coefficient with the analyte concentration, is summarised in Eqs. (2.71–2.72) and depicted in Fig. 2.22. The output signal V of the sensor system is given by Eq. (2.36), where the attenuation factor $\mathcal{T}$ is expressed by (2.63) with $\nu = 1$.

Firstly, it is assumed that the sensor system is configured in such a way that the value of the product $P_{\text{in}}\gamma_{\text{in}}\gamma_{\text{out}}\gamma_{\text{ec}}$ in (2.36) is equal to 10 V. This can be achieved by the initial adjustment of the amplification γ_{ec} of the electronic circuit. Furthermore, the initial off-set $V_0 = 0\,\text{V}$ is considered. The output signal which is calculated under these conditions will be referred to as the *raw* output signal.

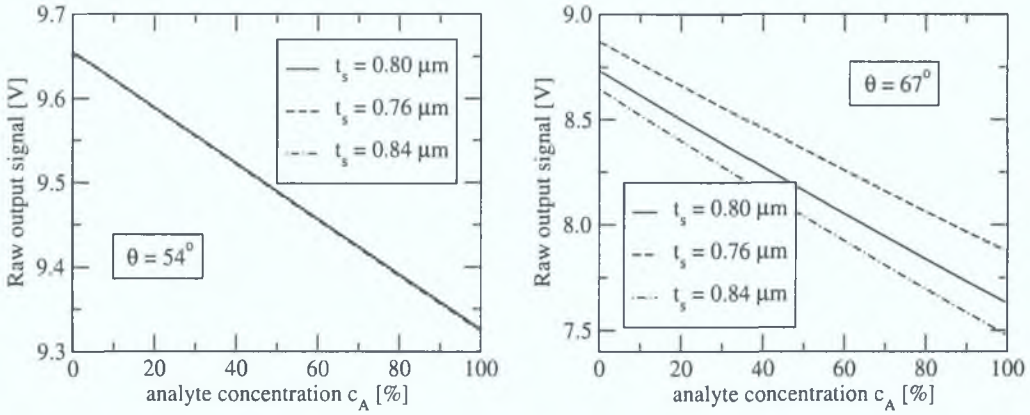

Figure 2.26: Raw output signal produced by the sensor system in response to the variation of the analyte concentration. The graphs (a) and (b) correspond to the incident angles of $\theta = \theta_{\text{opt,II}} = 54°$ and $\theta = \theta_{\text{opt,I}} = 67°$, respectively. The different lines correspond to different thicknesses of the sensing layer, as specified in the legend.

The variation of the raw output signal with the analyte concentration is shown in Fig. 2.26. The graphs (a) and (b) correspond to the incident angles $\theta = \theta_{\text{opt,II}} = 54°$ and $\theta = \theta_{\text{opt,I}} = 67°$, respectively. The response curve depicted by the solid line corresponds to the thickness of the sensing layer $t_s = t_{s,\text{opt,II}} = 0.8\,\mu\text{m}$.

As can be seen, the dynamic range of the raw sensor output corresponding to $\theta = \theta_{\text{out,I}}$, which extends from $V(0\%) \approx 8.75\,\text{V}$ to $V(100\%) \approx 7.65\,\text{V}$, is approximately 3.4 times greater than that associated with $\theta = \theta_{\text{out,II}}$, which ranges from $V(0\%) \approx 9.65\,\text{V}$ to $V(100\%) \approx 9.33\,\text{V}$. However, if the thickness of the sensing layer is different from the optimum value $0.8\,\mu\text{m}$ by as little as $\pm 40\,\text{nm}$, both the dynamic range and the absolute value of the raw signal for $\theta = 67°$ change significantly, as shown by the dashed and dash-dotted lines in Fig. 2.26(b). On the other hand, this change of the sensing layer thickness has only a negligible influence on the sensor response employing the incident angle $\theta = \theta_{\text{opt,II}} = 54°$, as shown by the dashed and dash-dotted lines in Fig. 2.26(a), which are barely visible as they lie so close to the solid line.

The difference between the two cases shown in Figs. 2.26(a) and 2.26(b) is not yet directly comparable. The quantitative comparison is possible only when the dynamic ranges of the two sensor configurations are matched. This matching proceeds as follows: it is assumed that the two sensor systems employ the same ideal sensing element with the thickness of the sensing layer equal to $t_{s,\text{opt,II}} = 0.8\,\mu\text{m}$. It is required that the dynamic range of the sensor output is between 5 V (at $c_A = 100\,\%$) and 10 V (at $c_A = 0\,\%$) for both sensor systems. This can be achieved by adjusting the gain (γ_{ec}) and off-set (V_0) of the electronic circuit (see Eq. (2.36)). Understandably, due to different dynamic ranges of the raw signals, this

adjustment is different for each of the sensor systems. Once this has been done, the response looks as shown in Fig. 2.27 by the solid line. Again, the graphs (a) and (b) correspond to the sensor systems characterised by the incident angles $\theta = \theta_{\mathrm{opt,II}} = 54°$ and $\theta = \theta_{\mathrm{opt,I}} = 67°$, respectively. This procedure also establishes the calibration functions associated with both sensor systems.

Now, the assumption of the sensing element being ideal is abandoned. This means that the thickness of the sensing layer can differ from the optimum one. Consequently, this can result in the alterations of the response of both sensor systems, as implied by the variations of the raw signal shown in Fig. 2.26.

In practical situations, the thickness of the sensing layer should not vary once the sensing element is incorporated into the sensor system. Moreover, if there is no possibility of movement of the sensing element, the response of the sensor should not change. However, if there is a need to replace the sensing element, it might pose a problem, since the calibration curve could be modified due to a slightly different thickness of the sensing layer or small misadjustments in the positioning of the new sensing element. At the same time, it is desirable that the calibration procedure should *not* be carried out again.

As mentioned at the end of Sec. 2.3.2 and is implied by Eq. (2.70), the problem can be solved by readjusting the gain of the electronic circuit γ_{ec} at *one* value of the analyte concentration, such as at $c_A = 0\,\%$. In this case, the gain factor γ_{ec} is adjusted so as to ensure that the output signal at $c_A = 0\,\%$ is equal to 10 V.

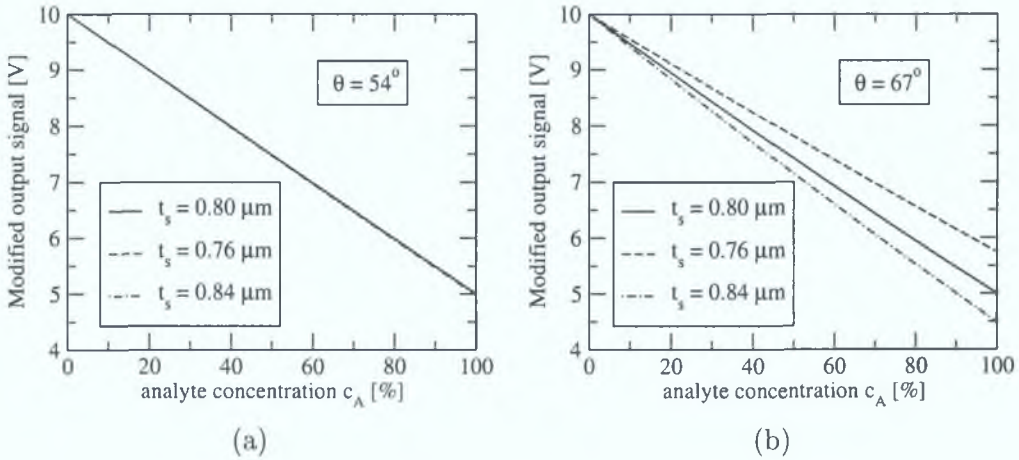

Figure 2.27: Modified output signal produced by the sensor system in response to the variation of the analyte concentration. The graphs (a) and (b) correspond to the incident angle of $\theta = \theta_{\mathrm{opt,II}} = 54°$ and $\theta = \theta_{\mathrm{opt,I}} = 67°$, respectively. The different lines correspond to different thicknesses of the sensing layer, as specified in the legend.

Once this is done, the response of the sensor systems looks like that depicted in Fig. 2.27. As can be seen, the calibration function of the sensor system employing the interrogation at $\theta = \theta_{\mathrm{opt,I}}$ is noticeably altered even by as small variations of the sensing layer thickness as $\pm 40\,\mathrm{nm}$. This drawback throws a question-mark over the advantages that make this configuration attractive, namely the enhanced sensitivity. This drawback remains significant unless it is feasible to produce the sensing elements with very good precision or it is affordable to perform the calibration procedure of the sensor system every time the sensing element is

exchanged.

On the other hand, small variations of the sensing layer thickness have only a negligible influence on the calibration function of the sensor system employing the interrogation at $\theta = \theta_{\mathrm{opt,II}}$, as shown in Fig. 2.27(a). This configuration could therefore be attractive from the point of view of the mass-production. Even though the provided sensitivity is not as large as in the previous configuration, it is still at least 3 times greater than that achievable by the evanescent wave interrogation, as follows from the graph (b) in Fig. 2.21.

2.5 Conclusion

In this chapter, a rigorous electromagnetic theory was developed which is suitable for the description of absorption-based optical chemical sensors employing a planar waveguide coated with a thin sensing layer. Using the theory, conditions were identified for which the performance of the sensor is optimised.

The detailed analysis focused on a highly multimode waveguide structure, such as a glass microscope slide, covered with a thin sensing film. These types of structures provide a number of advantages in comparison to their mono-mode counterparts, such as ease of preparation and handling, less elaborate coupling of light into the guided modes, etc.

Two approaches to the analysis of the sensor sensitivity as a function of the parameters describing the waveguide structure were developed, based on, respectively, wave optics and ray optics. These two approaches were found to be equivalent in the approximation of weak absorption and short interaction length. The use of the ray-based model is preferable if the ray, which is used as the approximation of the light propagating along the waveguide, undergoes only a small number of reflections from the sensing layer. This is because the results necessary to determine optimum sensing conditions can be calculated much faster. However, if the number of reflections increases the full wave-based description of the light propagation along the waveguide has to be employed to predict the optimum conditions more accurately.

A detailed numerical analysis was carried out for a structure comprising a glass slide (thickness ≈ 1 mm, refractive index 1.515) coated with a thin sensing layer (thickness ≈ 0.3–$0.8\,\mu$m, refractive index 1.43) and covered by the environment which was either air or water. The analysis showed that two types of criteria for the optimised sensor performance can be formulated.

The first criterion, which is applicable to structures whose parameters are characterised with very high accuracy (so-called 'ideal' structures), is based on the requirement of maximum sensitivity of the sensor output to the changes in the analyte concentration. It was found that such sensing conditions can be achieved if, for a given thickness of the sensing layer, weak absorption and short interaction length, the incident angle of light ray interrogating the sensing layer is equal to the optimum angle $\theta_{\mathrm{opt,I}}$. This angle was found to be *smaller* than the critical angle of the sensing layer/guiding layer interface but greater than that of the environment/guiding layer interface. This corresponds to the situation where the sensing layer is interrogated *not* by the evanescent wave but rather by a wave which is propagating (but not being guided!) in the sensing layer. It was found that the sensitivity of the sensor can be substantially enhanced at this angle, especially for thicker sensing layers.

This conclusion was, however, found to be valid only for a weakly absorbing sensing layer and for a short interaction length. A more detailed analysis showed that there exists some critical distance L_c for which the configuration employing the optimum angle $\theta_{\text{opt,I}}$ no longer provides maximum sensitivity. This distance can be determined from the wave-based description of the sensor operation.

The second criterion, which is applicable to structures whose parameters can be characterised only with limited accuracy (so-called 'real' structures), is based on the requirement that the output signal of the sensor is sensitive to the variation in the analyte concentration but insensitive to the variations of the thickness of the sensing layer, t_s, and incident angle, θ, of the interrogating ray. It was found that such sensing conditions can be achieved only for values of t_s and θ laying in *certain* intervals, namely around optimum values $t_{s,\text{opt,II}}$ and $\theta_{\text{opt,II}}$. These optimum values can be determined from the theoretical model, provided that the remaining parameters characterising the waveguide structure are known.

At the end of this chapter, the main conclusions drawn during the development of the theory were illustrated and explained further using a number of numerical examples. In these examples, the time-dependence of the output of a sensor system was simulated and the performance of various sensing configurations was compared. Furthermore, the variation of the calibration curve of a sensor system with the thickness of the sensing layer was analysed in order to demonstrate the different advantages and disadvantages provided by the configurations employing the optimum angles $\theta_{\text{opt,I}}$ and $\theta_{\text{opt,II}}$.

2.6 Bibliography for Chapter 2

[1] De-Kui Qing. A theoretical evaluation of the absorption coefficient of the optical waveguide chemical or biological sensors by group index method. *Journal of Lightwave Technology*, 14(8):1907–1916, August 1996.

[2] R. Srivastava, C. Bao, and C. Gómez-Reino. Planar-surface-waveguide evanescent-wave chemical sensors. *Sensors and Actuators*, A 51:165–171, 1996.

[3] A. Messica, A. Greenstein, and A. Katzir. Theory of fibre-optic, evanescent-wave spectroscopy and sensors. *Applied Optics*, 35(13):2274–2284, 1996.

[4] V. Brioude and O. Parriaux. Normalised analysis for the design of evanescent-wave sensors and its use for tolerance evaluation. *Optical and Quantum Electronics*, 32(6–8):899–908, August 2000.

[5] G. Pandraud, T. M. Koster, C. Gui, M. Dijkstra, A. van den Berg, and P. V. Lambeck. Evanescent wave sensing: new features for detection in small volumes. *Sensors and Actuators*, A 85:158–162, 2000.

[6] P. A. Wallace, N. Elliott, M. Uttamlal, A. S. Holmes-Smith, and M. Campbell. Development of a quasi-distributed optical fibre pH sensor using a covalently bound indicator. *Meas. Sci. Technol.*, 12:882–886, 2001.

[7] C. R. Lavers, K. Itoh, S. C. Wu, M. Murabayashi, I. Mauchline, G. Stewart, and T. Stout. Planar optical waveguides for sensing applications. *Sensors and Actuators*, B 69:85–95, 2000.

[8] M. Born and E. Wolf. *Principles of Optics.* Pergamon, Oxford, 1959.

[9] S. Visnovsky. Magneto-optical ellipsometry. *Czech J. Phys. B*, 36(625), 1986.

[10] P. Yeh. Optics of anisotropic layered media: a new 4×4 matrix algebra. *Surf. Sci*, 96(41), 1980.

[11] P. Yeh. *Optical Waves in Layered Media.* Wiley, New York, 1988.

[12] K. Ohta and H. Ishida. Matrix formalism for calculation of electric intensity of light in stratified multilayered films. *Applied Optics*, 29(13):1952–1959, 1990.

[13] B. D. Gupta and D. K. Sharma. Evanescent wave absorption based fiber optic pH sensor prepared by dye doped sol-gel immobilization technique. *Optics Communications*, 140:32–35, 1997.

[14] K. Ock, N. Jo, J. Kim, S. Kim, and K. Koh. Thin film optical waveguide type UV sensor using a photochromic molecular device, spirooxazine. *Synthetic Metals*, 117:131–133, 2001.

[15] C. Malins, M. Landl, P. Šimon, , and Brian D. MacCraith. Fibre optic ammonia sensing employing novel near infrared dyes. *Sensors and Actuators*, B 51:359–367, 1998.

[16] K. Li and J. Meichsner. In situ infrared fibre evanescent wave spectroscopy as a diagnostic tool for plasma polymerization in a gas discharge. *J. Phys. D: Appl. Phys.*, 34:1318–1325, 2001.

[17] G. Stewart, J. Norris, D. F. Clark, and B. Culshaw. Evanescent-wave chemical sensors—a theoretical evaluation. *Int. J. Optoelectron.*, 6:227–238, 1991.

[18] G. Stewart and B. Culshaw. Optical waveguide modeling and design for evanescent field chemical sensor. *Opt. Quantum. Electron.*, 26:S249–S259, 1994.

[19] J. Spinke, N. Oranth, Ch. Fattinger, H. Koller, C. Mangold, and D. Voegelin. The bidiffractive grating coupler: application to immunosensing. *Sensors and Actuators*, B 38–39:256–260, 1997.

[20] M. Wiki, H. Gao, M. Juvet, and R. E. Kunz. Compact integrated optical sensor system. *Biosensors and Bioelectronics*, 16:37–45, 2001.

[21] R. G. C. Oudshoorn, R. P. H. Kooyman, and J. Greve. Refractive index and layer thickness of an adsorbing protein as reporters of monolayer formation. *Thin Solid Films*, 284–285:836–840, 1996.

[22] D. Clerc and W. Lukosz. Direct immunosensing with an integrated-optical output grating coupler. *Sensors and Actuators*, B 40:53–58, 1997.

[23] D. Clerc and W. Lukosz. Real-time analysis of avidin adsorption with an integrated-optical output grating coupler: adsorption kinetics and optical anisotropy of adsorped monomolecular layers. *Biosensors and Bioelectronics*, 12(3):185–194, 1997.

[24] M. Wiki and R. E. Kunz. Wavelength-interrogated optical sensor for biochemical applications. *Optics Letters*, 25(7):463–465, April 2000.

[25] R. E. Kunz. *Integrated optical circuits and components.* Marcel Dekker, Inc., New York, Basel, 1999. `http://www.dekker.com`.

[26] A. D'Amico and C. Di Natale. A contribution on some basic definitions of sensors. *IEEE Sensors Journal*, 1(3):183–190, 2001.

[27] L.D. Landau and E.M. Lifschitz. *Electrodynamics of Continuous Media.* Pergamon Press, Oxford, 1960.

[28] K. T. V. Grattan and D. T. Sun. Fibre optic sensor technology: an overview. *Sensors and Actuators*, 82:40–61, 2000.

[29] Y. Kostov and G. Rao. Low-cost optical instrumentation for biomedical measurements. *Review of Scientific Instruments*, 71(12):4361–4374, 2000.

[30] B. D. MacCraith, C. M. McDonagh, G. O'Keffe, A. K. McEvoy, T. Butler, and F. R. Sheridan. Sol-gel coatings for optical chemical sensors and biosensors. *Sensors and Actuators*, B 29:51–57, 1995.

Chapter 3

Luminescence-based optical chemical sensors—theory and simulation

This chapter provides detailed analysis of two important issues that play a fundamental role in the area of optical chemical sensors and biosensors based on luminescence. The first issue is related to the luminescence capture efficiency, the second one to the problem of surface-generated luminescence.

It was mentioned in Chapter 1 that most luminescence-based sensor systems employ rather inefficient techniques for the collection of luminescence emitted by a thin sensing film or molecules attached to a surface. Recently, a number of authors have reported new ways of dealing with the issue of low luminescence intensity emitted by systems under study. Liebermann et al. [1] exploited the enhancement of the amplitude of the excitation light in the close vicinity of a metal surface provided by the efficient excitation of the surface plasmon wave. Blair & Chen [2] showed that luminescence of molecules can be enhanced by the use of planar cylindrical resonant optical cavities. Recently, very promising results related to the enhancement of the luminescence quantum yield have been reported by Mayer et al. [3] and Lakowicz et al. [4]. They showed that the use of metal nanoparticles can have a very positive influence on the intensity of luminescence emitted by molecules located in their close vicinity. Enhancement of the quantum yield in the order of 100-1000 was reported. Although these new developments are certainly valuable for the improvement of the performance of the luminescence-based chemical sensors and bio-sensors, they do not address the issue of efficiency of the luminescence collection.

Recently, a configuration enabling improved collection of light emitted from a single molecule was published by Enderlein et al. [5]. They exploited the fact that the radiation of a molecule located in the vicinity of a glass surface is highly anisotropic [6, 7, 8] and that a relatively large amount of light emitted by such a molecule is radiated *into* the glass substrate. They used a paraboloid glass segment to redirect the light radiated into the substrate towards the detector placed below the substrate. Zeller et al. [9] exploited the fact that the radiation of molecules located near a periodically corrugated surface, such as gratings, is highly directional. The efficiency of the luminescence capture was improved by positioning

the detector in the direction of this enhanced luminescence emission.

In this chapter, the idea of anisotropic radiation of molecules located near an interface is expanded to cover systems employing thin luminescent films or multilayer structures, which are of practical use in the area of optical chemical sensors. This is achieved by developing a rigorous electromagnetic theory of radiation of molecules embedded in an arbitrary multilayer system. Using this theory, the spatial properties of the light emitted by molecules incorporated in various multilayer structures are demonstrated by a number of numerical examples. Using this analysis, a number of configurations is proposed which provide enhanced efficiency of luminescence capture. Detailed numerical analysis is presented for one particular structure which offers the most promising enhancement factor.

The detection of luminescence from molecules attached to a planar surface is of primary importance in biotechnology, medical and pharmaceutical applications. In particular, this approach is used to monitor surface-specific binding of analyte molecules in order to check their presence in a solution under study. Typically, this is achieved by the *evanescent-wave excitation*, where the evanescent field of a guided mode, which is confined to a small region above the waveguide surface, is used to excite fluorescently-labelled surface attached molecules. This method is not particularly efficient, as only a small fraction of energy of the source of the excitation light is used for the actual excitation. This is predominantly due to the following reasons: (i) inefficient coupling of the light generated by the source into the guided mode(s), (ii) the fraction of the optical power contained in the evanescent field is very small in comparison to the power contained in the guiding layer.

In this chapter, a theoretical background is developed describing a novel method for the detection of surface-generated luminescence which employs the excitation of the luminescent molecules by *direct illumination*, i.e., using the full power of the source of the excitation light. Along with the theoretical background, two possible experimental implementations of the method are proposed.

3.1 Theory of radiation of dipoles embedded in a multilayer structure

In this section, a theory is developed that can describe the spatial distribution of the luminescence radiated by molecules embedded inside an arbitrary multilayer structure. The initial stages of the theory, in particular those prior to equation (3.17), are based on the theoretical analysis available in the literature [5, 10, 11]. The derivations appearing after equation (3.17) are original to this work. The theory is based on the radiation of a single point dipole and can be applied to systems consisting of arbitrarily distributed luminescent molecules across multilayer systems comprised of arbitrary linear, isotropic media. The implications of the theory will be extensively used in the following sections which deal with the issues of the luminescence capture efficiency and detection of the surface-generated luminescence.

3.1.1 Notation and assumptions

In the following derivations, a *point electric dipole* is used to model the radiation of a luminescent molecule. The dipole is embedded inside a multilayer system and oscillates at a discrete

angular frequency corresponding to the wavelength λ, as shown in Fig. 3.1(a). The calculation can easily be extended to the case where radiation is characterised by some broad-band spectrum simply by integrating the final results over the emission spectrum.

The multilayer system containing the radiating dipole is the same as that considered in Sec. 2.2.1. It consists of M layers separated by planar interfaces parallel to the x–y plane. The positions of the interfaces are characterised by the co-ordinates z_j, as shown in Fig. 3.1(b).

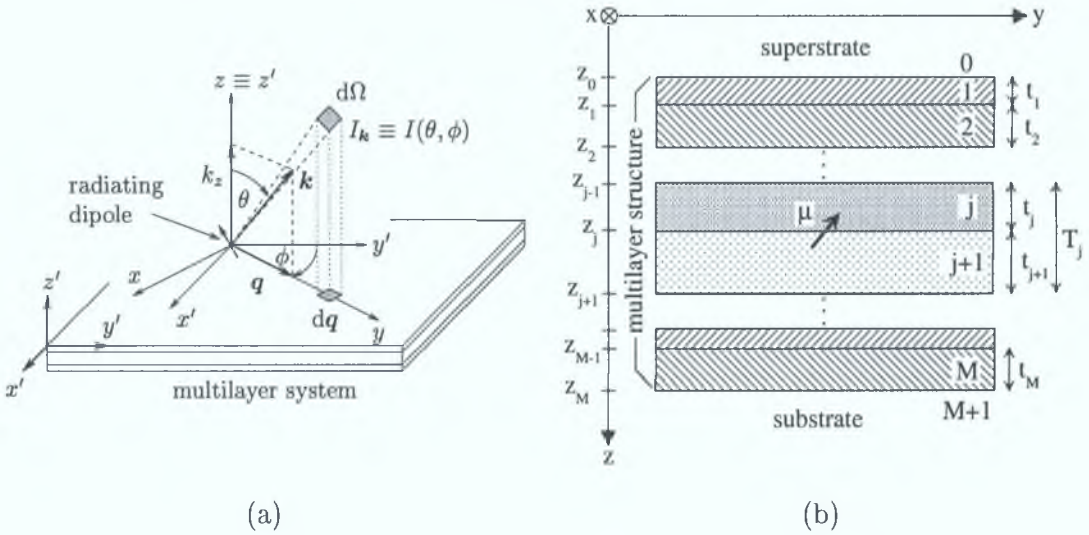

(a) (b)

Figure 3.1: (a) A schematic diagram of the 3D representation of the emitted luminescence originating from a dipole embedded inside a multilayer system. (b) A diagram of the multilayer system considered in the derivations. The radiating dipole positioned at the j^{th} interface is depicted by a thick arrow.

The optical properties of the layers are characterised by refractive indices n_j, where $j = 1, \ldots, M$. The multilayer system is surrounded by the superstrate ($z < 0$) and substrate ($z > 0$) of refractive index n_0 and n_{M+1}, respectively. In general, the values of the refractive indices can be complex, i.e., $n_j = \Re\{n_j\} + i\Im\{n_j\}$ with $\Im\{n_j\} \geq 0$, which allows for inclusion of lossy or metal layers in the multilayer system. However, the refractive indices of the surrounding media are considered to be real, which corresponds to the majority of practical situations.

The dipole, which oscillates at an angular frequency $\omega = 2\pi c_0/\lambda$, c_0 being the speed of light in vacuum, is located *at* the interface between the j^{th} and $(j+1)^{\text{th}}$ layers. By appropriate choice of the values of thickness and refractive index, all possible configurations of the dipole placement can be treated.

The field across the multilayer system is described in the same way as in Sec. 2.2.1. In particular, the field in the j^{th} layer can be decomposed into a sum of plane waves in the form

$$\boldsymbol{E}_j(\boldsymbol{r}) = \frac{1}{k_0^3} \int \mathrm{d}^3\boldsymbol{k}_j \, \boldsymbol{\mathcal{E}}_j(\boldsymbol{k}_j) \exp\left[i\,\boldsymbol{k}_j \cdot \boldsymbol{r}\right]. \tag{3.1}$$

The factor $1/k_0^3$, where $k_0 = 2\pi/\lambda$, ensures that the units of the plane wave vector amplitudes $\boldsymbol{\mathcal{E}}_j(\boldsymbol{k}_j)$ are the same as the units of the total field.

It is convenient to decompose vectors $\boldsymbol{k}_j$ and $\boldsymbol{r}$ into components lying in the x–y plane (which is parallel to the interfaces of the layers in the multilayer system) and those perpen-

dicular to that plane, i.e., $\boldsymbol{k}_j = [\boldsymbol{q}_j, k_{z,j}]$, $\boldsymbol{r} = [\boldsymbol{\rho}, z]$, as shown in Fig. 3.1(a). This leads to the expression

$$\boldsymbol{E}_j(\boldsymbol{\rho}, z) = \frac{1}{k_0^2} \int \mathrm{d}^2\boldsymbol{q}_j \, \boldsymbol{\mathcal{E}}_j(\boldsymbol{q}_j) \exp\left[i\, \boldsymbol{q}_j \cdot \boldsymbol{\rho}\right], \tag{3.2}$$

where

$$\boldsymbol{\mathcal{E}}_j(\boldsymbol{q}_j) = \frac{1}{k_0} \int \mathrm{d}k_{z,j} \, \boldsymbol{\mathcal{E}}_j([\boldsymbol{q}_j, k_{z,j}]) \exp\left[ik_{z,j} z\right]. \tag{3.3}$$

The vector $\boldsymbol{\mathcal{E}}_j(\boldsymbol{q}_j)$ can be interpreted as the complex amplitude of the field radiated in the direction which when projected onto the x–y plane is equal to $\boldsymbol{q}_j$.

Upon rotation of the laboratory co-ordinate system $[x', y', z']$ by angle ϕ around z'-axis, the expression for $\boldsymbol{q}_j$ in the new co-ordinate system $[x, y, z]$ becomes

$$\boldsymbol{q}_j = [0, q_j]. \tag{3.4}$$

As reversion to the laboratory system is straightforward and working in the co-ordinate system $[x, y, z]$ does not introduce any loss of generality, the following derivations will be restricted to this co-ordinate system. This is also convenient from the point of view of the matrix formalism which will be used to describe the response of the multilayer system. In these co-ordinates, the situation under consideration looks as depicted in Fig. 3.1(b).

The principal aim of this section is to derive expressions for the *angular distribution* of the intensity radiated by a single dipole, as well as a layer of dipoles, into the *surrounding* media. In particular, this study seeks to establish expressions for the functions $I_0(\theta_0, \phi_0)$ and $I_{M+1}(\theta_{M+1}, \phi_{M+1})$. They represent the angular distributions of the intensity radiated in the media characterised by refractive index n_0 and n_{M+1}, respectively.

As will be seen in the following sections, it is more convenient to express the electromagnetic field and thus the radiated intensity as a function of the wave-vector $\boldsymbol{k}$, i.e., in the form of the plane-wave decomposition given by Eq. (3.1). However, the components of the wave-vector, when expressed in the original co-ordinate system $[x', y', z']$, are related to the angles θ and ϕ by

$$\begin{aligned} \boldsymbol{k}_0 &= |\boldsymbol{k}_0| \left[\sin\theta_0 \sin\phi_0, \sin\theta_0 \cos\phi_0, \cos\theta_0\right], \\ \boldsymbol{k}_{M+1} &= |\boldsymbol{k}_{M+1}| \left[\sin\theta_{M+1} \sin\phi_{M+1}, \sin\theta_{M+1} \cos\phi_{M+1}, \cos\theta_{M+1}\right], \end{aligned} \tag{3.5}$$

as follows from Fig. 3.1(a). Therefore, it is sufficient to find the functions $\boldsymbol{\mathcal{E}}_0(\boldsymbol{k}_0)$ and $\boldsymbol{\mathcal{E}}_{M+1}(\boldsymbol{k}_{M+1})$ in order to determine the angular distributions $I_0(\theta_0, \phi_0)$ and $I_{M+1}(\theta_{M+1}, \phi_{M+1})$ of the radiated intensity, respectively.

3.1.2 Radiation of a point dipole embedded inside a multilayer system

The formalism for the description of the field across the multilayer system was developed in Secs. 2.2.1 and 2.2.2. All equations derived therein are also valid in this analysis, with the sole exception of Eq. (2.19). The problem with (2.19) is that it represents the boundary conditions for the electromagnetic field at the j^{th} interface, which is assumed to be free of surface charges and currents. However, due to the presence of the radiating dipole at this interface, this assumption is not valid in this case. Therefore, an equivalent to (2.19) has to be found.

Free oscillating dipole

Firstly, a point dipole $\boldsymbol{\mu}$ oscillating at an angular frequency ω and positioned at $\boldsymbol{r}_0 = \mathbf{0}$ in an unbounded medium is considered. The dipole acts as a current source that can be formally expressed as

$$\boldsymbol{j}(\boldsymbol{r}, t) = -i\omega\boldsymbol{\mu} \exp[-i\omega t]\, \delta(\boldsymbol{r} - \boldsymbol{r}_0). \tag{3.6}$$

To determine the space-time dependence of the field produced by the dipole, Maxwell's equations have to be solved using the current source (3.6). In the following derivations, the electric field produced by the dipole is denoted by $\boldsymbol{E}_j^{\mu}(\boldsymbol{r}, t)$. The subscript j refers to the fact that the medium surrounding the oscillating dipole is characterised by refractive index n_j.

The time-evolution of the field is assumed to have the same harmonic form as the dipole radiation, i.e., $\boldsymbol{E}_j^{\mu}(\boldsymbol{r}, t) = \boldsymbol{E}_j^{\mu}(\boldsymbol{r}) \exp[-i\omega t]$. To derive the space-variation of the field, a more elaborate procedure has to be applied. Firstly, the spatial component of the radiated field is expressed by the Fourier expansion

$$\boldsymbol{E}_j^{\mu}(\boldsymbol{r}) = \frac{1}{k_0^3} \int \mathrm{d}^3\boldsymbol{k}\, \boldsymbol{\mathcal{E}}_j^{\mu}(\boldsymbol{k}) \exp[i\,\boldsymbol{k}\cdot\boldsymbol{r}]\,. \tag{3.7}$$

As derived in Ref. [10], the expression for the vector amplitudes $\boldsymbol{\mathcal{E}}_j^{\mu}(\boldsymbol{k})$ can be written as

$$\boldsymbol{\mathcal{E}}_j^{\mu}(\boldsymbol{k}) = \frac{-1}{(2\pi)^3 \epsilon_0 n_j^2} \left(\boldsymbol{\mu} + \frac{\boldsymbol{k} \times (\boldsymbol{k} \times \boldsymbol{\mu})}{k^2 - k_j^2} \right), \tag{3.8}$$

where $k = |\boldsymbol{k}|$, $k_j = n_j k_0$ and ϵ_0 is the vacuum permittivity. When the vector $\boldsymbol{k}$ is decomposed into the x–y and z components as $\boldsymbol{k} = [\boldsymbol{q}, k_z]$, the expression (3.7) can be rewritten as

$$\boldsymbol{E}_j^{\mu}([\boldsymbol{\rho}, z]) = \frac{-1}{(2\pi)^3 \epsilon_0 n_j^2} \frac{1}{k_0^3} \int \mathrm{d}^2\boldsymbol{q} \exp[i\,\boldsymbol{q}\cdot\boldsymbol{\rho}] \int \mathrm{d}k_z \left\{ \boldsymbol{\mu} + \frac{\boldsymbol{k} \times (\boldsymbol{k} \times \boldsymbol{\mu})}{k_z^2 - k_{z,j}^2} \right\} \exp[ik_z z]\,, \tag{3.9}$$

where $k_{z,j}$ is given by

$$k_{z,j} = \sqrt{k_j^2 - q^2}, \quad \Im\{k_{z,j}\} \geq 0. \tag{3.10}$$

The integration over k_z can be performed using the contour integration in the k_z plane. Considering only the terms contributing to the power dissipation, the field produced by the dipole is expressed as

$$\boldsymbol{E}_j^{\mu}([\boldsymbol{\rho}, z]) = \frac{-i}{8\pi^2 \epsilon_0 n_j^2} \frac{1}{k_0^3} \int \mathrm{d}^2\boldsymbol{q} \exp[i\,\boldsymbol{q}\cdot\boldsymbol{\rho}] \exp[\pm ik_{z,j} z]\, \frac{\boldsymbol{k}_j^{\pm} \times (\boldsymbol{k}_j^{\pm} \times \boldsymbol{\mu})}{k_{z,j}}. \tag{3.11}$$

In this expression, the signs "+" and "−" correspond to the semi-spaces $z > 0$ and $z < 0$, respectively. Furthermore, the vectors $\boldsymbol{k}_j^{\pm}$ are given by

$$\boldsymbol{k}_j^{\pm} = [\boldsymbol{q}, \pm k_{z,j}]. \tag{3.12}$$

Using vector algebra, the vector product term in (3.11) can be written in a form which is more convenient for relating the field expression to the formalism used in Secs. 2.2.1 and 2.2.2. Due to the fact that the vectors $\hat{\boldsymbol{e}}_{j,s\pm}$, $\hat{\boldsymbol{e}}_{j,p\pm}$ and $\boldsymbol{k}_j^{\pm}$ form a complete base of a three-dimensional space, the vector $\boldsymbol{\mu}$ can be decomposed as

$$\boldsymbol{\mu} = (\boldsymbol{\mu}\cdot\hat{\boldsymbol{e}}_{j,s\pm})\, \hat{\boldsymbol{e}}_{j,s\pm} + (\boldsymbol{\mu}\cdot\hat{\boldsymbol{e}}_{j,p\pm})\, \hat{\boldsymbol{e}}_{j,p\pm} + (\boldsymbol{\mu}\cdot\boldsymbol{k}_j^{\pm})\, \boldsymbol{k}_j^{\pm}. \tag{3.13}$$

In this equation, the vectors $\hat{\boldsymbol{e}}_{j,s\pm}$ and $\hat{\boldsymbol{e}}_{j,p\pm}$, which characterise the s and p polarised light, can be calculated from (2.15) upon substitution $N_{y,j} = q$. Consequently, the expression (3.11) for the electric field produced by a free point dipole can be written in the form

$$\begin{aligned}
\boldsymbol{E}_j^{\mu}([\boldsymbol{\rho}, z]) &= \frac{i}{8\pi^2 k_0 \epsilon_0} \int \mathrm{d}^2\boldsymbol{q}\, \frac{1}{k_{z,j}} \left\{ (\boldsymbol{\mu} \cdot \hat{\boldsymbol{e}}_{j,s+})\, \hat{\boldsymbol{e}}_{j,s+} + (\boldsymbol{\mu} \cdot \hat{\boldsymbol{e}}_{j,p+})\, \hat{\boldsymbol{e}}_{j,p+} \right\} \exp\left[i\,\boldsymbol{q} \cdot \boldsymbol{\rho} + i k_{z,j} z\right], \quad z > 0, \\
\boldsymbol{E}_j^{\mu}([\boldsymbol{\rho}, z]) &= \frac{i}{8\pi^2 k_0 \epsilon_0} \int \mathrm{d}^2\boldsymbol{q}\, \frac{1}{k_{z,j}} \left\{ (\boldsymbol{\mu} \cdot \hat{\boldsymbol{e}}_{j,s-})\, \hat{\boldsymbol{e}}_{j,s-} + (\boldsymbol{\mu} \cdot \hat{\boldsymbol{e}}_{j,p-})\, \hat{\boldsymbol{e}}_{j,p-} \right\} \exp\left[i\,\boldsymbol{q} \cdot \boldsymbol{\rho} - i k_{z,j} z\right], \quad z < 0.
\end{aligned} \tag{3.14}$$

Equation (3.14) implies that the field radiated by the free dipole can be expressed as a superposition of the s and p polarised plane waves characterised by the vector amplitudes

$$\begin{aligned}
\boldsymbol{\mathcal{E}}_{j,s\pm}^{\mu}(\boldsymbol{q}) &\equiv \mathcal{E}_{j,s\pm}^{\mu}(\boldsymbol{q})\, \hat{\boldsymbol{e}}_{j,s\pm}, \\
\boldsymbol{\mathcal{E}}_{j,p\pm}^{\mu}(\boldsymbol{q}) &\equiv \mathcal{E}_{j,p\pm}^{\mu}(\boldsymbol{q})\, \hat{\boldsymbol{e}}_{j,p\pm},
\end{aligned} \tag{3.15}$$

where the magnitudes $\mathcal{E}_{j,s\pm}^{\mu}$ and $\mathcal{E}_{j,p\pm}^{\mu}$ are given by

$$\begin{aligned}
\mathcal{E}_{j,s\pm}^{\mu}(\boldsymbol{q}) &= \frac{i}{8\pi^2 \epsilon_0} \frac{k_0}{k_{z,j}} (\boldsymbol{\mu} \cdot \hat{\boldsymbol{e}}_{j,s\pm}), \\
\mathcal{E}_{j,p\pm}^{\mu}(\boldsymbol{q}) &= \frac{i}{8\pi^2 \epsilon_0} \frac{k_0}{k_{z,j}} (\boldsymbol{\mu} \cdot \hat{\boldsymbol{e}}_{j,p\pm}).
\end{aligned} \tag{3.16}$$

Oscillating dipole inside a multilayer system—field magnitudes

After the expressions for the electric field produced by a free oscillating point dipole have been derived, the analysis can proceed with the derivation of the field radiated by a dipole embedded inside the multilayer system.

It is assumed that the point dipole is the *only source* of the electromagnetic field present in the multilayer system and that there are no other external sources of the field. This means that the vectors $\boldsymbol{A}_0$ and $\boldsymbol{A}_{M+1}$ defined in (2.20) must take the form

$$\begin{aligned}
\boldsymbol{A}_0 &= [0, \mathcal{E}_{0,s-}, 0, \mathcal{E}_{0,p-}]^{\mathrm{T}}, \\
\boldsymbol{A}_{M+1} &= [\mathcal{E}_{M+1,s+}, 0, \mathcal{E}_{M+1,p+}, 0]^{\mathrm{T}}.
\end{aligned} \tag{3.17}$$

It is also assumed that the field generated by the dipole *does not influence* the dipole radiation. Although the results of Chance et al. [11] indicate clearly that the presence of a metal interface near the radiating dipole modifies the damping rate (inverse of the luminescence life-time) and the frequency at which the dipole oscillates, the modification of these *time*-domain characteristics of the dipole radiation is not of interest here. What is of interest is the influence of the surrounding multilayer system on the *angular distribution* of the dipole radiation, i.e., on the *space*-domain characteristics. Therefore it is considered that the influence of the surrounding multilayer system on the time-domain characteristics is already contained in expression (3.6) describing the dipole radiation in that ω represents the dipole oscillation frequency perturbed by the surrounding media. This will be particularly important in Sec. 3.1.3 where the layer of mutually incoherent oscillating dipoles is considered.

If the dipole was not inserted into the multilayer system, the vectors $\boldsymbol{A}_0$ and $\boldsymbol{A}_{M+1}$ would be related by

$$\begin{aligned} \boldsymbol{A}_0 &= L_j \boldsymbol{A}_j, \\ \boldsymbol{A}_{j+1} &= L_{j+1}^{-1} L_{M+1} \boldsymbol{A}_{M+1}, \end{aligned} \tag{3.18}$$

which can be derived by recursively applying equation (2.19). However, when the dipole is considered to be located at the j^{th} interface, this relation has to be modified so as to take into account the discontinuity of the field's tangential components across the j^{th} interface. The modification has the form

$$\begin{aligned} \boldsymbol{A}_0 &= L_j \left(\boldsymbol{A}_j + \mathrm{P}_j^{-1} \cdot \left[0, \mathcal{E}_{j,s-}^{\mu}, 0, \mathcal{E}_{j,p-}^{\mu} \right]^{\mathrm{T}} \right), \\ \left(\boldsymbol{A}_{j+1} + \left[\mathcal{E}_{j+1,s+}^{\mu}, 0, \mathcal{E}_{j+1,p+}, 0 \right]^{\mathrm{T}} \right) &= L_{j+1}^{-1} L_{M+1} \cdot \boldsymbol{A}_{M+1}. \end{aligned} \tag{3.19}$$

This is a crucial step in this analysis.

Now, it is assumed that the refractive indices of layers j and $j+1$ are equal. Although this does not introduce any loss of generality to the description of the dipole + multilayer system (all possible configurations of positions of the dipole inside the multilayer structure can be achieved by the appropriate choice of the values of refractive index and layer thickness), it allows for writing the equations (3.19) in a more explicit form. After some rearrangements, equation (3.19) can be rewritten as

$$\boldsymbol{A}_0 = L_{M+1} \boldsymbol{A}_{M+1} + L_j P_j^{-1} \boldsymbol{A}_j^{\mu}, \tag{3.20}$$

where the vector $\boldsymbol{A}_j^{\mu}$ is defined as

$$\boldsymbol{A}_j^{\mu} \equiv \left[-\mathcal{E}_{j,s+}^{\mu}, \mathcal{E}_{j,s-}^{\mu}, -\mathcal{E}_{j,p+}^{\mu}, \mathcal{E}_{j,p-}^{\mu} \right]^{\mathrm{T}}. \tag{3.21}$$

Equation (3.20) is an analogue of Eq. (2.25) for the multilayer system containing a single point dipole located at the j^{th} interface.

Equation (3.20) shows that the contribution of the dipole to the external field (represented by the vectors $\boldsymbol{A}_0$ and $\boldsymbol{A}_{M+1}$) consists of a product of three quantities that can be easily interpreted. Firstly, the *radiation characteristics* of the dipole are given by the vector $\boldsymbol{A}_j^{\mu}$. Secondly, the *position* of the dipole at a distance t_j from the $(j-1)^{\text{th}}$ interface is represented by the matrix P_j^{-1}. Finally, the matrix L_j describes the *response* of that region of the *multilayer system* which is above the layer containing the dipole, i.e., at $z \leq z_{j-1}$. This factorised form is very advantageous, as it allows for significant simplification of the formulæ describing the radiation of multiple dipoles embedded inside the multilayer system, as will be shown in the next section.

In order to find explicit expressions for the magnitudes of the plane waves radiated into the surrounding media, equation (3.20) must be solved. After some simple algebraic manipulations, one arrives at

$$\begin{aligned} \mathcal{E}_{M+1,s+}(\boldsymbol{q}) &= U_{j,s+} \exp\left[-ik_{z,j}t_j\right] \mathcal{E}_{j,s+}^{\mu}(\boldsymbol{q}) + U_{j,s-} \exp\left[+ik_{z,j}t_j\right] \mathcal{E}_{j,s-}^{\mu}(\boldsymbol{q}), \\ \mathcal{E}_{M+1,p+}(\boldsymbol{q}) &= U_{j,p+} \exp\left[-ik_{z,j}t_j\right] \mathcal{E}_{j,p+}^{\mu}(\boldsymbol{q}) + U_{j,p-} \exp\left[+ik_{z,j}t_j\right] \mathcal{E}_{j,p-}^{\mu}(\boldsymbol{q}) \end{aligned} \tag{3.22}$$

for the magnitudes of the plane waves propagating in the substrate, and

$$\begin{aligned}\mathcal{E}_{0,s-}(\boldsymbol{q}) &= V_{j,s+}\exp\left[-ik_{z,j}t_j\right]\mathcal{E}^{\mu}_{j,s+}(\boldsymbol{q}) + V_{j,s-}\exp\left[+ik_{z,j}t_j\right]\mathcal{E}^{\mu}_{j,s-}(\boldsymbol{q}),\\ \mathcal{E}_{0,p+}(\boldsymbol{q}) &= V_{j,p+}\exp\left[-ik_{z,j}t_j\right]\mathcal{E}^{\mu}_{j,p+}(\boldsymbol{q}) + V_{j,p-}\exp\left[+ik_{z,j}t_j\right]\mathcal{E}^{\mu}_{j,p-}(\boldsymbol{q})\end{aligned} \tag{3.23}$$

for the magnitudes of the plane waves propagating in the superstrate. The coefficients $U_{j,s\pm}$, $U_{j,p\pm}$, $V_{j,s\pm}$, and $V_{j,p\pm}$ are calculated as follows:

$$\begin{aligned}U_{j,s+} &= L_{11,j}/L_{11,M+1}, \quad U_{j,s-} = -L_{12,j}/L_{11,M+1},\\ U_{j,p+} &= L_{33,j}/L_{33,M+1}, \quad U_{j,p-} = -L_{34,j}/L_{33,M+1},\end{aligned} \tag{3.24}$$

and

$$\begin{aligned}V_{j,s+} &= L_{21,M+1}U_{j,s+} - L_{21,j}, \quad V_{j,s-} = L_{21,M+1}U_{j,s-} + L_{22,j},\\ V_{j,p+} &= L_{43,M+1}U_{j,p+} - L_{43,j}, \quad V_{j,p-} = L_{43,M+1}U_{j,p-} + L_{44,j}.\end{aligned} \tag{3.25}$$

In these expressions, $L_{kl,j}$ represents the $[k,l]$ element of the matrix L_j defined in (2.26).

Radiated intensity

The intensity (or irradiance) of a plane electromagnetic wave characterised by the wave vector $\boldsymbol{k}$ and the corresponding complex amplitude $\boldsymbol{\mathcal{E}}(\boldsymbol{k})$ is given by [12, 13]

$$I(\boldsymbol{k}) \equiv |\langle \boldsymbol{S}(\boldsymbol{k})\rangle|, \tag{3.26}$$

where the time-average of the Poynting vector $\langle \boldsymbol{S}(\boldsymbol{k})\rangle$ is given by

$$\langle \boldsymbol{S}(\boldsymbol{k})\rangle = \frac{1}{2}\Re\{\boldsymbol{E}(\boldsymbol{k})\times\boldsymbol{H}^{\star}(\boldsymbol{k})\} = \Re\left\{\frac{1}{2\eta}\frac{\boldsymbol{k}}{|\boldsymbol{k}|}\right\}|\,\boldsymbol{\mathcal{E}}(\boldsymbol{k})|^2. \tag{3.27}$$

In this equation, $\Re\{x\}$ denotes the real part of x, $x^{\star}$ denotes the complex conjugate of x, and η is the medium impedance evaluated as $\eta = \sqrt{\mu/\epsilon}$.

As can be seen from equations (3.22) and (3.23), the expressions for the plane wave magnitudes of the field propagating in the substrate and superstrate are parametrised by $\boldsymbol{q}$, i.e., by the projection of the $\boldsymbol{k}$-vector to the x–y plane. The corresponding expressions parametrised by $\boldsymbol{k}$ can be found easily. Due to the relation $\mathrm{d}^3\boldsymbol{k} = (k_j/k_{z,j})\mathrm{d}k_j\mathrm{d}^2\boldsymbol{q}$, which follows from geometry (see Fig. 3.1(a)), the vector field amplitudes are related by

$$\begin{aligned}\boldsymbol{\mathcal{E}}_{j,s\pm}(\boldsymbol{k}) &= \frac{k_{z,j}}{k_j}\boldsymbol{\mathcal{E}}_{j,s\pm}(\boldsymbol{q}),\\ \boldsymbol{\mathcal{E}}_{j,p\pm}(\boldsymbol{k}) &= \frac{k_{z,j}}{k_j}\boldsymbol{\mathcal{E}}_{j,p\pm}(\boldsymbol{q}).\end{aligned} \tag{3.28}$$

Using expressions (3.22–3.28) and the fact that the s and p polarised modes are orthogonal, the expression for the intensity radiated by the dipole into the substrate by means of a mode characterised by the wave-vector $\boldsymbol{k}$ can be written as

$$I_{(j)\to M+1,x}(\boldsymbol{k},\boldsymbol{\mu},t_j) = \frac{\Re\{n_{M+1}\}}{2\eta_0}\left|\frac{k_{z,M+1}}{k_{M+1}}\right|^2\left[I^{++}_{(j)\to M+1,x}(\boldsymbol{q}) + I^{--}_{(j)\to M+1,x}(\boldsymbol{q}) + I^{+-}_{(j)\to M+1,x}(\boldsymbol{q})\right], \tag{3.29}$$

where

$$
\begin{aligned}
I^{++}_{(j)\to M+1,x}(\boldsymbol{q}) &= \left|U_{j,x+}\right|^2 \left|\mathcal{E}^{\mu}_{j,x+}(\boldsymbol{q})\right|^2 \exp\left[+2\Im\{k_{z,j}t_j\}\right], \\
I^{--}_{(j)\to M+1,x}(\boldsymbol{q}) &= \left|U_{j,x-}\right|^2 \left|\mathcal{E}^{\mu}_{j,x-}(\boldsymbol{q})\right|^2 \exp\left[-2\Im\{k_{z,j}t_j\}\right], \\
I^{+-}_{(j)\to M+1,x}(\boldsymbol{q}) &= 2\Re\Big\{U_{j,x+}\left[U_{j,x-}\right]^{\star} \mathcal{E}^{\mu}_{j,x+}(\boldsymbol{q}) \left[\mathcal{E}^{\mu}_{j,x-}(\boldsymbol{q})\right]^{\star} \exp\left[-2i\Re\{k_{z,j}t_j\}\right]\Big\}.
\end{aligned}
\tag{3.30}
$$

In these equations, x represents the polarisation states of the radiated field, i.e., $x = s, p$. A similar expression can be obtained for the intensity radiated into the superstrate. It is given by equations (3.29) and (3.30), where $M+1$ and $U_{j,x\pm}$ are substituted by 0 and $V_{j,x\pm}$, respectively. The arguments $\boldsymbol{k}$, $\boldsymbol{\mu}$ and t_j in the expression (3.29) indicate that the radiated intensity is a function of the wave vector, the point dipole amplitude and its position. The subscript (j) refers to the fact that the expression represents the radiation of a single point dipole located at the j^{th} *interface*.

The *angular* distribution of the luminescence intensity radiated into the substrate can be obtained by considering the equation

$$
(1/k_0^2) \int\limits_{\substack{|\boldsymbol{k}|=k_{M+1} \\ k_z>0}} I_{(j)\to M+1,x}(\boldsymbol{k}, \boldsymbol{\mu}, t_j)\, \mathrm{d}^3\boldsymbol{k} = \int I_{(j)\to M+1,x}(\theta, \phi, \boldsymbol{\mu}, t_j)\, \mathrm{d}\Omega_{M+1}, \tag{3.31}
$$

which represents two equivalent ways of evaluating the *total* energy radiated into the superstrate by means of the modes characterised by a constant value of $|\boldsymbol{k}|$ and equal to $|\boldsymbol{k}| = k_{M+1} \equiv (2\pi/\lambda)\, n_{M+1}$. In this equation, $\mathrm{d}\Omega = \sin\theta\, \mathrm{d}\phi\, \mathrm{d}\theta$ is the element of the solid angle in the direction $\boldsymbol{k} = |\boldsymbol{k}|\,[\sin\theta\sin\phi, \sin\theta\cos\phi, \cos\theta]$, as shown in Fig. 3.1(a). Equation (3.31) implies the relation

$$
I_{(j)\to M+1,x}(\theta, \phi, \boldsymbol{\mu}, t_j) = n^2_{M+1}\, I_{(j)\to M+1,x}(\boldsymbol{k}, \boldsymbol{\mu}, t_j), \tag{3.32}
$$

which has to be considered when transforming the results from the $\boldsymbol{k}$-space to the (θ, ϕ)-space and vice versa. When $M+1$ is substituted by 0 in (3.32), the angular distribution of the luminescence intensity radiated into the superstrate is obtained.

3.1.3 Luminescence emitted by a layer of oscillating dipoles

In sensor applications employing luminescent coatings, one typically has a thin dielectric layer doped with radiating dipoles. Therefore, it is useful to find expressions for the radiated intensity produced by an *ensemble* of dipoles distributed across a layer which is embedded inside a multilayer system.

For simplicity, it is assumed that the oscillating dipoles are *evenly* distributed across a layer of total thickness T_j and refractive index n_j, and that the radiation of any of two radiating dipoles is mutually *incoherent*. Furthermore, it is assumed that the vector $\boldsymbol{\mu}$ in (3.6) has the same magnitude and orientation for all dipoles. The case of random dipole orientations will be considered later.

At this point, an advantage is taken of the factorised form of the expression for the dipole radiation, as discussed in Sec. 3.1.2. Due to the mutual incoherence of the dipoles' radiation,

the total intensity radiated by the layer of dipoles is given by the integral of intensities (3.29) over the positions of the dipoles. Due to the factorisation (3.30), the integration is easily carried out as it is only the exponential terms $\exp[\pm 2\Im\{k_{z,j}t_j\}]$ and $\exp[-2i\Re\{k_{z,j}t_j\}]$ that have to be integrated.

As mentioned previously, the j^{th} interface is not an interface in the actual meaning of the word, as it is separating layers of equal refractive indices, i.e., $n_j = n_{j+1}$. The thicknesses of these two layers t_j and t_{j+1} are assumed to fulfill the relation $t_j + t_{j+1} = T_j$ (see Fig. 3.1(b)). Consequently, the integration of (3.29) over $t_j \in \langle 0, T_j \rangle$ can easily be performed and the expression for the intensity radiated by the dipoles uniformly distributed across the layer of thickness T_j can be written as

$$I_{[j]\to M+1,x}(\boldsymbol{k},\boldsymbol{\mu}) = \frac{\Re\{n_{M+1}\}}{2\eta_0}\left|\frac{k_{z,M+1}}{k_{M+1}}\right|^2\left[I^{++}_{[j]\to M+1,x}(\boldsymbol{q}) + I^{--}_{[j]\to M+1,x}(\boldsymbol{q}) + I^{+-}_{[j]\to M+1,x}(\boldsymbol{q})\right], \tag{3.33}$$

where

$$\begin{aligned}
I^{++}_{[j]\to M+1,x}(\boldsymbol{q}) &= \left|U_{j,x+}\right|^2\left|\mathcal{E}^{\mu}_{j,x+}(\boldsymbol{q})\right|^2\exp\left[+\Im\{k_{z,j}T_j\}\right]T_j\,\mathrm{sinch}\left[\Im\{k_{z,j}T_j\}\right],\\
I^{--}_{[j]\to M+1,x}(\boldsymbol{q}) &= \left|U_{j,x-}\right|^2\left|\mathcal{E}^{\mu}_{j,x-}(\boldsymbol{q})\right|^2\exp\left[-2\Im\{k_{z,j}T_j\}\right]T_j\,\mathrm{sinch}\left[\Im\{k_{z,j}T_j\}\right],\\
I^{+-}_{[j]\to M+1,x}(\boldsymbol{q}) &= 2\Re\Big\{U_{j,x+}\left[U_{j,x-}\right]^{\star}\mathcal{E}^{\mu}_{j,x+}(\boldsymbol{q})\left[\mathcal{E}^{\mu}_{j,x-}(\boldsymbol{q})\right]^{\star}\exp\left[-i\Re\{k_{z,j}T_j\}\right]\Big\}T_j\,\mathrm{sinc}\left[\Re\{k_{z,j}T_j\}\right].
\end{aligned} \tag{3.34}$$

In these equations, $\mathrm{sinc}[x] = \sin[x]/x$ and $\mathrm{sinch}[x] = \sinh[x]/x$. The arguments $\boldsymbol{k}$ and $\boldsymbol{\mu}$ indicate that the radiated intensity depends on the wave vector and the vector amplitude of the point dipole. The subscript $[j]$ refers to the fact that the expression represents the radiation originating from the dipole *layer* characterised by the index j (refractive index n_j, thickness T_j). The angular distribution of the radiated intensity is obtained using Eq. (3.32), in which (j) is substituted by $[j]$. The expression for the intensity radiated into the superstrate can be obtained from (3.33) upon substitution of $M+1$ by 0.

3.1.4 Radiation of randomly oriented dipoles

Expressions (3.29) and (3.33) represent the angular distributions of the intensity radiated by a single dipole and a layer of dipoles embedded inside the multilayer system, respectively. In both cases, the strength and orientation of the dipoles were assumed to be constant and equal to $\boldsymbol{\mu}$. However, in the vast majority of sensor applications, there is no special attention being paid to the orientation of luminescent molecules during the technological process of the layer preparation. In other words, while the strength of the dipoles can be assumed to be constant for all radiating molecules, the dipole orientation can be considered as being random. Therefore, it is desirable to find an expression for the intensity radiated by randomly oriented dipoles.

To obtain such an expression, an integration of the intensities $I_{(j)\to M+1,x}$ and $I_{[j]\to M+1,x}$ over the random orientations of the vector $\boldsymbol{\mu}$ needs to be carried out. However, due to the symmetry of the problem, this rather exhaustive step can be bypassed and the result can be obtained by simply averaging Eqs. (3.29) and (3.33) over a complete set of arbitrary

orthogonal dipole orientations. One possibility is to consider the set

$$\begin{aligned} \boldsymbol{\mu}_{\hat{x}} &\equiv [\mu, 0, 0], \\ \boldsymbol{\mu}_{\hat{y}} &\equiv [0, \mu, 0], \\ \boldsymbol{\mu}_{\hat{z}} &\equiv [0, 0, \mu]. \end{aligned} \tag{3.35}$$

Consequently, the expressions for the intensities radiated by the randomly oriented dipoles can be written as

$$I_{(j)\to M+1,x}(\boldsymbol{k}) = \frac{1}{3} \sum_{\boldsymbol{\mu}=\boldsymbol{\mu}_{\hat{x}},\boldsymbol{\mu}_{\hat{y}},\boldsymbol{\mu}_{\hat{z}}} I_{(j)\to M+1,x}(\boldsymbol{k},\boldsymbol{\mu}) \tag{3.36}$$

and

$$I_{[j]\to M+1,x}(\boldsymbol{k}) = \frac{1}{3} \sum_{\boldsymbol{\mu}=\boldsymbol{\mu}_{\hat{x}},\boldsymbol{\mu}_{\hat{y}},\boldsymbol{\mu}_{\hat{z}}} I_{[j]\to M+1,x}(\boldsymbol{k},\boldsymbol{\mu}). \tag{3.37}$$

In this equation the superscript x refers to the polarisation state of the radiated field, i.e., $x = s, p$. Furthermore, the expressions for the intensity radiated into the superstrate can be obtained upon substitution of $M + 1$ by 0.

Due to the symmetry considerations, the dependence of the radiated intensity on angle ϕ vanishes after the integration (averaging) over the dipole orientations. Consequently, the expressions (3.36) and (3.37) describe the dependence of the radiated intensity on the azimuthal angle θ, i.e., the angle between the axis z and the direction of observation (see Fig. 3.1(a)).

3.2 Numerical examples

In this section, a number of numerical examples is provided to illustrate the results obtained in the previous section. The numerical values were obtained by a self-developed code written in Matlab. The parameters used in the calculations correspond to the materials that are extensively used in the laboratory where this research was conducted [14]. For the purpose of the calculation, they are considered to be independent on wavelength. A typical substrate supporting the luminescent media consists of glass ($n_s = 1.515$). As for the luminescent medium, micro-porous glass media doped with a ruthenium complex are commonly used [15, 16, 17, 18]. A typical value of the refractive index of these materials is $n_l = 1.43$. In typical applications, the sol-gel is coated on a glass slide and is covered by the environment, whose refractive index is denoted by n_e. The environment is typically either air ($n_e = n_a = 1.0$) or water ($n_e = n_w = 1.33$).

3.2.1 Radiation of a point dipole placed at a surface

Firstly, a point dipole placed *at* the surface of a glass substrate is considered [5]. The orientation of the dipole is considered to be random, i.e., equation (3.36) can used to calculate the angular distribution of the radiated intensity. The angular distribution plotted in a spherical co-ordinates is shown in Fig. 3.2. The graphs (a) and (b) correspond to the situation where the medium covering the glass substrate is air and water, respectively. The radiation propagating in the positive (down) and negative (up) z-directions correspond to that radiated into the glass substrate and the environment, respectively.

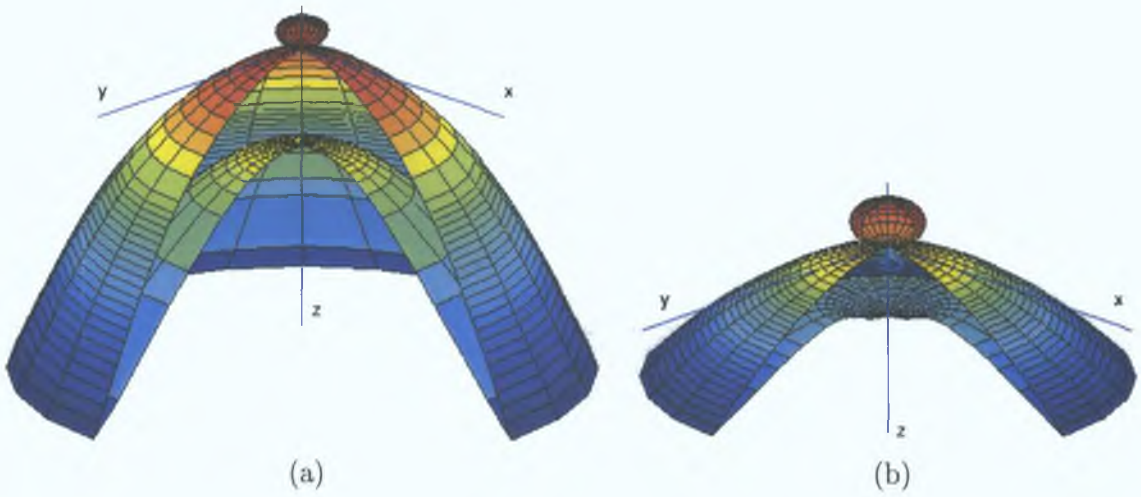

Figure 3.2: Angular distributions of intensity of luminescence radiated by a randomly oriented dipole located *at* the glass substrate. The environment covering the substrate is either air (a) or water (b). The three-dimensional graphs are plotted in a spherical system of co-ordinates.

It is well known that when a randomly oriented radiating dipole is located in a free unbound space, its radiation is isotropic [12, 13]. In the spherical representation used in Fig. 3.2, the angular distribution of the radiated intensity would look like a sphere. As can be seen, however, the angular distribution is significantly altered when the radiating dipole is placed at the interface. Firstly, it can be noted that the radiation is highly anisotropic. Secondly, a significant part of the luminescence is radiated into the glass substrate, which has a higher refractive index than the environment above it.

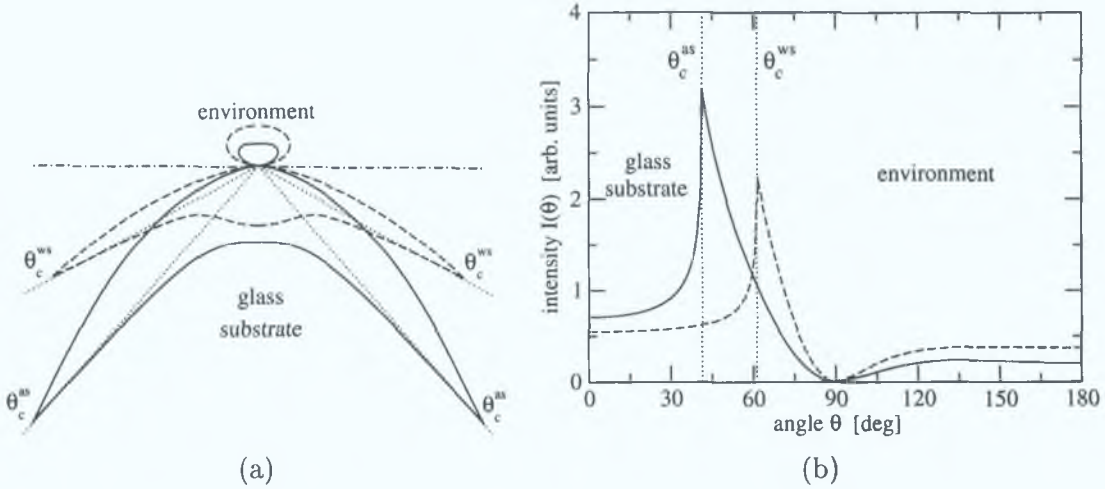

Figure 3.3: Angular distributions of intensity of luminescence radiated by a randomly oriented dipole located *at* the glass substrate. The solid and dashed lines correspond to the situations where the environment covering the substrate is air and water, respectively. The graphs (a) and (b) correspond to the polar and Cartesian representations of the intensity distribution, respectively. In graph (b), the intervals $\theta \in \langle 0°, 90° \rangle$ and $\theta \in \langle 90°, 180° \rangle$ correspond to the intensity radiated into the substrate and environment, respectively.

Due to the fact that the angular distribution is axially symmetric, it is possible to plot

an intersection of the distribution at a particular angle ϕ, such as $\phi = 0$. These distributions are shown in Fig. 3.3, where the graphs (a) and (b) are plotted in the polar and Cartesian co-ordinates, respectively.

As can be seen, the angular distribution exhibits a sharp peak whose position corresponds to the radiation into the substrate. Further investigation reveals that the angular position of this peak is equal to the critical angle corresponding to the environment/substrate interface, i.e., $\theta_c^{es} = \arcsin(n_e/n_s)$. For the particular values used in this calculation, the values of the critical angle are $\theta_c^{as} = 41.3°$ and $\theta_c^{ws} = 61.3°$ when the environment is air and water, respectively. Therefore it can be concluded that the dipole located at a surface preferably radiates into the higher refractive index substrate at angles close to the critical angle θ_c^{es}. The intensity radiated into the environment is relatively small, as can be seen from Fig. 3.3.

3.2.2 Radiation of a point dipole vs distance from a surface

This section considers a randomly oriented dipole placed in the environment at various distances from the glass substrate, as shown in Fig. 3.4. Figure 3.5 shows the angular distributions of intensity of the radiated luminescence for three distances t_s of the radiating dipole from the glass substrate (see the legends of the graphs). The graphs (a) and (b) correspond to the situations where the environment covering the glass substrate is air and water, respectively.

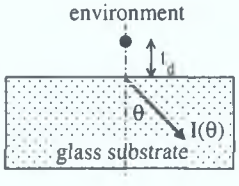

Figure 3.4: A schematic diagram of a point dipole (depicted by the black point) located in the environment at a distance t_d from the glass surface.

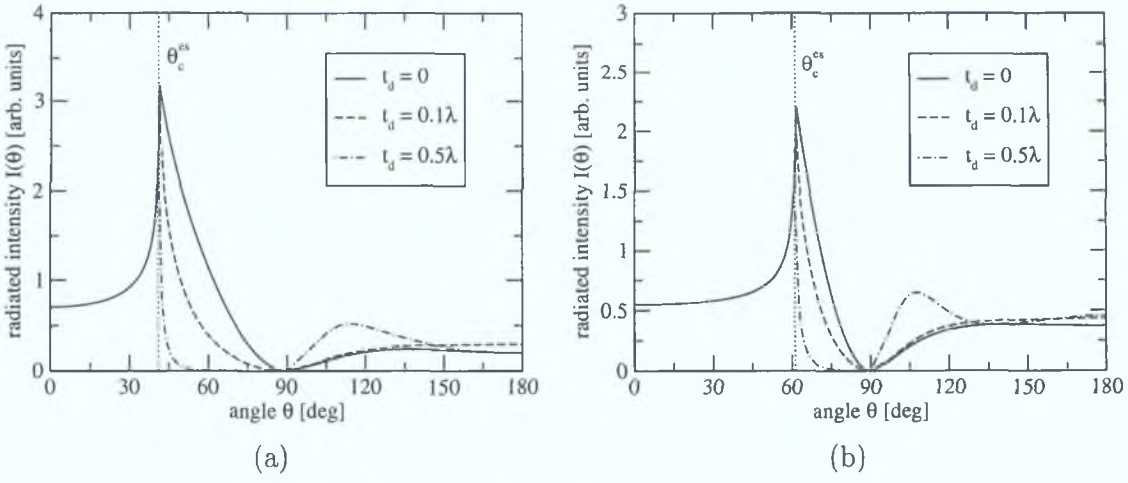

Figure 3.5: Angular distributions of intensity of luminescence radiated by a dipole located in air (a) and water (b) at various distances t_d from the glass substrate, as shown in Fig. 3.4. The particular values of the distances are specified in the legends.

As can be seen from the graphs in Fig. 3.5, the angular distribution of the intensity radiated below the critical angle θ_c^{es} does not change with the distance t_d of the dipole from the glass substrate. The intensity radiated into the environment, i.e., at angles $\theta \in \langle 90°, 180° \rangle$, varies in that its total amount increases with increasing value of t_d. Furthermore, a peak starts emerging at $\theta \approx 110°$ for greater values of t_d. Application of the theory developed in Sec. 3.1 would show that this is due to interference of the luminescence radiated directly into the environment and that reflected from the environment/substrate interface. The number of these peaks, which form a fringe-like pattern in the angular distribution of the intensity, would increase with increasing distance t_d (not shown in the figure).

The most significant changes in the intensity profile are observed within the angular range $\theta \in \langle \theta_c^{es}, 90° \rangle$, where θ_c^{es} is either $\theta_c^{as} = 41.3°$ or $\theta_c^{ws} = 61.3°$, depending on whether the environment is air or water, respectively. In particular, the intensity fall-off above the critical angle is more abrupt for greater distances t_d. Furthermore, for a distance as low as $t_d = 0.5\lambda$, there is almost no luminescence radiated above the critical angle θ_c^{es}, as shown by the dash-dotted line. These important features can be explained as follows. The electromagnetic field which propagates in the glass substrate at angles $\theta \in \langle \theta_c^{es}, 90° \rangle$ is exponentially decreasing in the environment. A characteristic penetration depth of this so-called evanescent field is approximately λ and it decreases with the increasing propagation angle θ. Because the luminescence at these angles is provided by coupling of the dipole's *near-field* with the evanescent field, it is understandable that its intensity is decreasing for increasing θ. Moreover, for a sufficiently large distance of the dipole from the surface, the evanescent field does not reach dipole's position. This implies that there is very little luminescence radiated above the critical angle for such large distances due to a weak coupling of the evanescent field and the dipole's near-field, as concluded above.

3.2.3 Radiation of a thin luminescent layer deposited on a substrate

In this section, the angular distribution of the intensity radiated by a thin luminescent layer deposited on a planar glass substrate is analysed. The layer is formed by a sol-gel layer of refractive index $n_l = 1.43$ doped with a luminescent ruthenium complex [15, 16, 17]. The environment covering the layer is either air or water. The structure is shown in Fig. 3.6.

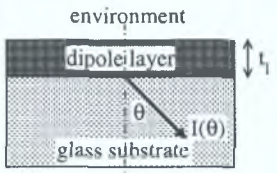

Figure 3.6: A schematic diagram of a thin dipole layer (refractive index $n_l = 1.43$, thickness t_l) deposited on a planar glass substrate. The environment covering the layer is either air or water.

Figure 3.7 shows the angular distributions of intensity of the luminescence radiated from the luminescent layer whose thickness takes values $t_l = 0.1\lambda, 0.5\lambda, 1.5\lambda$, where λ is the wavelength of luminescence. Only the intensity radiated into the glass substrate is shown. As can be seen, the angular distribution at angles below the critical angle θ_c^{es} does not change significantly with the thickness of the dipole layer, and is close to that corresponding to the

point dipole radiation (see Sec. 3.2.2 and Fig. 3.5).

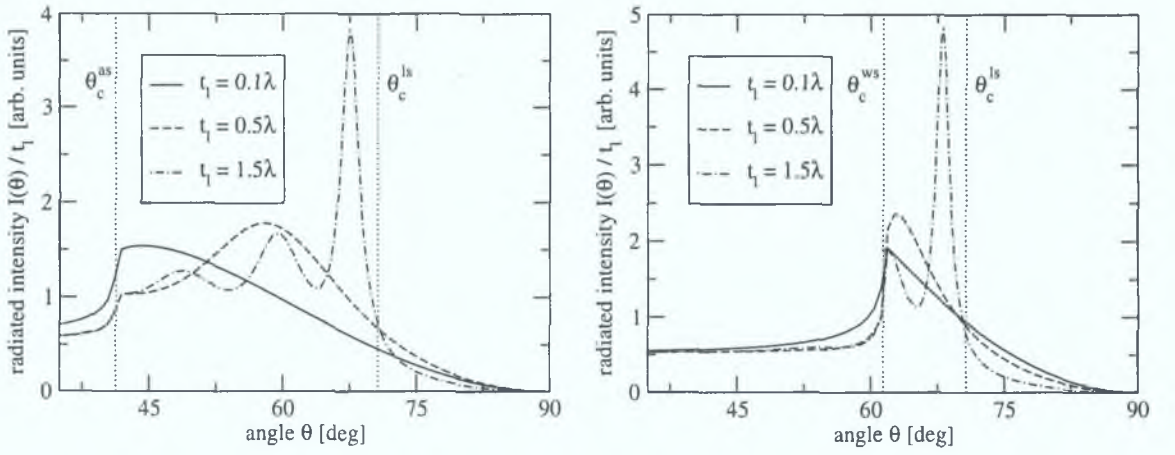

Figure 3.7: Angular distributions of intensity of the luminescence radiated from a thin luminescent layer deposited on a planar glass substrate (see Fig. 3.6). The environment covering the layer is air (a) and water (b). The thickness of the luminescent layer varies between values $t_l = 0.1\lambda, 0.5\lambda, 1.5\lambda$, as shown in the legend. In order to make the differences between the angular profiles more visible, the normalised intensity, i.e., $I(\theta)/t_l$ is plotted.

Notable changes are observed at angles $\theta \in \langle \theta_c^{es}, \theta_c^{ls} \rangle$, where $\theta_c^{ls} = \arcsin(n_l/n_s) \approx 70.7°$ is the critical angle of the layer/substrate interface. Within this angular range, the angular distribution of intensity exhibits a distinct peak. This peak is more pronounced and shifted towards θ_c^{ls} for greater values of the thickness of the dipole layer. Furthermore, at these greater thicknesses, the sharp peak is accompanied by several less significant peaks, which "emerge" from the angular position determined by θ_c^{es}. This is demonstrated by the dash-dotted line in Fig. 3.7(a). This feature is not yet visible in Fig. 3.7(b) as the thickness of the luminescent layer is not sufficiently large.

The behaviour of the radiated intensity described above can be qualitatively understood by considering the following arguments. The electromagnetic field, which corresponds to the modes propagating in the glass substrate at angles $\theta \in \langle \theta_c^{es}, \theta_c^{ls} \rangle$, is *propagating* within the dipole layer. Due to interference effects caused by the reflections at the substrate/layer and layer/environment interfaces, the magnitude of the field can be considerably enhanced for a certain value of the angle θ. (An example of the field distribution across the structure corresponding to this angle is shown in graphs (2) in Fig. 2.6, Chapter 2.) The coupling efficiency between the near-field of the dipoles inside the layer and the far-field propagating in the glass is proportional to the magnitude of the field inside the dipole layer. Therefore, the enhancement of the radiated intensity at a particular angle θ is a consequence of the enhancement of the field corresponding to the modes propagating at this angle.

3.2.4 Radiation of a thin luminescent layer separated by a buffer layer

In this section, a the two-layer system shown in Fig. 3.8 is considered. The system consists of a glass substrate covered by a buffer layer of refractive index $n_l = 1.43$ and variable thickness t_b. On top of the buffer layer is a luminescent dipole layer of refractive index $n_l =$

1.43 and thickness $t_l = 0.1\lambda$. The luminescent layer is covered by the environment which is either air or water. This example is chosen in order to demonstrate the influence of the buffer layer thickness on the angular profile of intensity of the radiated luminescence.

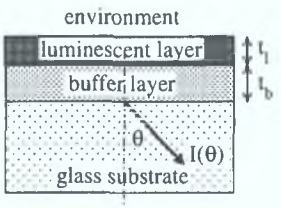

Figure 3.8: A schematic diagram of a two-layer system comprising a thin luminescent layer (refractive index $n_l = 1.43$, thickness t_l) and a thin buffer layer (refractive index $n_l = 1.43$, thickness t_b) deposited on a planar glass substrate. The structure is covered by the environment which is either air or water.

The angular dependence of intensity of the luminescence radiated into the glass substrate is shown in Fig. 3.9. The graphs (a) and (b) correspond to the situations where the luminescent layer is covered by air and water, respectively. The thickness of the buffer layer varies between $t_b = 0\lambda, 0.5\lambda, \lambda$.

As can be seen, the influence of the buffer layer on the angular profile of the radiated intensity is two-fold. Firstly, in the angular range $\theta \in \langle \theta_c^{es}, \theta_c^{ls} \rangle$, the smooth decrease of the intensity with the increasing angle θ is changed to a more complex profile containing peaks and dips, the number of which depends on the thickness t_b of the buffer layer. These peaks are due to the same interference effects as those discussed in Sec. 3.2.3.

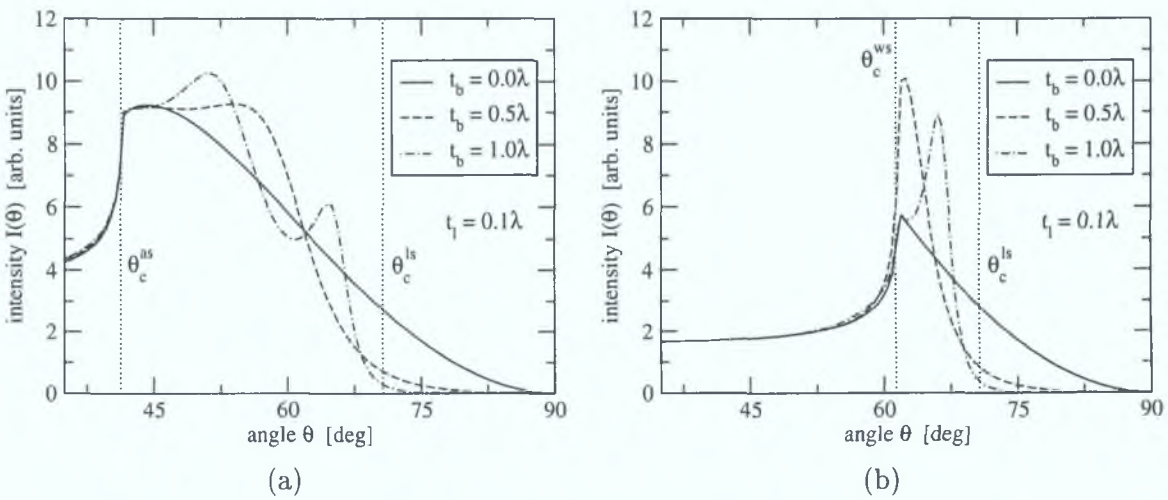

Figure 3.9: Angular distributions of intensity of the luminescence radiated into the glass substrate and originating from a thin luminescent layer (thickness $t_l = 0.1\lambda$, refractive index $n_l = 1.43$) which is separated from the substrate by a buffer layer (refractive index $n_l = 1.43$), as shown in Fig. 3.8. The luminescent layer is covered by air (a) and water (b). The values of the thicknesses t_b of the buffer layer for which the distributions are plotted are shown in the legend.

The second important influence of the buffer layer can be observed at angles above the critical angle θ_c^{ls} of the buffer layer/substrate interface. The total amount of luminescence radiated above this angle is decreased substantially even for as thin a buffer layer as $t_b = \lambda$

(see the dash-dotted line). This is due to the same reasons as already discussed in Sec. 3.2.2. In particular, the field corresponding to the intensity observed at these angles is evanescent in the buffer layer. When the thickness of the buffer layer is sufficiently large, the field barely reaches the luminescent layer, which decreases the coupling efficiency between the near-field of the radiating dipoles and the radiated field. Consequently, the amount of luminescence propagating in the glass substrate at angles $\theta > \theta_c^{ls}$ is very small for greater values of t_b.

3.2.5 Radiation of dipoles—thin layer vs bulk contribution

This section considers a configuration similar to that discussed in the previous section. The results obtained from this numerical analysis will have very important implications for practical applications where the surface-generated luminescence is of interest.

The two-layer system under consideration is shown in Fig. 3.10. It consists of a glass substrate, which is covered by a sol-gel layer of refractive index $n_l = 1.43$ and thickness $t_l = 1.5\lambda$. This layer is either luminescent or non-luminescent. On top of this layer is a bulk layer of water (thickness t_b), which either does or does not contain luminescent molecules. The purpose of this bulk layer is to model the contribution to the radiated luminescence originating from the *volume* above the thin sol-gel layer. The bulk layer is covered by water.

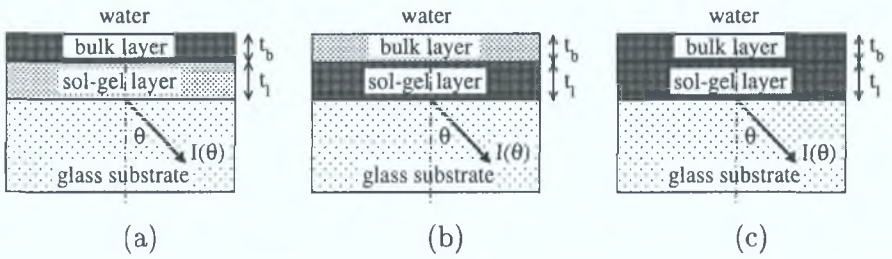

Figure 3.10: Schematic diagrams of two-layer systems consisting of a glass substrate, sol-gel layer and a bulk layer. The structures are covered by water. Diagrams (a), (b) and (c) correspond to the following situations: (a) the bulk layer contains luminescent molecules while the sol-gel layer does not; (b) the bulk layer does not contain luminescent molecules while the sol-gel layer does; (c) both the bulk and sol-gel layers contain luminescent molecules.

Firstly, it is considered that the sol-gel layer does not and the bulk layer does contain luminescent molecules, as shown in Fig. 3.10(a). The corresponding angular profile of intensity of the luminescence radiated into the glass substrate is shown in Fig. 3.11(a). As can be seen, the luminescence radiated from the bulk layer can be observed mainly at angles below the critical angle of the water/substrate interface (θ_c^{ws}). The greater is the thickness t_b of the bulk layer, the greater is the amount of luminescence observed below the critical angle θ_c^{ws}. On the other hand, the contribution of the bulk layer to the luminescence observed within the angular range $\theta \in \langle \theta_c^{ws}, \theta_c^{ls} \rangle$ is small and does not significantly change when the bulk layer thickness exceeds the value of approximately 4λ, as demonstrated by the dash and dash-dotted lines in Fig. 3.11(a). This is an important observation because it enables one to extend the thickness of the bulk layer to an arbitrarily large value without modifying the angular distribution of the luminescence radiated within this angular range. Last but not least, it is worth noting that there is only a negligible contribution of the bulk layer to the luminescence observed above the critical angle θ_c^{ls}.

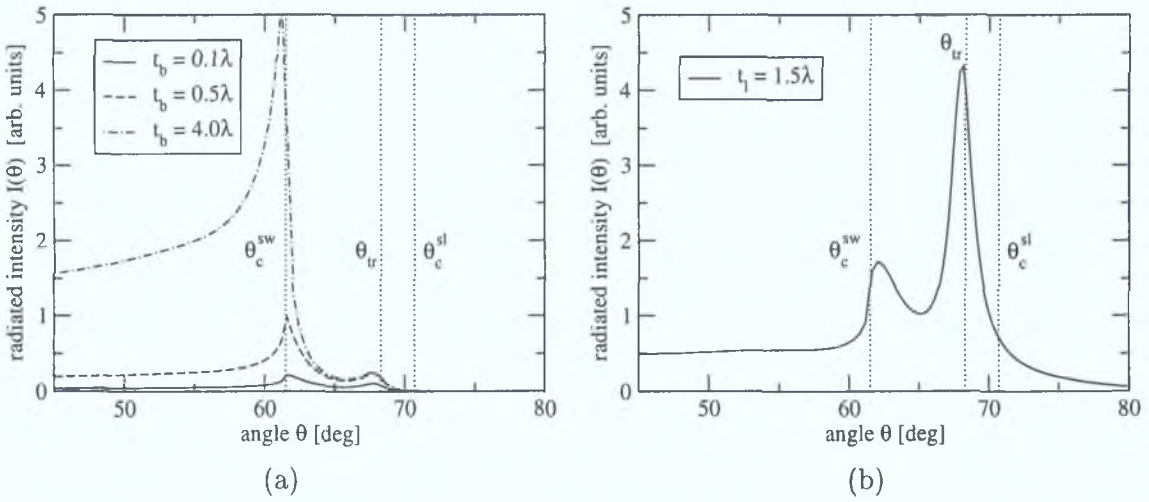

Figure 3.11: Angular distributions of intensity of luminescence generated by a multilayer structure shown in Fig. 3.10. The bulk layer is characterised by refractive index $n_b = 1.33$ and thickness t_b, while the sol-gel layer is characterised by $n_l = 1.43$ and $t_l = 1.5\lambda$. The graphs (a) and (b) correspond to the situations depicted in Figs. 3.10(a) and 3.10(b), respectively.

Now, the opposite case is considered, i.e., the sol-gel layer does and the bulk layer does not contain luminescent molecules. The corresponding angular distribution of the intensity observed in the glass looks as depicted in Fig. 3.11(b). The features of this profile were already discussed in Sec. 3.2.3. In contrast to the situation depicted in Fig. 3.11(a), the main contribution to the luminescence originating from the sol-gel layer is observed at angles $\theta \in \langle \theta_c^{ws}, \theta_c^{ls} \rangle$. Furthermore, there is a considerable amount of luminescence radiated above the critical angle θ_c^{ls}.

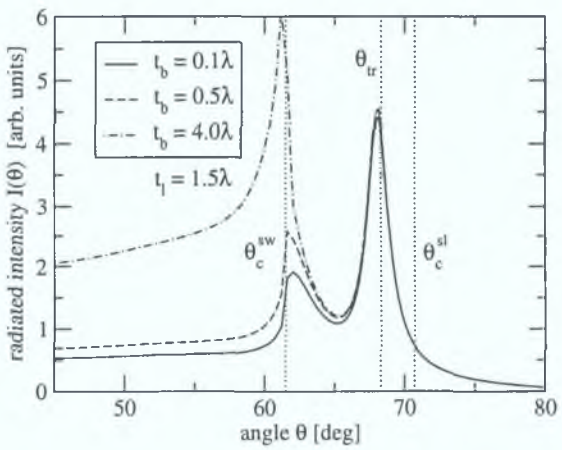

Figure 3.12: An example of the angular distribution of intensity generated by a multilayer structure shown in Fig. 3.10(c). The bulk layer is characterised by refractive index $n_b = 1.33$ and thickness t_b, while the sol-gel layer is characterised by $n_l = 1.43$ and $t_l = 1.5\lambda$. Both the sol-gel and bulk layers contain luminescent molecules with equal concentrations.

When both the sol-gel and bulk layers contain the luminescent molecules,[1] as shown in

[1] For simplicity, both layers are assumed to have equal densities of the luminescent molecules.

Fig. 3.10(c), the angular distribution of intensity looks as shown in Fig. 3.12. Due to the fact that the contributions to the luminescence originating from different parts of the structure are considered to be uncorrelated (in the statistical sense), the total intensity is given by the sum of the contributions from the sol-gel and bulk layers.

The graph demonstrates that it is possible to *distinguish* between the contributions originating from the doped sol-gel layer and the luminescent bulk layer. This is due to the fact that these two contributions are observed within different angular regions. In particular, the main contribution originating from the bulk layer is radiated at angles *below* the critical angle θ_c^{ws}, while the main contribution originating from the thin sol-gel layer is observed at angles *above* the critical angle θ_c^{ws}. Although the distinction between the two contributions is not sharp around the critical angle θ_c^{ws}, there is a definite angle, denoted by θ_{tr}, above which the contribution originating from the bulk layer is negligible in comparison to the contribution originating from the sol-gel layer. The value of this angle can be determined by combining this analysis and the noise characteristics of the particular detection system. This will be more extensively studied in Sec. 3.4.

3.2.6 Radiation of dipoles—surface vs bulk contribution

In this section, another implication of the theory that could be exploited in a technique suitable for distinguishing between the surface and bulk-generated luminescence is discussed.

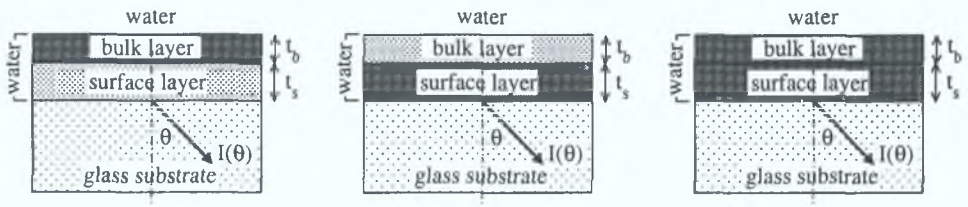

Figure 3.13: Schematic diagrams of a two-layer system consisting of a glass substrate covered with water. The water above the substrate is divided into a surface layer and a bulk layer. Diagrams (a), (b) and (c) correspond to the following situations: (a) the bulk layer contains luminescent molecules while the surface layer does not; (b) the bulk layer does not contain luminescent molecules while the surface layer does; (c) both the bulk and surface layers contain luminescent molecules.

The structure under consideration consists of a glass substrate covered by water. The water environment is divided into a "surface" layer, a "bulk" layer and the bulk itself. The surface layer is a layer of water of thickness t_s adjacent to the glass substrate. The bulk layer is another layer of water (thickness t_b) covering the surface layer. The purpose of this division is to model the contributions to the radiated luminescence originating from molecules located close to the surface of the substrate and those located further away from the surface. The situation is depicted in Fig. 3.13.

Firstly, it is assumed that both the surface and bulk layers contain luminescent molecules. This means that the luminescence originates from a layer of thickness $t_s + t_b$, as shown in Fig. 3.13(c). The angular distribution of intensity of the luminescence radiated into the glass substrate from such a system is shown in Fig. 3.14(a) for $t_s = \lambda$ and various values of the bulk layer thickness (see the legend of the graph). As can be seen, the increased value of the

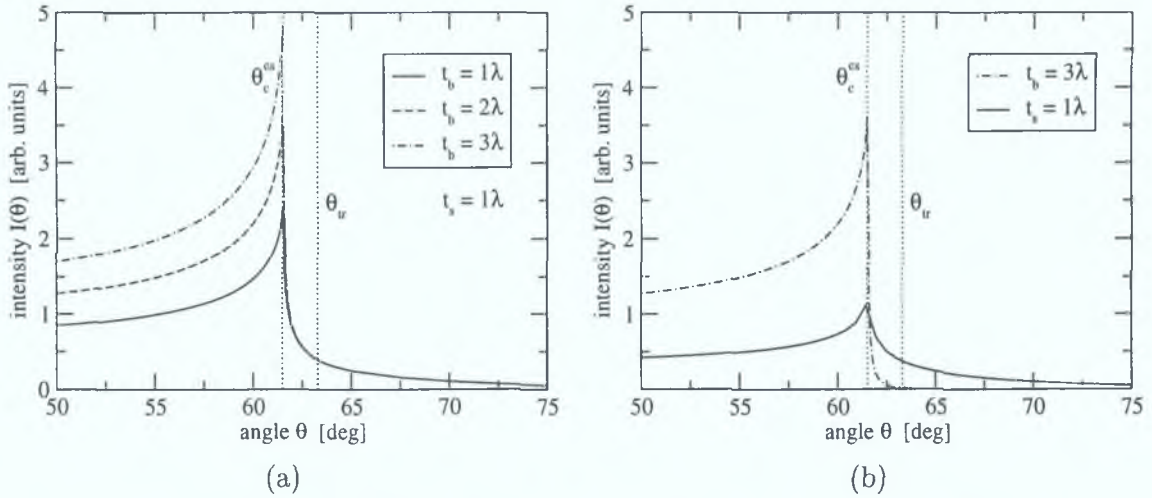

Figure 3.14: (a) Angular distributions of the total intensity of luminescence radiated into the glass substrate, which is given as a sum of the contributions originating from the "surface" and "bulk" layers, i.e., from a layer of total thickness $t_s + t_b$. (b) Separate contributions to intensity of the luminescence originating from the surface layer of thickness $t_s = \lambda$ (solid line) and the bulk layer of thickness $t_b = 3\lambda$ (dash-dotted line). Both the surface and bulk layers are comprised of water (see Fig. 3.13 for the explanation of the structure under consideration).

bulk layer thickness results only in increase of the level of luminescence intensity below the critical angle of the environment/substrate interface θ_c^{es}. Above this angle, the intensity of luminescence remains practically unchanged for all values of the bulk layer thickness t_b.

To explain this behaviour, the contributions originating from the surface and bulk layers are plotted separately. This is shown in Fig. 3.14(b) by the solid and dash-dotted lines, respectively. The dash-dotted line indicates that the luminescence originating from the bulk layer falls rapidly above the critical angle θ_c^{es}. Above the threshold value of the observation angle θ_{tr}, the luminescence intensity arising from the bulk is negligible in comparison with the contribution of the surface layer. As follows from the graphs (a) and (b) in Fig. 3.14, it is the surface layer that contributes to the luminescence radiated well above the critical angle θ_c^{es} or, more precisely, above the threshold angle θ_{tr}. Therefore, by defining the value of θ_{tr} and observing the angular distribution of the luminescence radiated into the (higher refractive index) substrate above θ_{tr}, one can establish a useful detection technique. Employing this technique, one can distinguish between the luminescence originating from the surface layer and the luminescence originating from the bulk covering the surface layer. The thickness of the surface layer has to be determined by the particular application exploiting this principle. Once it is known, the threshold angular position θ_{tr} can be calculated. Further details of this calculation will be treated more extensively in Sec. 3.4.

3.3 Optimisation of luminescence capture efficiency

Following the theoretical and numerical analysis of the properties of luminescence generated from structures employing thin luminescent films, it is now possible to address the issue of the luminescence capture efficiency. Firstly, a numerical analysis of the capture efficiency

for conventional detection systems is analysed. Subsequently, a list of novel configurations, which can substantially increase the efficiency of the luminescence capture, are proposed and discussed in detail.

3.3.1 Numerical analysis of luminescence capture efficiency

As mentioned in Sec. 1.4, a typical configuration in many luminescence-based sensor applications involves a thin luminescent film or spot deposited onto a planar substrate. In the following discussion, the element containing the planar substrate and the luminescent layer or spot will be referred to as the sensing element or sensor chip. The sensor chip is considered to be designed independently of the sensor system in which it is to be incorporated.

One possible and very simple implementation of the sensing element comprises a higher refractive index substrate, such as a glass slide, on top of which a luminescent film or spot is deposited. This configuration is widely used in the laboratory where this research was conducted and therefore will be the primary focus of the following discussion.

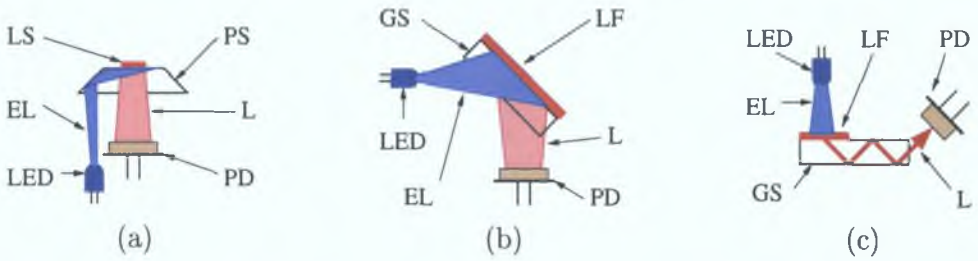

Figure 3.15: (a) A diagram of the sensor chip used in the probe of the dissolved oxygen optical sensor [17]. The sensor chip employs a plastic substrate (PS) coated with a small luminescent spot (LS). The LED provides the excitation light (EL), while the photodiode (PD) collects the luminescence (L) transmitted through the substrate. (b) A diagram of the sensor chip used in the O_2 or CO_2 laboratory sensor system [19, 20]. The sensor chip employs a glass substrate (GS) coated with a thin luminescent film (LF). The LED provides the excitation light (EL), while the photodiode (PD) collects the luminescence (L) transmitted through the substrate. (c) A diagram of the configuration employing the edge-detection of the luminescence (L) which is trapped inside and propagating along the glass substrate (GS) towards the slide edge [21]. The LED provides the excitation light (EL), while the photodiode (PD) transforms the luminescence to an electrical signal.

When the sensing element is incorporated into the sensor system, the excitation of the luminescence is typically provided by a direct illumination of the luminescent layer or spot. Furthermore, the detector is placed directly (or almost directly) under or above the sensing chip. Examples of the typical configurations using this geometry are shown in Fig. 3.15(a–b). Although another configuration employing the edge detection (see Fig. 3.15(c)) was recently developed [21], the improvement of the luminescence capture efficiency was not adequately analysed nor yet fully exploited.

Based on the theory developed in Sec. 3.1, the problems with the detection of the directly transmitted light are now highlighted. Firstly, the sensing element, for which a thorough investigation is carried out, is precisely defined. Although particular values of the material and other geometrical parameters are assumed, the same analysis can be performed for any other set of parameters.

The sensing element under consideration is shown in Fig. 3.16. It consists of a "thick" glass slide substrate (refractive index $n_s = 1.515$, thickness $\approx$ 1mm) on top of which a small spot of luminescent material (refractive index $n_l = 1.43$) is deposited. The thickness t_l of the layer forming the spot is assumed to be uniform and in the range of hundreds of nanometers. Furthermore, for simplicity, the size of the spot is assumed to be small compared to the size of the area of the detection system which is used to detect the luminescence produced by the spot. The latter restriction is assumed only to ensure that the luminescent spot "appears" to the detector as a spot rather than as an area over which the radiated intensity would have be integrated. Consequently, the lateral (x–y) dimensions do not have to be considered and only the angular dependence of the radiated intensity needs to be taken into account in the following analysis. The luminescent spot is assumed to be covered by the environment, which is either air ($n_a = 1.0$) or water ($n_w = 1.33$). The slide is surrounded by air from below.

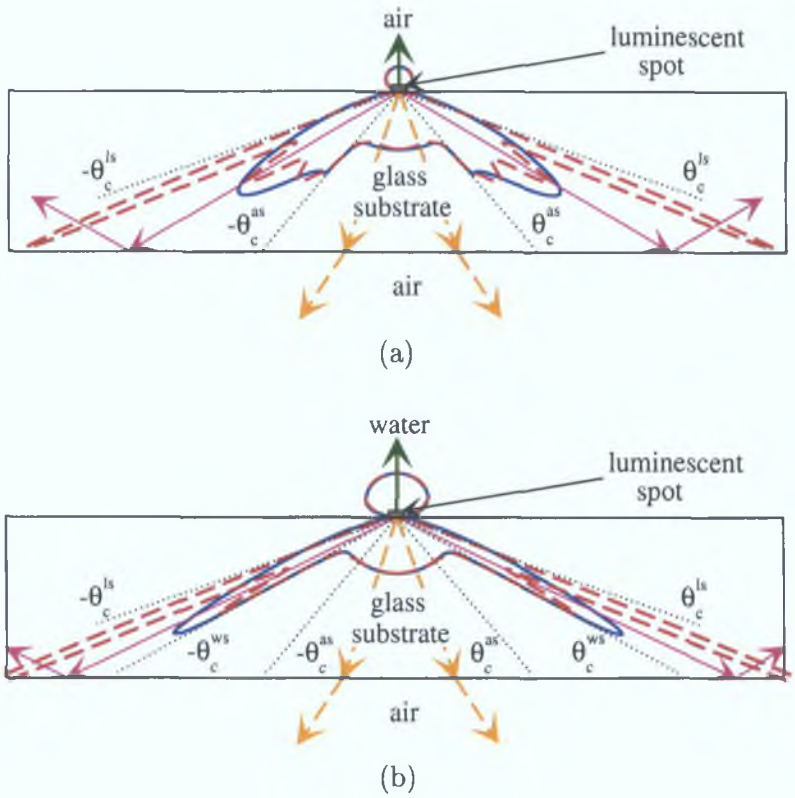

Figure 3.16: Angular properties of luminescence radiated from a small luminescent spot deposited on a glass substrate. The substrate is surrounded by air from below and by air (graph a) or water (graph b) from above. The blue solid line and the red dashed line represent the angular distributions of luminescence radiated from the luminescent spot of thickness $t_l = 0.5\lambda$ and $t_l = 1.5\lambda$, respectively.

The predicted angular distribution of the luminescence emerging from the small luminescent spot deposited on the glass substrate is shown in Fig. 3.16. The graphs (a) and (b) correspond to the situation where the environment covering the spot is air and water, respectively. In both graphs, the solid blue line and the dashed red line correspond to the thicknesses of the luminescent spot equal to $t_l = 0.5\lambda$ and $t_l = 1.5\lambda$, respectively, where λ is the luminescence wavelength. Although this situation was already discussed in Sec. 3.2.3,

the results will now be evaluated from a different perspective.

Luminescence that can be detected by the detector placed *above* the glass substrate is schematically shown by the green arrow. As can be seen from the blue or red line located in air or water above the glass substrate, the amount of luminescence radiated into the environment covering the spot is relatively small.

The situation is similar when the detector is placed below the glass substrate. Due to the reflections taking place at the bottom glass/air interface, the light impinging at this interface is transmitted to air only if the incident angle lies within the angular range $\theta \in \langle -\theta_c^{as}, \theta_c^{as} \rangle$, where $\theta_c^{as} = \arcsin(n_a/n_s) \approx 41.3°$ is the critical angle of the substrate (glass)/air interface. This light is schematically depicted by the dashed orange arrows. Due to the refraction, the light propagating inside the substrate at angles $\theta \in \langle -\theta_c^{as}, \theta_c^{as} \rangle$ is partially transmitted into the air under the substrate at angles $\theta \in \langle -90°, 90° \rangle$. The blue and red lines within the angular range $\theta \in \langle -\theta_c^{as}, \theta_c^{as} \rangle$ demonstrate that the amount of luminescence transmitted to air below the glass substrate is also relatively small.

The light propagating inside the substrate at angles greater than the critical angle θ_c^{as} is totally reflected at the lower substrate/air interface. If the environment covering the slide is air, as shown in Fig. 3.16(a), this light is also totally reflected at the upper layer/air interface and is effectively trapped (or confined) within the waveguiding glass substrate. If the environment above the slide is water, as shown in Fig. 3.16(b), the part of the light propagating in the substrate at angles $\theta \in \langle \theta_c^{as}, \theta_c^{ws} \rangle$ and $\theta \in \langle -\theta_c^{as}, -\theta_c^{ws} \rangle$ is partially transmitted into water and partially reflected back to the substrate. Furthermore, the part of light propagating at angles $\theta \in \langle \theta_c^{ws}, 90° \rangle$ and $\theta \in \langle -\theta_c^{ws}, -90° \rangle$ is totally reflected at the upper layer/water interface. In any case, due to the relation $\theta_c^{ws} > \theta_c^{as}$, the light exhibiting the enhanced intensity is always trapped inside the substrate due to the total internal reflection at both the upper and lower interfaces.

This analysis clearly explains why large values of the luminescence capture efficiency cannot be achieved by the conventional detection technique employing detection above or below the substrate. It is mainly due to the fact that this technique facilitates the detection only of the low-intensity modes generated by the luminescent spot. The analysis also demonstrates that a higher capture efficiency could be achieved if the more intense modes, i.e., those propagating at angles $\theta \in \langle \theta_c^{es}, \theta_c^{ls} \rangle$ and $\theta \in \langle -\theta_c^{es}, -\theta_c^{ls} \rangle$, are detected. In these expressions, θ_c^{es} is equal either to θ_c^{as} or θ_c^{ws}, depending on whether the environment covering the luminescent spot is air or water, and θ_c^{ls} is the critical angle of the layer/substrate interface.

To simplify the subsequent discussion, the following terminology is introduced. The luminescence directly transmitted to air or water above the substrate will be called the air-transmitted or the water-transmitted luminescence. The corresponding modes of the electromagnetic field will be called the air-transmitted or water-transmitted modes or, shortly, AT or WT modes. The luminescence radiated into the substrate at angles $\theta \in \langle -\theta_c^{as}, \theta_c^{as} \rangle$, which is eventually transmitted into air under the substrate, will be called the substrate-transmitted luminescence. The corresponding modes will be called the substrate-transmitted (ST) modes. The luminescence radiated into the substrate at angles $\theta \in \langle \theta_c^{es}, \theta_c^{ls} \rangle$ and $\theta \in \langle -\theta_c^{es}, -\theta_c^{ls} \rangle$, which is trapped (confined) inside the substrate, will be called the substrate-confined luminescence.[2] The corresponding modes will be called the substrate-confined (SC) modes. The

[2]Even though the term substrate-trapped luminescence would be more suitable, it will not be used here

luminescence propagating at angles $\theta \in \langle \theta_c^{ls}, 90° \rangle$ and $\theta \in \langle -\theta_c^{ls}, -90° \rangle$ will be called the evanescent-wave (EW) luminescence. Although it is also trapped (confined) inside the substrate, this name reflects better the character of the field corresponding to these modes, which is *evanescent* in the luminescent layer. This is qualitatively different from the SC modes, whose field is *propagating* (i.e., described by a harmonic function) inside the luminescent layer.

To provide quantitative analysis of the improvement in the luminescence capture efficiency that could be achieved by employing the detection of the SC modes, the total optical power carried by the AT/WT modes, ST modes, SC modes and the EW modes is calculated and compared. This comparison is shown in Figs. 3.17 and 3.18. The graphs (a) and (b) in both figures correspond to the situations where the environments covering the luminescent spot are air and water, respectively.

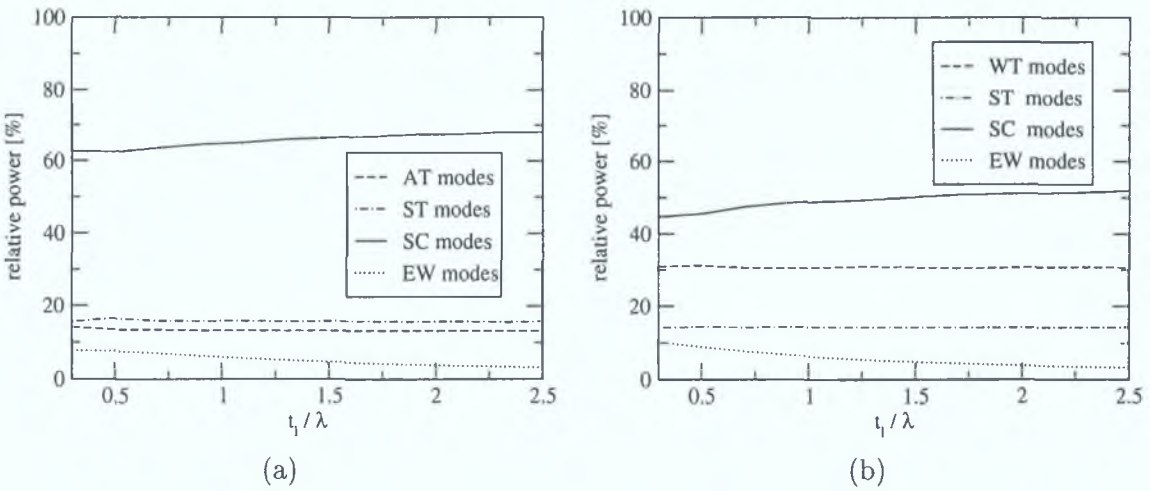

Figure 3.17: Relative optical power carried by the AT/WT, ST, SC and EW modes as a function of the thickness t_l of the luminescent spot, while the refractive index of the layer is constant an equal to $n_l = 1.43$. The graphs (a) and (b) correspond to the situations where the luminescent spot is covered by air and water, respectively.

Figure 3.17 shows the relative power carried by the modes as a function of the thickness t_l of the luminescent layer, where the refractive index of the layer is assumed to be constant and equal to $n_l = 1.43$. As follows from Eq. (3.34), the total power carried by all the modes is proportional to the thickness t_l (T_j in Eq. (3.34)). However, as can be seen from both graphs in Fig. 3.17, the relative *fraction* of the power carried by each of the modes remains practically *constant* over a substantially large interval of t_l. The notable variation is exhibited by the SC modes which gain the relative power at the expense of the EW modes. This is due to the fact that for greater values of t_l the coupling between the more distant regions of the luminescent layer from the substrate and the EW modes is weaker (due to the finite penetration depth of the evanescent field).

The graph (a) in Fig. 3.17 indicates that the SC modes carry approximately 66 % of the total luminescence radiated by the spot when the spot is covered by air.[3] This number is somewhat smaller when the luminescent spot is covered by water ($\approx 50\,\%$), which is caused by

since the abbreviation ST would be the same as that for the term surface-transmitted luminescence.

[3]Understandably, the numerical values depend on the parameters used in the calculation.

the increase of the fraction of luminescence radiated into water by means of the WT modes, as follows from the comparison of the dashed lines in graphs (a) and (b). Although these numbers might not seem too large when compared to the fractions of the power carried by the AT modes ($\approx 15\,\%$), WT modes ($\approx 30\,\%$) or the ST modes ($\approx 15\,\%$), it is important to realise that the SC modes are "localised" in a narrower angular range ($\Delta\theta = \theta_c^{ls} - \theta_c^{as} \approx 30°$ and $\Delta\theta = \theta_c^{ls} - \theta_c^{ws} \approx 10°$ for the situations where the spot is covered by air and water, respectively) than the other modes, which are propagating in the full range $\theta \in \langle -90°, 90° \rangle$. To facilitate the detection of the full power carried by the AT, WT, or ST modes, one would have to use a detection system with the value of the numerical aperture equal to 1, which is practically impossible. On the other hand, the large power carried by the SC modes could be detected using a detection system with a *low* value of the numerical aperture (not exceeding $\sin 15° \approx 0.26$ for $\Delta\theta = 30°$ or $\sin 5° \approx 0.09$ for $\Delta\theta = 10°$).

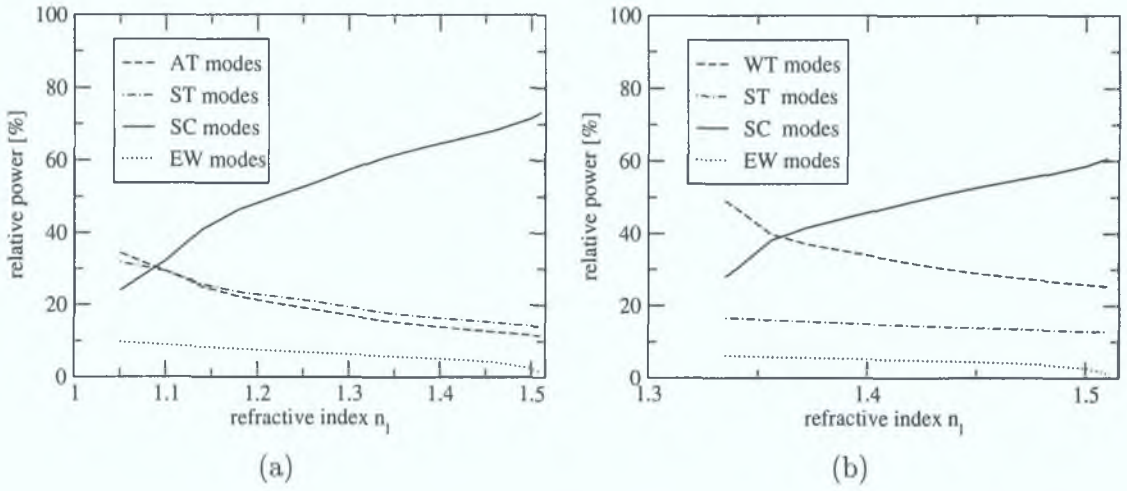

Figure 3.18: Relative optical power carried by the AT/WT, ST, SC and EW modes as a function of the refractive index n_l of the luminescent spot, while the thickness of the layer is constant an equal to $t_l = 1.5\lambda$. The graphs (a) and (b) correspond to the situations where the luminescent spot is covered by air and water, respectively.

Figure 3.18 shows the relative power carried by the modes as a function of the refractive index n_l of the luminescent layer, where the layer thickness is assumed to be constant and equal to $t_l = 1.5\lambda$. It can be seen that the power carried by the SC modes increases rapidly as n_l approaches the value of the substrate refractive index ($n_s = 1.515$). This is mainly due to the shift of the critical angle θ_c^{ls}, which converges to 90° as n_l approaches n_s. As in the case discussed above, the fraction of the power carried by the SC modes is generally smaller when the environment covering the luminescent spot is water. This is again due to the fact that the luminescence radiated into water has higher intensity, as follows from the comparison of the dashed lines in the graphs (a) and (b) of Fig. 3.18. Nevertheless, figure 3.18 demonstrates that a greater fraction of the energy carried by the SC modes is obtained when the refractive index of the luminescent layer is chosen as close to that of the substrate as possible.

The above analysis considers the *total optical power* carried by the various types of modes radiated from the luminescent spot. This means that in order to make these quantities comparable as measures of the luminescence capture efficiency, a detection system which is able to capture *all* the power carried by the particular modes would have to be employed.

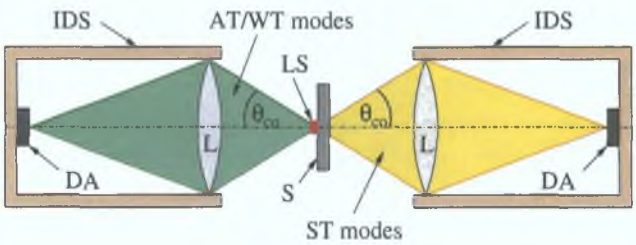

Figure 3.19: A schematic diagram of an ideal detection system (IDS) characterised by a numerical aperture NA $= \sin\theta_{co}$, where θ_{co} is the cone angle associated with the cone of light entering the system. The system employs an ideal lens (L) which redirects the beams corresponding to the AT/WT and ST modes to the detector array (DA). S denotes the substrate containing the luminescent spot (LS), as shown in Fig. 3.16.

For example, in case of the AT, WT or ST modes, the detection system would have to be able to detect light beams propagating in the cone with the cone angle of 90°, i.e., characterised by the numerical aperture NA = 1.

In order to provide a better quantitative comparison between the different types of modes, it is necessary to consider them in the context of the detection system. This can be done by evaluating the detected power as a function of the numerical aperture of the detection system.

In the following analysis, an ideal detection system, which is depicted in Fig. 3.19, is considered. It is assumed to be placed directly below or above the luminescent spot, i.e., its axis (dashed-dotted line) is perpendicular to the surface of the substrate and intersects the luminescent spot.

One of the most important quantities characterising the detection system is its numerical aperture (NA). It is related to the value of the cone angle θ_{co} by NA $= \sin\theta_{co}$. The fact that the system is ideal means that *all* the light propagating within the cone characterised by the cone angle $\theta_{co} = \arcsin$ NA is detected and converted to the signal proportional to the total power carried by the corresponding modes.

At this stage, only the AT, WT and ST modes are considered. The SC modes will be considered in the following section, where several novel configurations enabling their efficient detection will be proposed.

Figure 3.20 shows the efficiency of detection of the AT, WT and ST modes as a function of the numerical aperture of the ideal detection system described above. In the calculation, the values $n_l = 1.43$ and $t_l = 1.5\lambda$ were considered.

It can be seen from the graph that the relative values of the detected optical power, which are listed in Table 3.1, can be achieved only with a detection system whose numerical aperture is equal to unity. For NA < 1, the capture efficiency decreases rapidly. For example, it falls below 5 % for NA < 0.5. This means that even an ideal detection system *cannot* detect more than 5 % of the *total* power radiated by the luminescent spot when its numerical aperture is lower than 0.5. This makes the SC modes attractive because they carry more power which is concentrated within a narrower angular range, thus allowing for a greater capture efficiency at a lower numerical aperture of the detection system. The following section will provide details on how these modes can be effectively detected. Furthermore, it will present quantitative

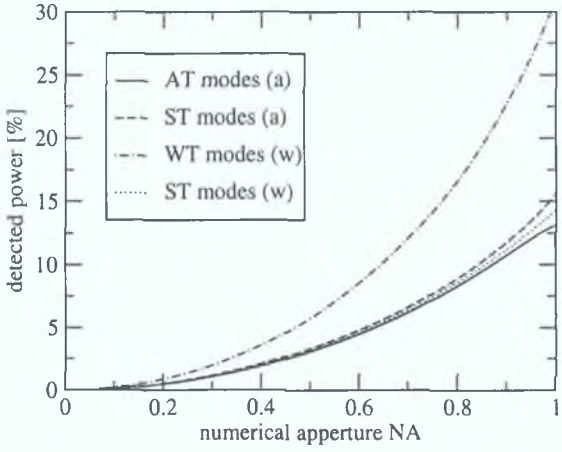

Figure 3.20: Efficiency of the detection of optical power carried by various types of modes radiated by the luminescent spot. The efficiency is plotted for the ideal detection system depicted in Fig. 3.19 as a function of its numerical aperture NA. The lines marked by (a) and (w) correspond to the situations where the luminescent spot is covered by air and water, respectively.

comparison with the results obtained in this section.

The numerical analysis presented in this section serves only as an example. It focused only on particular configurations using particular values of the refractive index and thickness of the luminescent layer and other materials involved. However, using the theory developed in Sec. 3.1, a similar analysis with qualitatively similar results can be carried out for any other set of parameters.

luminescent spot covered by	
air	water
AT modes: $\approx 13\,\%$	WT modes: $\approx 31\,\%$
ST modes: $\approx 16\,\%$	ST modes: $\approx 14\,\%$
SC modes: $\approx 66\,\%$	SC modes: $\approx 50\,\%$
EW modes: $\approx 5\,\%$	EW modes: $\approx 5\,\%$

Table 3.1: Relative values of total optical power carried by specified modes calculated for a sensor chip depicted in Fig. 3.16. The thickness and refractive index of the luminescent spot for which these values were calculated are $t_l = 1.5\lambda$ and $n_l = 1.43$, respectively.

3.3.2 Configurations with enhanced luminescence capture efficiency

The previous section concluded that the luminescence radiated from a luminescent spot or layer by means of the SC modes should be detected in order to improve luminescence capture efficiency. This section provides a list of configurations which facilitate the detection of the SC modes. Detailed analysis of the luminescence capture efficiency for one particularly promising configuration is presented and compared to the results obtained in the previous section.

The underlying principle of all the configurations is the modification of the geometry of the top or bottom interface of the substrate in order to redirect the SC modes towards

the detector placed above or under the substrate. This modification can be achieved by employing macroscopic or microscopic structures at the top or bottom substrate interface, which, by means of reflection, refraction or diffraction, change the direction of propagation of the SC modes.

Edge detection

This configuration was already mentioned in Sec. 3.3.1. It takes advantage of the fact that the luminescence radiated by means of the SC modes propagates along the substrate and is radiated out of the substrate at the edge, as shown in Fig. 3.21(a). This concept has already been demonstrated in the laboratory where this research was conducted [21, 22] as well as by other authors [23, 24, 25, 26, 27]. Although this configuration facilitates the detection of the SC modes, the detection is not optimised. This is due to the fact that only a *fraction* of the SC modes is detected, in particular that corresponding to the modes propagating within the angular range of $\Delta\phi$, as shown in Fig. 3.21(b). In order to maximise this fraction, the detectors would have to be put all around the substrate, which is not feasible in most practical applications. The situation could be improved by employing a channel waveguide, as shown in Fig. 3.21(c). In this case, a fraction of the SC modes would be coupled into the channel waveguide and subsequently detected at the edge. This fraction could be considerably greater than that for the configuration without the channels, especially if the number of channel waveguides "emerging" from the luminescent spot is greater. However, this structure would be more demanding from the point of view of the technological processes involved in preparation of the substrate as well as the requirements on the number of detectors. Due to these reasons, further numerical estimation of the improvement of the luminescence capture efficiency will not be given for this configuration.

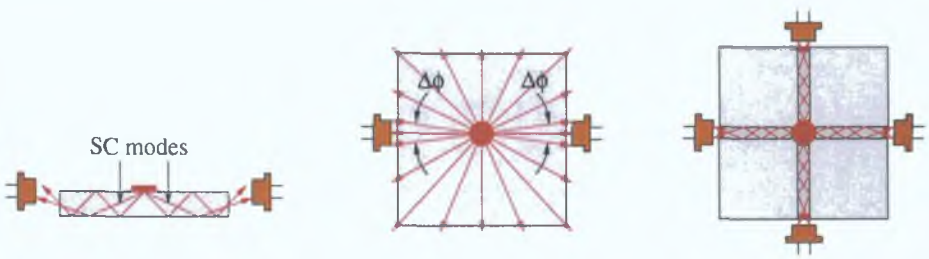

Figure 3.21: Side (a) and top (b) views of the configuration employing the edge detection of the SC modes. The configuration (c) employs channel waveguides to deliver a greater fraction of the SC modes into the detectors than that in the configuration (b). The red spot in the centre of the waveguides represents the luminescent spot.

Combination of refractive and reflective elements at the bottom interface

A configuration which employs a combination of refractive and reflective elements at the bottom interface of the substrate is shown in cross-section in Fig. 3.22. Total internal reflection at the bottom interface of the substrate is avoided by configuring the plane of the interface so as to decrease the angles of incidence of the SC modes to values lower than the critical

angle θ_c^{as}. This plane, through which the SC modes are refracted and transmitted outside the substrate, is denoted by A. If it is required that the detection takes place under the substrate below the luminescent spot, an additional air-substrate interface, denoted by B, can be incorporated in order to reflect the SC modes, as shown in Fig. 3.22(b).

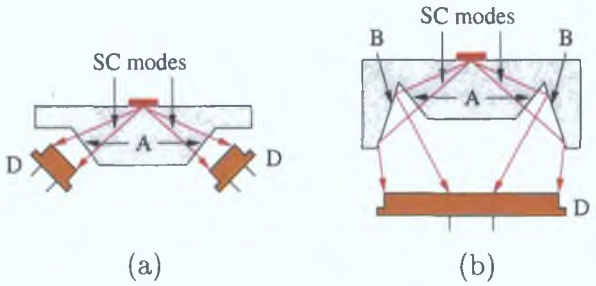

Figure 3.22: Side views of the configurations employing a combination of refractive and reflective elements. The SC modes are transmitted through the plane A. In the diagram (b), they are further reflected by the plane B and redirected towards the detector (D) placed under the substrate.

A particular advantage of this configuration is that the *top* interface containing the luminescent spot is *planar*. This is important if the system is required to be compatible with another system employing a planar architecture. Furthermore, the orientation of the plane A is designed so as to ensure that the SC modes impinge on the plane A at angles close to 0°, i.e., almost at normal incidence. This is important because the fraction T of the power transmitted through this plane, which is determined by $T \approx 1 - |(n_s - n_a)/(n_s + n_a)|^2$, is large ($T \approx 96\,\%$).

Although the tilted interface A provides efficient out-coupling of the SC modes outside the substrate, the modes propagate in air immediately after the interface A at large angles. This would make it difficult to detect the SC modes effectively by a detector placed under the substrate. For this reason the reflecting interface B is provided in the configuration. Its function is to redirect the SC modes towards the detector. However, a high reflectivity of this interface cannot be achieved if it is determined solely by the differences between the refractive indices of the substrate and air. For example, for $n_s = 1.515$ and $n_a = 1.0$, the reflectivity is approximately $|(n_s - n_a)/(n_s + n_a)|^2 \approx 4\,\%$ for the incident angles up to $\approx 50°$ and is still less then $\approx 50\,\%$ for angles as high as 80°. Therefore, unless the reflectivity of the interface B is increased, e.g., by depositing a reflective metal layer, the poor reflectivity of this interface makes the redirection and thus the detection of the SC modes under the substrate rather ineffective. Due to these reasons, further analysis of the luminescence capture efficiency of this configuration will not be conducted here.

Diffractive elements at the bottom interface

Another way of out-coupling the SC modes from the substrate and redirecting them towards the detector placed under the substrate is to use diffraction. For example, if a diffractive element, such as a grating or a more general diffractive optical element (DOE), is placed in the position where the SC modes hit the bottom interface of the substrate, the light propagated by means of the SC modes can be out-coupled and redirected towards the detector at the same time. This configuration is shown in Fig. 3.23.

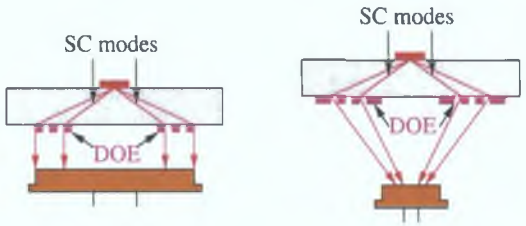

(a) (b)

Figure 3.23: Side views of the configurations employing a diffractive optical element (DOE) placed at the bottom interface of the substrate. The diffractive element facilitates both out-coupling of the SC modes from the substrate and redirecting them towards the detector placed under the substrate.

The advantage of this configuration is that both the top and bottom interfaces of the substrate are planar.[4] Furthermore, the DOE can be designed so as, for example, to facilitate focusing of the SC modes into the detector, as shown in Fig. 3.23(b).

However, there are also great disadvantages to this configuration. The first one is implied by the complex technological processes involved in the preparation of the diffraction elements. The second and a more important one is associated with the fact that even the best DOEs available on the market have still very low diffraction efficiencies (in the order of a few percent). This makes the overall out-coupling efficiency of the SC modes rather low and so their detection below the substrate rather ineffective.

Modification of the top interface

The final configuration, which is designed to provide increased efficiency of the luminescence capture, is shown in Fig. 3.24. In contrast to the previously discussed configurations, the out-coupling and redirection of the SC modes radiated from the luminescent spot are facilitated by the modification of the top interface.

The principle behind this design is the total internal reflection of the SC modes radiated from the luminescent spot by the tilted interface A, as shown in Fig. 3.24(a). The advantage of this configuration is two-fold. Firstly, the total internal reflection at this interface is feasible for *all* the SC modes and can be achieved by a proper choice of the tilt angle α. Secondly, the redirected SC modes impinge on the bottom interface of the substrate at angles close to 0° which guarantees that a large fraction of the power is transmitted out of the substrate towards the detector (transmittivity $T \approx 96\,\%$, as discussed above). The disadvantage of this configuration is that the top interface of the substrate needs to be modified which makes it not directly compatible with systems employing pure planar architecture.

Detailed analysis of the improvement in the luminescence capture efficiency is based on figures 3.16(a) and 3.24(b). In this analysis, the substrate containing the luminescent spot is assumed to be made of glass ($n_s = 1.515$) and surrounded by air ($n_a = 1.0$) both from the top and bottom. The analysis can be, however, extended to any other set of parameters. The properties of the luminescent spot are the same as those used in the numerical analysis presented in Sec. 3.3.1, i.e., $n_l = 1.43$ and $t_l = 0.5\lambda$.

[4] The bottom one at least in the macroscopic sense.

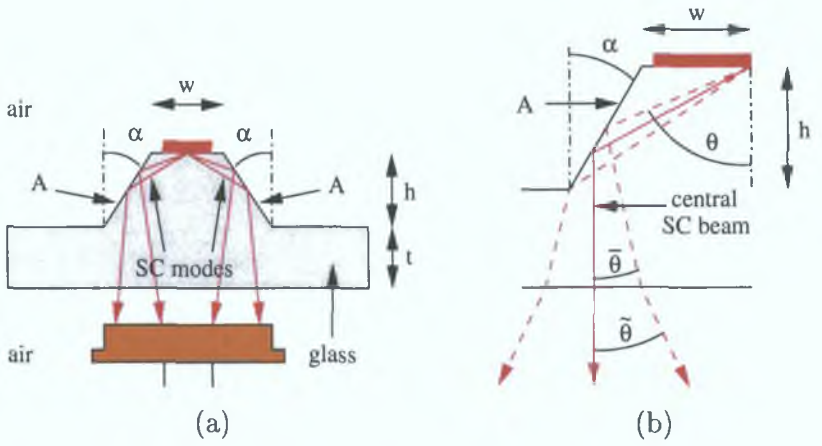

Figure 3.24: (a) Cross section of the configuration facilitating improved efficiency of the luminescence capture. The configuration employs a *frustrated cone* located at the top side of the substrate. The SC modes radiated from the luminescent spot are redirected towards the detector placed below the substrate by means of a total internal reflection at the interface A. (b) Detailed diagram of the design in (a). See text for further explanation.

As is shown in Fig. 3.16(a), the SC modes propagate in the glass substrate at angles $\theta \in \langle \theta_c^{as}, \theta_c^{ls} \rangle$, where $\theta_c^{as} = \arcsin(n_a/n_s) \approx 41.3°$ and $\theta_c^{ls} = \arcsin(n_l/n_s) \approx 70.7°$ are the critical angles of the air/substrate and layer/substrate interfaces, respectively. The choice of the tilt angle α can be based on various criteria. In this analysis, the requirement is that the *central* SC beam, i.e., the light corresponding to the SC modes propagating in the glass at an angle $\theta_{\text{centre}} \equiv (\theta_c^{as} + \theta_c^{ls})/2$, is redirected *straight down* upon total internal reflection from the interface A, as shown in Fig. 3.24(b).

Simple geometrical analysis implies that the angles θ and $\bar{\theta}$, i.e., the propagation angles of the light before and after the total internal reflection from the interface A, are related by

$$\bar{\theta} + \theta = 2\alpha. \tag{3.38}$$

Due to the fact that $\theta = \theta_{\text{centre}}$ and $\bar{\theta} = 0$ for the central SC beam, the tilt angle α can be calculated as

$$\alpha = \frac{1}{2}\theta_{\text{center}} = \frac{1}{4}(\theta_c^{as} + \theta_c^{ls}) \approx 28°. \tag{3.39}$$

Using this value of α, the beams corresponding to the SC modes propagating at angles θ_c^{as} and θ_c^{ls} before the total internal reflection at the interface A are propagating at angles $\bar{\theta}_c^{as} = \Delta\theta_c^{la}/2$ and $\bar{\theta}_c^{ls} = -\Delta\theta_c^{la}/2$, respectively, where

$$\Delta\bar{\theta}_c^{la} \equiv (\theta_c^{ls} - \theta_c^{as}) \approx 29.4°. \tag{3.40}$$

This means that the SC modes propagate within the angular range of

$$\bar{\theta} \in \left\langle -\frac{\Delta\bar{\theta}_c^{la}}{2}, \frac{\Delta\bar{\theta}_c^{la}}{2} \right\rangle \approx \langle -14.7°, 14.7° \rangle \tag{3.41}$$

immediately after the total internal reflection at the interface A.

When the refraction at the bottom interface of the substrate is considered, the SC beam propagating in the glass substrate at an angle $\bar{\theta}$ is found to be propagating in air below the

substrate at an angle $\tilde{\theta}$, as shown in Fig. 3.24(b). These angles are related by the Snell law, i.e.,

$$n_a \sin\tilde{\theta} = n_s \sin\bar{\theta}. \tag{3.42}$$

Consequently, the SC modes propagate in air below the substrate within the angular range of

$$\tilde{\theta} \in \left\langle -\frac{\Delta\tilde{\theta}_c^{la}}{2}, \frac{\Delta\tilde{\theta}_c^{la}}{2} \right\rangle \approx \langle -22.6°, 22.6° \rangle. \tag{3.43}$$

This implies that *all* the power carried by the SC modes can be captured by a detector whose numerical aperture corresponds to the cone angle of $\theta_{co} = 22.6°$, i.e., $\mathrm{NA} = \sin 22.6° \approx 0.38$. The schematic diagram of such a situation is shown in Fig. 3.25.

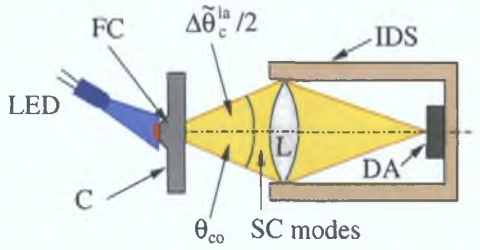

Figure 3.25: A schematic diagram of a sensor system in the configuration with improved luminescence capture efficiency. The sensor system employs an ideal detection system (IDS) consisting of a lens (L) and a detector array (DA). The sensor chip (C) contains the luminescent spot which is deposited on top of the frustrated cone, as shown in Fig. 3.24. The SC modes of the luminescence, which is excited by an LED, are redirected towards the detector in such a way that they propagate within the cone characterised by the cone angle $\Delta\tilde{\theta}_c^{la}/2$. The cone angle can be calculated from (3.40) and (3.42). The ideal detection system is characterised by the numerical aperture NA which is related to the cone angle θ_{co} by $\mathrm{NA} = \sin\theta_{co}$.

After the propagation characteristics of the luminescence have been found, it is possible to make a comparison between the luminescence capture efficiency of the conventional detection technique (see Figs. 3.19 and 3.20) and that of the improved configuration depicted in Fig. 3.24. In a similar way to the treatment in Sec. 3.3.1, the improved configuration is assumed to be incorporated in a sensor system employing an ideal detection system, as shown in Fig. 3.25.

Figure 3.26 shows the efficiency of the luminescence detection as a function of the numerical aperture of the ideal detection system. The dashed and dash-dotted lines correspond to the conventional technique employing detection of the luminescence radiated from the luminescent spot by means of the AT and ST modes, respectively. This technique was discussed in detail in Sec. 3.3.1 (see Figs. 3.19 and 3.20 in that section). The solid line corresponds to the configuration employing frustrated cones (see Figs. 3.24 and 3.25).

In the calculation, the values $n_s = 1.515$, $n_a = 1.0$, $n_l = 1.43$ $t_l = 0.5\lambda$ and $\alpha = 28°$ were considered. Furthermore, the transmittivity of the bottom substrate/air interface was assumed to be independent of the incident angle and equal to its value at the normal incidence, i.e., $T = 1 - |(n_s - n_a)/(n_s + n_a)|^2 \approx 96\,\%$.

As already mentioned in Sec. 3.3.1, the conventional detection technique can capture a maximum of approximately 15 % of the total emitted luminescence. However, this is possible

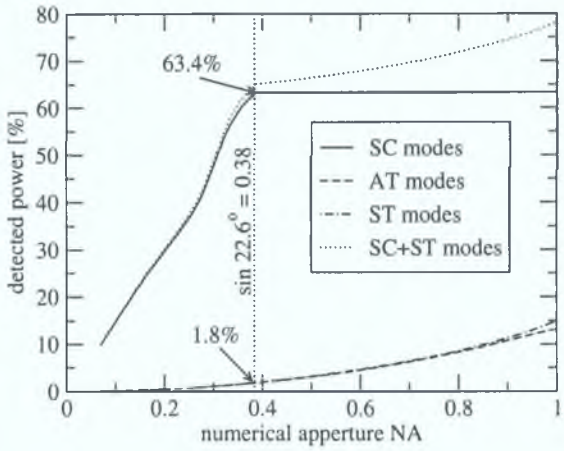

Figure 3.26: Fraction of the luminescence detected by an ideal detection system as a function of its numerical aperture NA. The dashed and dash-dotted lines correspond to the conventional detection technique, which is depicted in Fig. 3.19. The solid and dotted lines correspond to the improved detection technique, which is depicted in Fig. 3.25.

only with a detection system characterised by NA = 1. On the other hand, the detection system with NA $\approx$ 0.38 is able to detect approximately 63 % of the total luminescence radiated from the luminescent spot if the improved detection configuration is employed to redirect the SC modes towards the detector. This clearly represents a substantial improvement.

As can be seen from Fig. 3.26, the efficiency of the luminescence capture achieved by the improved configuration does not increase above 63 % for NA > 0.38. This is because only the SC modes are considered in the evaluation of the capture efficiency. In reality, however, the detector placed below the substrate would also detect the ST modes in addition to the SC modes. Consequently, the capture efficiency of such a system would continue increasing above NA = 0.38. This is depicted by the dotted curve, which is obtained as a sum of the solid (SC modes) and dash-dotted (ST modes) curves.

When the luminescence capture efficiency of the conventional detection technique at NA $\approx$ 0.38 is evaluated, a value of only $\approx$ 1.8 % is found (see Fig. 3.26). This means that for this given value of NA, the improved configuration provides approximately 35-fold (!) increase in the luminescence capture efficiency. This remarkably large increase makes the configuration very attractive, despite the fact that it is not entirely compatible with the planar architecture.

In the design of the configuration with improved luminescence capture efficiency, the tilt angle α plays a fundamental role. As mentioned earlier, its evaluation can be based on various criteria. The criterion employed in this analysis leads to α given by (3.39). Once this angle is determined, the values of the other parameters characterising the configuration, such as w, h and t (see Fig. 3.24), can be found from simple geometry. Subsequently, the values can be proportionately scaled up or down. The scaling factor is primarily determined by the target application and the technology employed in the fabrication process.

If the parameters characterising the properties of the substrate, luminescent spot or the environment covering the spot are different, the geometrical parameters of the configuration with improved luminescence capture efficiency would change. However, these parameters can easily be found by adopting the above analysis to such a system. Following the same

steps as those discussed above, the tilt angle (3.39) together with the angular range (3.43) can be found. Furthermore, the dependence of the luminescence capture efficiency on NA, which would be similar to that shown in Fig. 3.26, can be evaluated in order to determine the optimum design parameters.

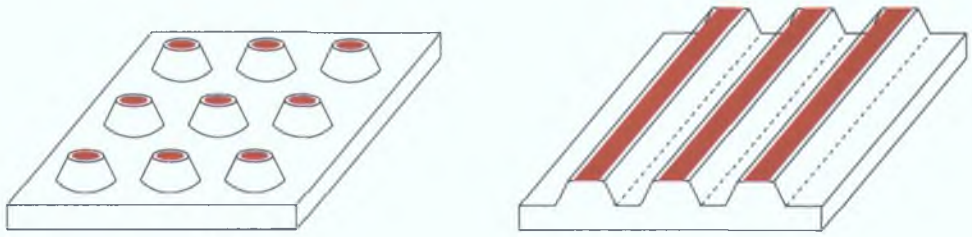

Figure 3.27: Schematic diagrams of sensor chips with an improved luminescence capture efficiency.

Last but not least, it is important to mention that the schematic diagram in Fig. 3.24 shows only the cross section of the configuration with improved luminescence capture efficiency. The real design would however involve a 3D structure. In this context, there are two feasible options. The first option could employ an axially symmetric structures, i.e., the frustrated cones analysed above. Figure 3.27(a) shows an example of a planar substrate containing a 2D array of frustrated cones with luminescent spots deposited on the top of the frustrated cones. The second option could employ a grove-like pattern, as shown in Fig. 3.27(b). This design could be used in applications where linear micro-channels are employed to facilitate the delivery of the analyte. As follows from the above analysis, these platforms should provide a considerable improvement in the efficiency of the luminescence detection and thus be attractive in practical applications.

3.4 Collection of surface generated luminescence

As discussed earlier in Sec. 1.4, the detection of surface generated luminescence is particularly important in biosensors in order to discriminate between surface-bound and bulk molecules which are luminescently labelled. The theoretical and numerical analyses of the properties of the surface-generated luminescence were presented in Sec. 3.2.6. This section provides technical details of a novel detection technique which enables detection of the luminescence originating from a region adjacent to the substrate interface and excited by a direct illumination. The thickness of the region of interest, which is in the order of the luminescence wavelength λ, can be tailored according to the needs of a particular application.

In the following analysis, the substrate is considered to be made of glass ($n_s = 1.515$) and the environment containing the luminescent species is water ($n_w = 1.33$). Similar conclusions can be, however, drawn for any other set of parameters.

It was concluded in Sec. 3.2.6 that the detection of the luminescence originating from a thin layer adjacent to the (glass) substrate, i.e., the surface layer, can be achieved by measuring a *specific fraction* of the luminescence, in particular that propagating in the (glass) substrate *above* the threshold angle $\theta_{\rm tr}$. This conclusion is demonstrated in Fig. 3.14(b) where the difference between the angular profiles of the luminescence originating from the surface

layer of thickness $t_s = \lambda$ (solid line) and the bulk layer of thickness $t_b = 3\lambda$ (dash-dotted line) are clearly visible.

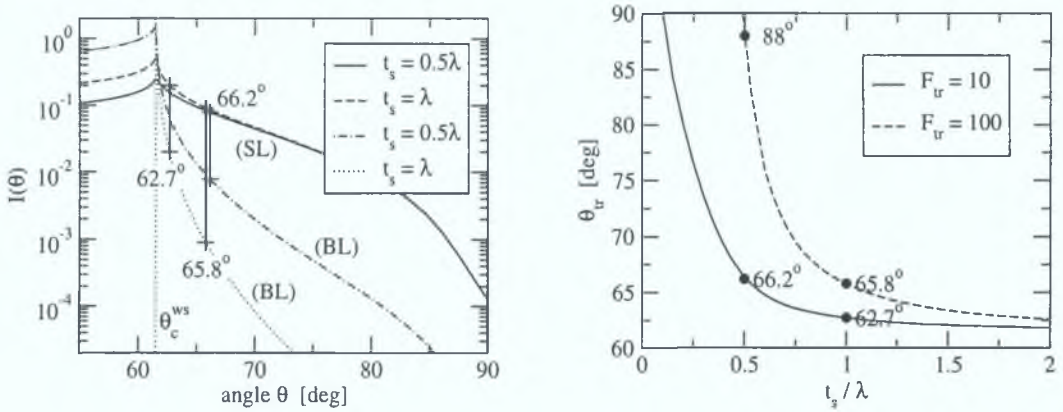

(a) (b)

Figure 3.28: (a) Angular distributions of the luminescence radiated by a 2-layer system depicted in Fig. 3.13. The curves denoted by (BL) and (SL) correspond to the situations where the luminescence originates from the bulk and surface layers, i.e., to the situations shown in Fig. 3.13(a) and Fig. 3.13(b), respectively. (b) Threshold angle $\theta_{\rm tr}$ as a function of the surface layer thickness t_s for two different values of the threshold factor $F_{\rm tr}$.

From the application point of view, it is important to know the relation between the *thickness* t_s of the surface layer from which the luminescence originates and the *threshold angle* $\theta_{\rm tr}$ above which the luminescence should be observed. Figure 3.28(a) shows the angular distributions of the luminescence radiated from a 2-layer system depicted in Fig. 3.13. The distributions are plotted for two values of the surface layer thickness, namely $t_s = 0.5\lambda$ and $t_s = \lambda$, and for one value of the bulk layer thickness, namely $t_b = 3\lambda$. In order to see the relative relation between the various curves, the y-axis employs a logarithmic scale.

From Fig. (3.28)(a), it can be seen that there is a significant difference between the contributions to the luminescence originating from the surface and bulk layers, particularly above the critical angle θ_c^{ws} of the water/substrate (glass) interface. While the intensity corresponding to the bulk layer decreases abruptly for $\theta > \theta_c^{ws}$, this decrease is not so rapid for the intensity corresponding to the surface layer. Furthermore, the *rate* of this decrease varies with the thickness of the surface layer, which is the fundamental feature that can be exploited for determining the relation between t_s and $\theta_{\rm tr}$.

The threshold angle $\theta_{\rm tr}$ can be defined as the angle above which the ratio between the intensity of the luminescence originating from the surface layer (I_s) and that originating from the bulk layer (I_b) is greater than a specified threshold factor $F_{\rm tr}$. This definition of $\theta_{\rm tr}$ can be formally expressed as

$$\frac{I_s(\theta_{\rm tr})}{I_b(\theta_{\rm tr})} > F_{\rm tr}. \tag{3.44}$$

In a real application, the intensity of luminescence is always characterised by some level of uncertainty due to the electronic and other sources of noise. Therefore, the value of $\theta_{\rm tr}$ can be chosen in such a way that $I_b(\theta_{\rm tr})$ in (3.44) corresponds to this noise level. Consequently, the definition (3.44) is simply a formal expression of the requirement that the signal-to-noise

ratio of the measurement of the luminescence originating from the surface layer be greater than some specified value $F_{\rm tr}$. This also justifies the definition of $\theta_{\rm tr}$ given by (3.44).

It can be seen from Fig. 3.28(a) that the intensity of the luminescence originating from the surface layer of thickness $t_s = \lambda$ is 10 times greater at $\theta_{\rm tr} = 62.7°$ and 100 times greater at $\theta_{\rm tr} = 65.8°$ than the intensity of the luminescence originating from the bulk layer. Therefore, by measuring the luminescence at angles $\theta \geq 62.7°$ and $\theta \geq 65.8°$, the certainty that only the luminescence originating from the surface layer of thickness $t_s = \lambda$ is measured is 10 and 100, respectively.

As follows from the curves in Fig. 3.28(a) calculated for a different value of t_s, the value of the threshold angle $\theta_{\rm tr}$ varies with the desired thickness of the surface layer. For example, $\theta_{\rm tr} = 62.7°$ for $t_s = \lambda$ and $F_{\rm tr} = 10$ but it increases to $\theta_{\rm tr} = 66.2°$ for $t_s = 0.5\lambda$ and $F_{\rm tr} = 10$. Therefore, from the practical application point of view, it is necessary to establish the relation between t_s and the corresponding value of $\theta_{\rm tr}$. Understandably, this relation is parametrised by the threshold factor $F_{\rm tr}$.

An example of $\theta_{\rm tr}$ as a function of t_s is shown in Fig. 3.28(b), where the solid and dashed lines correspond to $F_{\rm tr} = 10$ and $F_{\rm tr} = 100$, respectively. The graph implies that, for example, if an application requires that only the luminescence originating from a surface layer of thickness $t_s = 0.5\lambda$ and $t_s = \lambda$ be detected with a certainty characterised by $F_{\rm tr} = 10$, the detector should measure only the luminescence radiated at angles greater than $\theta_{\rm tr} = 66.2°$ and $\theta_{\rm tr} = 62.7°$, respectively. These angles increase to approximately 88° and 65.8°, respectively, if a greater level of certainly, namely $F_{\rm tr} = 100$, is required.

The graph in Fig. 3.28(b) also shows that there are some limits with regard to the minimum thickness of the surface layer that can be resolved by this method. For example, the luminescence originating from a surface layer thinner than approximately 0.2λ *cannot* be detected with a certainty level of $F_{\rm tr} \geq 10$, as indicated by the solid line which is not defined for $t_s \lesssim 0.2\lambda$. This minimum thickness is increased to $\approx 0.5\lambda$ if the certainty level is increased to 100. This feature is related to the fact that the penetration depth of the evanescent field is greater than zero even for an incident angle approaching or equal to 90°.

The graph also shows that if the surface region of thickness not exceeding $t_s = 2\lambda$ is of interest, it can be probed with a high certainty ($F_{\rm tr} = 100$) by measuring the luminescence radiated above approximately 65°. This value is sufficiently small to be accessible by a simple experimental setup, such as that proposed below.

It is important to emphasize that the *excitation* of luminescence was *not* mentioned in the above analysis at all. This is because the angular properties of the emitted luminescence, which are exploited in this technique, are independent of the way how the luminescent molecules are excited. Therefore, it is possible to use *direct* illumination for *efficient* excitation of the molecules while detecting the luminescence originating specifically from a close vicinity of the surface. This is what makes this technique very attractive.

Experimental setup for collection of surface-generated luminescence

Following the above numerical analysis, experimental configurations facilitating the detection of a surface-generated luminescence can be proposed. The schematic diagrams of two possible setups are shown in Fig. 3.29.

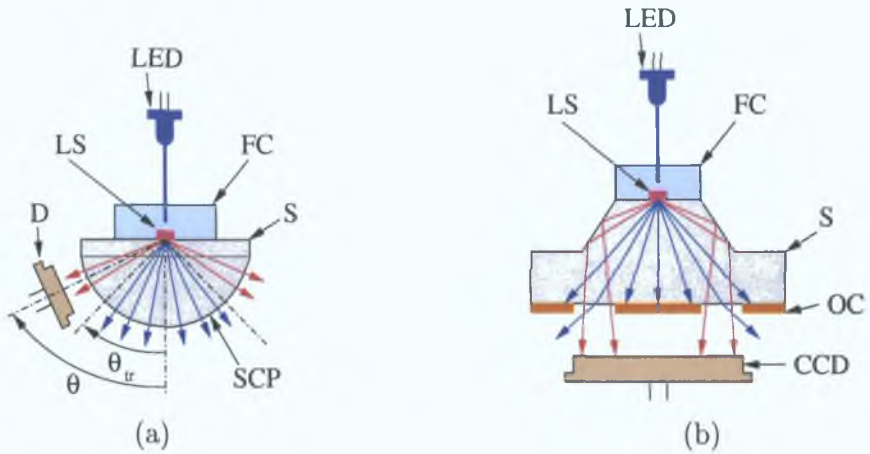

Figure 3.29: Schematic diagrams of experimental configurations for measuring the surface-generated luminescence employing direct illumination for the luminescence detection. The configurations comprise the following parts: (a) substrate (S), semi-cylindrical prism (SCP), detector (D), flow-cell (FC), luminescent solution (LS), light-emitting diode (LED). (b) substrate (S) with a modified top interface (frustrated cone), CCD detector array, flow-cell (FC), luminescent solution (LS), light-emitting diode (LED), opaque coatings (OC). In both diagrams, the surface-generated luminescence is depicted by the red arrows while the blue arrows depict the bulk-generated luminescence.

In the first setup, which is shown in Fig. 3.29(a), the substrate, above which the luminescent solution can flow, is attached to a semi-cylindrical prism made from the same material as the substrate, e.g., glass. This way, the luminescence propagating in the substrate above the threshold angle θ_{tr}, i.e., the surface-generated luminescence, can be detected by a detector positioned at $\theta > \theta_{\mathrm{tr}}$, as shown in Fig. 3.29(a). The detector in this setup can be either a linear detector or a photodiode with a small detection area. Luminescence is excited by an LED placed above the luminescent solution, i.e., by direct illumination.

The second setup, which is depicted in Fig. 3.29(b), comprises a substrate whose top interface is modified in a manner similar to that shown in Fig. 3.24. In this case, the surface-generated luminescence (depicted by the red arrows) is imaged to an area at the detector which is *spatially separated* from the area where the luminescence generated by the bulk layer (depicted by the blue arrows) is imaged to. Therefore, measuring the luminescence below the substrate by a two-dimensional detector array, such as a CCD camera, enables one to distinguish between the surface and bulk-generated luminescence by acquiring the signal from different parts of the image. To prevent the imaging of the bulk-generated luminescence to the same areas on the detector where the surface-generated luminescence is imaged, opaque coatings can be placed at the bottom interface of the substrate to block out this undesirable luminescence, as shown in Fig. 3.29(b). Although this design is feasible from the theoretical point of view, its practical realisation could become rather elaborate.

3.5 Conclusion

In this chapter, a rigorous electromagnetic theory was developed which is suitable for the description of the angular anisotropy of radiation of molecules embedded in an arbitrary multilayer system. The theory was applied to two main areas.

Firstly, the angular anisotropy of luminescence emitted from a thin luminescent layer deposited on a higher refractive index substrate was studied. It was found that, with respect to the character of the field inside the luminescent layer and in the surrounding media, the modes of the electromagnetic field radiated by a thin film can be divided into four categories. One category of the modes, the so-called substrate-confined (SC) modes, was found to be particularly attractive for luminescence-based sensing applications. These modes propagate in the substrate at angles greater than the critical angle of the environment/substrate interface and lower than the critical angle of the luminescent layer/substrate interface. Their attractiveness is derived from the fact that they carry a relatively large proportion of the emitted optical power in a relatively narrow angular range. (For example, the fraction is more than 60 % and the angular width is approximately 30° if the substrate is glass and the environment is air.)

Even though these modes are attractive for sensing applications, they are not exploited in conventional thin film-based sensor systems which typically employ detection of luminescence directly above or below a planar substrate on top of which the luminescent layer is deposited. This is mainly due to the fact that these modes are trapped in the planar substrate (hence the name) and thus cannot be directly detected unless special configurations are employed. Based on the theory, a number of such configurations were proposed. They provide efficient detection of the SC modes and thus could be used in order to improve the luminescence capture efficiency. One particular configuration that provides the most benefits was studied in more detail. This configuration employs frustrated cones on top of which the luminescent layer is deposited. It was found that, for certain values of parameters characterising the structure and the detection system, the collection of luminescence could be improved by as much as 35 times in comparison with the collection efficiency that can be achieved using conventional techniques.

The theory was also applied to the area where the luminescence of interest is that generated specifically by the molecules located in close vicinity to the surface. In particular, a detailed theoretical analysis was presented which described the realisation of a novel method for the detection of such luminescence. In contrast to the conventional method that employs evanescent-wave excitation, this method enables one to use *direct* illumination to excite the luminescent molecules. The distinction between the luminescence radiated by molecules located in the bulk and near the surface is achieved by the measurement and appropriate treatment of the angular profile of luminescence intensity. In particular, by measuring the emitted luminescence *above* a certain threshold angle θ_{tr}, only the luminescence originating from molecules located closer to the surface than some corresponding distance d_{tr} is detected. Taking into account that the excitation by direct illumination is much more effective than that provided by the evanescent-wave excitation technique, this new method can be particularly attractive in immunosensing applications.

3.6 Bibliography for Chapter 3

[1] T. Liebermann and W. Knoll. Surface-plasmon field-enhanced fluorescence spectroscopy. *Colloids and Surfaces*, A: Physicochemical and Engineering Aspects 171:115–130, 2000.

[2] S. Blair and Y. Chen. Resonant-enhanced evanescent-wave fluorescence biosensing with cylindrical optical cavities. *Applied Optics*, 40(4):570–581, 2001.

[3] C. Mayer, R. Verheijen, N. Stich, and T. G. M. Schalkhammer. Food-allergen assays on chip based on metal nano-cluster resonance. In Raymond P. Mariella and Dan V. Nicolau, editors, *Proceedings of SPIE*, volume 4265, pages 134–141, 2001.

[4] J. R. Lakowicz, I. Gryczynski, Y. Shen, J. Malicka, and Z. Gryczynski. Intensified fluorescence. *Photonics Spectra*, pages 96–104, October 2001.

[5] Jörg Enderlein, Thomas Ruckstuhl, and Stefan Seeger. Highly efficient optical detection of surface-generated fluorescence. *Applied Optics*, 38(4):724–732, February 1999.

[6] El-Hang Lee, R.E. Benner, J.B. Fenn, and R.K. Chang. Angular distribution of fluorescence from liquids and monodispersed spheres by evanescent wave excitation. *Applied Optics*, 18(6):862–868, March 1979.

[7] W.Lukosz and R. E. Kunz. New method for determining refractive index and thickness of fluorescent thin films. *Optics Communications*, 31(3):251–256, December 1979.

[8] R. E. Kunz and W. Lukosz. Changes in fluorescence lifetimes induced by variable optical environments. *Physical Review B*, 21(10):4814–4828, 1980.

[9] P. N. Zeller, G. Voirin, and R. E. Kunz. Single-pad scheme for integrated optical fluorescence sensing. *Biosensors and Bioelectronics*, 15:591–595, 2000.

[10] G.W. Ford and W.H. Weber. Electromagnetic interactions of molecules with metal surfaces. *Physics Reports (Review Section of Physics Letters)*, 113(4):195–287, 1984.

[11] R.R. Chance, A. Prock, and R. Silbey. Molecular fluorescence and energy transfer near interfaces. *Adv. Chem. Phys.*, 37:1–65, 1978.

[12] L.D. Landau and E.M. Lifschitz. *Electrodynamics of Continuous Media.* Pergamon Press, Oxford, 1960.

[13] M. Born and E. Wolf. *Principles of Optics.* Pergamon, Oxford, 1959.

[14] `http://www.physics.dcu.ie/OSL/`. Webpage of the Optical Sensors Laboratory, Dublin City University.

[15] B. D. MacCraith, C. M. McDonagh, G. O'Keffe, A. K. McEvoy, T. Butler, and F. R. Sheridan. Sol-gel coatings for optical chemical sensors and biosensors. *Sensors and Actuators*, B 29:51–57, 1995.

[16] C. McDonagh, B.D. MacCraith, and A.K. McEvoy. Tailoring of sol-gel films for optical sensing of oxygen in gas and aqueous phase. *Anal. Chem.*, 70(1):45–50, 1998.

[17] C. McDonagh, C. Kolle, A.K. McEvoy, D. Dowling, A. A. Cafolla, S. J. Cullen, and B. D. MacCraith. Phase fluorometric oxygen sensor. *Sensors and Actuators B-Chem*, 74(1–3):123–129, April 2001.

[18] B. D. MacCraith, L. Polerecky, A. M. Doyle, C. Burke, A. K. McEvoy, and C. M. McDonagh. Optical waveguide sensing platforms based on sol-gel-derived materials.

Presented at Photonics West SPIE conference No. 3943, San Jose, CA, January 2000. Private communication.

[19] B. D. MacCraith, C. von Bültzingslöwen, A. K. McEvoy, C. McDonagh, and L. Polerecky. Sol-gel waveguide fluorescence sensors for food packaging. In *Oral presentation at PITTCON 2000*, 12-17 March 2000.

[20] B. D. MacCraith, C. von Bültzingslöwen, A. K. McEvoy, C. McDonagh, and L. Polerecky. Sol-gel waveguide fluorescence sensors for food packaging. In *Oral presentation at Photonics East*, Boston, Massachusetts, USA, 5–8 November 2000.

[21] J.-F. Gouin, A. Doyle, and B.D. MacCraith. Fluorescence capture by planar waveguide as platform for optical sensors. *Electronics Letters*, 34(17):1685–1687, August 1998.

[22] B. D. MacCraith, S. Aubonnet, H. Barry, C. von Bültzingslöwen, J. M. Sabattié, and C. S. Burke. Optical chemical sensor systems based on photosensitive hybrid sol-gel waveguides. In *Poster presentation at 11th International workshop on glasses, ceramics, hybrids and nano-composites from gels*, Padova, Italy, September 16–21 2001.

[23] C. D. Geddes, P. Douglas, C. P. Moore, T. J. Wear, and P. L. Egerton. A compact optical flow cell for use in acqueous halide determination. *Meas. Sci. Technol*, 10:N34–N37, 1999.

[24] M. E. Lippitsch, S. Draxler, and D. Kieslinger. Luminiscence life-time based sensing: new materials, new devices. *Sensors and Actuators*, B 38–39(1–3):96–102, 1997.

[25] Y. Zhou, P. J. Laybourn, J. V. Magill, and R. M. De La Rue. An evanescent fluorescence biosensor using ion-exchanged buried waveguides and the enhancement of peak fluorescence. *Biosensors and Bioelectronics*, 6(7):595–607, 1991.

[26] M. Pawlak, E. Grell, E. Schick, D. Anselmetti, and M. Ehrat. Functional immobilization of biomembrane fragments on planar waveguides for the investigation of side-directed ligand binding by surface-confined fluorescence. *Faraday Discussions*, 111:273–288, 1998. discussion 331–343.

[27] Y. Zhao, I. Avruthsky, and B. Li. Optical coupling between monocrystalline colloidal crystals and a planar waveguide. *Applied Physics Letters*, 75(23):3596–3598, 1999.

Chapter 4

Absorption-based optical chemical sensors—experimental work

This chapter presents an experimental investigation of the theoretical predictions discussed in Chapter 2. Firstly, the angular dependence of sensitivity of an absorption-based sensor is verified experimentally using a multimode waveguide sensing platform comprising a glass slide coated with a thin sensing film. Based on the theoretical analysis of optimised sensing conditions, a prototype LED-based sensor system was designed and fabricated. Technical details of the compact and portable sensor unit are presented along with the results displaying the sensor performance using gaseous ammonia and pH as the analytes.

4.1 Angular distribution of sensor sensitivity

In this section, the angular distribution of the sensitivity of an absorption-based optical chemical sensor is studied experimentally. This experimental work was conducted in order to investigate the theoretical predictions discussed in Secs. 2.2.7–2.2.9. Firstly, the preparation of the sensor element which was used in the experiments is briefly described. Then the description of the experimental apparatus is provided. Finally, the experimental results are presented and discussed in detail.

4.1.1 Preparation of the sensor element

Throughout the experimental work presented here, the multimode planar waveguide platform, which was thoroughly studied in Chapter 2, consisted of a standard glass microscope slide. The refractive index of the glass slide at the analytical wavelength was $n_g = 1.515$. The thickness of the slide was approximately 1 mm, which guarantees a highly multimode character of the planar waveguide.

The sensing layer was prepared using a sol-gel technique which is well established in the laboratory where this research was conducted [1, 2, 3]. A typical sol was prepared as described in the literature [4] and was doped with Bromocresol Purple (BCP). The composition and steps of preparation of the sol are summarised in Table 4.1. The thin sensing layer was deposited by dip-coating the sol on one side of the glass slide at a speed of 1 mm/s, which

dissolve 30 mg of BCP in 4 g of ethanol and stir for 10 mins
add 2 g pH1 HCl dropwise and stir for 10 mins
add 6 g TEOS dropwise and stir for 1 hour

Table 4.1: Recipe for the preparation of the BCP-doped sol. See Appendix A for the explanation of abbreviations used.

produced a uniform layer of thickness $t_s \approx 0.4\,\mu$m. Following this, the film was oven-dried at 70°C for 17 hours.

BCP is a pH indicator dye with an absorption band displaying a maximum at ≈ 580 nm corresponding to its deprotonated state. The magnitude of this peak varies with the pH of the environment. This is shown in Fig. 4.1, where the dash-dotted and dashed lines represent the absorption spectra of the BCP-doped sol-gel film in presence (2 ppm) and absence (0 ppm) of ammonia, respectively.

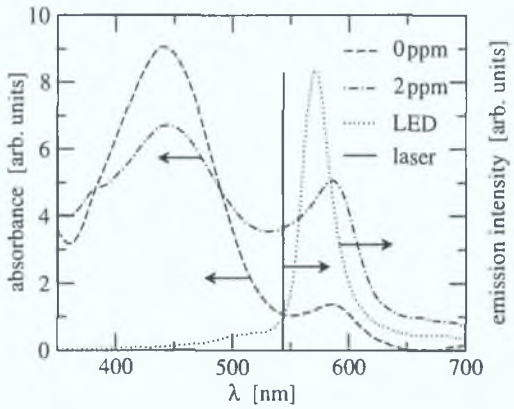

Figure 4.1: Absorption spectra of a BCP-doped sol-gel film in presence (2 ppm, dash-dotted line) and absence (0 ppm, dashed line) of ammonia. The solid and dotted lines correspond to the emission spectra of the green He-Ne laser and LED, respectively.

4.1.2 Laser-based experimental apparatus

The experimental apparatus which was used to measure the angular distribution of sensitivity (see Sec. 2.2.7) is shown in Fig. 4.2.

The core element of the experimental apparatus was the semi-cylindrical prism. The sensing element described in Sec. 4.1.1 was in optical contact with the prism via an index-matching immersion liquid. The dimensions of the prism were designed to be such that the addition of the glass slide resulted in a perfect semi-cylinder. This element was then incorporated into a flow cell which enabled a controlled flow of the gaseous analyte above the sensing layer.

The light interrogating the sensing layer was provided by the green He-Ne laser ($\lambda = 543.5$ nm). The light was s-polarised. The beam was passed through a chopper which modulated its intensity at a frequency of approximately 2 kHz. Subsequently, the beam was incident on a beam splitter (BS) which provided reference and signal beams. The reference beam was detected by the detector D1 while the signal beam was detected by the detector D2

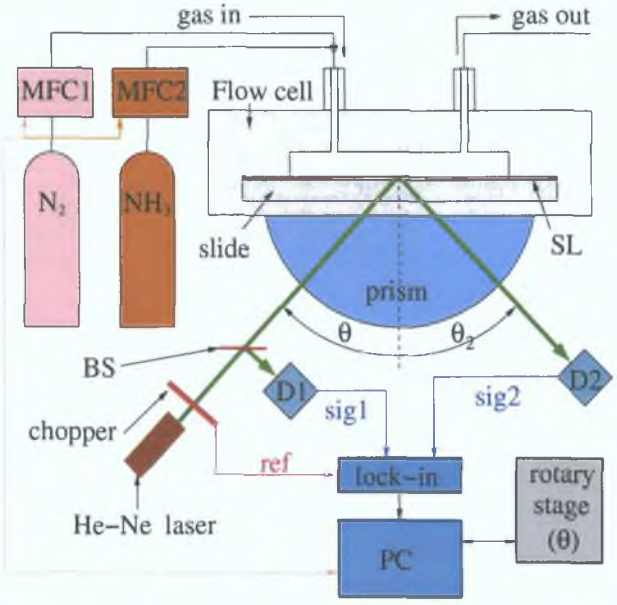

Figure 4.2: A schematic diagram of the laser-based experimental apparatus for measuring the angular distribution of the sensor sensitivity. In order to facilitate the interrogation of sensing layer (SL) by the laser beam at incident angles greater than the critical angle of the air/glass interface, the glass slide supporting the sensing layer was attached to a semi-cylindrical prism. See text for further description of the system.

after reflection from the sensing element.

Detection of the light intensity was provided by two lock-in amplifiers (Stanford Research Systems, SR510) which used the signal from the light chopper as a reference (ref). Using this technique, the signals sig1 and sig2 corresponding to the light intensity entering the detectors D1 and D2, respectively, could be determined independently of the ambient light intensity.

The system consisting of the semi-cylindrical prism, sensing element and the flow cell was mounted on a high-precision rotary stage (Physik Instrumente, M-038, unidirectional repeatability 20 μrad) which facilitated variation of the incident angle θ. This angle could be varied within the angular range of $\theta \in \langle 20°, 75° \rangle$. The upper limit of 75° was due to the restrictions determined by the dimensions of the flow cell and the prism. The detector D2 was mounted onto an independently rotating arm to facilitate detection of the reflected laser beam whose angular position θ_2 followed the incident angle θ, i.e., $\theta_2 = \theta$.

Gaseous ammonia (NH_3) was the analyte chosen for the experiments. A controlled mixture of NH_3 in N_2 was provided by mass flow controllers—MFC1 for N_2 (5 l/min) and MFC2 for 1 % NH_3 in N_2 (5 sccm). By using these controllers, the relative ratio of NH_3 in N_2 could be varied between $c_A = 0$ ppm and $c_A = 20$ ppm.

The entire experiment was controlled by a personal computer (PC) via a data acquisition card (Bytronics, MBIBM3). The analogue outputs of the card controlled the mass flow controllers MFC1 and MFC2. The digital outputs of the card controlled the movement of the detector D2. The DC analogue signals corresponding to sig1 and sig2 were converted to the digital values using the 12-bit analog-to-digital converters on the card. Rotation of the high-precision rotary stage was controlled by the PC via the PIC842 card supplied by the

manufacturer.

The program controlling the experiment was written in `LabView`. The screenshot of the program is shown in Fig. 4.3. The algorithm implemented in the program proceeded as follows:

1. the positions of the rotary stage and the detector D2 were set to the initial values and the concentration of NH_3 in N_2 was set to 0 ppm;
2. 2000 acquisitions of the signals sig1 and sig2 were made and the mean values together with the standard deviations calculated;
3. the values of the incident angle, the mean values and the standard deviations of the signals were appended to the output file;
4. the rotary stage with the semi-cylinder, sensing element and flow cell was rotated by $\Delta\theta = 2°$ and the position of the detector D2 was changed by $2\Delta\theta = 4°$;
5. steps 2–4 were repeated until the maximum value of the incident angle was reached;
6. steps 1–5 were repeated for the concentration of NH_3 in N_2 equal to 2 ppm.

After the experimental data were acquired, the reflectivities R_0 and R_2 were calculated from the values stored in the output file using the formula $R_c = \mathrm{sig2}_c/\mathrm{sig1}_c$, where $c = 0$ and $c = 2$ for the concentration of NH_3 in N_2 equal to 0 ppm and 2 ppm, respectively. This way, possible variations in the intensity of the laser beam were referenced out.

4.1.3 Experimental data

An example of the data measured by the experimental apparatus described in Sec. 4.1.2 is shown in Fig. 4.4. The graph (a) shows the angular distribution of reflectivity corresponding to 0 ppm (R_0) and 2 ppm (R_2) of NH_3 in N_2. The graph (b) shows the corresponding sensitivity calculated as $S = |R_2 - R_0|$. The data in the graph (a) were fitted using the expression (2.61) for reflectivity. The corresponding fitting parameters are listed in Table 4.2.

As can be seen from Fig. 4.4, the agreement between the experimental and theoretical data is excellent. The thickness of the sensing layer was found to be $t_s = (0.40 \pm 0.01)\,\mu$m. Both the normalisation factor (i.e., the ratio between the experimental and theoretical data) and the thickness of the sensing layer were found to be the same for both analyte concentrations. This confirms reliability of the experimental data as well as the fitting procedure. Table 4.2 suggests, however, that the real part of the refractive index of the sensing layer changed from $n_{s0} = 1.420 \pm 0.002$ to $n_{s2} = 1.450 \pm 0.002$ when the concentration of NH_3 in N_2 changed from 0 ppm to 2 ppm, which is a rather significant change. This means that the analyte did not change only the absorption properties (determined by the imaginary part of the refractive index) but also the optical density of the BCP-doped sol-gel film.

The experimental data in Fig. 4.4(b) show a distinct peak in sensitivity at the angle of incidence equal to $\theta = \theta_{\mathrm{opt}} \approx 66°$, as predicted by the theory. However, the enhancement with respect to the sensitivity that can be achieved in the configuration employing evanescent-wave absorption (i.e., by means of the interrogation at incident angles $\theta > \theta_c^{sg} =$

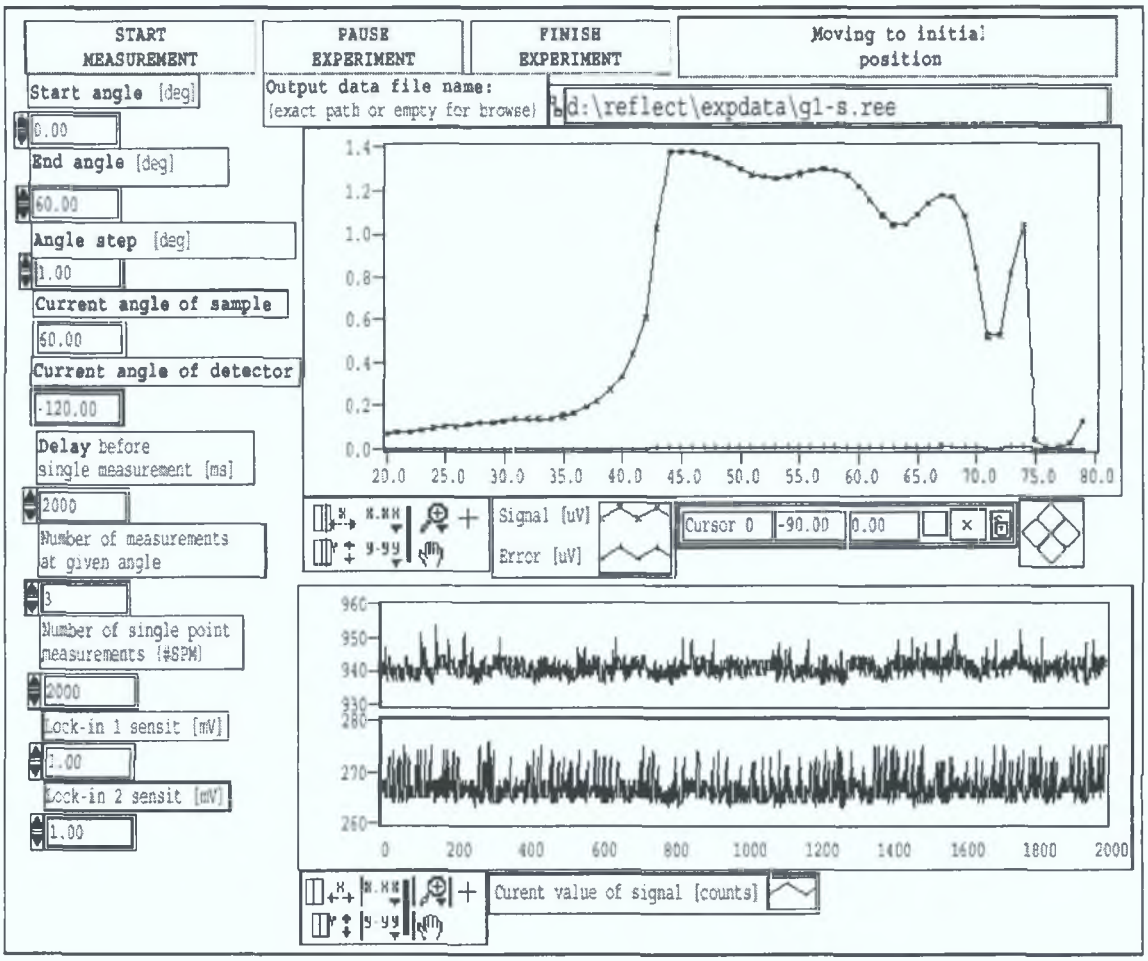

Figure 4.3: A screenshot of the LabView program controlling the experiment measuring the angular distribution of sensitivity of the absorption-based optical sensor system depicted in Fig. 4.2.

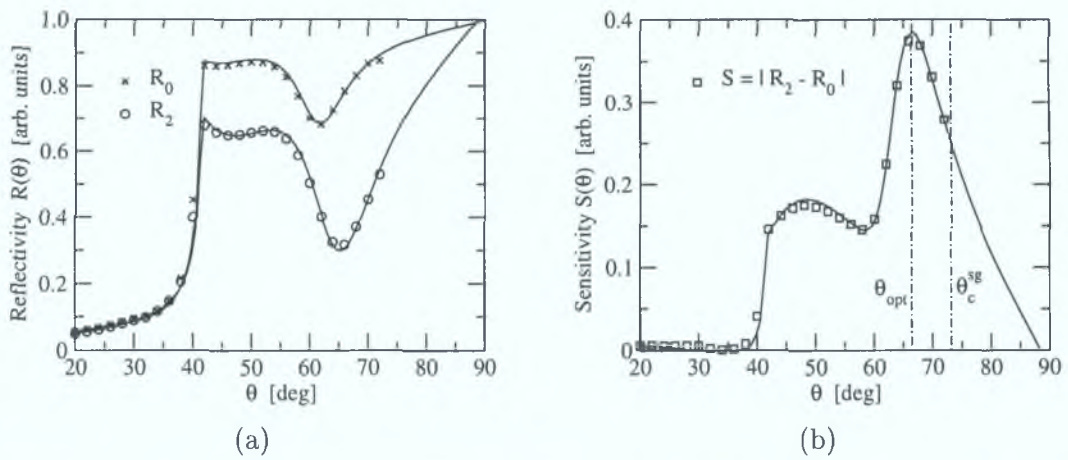

Figure 4.4: (a) Experimental data of reflectivity as a function of the incident angle θ. The values denoted as R_0 and R_2 correspond to the concentrations 0 ppm and 2 ppm of NH_3 in N_2, respectively. (b) Experimental data of sensitivity as a function of the incident angle θ obtained from the data in the graph (a) by $S = |R_2 - R_0|$. The solid lines represent the theoretical fit.

parameter	fit of R_0 (0 ppm)	fit of R_2 (2 ppm)
n_s	1.420 ± 0.002	1.450 ± 0.002
κ_s	0.0043 ± 0.0001	0.0130 ± 0.0003
t_s [μm]	0.40 ± 0.01	0.40 ± 0.01
normalisation factor	0.80 ± 0.01	0.80 ± 0.01
parameter	fit of $S = \lvert R_2 - R_0 \rvert$	
interrogation angle θ_{opt}	$66° \pm 1°$	

Table 4.2: Parameters of the sensing layer obtained from the fit of the experimental data in Fig. 4.4 by a function given by Eq. (2.61).

arcsin(1.45/1.515) $\approx 73°$) is not very significant. The reason for this is two-fold. Firstly, it is due to a relatively small thickness of the sol-gel layer for which the peak in sensitivity is not so pronounced (see Fig. 2.14). Secondly, it is due to a relatively large value of the extinction coefficient of the sol-gel layer, as discussed below.

Table 4.2 shows that both the absolute value and the relative change of the extinction coefficient of the BCP-doped sol-gel layer are relatively large ($\kappa_{s0} = 0.0043$, $\kappa_{s2} = 0.013$, $\Delta\kappa_s \equiv \kappa_{s2} - \kappa_{s0} \approx 0.009$). This means that the BCP-doped sol-gel in the composition specified in Sec. 4.1.1 provides a large value of sensitivity even in a configuration employing a single reflection. Although this may be advantageous in sensor systems where only a *single-reflection configuration* is required, it has an important negative drawback when interrogation by means of multiple reflections is considered.

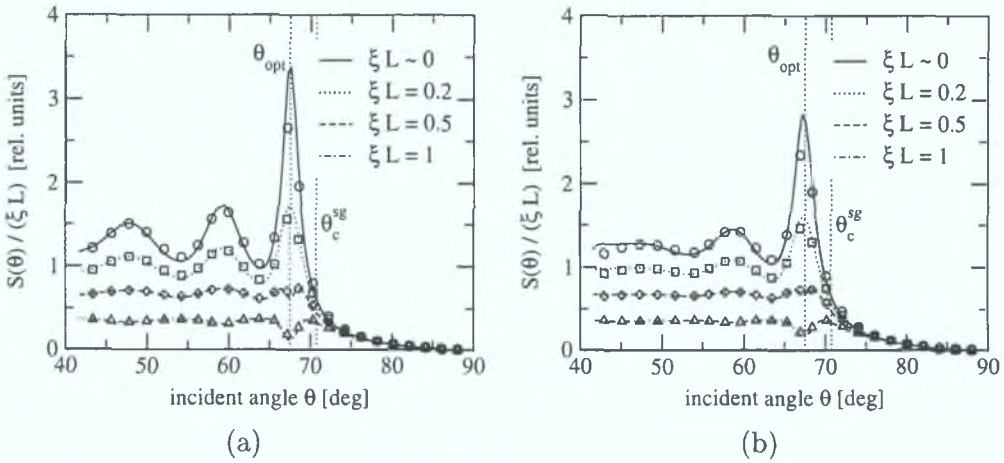

Figure 4.5: Distributions of the values of sensitivity S among the guided modes of the waveguide structure. To facilitate the easy viewing of the graph, it has been reproduced here. For a more detailed description, see Fig. 2.9 in Chapter 2.

Due to a large absolute value of the extinction coefficient, the attenuation of the light reflected from the sol-gel film is large (reflectivity in the order of approximately 0.5, as shown in Fig. 4.4(a)). Consequently, the effect of multiple reflections is not only a decrease in the absolute value of the intensity of light undergoing the multiple reflections, but also a *decrease in sensitivity*. This effect is demonstrated in Fig. 4.5 (reproduction of Fig. 2.9) where the sensitivity at the optimum angle θ_{opt} decreases with the increasing value of the

parameter ξL. It is important to realise that this parameter increases not only with the interaction length L but also with the extinction coefficient κ_s of the sol-gel (sensing) layer (see Eqs. (2.35) and (2.56)). For some critical value of the interaction length L_c ($L_c \approx 0.5/\xi$), the sensitivity at the angle θ_{opt} no longer corresponds to the maximum sensitivity, as shown by the dashed line (the line for $\xi L = 0.5$) in Fig. 4.5. Furthermore, the sensitivity provided by the evanescent-wave absorption is comparable to that achievable at the incident angle $\theta = \theta_{\text{opt}}$. Therefore, the angle θ_{opt} can no longer be called the optimum angle of interrogation for $L \geq L_c$.

For the experimentally obtained parameters (see Table. 4.2), the parameter ξ varies between $\xi_0 \approx 1.4 \times 10^5\,\text{m}^{-1}$ and $\xi_2 = 4.4 \times 10^5\,\text{m}^{-1}$, which implies the values of the critical interaction length of $L_{c0} \approx 3.5\,\mu\text{m}$ and $L_{c2} \approx 1.1\,\mu\text{m}$. The subscripts 0 and 2 correspond to the concentrations 0 ppm and 2 ppm of NH_3 in N_2, respectively. When these values of the interaction length are substituted into (2.62) and the thickness of the guiding layer of $t_g = 1\,\text{mm}$ is considered, the number of reflections is found to be equal to one. This rough calculation therefore proves that the interrogation of the light with the sensing element described in Sec. 4.1.1 provides enhanced sensitivity at the incident angle $\theta = \theta_{\text{opt}} \approx 66°$ indeed *only* in the single-reflection configuration, as concluded above. In other words, the configuration employing multiple-reflections provides real benefits only when the absorption coefficient of the sensing layer is much lower than that obtained in the experiment discussed in this section, e.g., $\kappa_s \lesssim 0.001$.

4.2 LED-based prototype sensor system

In this section, the design, construction and performance characteristics of a prototype LED-based sensor system are described. The parameters of the sensor design are based on the optimised values provided in Sec. 4.1. Technical details of all the parts of the sensor system are provided and discussed in detail.

4.2.1 Design of the sensor unit

The design of the prototype sensor system is based on the sensing element which was described and analysed in Secs. 4.1.1 and 4.1.3. The fundamental parameters characterising the properties of the sensing element relevant to the sensor design are summarised in Table 4.2.

It was concluded in Sec. 4.1.3 that the sensing element is suitable only for sensing in the single-reflection configuration. Furthermore, the numerical analysis presented in section 2.2.9 demonstrated that the angular variation of sensitivity does not change significantly when the monochromatic light interrogating the thin sensing layer is substituted by a source with a broad emission spectrum, such as an LED (see Fig. 2.16). Therefore, the prototype sensor was designed so that the light emitted from an LED (its emission spectrum is shown in Fig. 4.1) would interrogate the sensing layer in a single-reflection configuration at the interrogation angle $\theta = \theta_{\text{opt}} = 66°$.

The schematic diagram of the prototype sensor system is shown in Fig. 4.6(a). The core feature of the sensor unit is a metal holder (MH) which provides a rigid support for the LED and Si-photodiode. The drawing of the metal holder containing all the dimensions is shown

in Fig. 4.6(b–c). The orientations of the LED and detector are selected so as to ensure that the centre angle of interrogation corresponds to the point where maximum sensitivity can be achieved, i.e., $\theta = \theta_{opt} = 66°$. The dimensions of the LED and detector apertures (A) are designed so as to allow only the light within a narrow angular width (full angular width is approximately 8°) to interrogate the sensing layer and be detected by the detector. As can be seen from Fig. 4.4(b), the light within this angular region is not incident solely in the region of optimum sensitivity but also in a region where sensitivity decreases to approximately half of its maximum value. This results in a reduction of the maximum achievable sensitivity. Further optimisation is possible by reducing the diameters of the LED and detector apertures so as to decrease this angular width. However, this step has to be taken with care. Although the reduction of the aperture size could increase the sensitivity, it would also decrease the signal-to-noise ratio due to lower levels of intensity, which might result in the deterioration of the sensor performance.

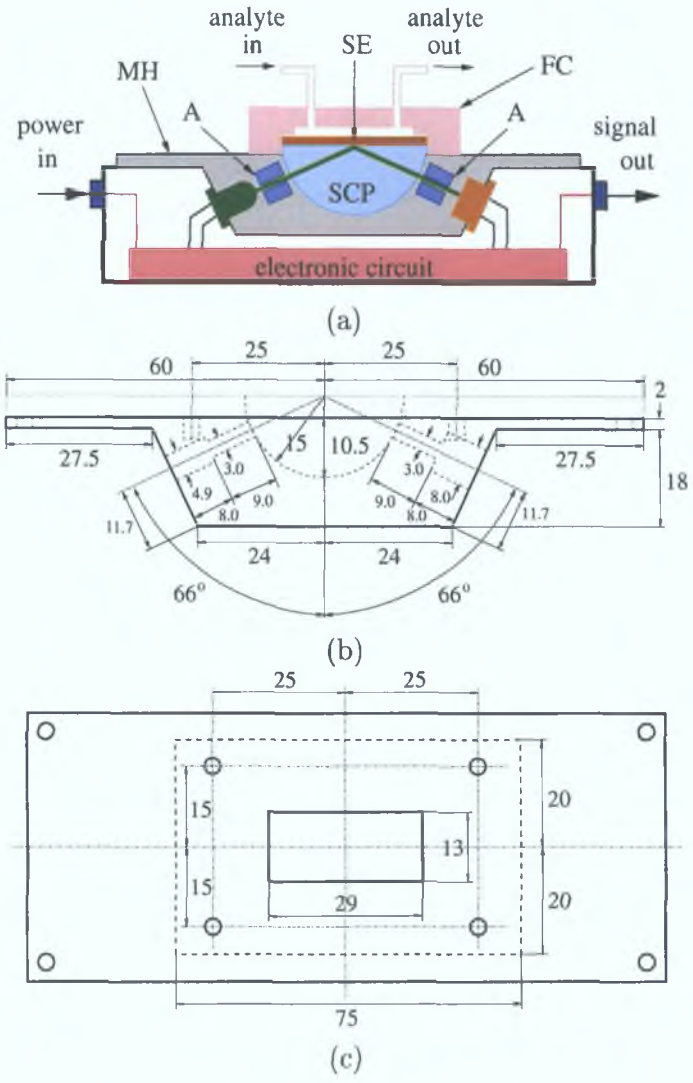

Figure 4.6: (a) A schematic diagram of the LED-based prototype sensor system working in a single-reflection configuration. The side and top views of the metal holder are shown in diagrams (b) and (c), respectively. The dimensions are in millimeters.

The flow cell (FC) facilitating the flow of the analyte above the sensing layer was designed so as to provide sealed enclosure of the sensing element (SE) inside while leaving an opening through which the semi-cylindrical prism (SCP) could be attached to the bottom side of the sensing element.

The sensor unit is assembled by attaching the box containing the electronic circuit, the metal holder containing the LED and photodiode, and the flow cell containing the sensing element and semi-cylindrical prism. The power is supplied externally by either a standard, commercially available power supply or batteries. The sensor unit provides a DC signal in the range of 0–10 V that can be fed directly to a voltmeter or a data acquisition card. The photograph of the sensor unit is shown in Fig. 4.7.

Figure 4.7: A photograph of the LED-based prototype sensor system. The sensor unit is assembled by attaching the box (1) containing the electronic circuit, the metal holder (2) containing the LED and photodiode, and the flow cell (3) containing the sensing element and semi-cylindrical prism.

4.2.2 Design of the electronic circuit

The purpose of the electronic circuit was to measure the *intensity* of the light emitted from an LED and reflected from the sensing element. In order to make the output signal independent of the ambient light intensity, a lock-in detection technique was employed.

The scheme and the photograph of the electronic circuit used in the LED-based prototype sensor system are shown in Figs. 4.8 and 4.9, respectively. As follows from the diagram, the circuit consists of three main parts:

1. an LED driving circuit, i.e., the circuit providing an alternating current through the LED,

2. a detection circuit, i.e., the circuit providing detection and further processing of the signal, and

3. a power supply circuit, i.e., the circuit for conversion of the external power supply to the levels suitable for the operation of circuits 1 and 2.

In the following, the function of each part of the circuit is discussed in greater detail.

The LED driving circuit is based on the ICM7555 timer chip. This chip produces a square wave with $V_{\mathrm{LO}} = 0\,\mathrm{V}$ and $V_{\mathrm{HI}} = 12\,\mathrm{V}$. The frequency and duty cycle of the square wave can

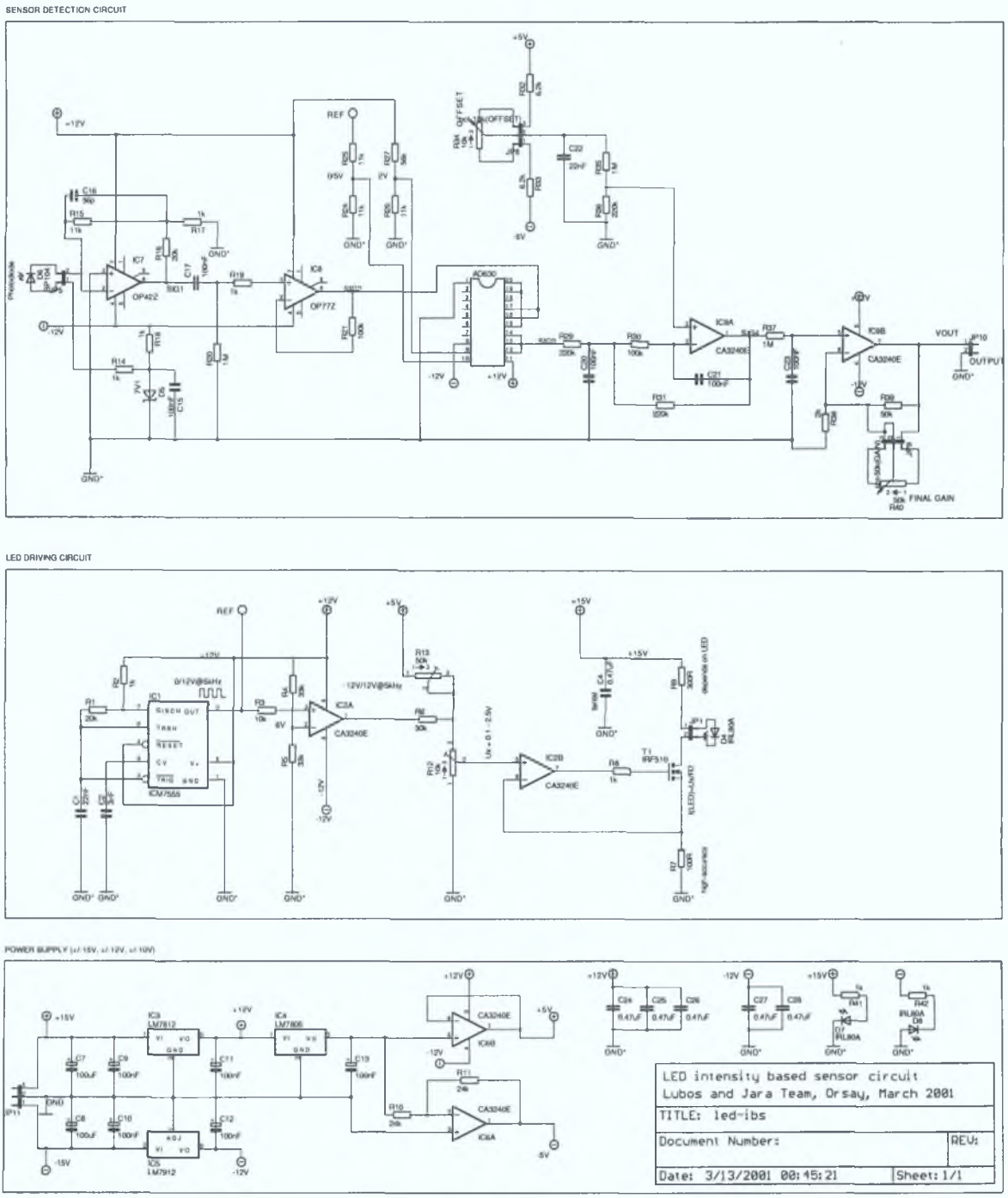

Figure 4.8: Scheme of the electronic circuit used in the LED-based prototype sensor system. The circuit provides a square wave current to drive the LED (D4) and employs a lock-in detection technique for the measurement of the light intensity detected by the photodiode (D6).

Figure 4.9: A photograph of the electronic circuit used in the LED-based prototype sensor system.

be adjusted by the values of the resistors R_1 and R_2 and capacitors C_1 and C_2 and is equal to approximately 5 kHz and 50 %, respectively. This square wave is subsequently modified to a square wave denoted by U_x with $V_{\mathrm{LO}} = 0.1\,\mathrm{V}$ and $V_{\mathrm{HI}} = 2.5\,\mathrm{V}$. The high and low values can be adjusted by the variable resistors R_{12} and R_{13} and depend on what current is required to drive the LED. Finally, the square wave U_x is converted via the operational amplifier (IC2B) with the FET transistor in the feedback to the current wave U_x/R_7 whose high and low values are very stable. This current then flows through the LED resulting in the light intensity alternating at a frequency of 5 kHz. The choice of the value $R_7 = 100\,\Omega$ results in the high and low values of the current through the LED (D4) to be $I_{\mathrm{HI}} = 25\,\mathrm{mA}$ and $I_{\mathrm{LO}} = 1\,\mathrm{mA}$, respectively. These values correspond to the optimum values of the current through the LED in order to vary the emitted light intensity between $J_{\mathrm{HI}} = J_{\mathrm{max}}$ and $J_{\mathrm{LO}} = 0$, respectively.[1] The light intensity levels J_{HI} and J_{LO} are very stable due to high stability of the current U_x/R_7 and due to an excellent stability of the LED's emission characteristics. This is important to note because in the version of the circuit shown in Fig. 4.8 the detection circuit does not provide any means to reference out the variation of the light intensity emitted by the LED.

The light emitted from the LED interrogates the sensing layer and is reflected towards the detector, which is a standard Si photodiode (D6). The signal from the photodiode is DC decoupled and amplified which results in a signal (SIG2) in the form of a symmetrical square wave whose magnitude is proportional to the high[2] level of the input light intensity $J_{\mathrm{in,HI}}$ entering the photodiode, i.e., $V_{2,\mathrm{HI}} = -V_{2,\mathrm{LO}} \propto J_{\mathrm{in,HI}}$. This signal is fed to the AD630 balanced modulator/demodulator which is connected so as to provide lock-in amplification. The reference signal (REF) to the AD630 chip is supplied from the ICM7555 timer chip whose output is modified from the 0/12 V square wave to the 0/5 V square wave.

The principle function of the AD630 chip connected as a lock-in amplifier is that it multiplies the input signal (SIG2) by factors F or $-F$ depending on whether the difference of the signals at the gates 9 and 10 is positive or negative, respectively. The levels of the signal SIG2 were sufficiently high and so the factor F was chosen to be $F = 1$, i.e., no additional

[1] To avoid confusion, the light intensity is denoted by J as opposed to the electrical current, which is denoted by I.

[2] The low value of the input light $J_{\mathrm{in,LO}}$ intensity is zero due to $J_{\mathrm{LO}} = 0$.

amplification. Consequently, the output signal (SIG3) is equal to SIG3 = SIG2 = $V_{2,HI}$ and SIG3 = −SIG2 = $-V_{2,LO}$ when the reference signal REF is equal to REF = 0 and and REF = 12 V, respectively. In other words, the signal SIG3 is equal to $V_{2,HI}$, which is proportional to the input light intensity $J_{in,HI}$, for the whole cycle of the reference signal.

Although this would be valid in an ideal case, the signal SIG3 produced by the real AD630 chip has some spikes due to fast switching taking place in the processes described above. These spikes are removed by a low-pass filter. Finally, the resulting DC signal is passed through a set of operational amplifiers using which the final off-set and gain of the output signal VOUT can be adjusted by variable resistors R_{34} and R_{40}, respectively.

This feature is useful when the dynamic range of the sensor output is to be adjusted to meet the requirements of a particular application or to make effective use of the resolution of the data acquisition device. For example, if the input intensity J_{in} changes between $J_{in,1}$ and $J_{in,2}$ for the concentrations of the analyte varying between $c_{A,1}$ and $c_{A,2}$, respectively, and the working range of the analogue input channel of the DAQ card is 0–10 V, the variable off-set and final gain of the signal allow for adjusting the output signal to VOUT = 0 V and VOUT = 10 V for $J_{in} = J_{in,1}$ and $J_{in} = J_{in,2}$, respectively, thus using the entire dynamic range of the data acquisition device.

As can be seen from the schematic diagram in Fig. 4.8, the components comprising the LED driving circuit and the detection circuit have various power supply requirements. To meet these requirements, the power supply circuit is provided which converts the external input supply of GND/ ± 15 V to power supplies ±12 V and ±5 V. The supply ±12 V is obtained using the standard 7812 and 7912 voltage regulators. On the other hand, the ±5 V supply is obtained by feeding the output of the 7805 voltage regulator to the inverting and non-inverting inputs of two operational amplifiers (IC6A and IC6B) connected as the voltage followers. This is done due to high requirements on the stability of symmetry of the +5 V and −5 V supply in the part of the circuit where the final off-set of the output signal VOUT is adjusted (see resistors R_{32}–R_{34}).

4.2.3 Performance of the LED-based sensor system

The response of the LED-based sensor unit in both aqueous (various pH buffers) and gaseous (NH_3 in N_2) environments was investigated and is summarised below. It is important to emphasize that it is the *efficiency* of the sensing platform, and *not* any limitations of the sensing chemistry, which are of relevance in the following discussion.

Response to pH buffer solutions

The response of the sensor unit to various buffer solutions with pH values ranging from pH5 to pH11 is shown in Fig. 4.10(a). It can be seen that the typical response time of the sensor was approximately 15 minutes. The output signal of the sensor varied from approximately 5.45 V (for pH5) to 1.76 V (for pH11). The response over the entire range pH5–pH11 could be very well approximated by a linear function. This is demonstrated in Fig. 4.10(b) which shows the calibration function of the sensor unit obtained from the data in the graph (a).

The noise level of the output signal could be expressed by the standard deviation of the output signal after reaching its equilibrium for a particular value of pH. This value was found

to be equal to $\Delta V \approx 1.5\,\mathrm{mV}$ independent of the signal level. Consequently, using Eq. (2.37), the resolution of the sensor system was found to be approximately *0.007 pH units* over the range of pH5 to pH11.

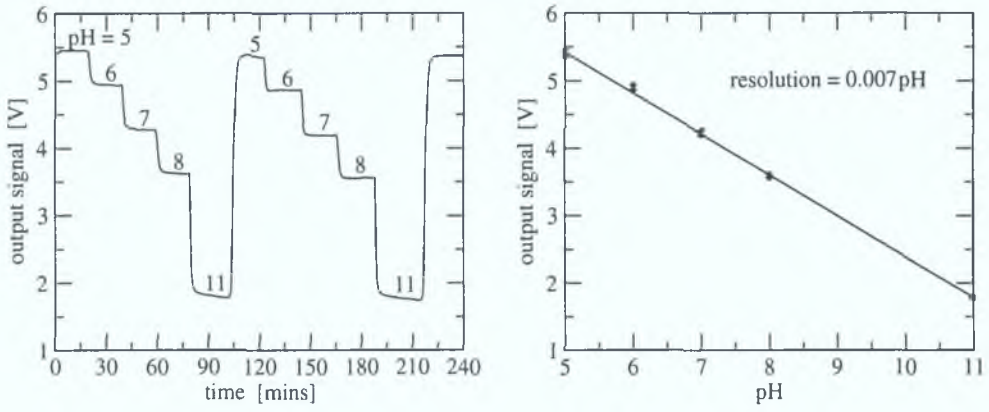

Figure 4.10: (a) An example of the response of the LED-based optical chemical sensor to various buffer solutions with pH values ranging from pH5 to pH11. (b) Calibration function of the LED-based optical pH-sensor obtained from the data in the graph (a). The data points, which were obtained from both pH-cycles, were fitted by a linear function.

This result, which is achieved with an LED-based single-reflection prototype sensor system, compares favourably with the performance of an optical fibre-based sensor system employing evanescent wave absorption developed by Butler et al. [5]. In that case, a multimode optical fibre (core diameter $600\,\mu\mathrm{m}$) was employed and a declad section of the fibre was coated with a sol-gel-derived film which was doped with a pH-sensitive indicator. Although a significant interaction length (approximately 5 cm) was used and high-order mode selection techniques employed to enhance sensitivity, a resolution of only 0.025 pH units was achieved. In such situations, sensitivity can be enhanced by increasing the interaction length but this enhancement does not scale linearly with the coating length and problems such as mode stability render this approach impractical beyond a few centimeters.

Response to gaseous ammonia

Figure 4.11(a) shows a typical example of the response of the sensor system to various concentrations of NH_3 in N_2. It can be seen that the response of the sensor was very slow as the signal did not reach equilibrium for any concentration even after approximately 2 hours. This was mainly due to complex water mediated chemistry involved in the sensing layer [4]. This suggests that the sensor chemistry needs to be substantially improved if it is to be used in practical applications involving ammonia sensing.

The calibration curve based on the sensor response shown in Fig. 4.11(a) is plotted in Fig. 4.11(b). With this typical non-linear response, the greatest resolution is achieved at low ammonia concentrations ($\lesssim 2\,\mathrm{ppm}$). Taking into account the noise level of the output signal of $\Delta V \approx 1.5\,\mathrm{mV}$, the calibration curve yields a limit of detection of LOD $\approx 10\,\mathrm{ppb}$. At higher concentrations (6–12 ppm) the sensor resolution increases by a factor of approximately 30 due to the fall-off in sensitivity, which is again determined by the sensor chemistry.

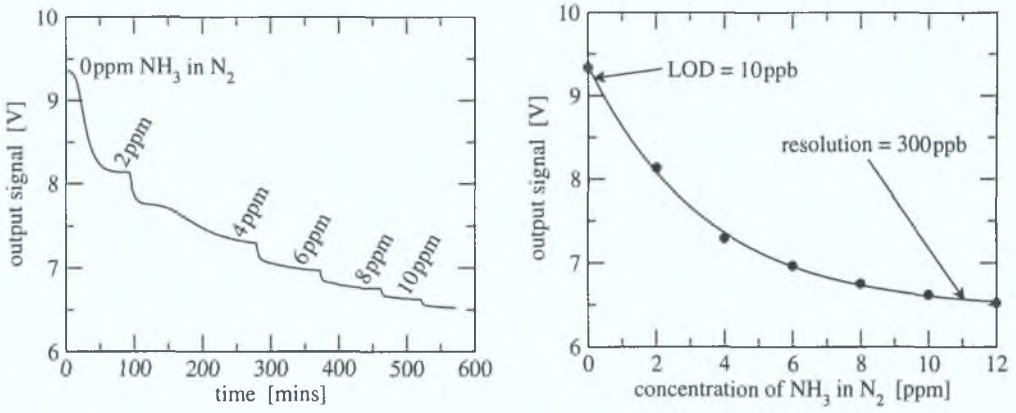

(a) (b)

Figure 4.11: (a) An example of the response of the LED-based optical chemical sensor to concentrations of NH_3 in N_2 ranging from 0 ppm to 12 ppm. (b) A calibration function of the LED-based optical NH_3-sensor obtained from data in the graph (a).

The significance of these data becomes apparent when compared with published results [6] where a more complex, multimode fibre-based system was employed. A LOD in the ppb range was inferred in this work and this corresponds to the value obtained with the optimised, single-reflection system presented here.

4.3 Conclusion

In this chapter, the experimental corroboration of the angular dependence of the sensitivity of absorption-based sensors was presented. Using the experimental data, the thickness and refractive index of the sensing layer was determined. Furthermore, the optimum conditions for the sensor performance were identified.

Based on these optimum conditions, an LED-based sensor system was designed and fabricated. The sensor operated in a single-reflection configuration, since it was predicted by the theory that more than one reflection would result in decreased sensitivity. The prototype sensor unit was tested both for gaseous (NH_3) and liquid (pH) analytes. In the former case, a limit of detection of 10 ppb of NH_3 in N_2 was achieved. In the later case, a resolution of 0.007 pH units over the pH range 5–11 was achieved.

These performance data, which compare favourably with the performance data of more complicated laser-based sensor systems reported in the literature, were mainly determined by the optimum sensing conditions employed and the low noise of the electronic circuit. The sensor system described in this chapter is an example of a generic, compact and high-performance platform for absorption-based optical chemical sensing.

4.4 Bibliography for Chapter 4

[1] B. D. MacCraith, C. M. McDonagh, G. O'Keffe, A. K. McEvoy, T. Butler, and F. R. Sheridan. Sol-gel coatings for optical chemical sensors and biosensors. *Sensors and Actuators*, B 29:51–57, 1995.

[2] C. McDonagh, B.D. MacCraith, and A.K. McEvoy. Tailoring of sol-gel films for optical sensing of oxygen in gas and aqueous phase. *Anal. Chem.*, 70(1):45–50, 1998.

[3] `http://www.physics.dcu.ie/OSL/`. Webpage of the Optical Sensors Laboratory, Dublin City University.

[4] Chris Malins, Thomas M. Butler, and Brian D. MacCraith. Influence of the surface polarity of dye-doped sol-gel glass films on optical ammonia sensor response. *Thin Solid Films*, 368:105–110, 2000.

[5] T. M. Butler, B. D. MacCraith, and C. M. McDonagh. Development of an extended range fiber optic pH sensor using evanescent wave absorption of sol-gel entrapped pH indicators. In Annamaria V. Scheggi, editor, *Chemical, Biochemical, and Environmental Fiber Sensors VII*, volume 2508, pages 168–178, 1995.

[6] R. Klein and E. Voges. Integrated-optic ammonia sensor. *Sensors and Actuators*, B 11:221–225, 1993.

Chapter 5

Luminescence-based optical chemical sensors—experimental work

This chapter presents an experimental investigation of the theoretical predictions discussed in Chapter 3. Firstly, the angular dependence of luminescence intensity emitted from a thin luminescent film is verified experimentally. Then, experimental data is presented which demonstrate significant improvement of the luminescence capture efficiency provided by a particular optimised structure. Finally, preliminary experimental results are presented which demonstrate the successful implementation of the novel technique for the detection of surface-generated luminescence.

5.1 Angular distribution of luminescence emitted from a thin layer

This section presents experimental results which corroborate the theory developed in Sec. 3.1. In particular, the angular distribution of luminescence radiated by a thin luminescent film deposited onto a glass substrate is investigated. Firstly, the studied samples are characterised. Then the experimental apparatus is described. Finally, the experimental data are presented and their relation to the theoretical predictions is discussed.

5.1.1 Preparation of the samples

The samples under study consisted of a standard glass microscope slide coated with a thin sol-gel layer. The recipe for the preparation of the luminescent sol-gel film was reported in the literature [1, 2]. The details are listed in Table 5.1. After the sol was prepared, it was deposited onto one side of the glass microscope slide by dip-coating. A protective tape was used to cover one side of the slide during the deposition. The dipping speeds varied from 0.2 mm/s to 3 mm/s. The final step involved oven drying of the samples at 70°C for 17 hours.

The sol-gel film doped with the Ruthenium complex emits luminescence in the orange region of the visible spectrum when excited by blue light. The excitation and emission

dissolve 21 mg of $Ru(dpp)_3$ in 5.1 ml of ethanol
add 6.0 ml of MTEOS and 2.18 ml of 0.1 M HCl and stir for 1 hour
add 750 μl of 0.3 M NaOH

Table 5.1: Recipe for the preparation of the sol doped with Ruthenium complex. See Appendix A for the explanation of abbreviations used.

spectra together with the spectrum of the excitation light provided by an LED is shown in Fig. 5.1.

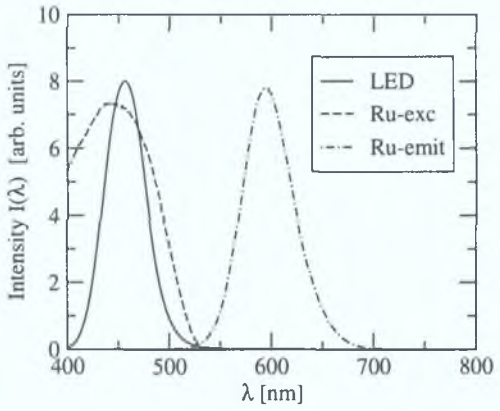

Figure 5.1: Emission spectra of the blue LED (solid line) and the sol-gel material doped with Ru-$(dpp)_3$ (dash-dotted line). The excitation spectrum of the $Ru(dpp)_3$-doped sol-gel, which is depicted by the dashed line, overlaps very well with the emission spectrum of the blue LED.

5.1.2 Experimental apparatus

The experimental appartus which was used to measure the angular distribution of luminescence intensity is shown in Fig. 5.2.

The core element of the experimental apparatus was a semi-cylindrical prism (SCP) on top of which a glass slide (GS) coated with the luminescent layer (LL) was attached by an index-matching immersion liquid. The dimensions of the prism were such that the addition of the glass slide resulted in a perfect semi-cylinder. This configuration facilitated the measurement of the luminescence intensity radiated into the glass substrate in the entire range of angles $\theta \in \langle -90°, 90° \rangle$.

The excitation light was provided by a blue LED (see Fig. 5.1 for the emission spectrum). Its intensity was modulated by a frequency generator (FG) at a frequency of approximately 2 kHz. The light from the LED was coupled into a short multimode fibre (MF) with a core diameter of 600 μm. The position of the fibre tip was adjusted so as to provide a small spot of the blue (excitation) light (diameter of $\approx$ 1 mm) in the centre of the sample which coincided with the centre of the semi-cylinder.

The prism with the attached sample and the holder of the LED and fibre were mounted on a high precision rotary stage (Physik Instrumente, M-038, unidirectional repeatability 20 μrad). Their position was adjusted so that the spot of the blue (excitation) light at the sample coincided with the rotation axis of the rotary stage, as shown in Fig. 5.2.

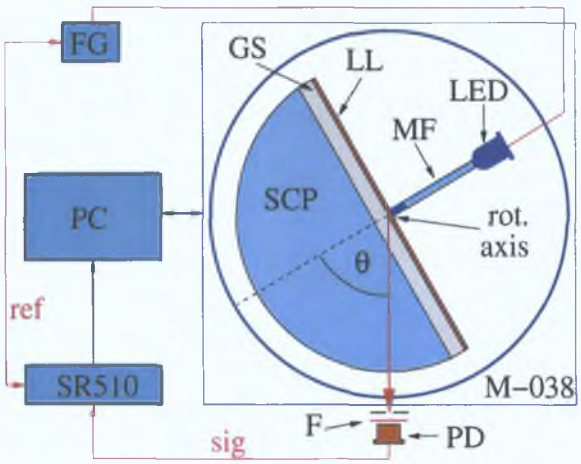

Figure 5.2: A schematic diagram of the experimental apparatus for measuring the angular distribution of luminescence intensity radiated from a thin luminescent layer (LL) deposited on a planar glass substrate (GS). To facilitate the measurement of the luminescence radiated into the substrate, the glass slide was attached to a semi-cylindrical prism (SCP) by an index-matching immersion liquid.

The luminescence was detected by a Si photodiode (PD) which was in a fixed position. A red filter (F) was used to prevent the blue excitation light entering the photodiode. Furthermore, a narrow slit approximately 0.5 mm wide was placed in front of the photodiode to facilitate the measurement of the luminescence intensity radiated into a narrow range of angles ($\Delta\theta \lesssim 1°$). The signal from the photodiode was fed into a lock-in amplifier (SR510) which used the signal from the frequency generator as the reference.

The entire experiment was controlled by a personal computer (PC). The rotation of the high precision rotary stage was controlled via the PIC842 card supplied by the manufacturer (Physik Instrumente). The analogue output from the lock-in amplifier was acquired by the data acquisition card (Bytronics, MPIBM3).

The program controlling the experiment was written in `LabView`. A screenshot of the program is shown in Fig. 5.3. The algorithm implemented in the program proceeded as follows:

1. the position of the rotary stage was set to the initial value $\theta = -90°$,
2. 3000 acquisitions of the output signal were made and this was repeated 3 times in order to evaluate the standard deviation of the signal,
3. the value of the angle of observation (θ) together with the mean value and the standard deviation of the signal were appended to the output file,
4. the rotary stage was rotated by $\Delta\theta = 1°$;
5. steps 2–4 were repeated until the maximum value of the observation angle, i.e., $\theta = 90°$, was reached.

Over the course of the experiment, the lock-in sensitivity and time-constant were kept constant and equal to $10\,\mu$V and 3 s, respectively. Furthermore, the properties of the excitation light (the modulation frequency and the minimum/maximum values of intensity) were

kept unchanged. Consequently, the values of the signal originating from different samples were in relative proportion and could be therefore directly compared.

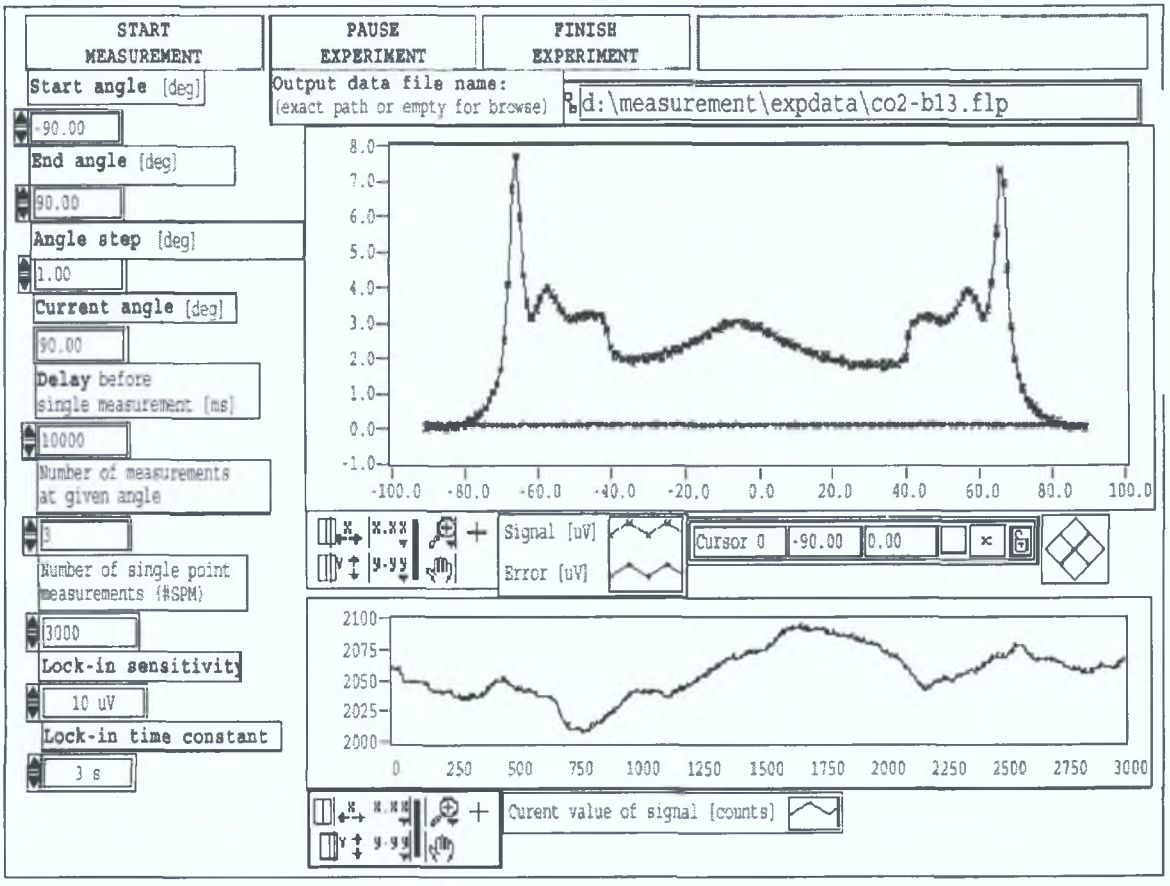

Figure 5.3: A screenshot of the LabView program controlling the experiment for measuring the angular distribution of the luminescence intensity.

5.1.3 Experimental results

An example of the raw experimental data is shown in Fig. 5.4. It can be seen that the signal was symmetric around $\theta = 0°$. The features at angles $\theta \in \langle -90°, -\theta_c^{as} \rangle$ and $\theta \in \langle \theta_c^{as}, 90° \rangle$, where $\theta_c^{as} = \arcsin(n_a/n_s) = 41.3°$, are clearly visible and agree with those predicted by the theory (see Sec. 3.2.3). The broad peak at around $\theta = 0°$ corresponds to the transmitted excitation light detected in this angular region, which could not be completely removed by the filter used. This is evident from the data depicted by "+" which correspond to the sample coated with an undoped sol-gel layer. To obtain the data corresponding solely to the luminescence intensity, this background signal was subtracted from the signal for each sample. Examples of this processed experimental data are shown in Fig. 5.5. The experimental data were fitted using the theoretical model developed in Sec. 3.1 (see Eq. (3.37)). During the fitting procedure, the emission *spectrum* of the luminescence (see Fig. 5.1) was also considered.

As can be seen form Fig. 5.5, the agreement between the experimental and theoretical data is excellent. From this fit, the value of the refractive index of the $Ru(dpp)_3$-doped sol-gel layer was found to be $n_l = 1.425 \pm 0.002$. Furthermore, the fit was used to calculate the

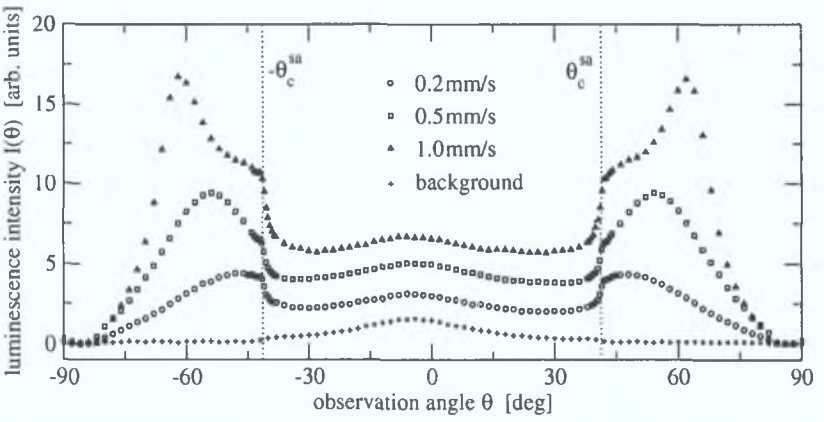

Figure 5.4: An example of the raw experimental data of the angular distribution of luminescence radiated from a thin sol-gel film doped with $Ru(dpp)_3$ dye.

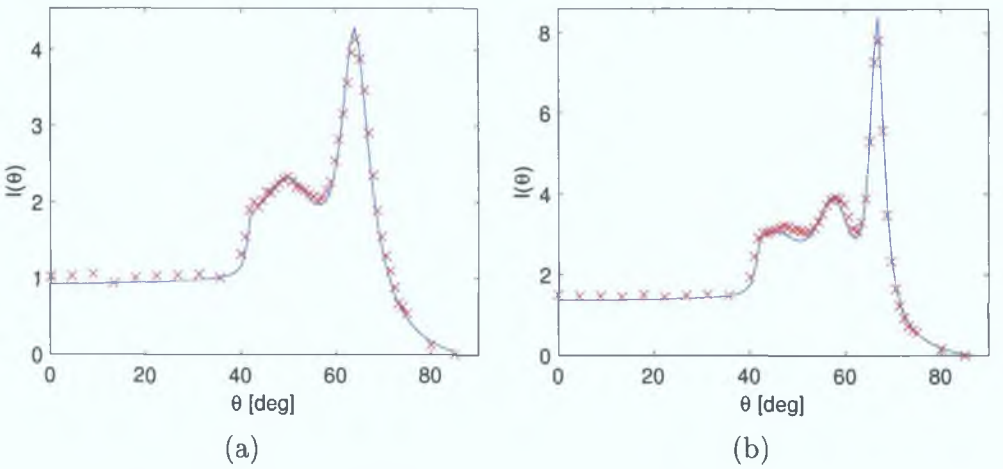

Figure 5.5: An example of the data with the background signal subtracted. The crosses represent the experimental data, the solid lines represent the fit based on expression (3.37). The graphs (a) and (b) correspond to the luminescent layers deposited at dipping speeds 1.5 mm/s and 3 mm/s, respectively.

values of the thickness of the layers obtained at different dipping speeds [3]. These values are plotted in Fig. 5.6(a). It can be seen that the relationship between the layer thickness t_l and the dipping speed s_d can be very well approximated by a linear function. The coefficients are listed in Fig. 5.6(b).

The data shown in Figs. 5.5 provides experimental corroboration of the theory developed in Sec. 3.1. It demonstrates that a maximum of the luminescence intensity occurs at an angle θ which lies within the angular range $\theta \in \langle \theta_c^{as}, \theta_c^{ls} \rangle$, where $\theta_c^{as} = \arcsin(1.0/1.515) \approx 41.3°$ and $\theta_c^{ls} = \arcsin(1.425/1.515) \approx 70°$ are the critical angles of the air/glass and sol-gel layer/glass interfaces, respectively. The data also demonstrates that the peak shifts towards θ_c^{ls} and is more pronounced for greater values of the luminescent layer thickness, as predicted by the theory.

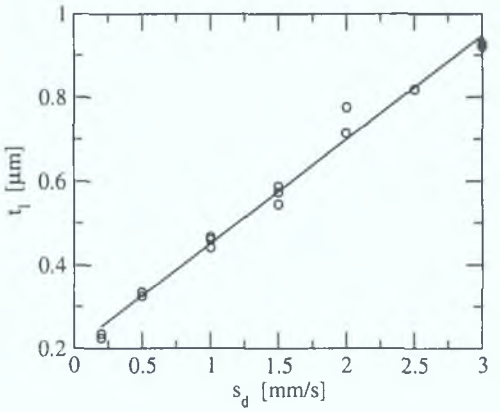

(a)

$n_l = 1.425 \pm 0.002$
$t_l = As_d + B$
$A = (0.25 \pm 0.01)\,\mu\text{m}/(\text{mm.s}^{-1})$
$B = (0.20 \pm 0.02)\,\mu\text{m}$

(b)

Figure 5.6: (a) Thickness of the luminescent layer t_l as a function of the dipping speed s_d. The points correspond to the values obtained from fitting the angular distribution of luminescence by the expression (3.37). The line represents the linear fit of the data. The corresponding fitting parameters are listed in table (b).

5.2 Configuration with enhanced luminescence capture efficiency

Section 3.3 concluded that the so-called substrate-confined (SC) modes are very attractive when efficient capture of the luminescence radiated from thin luminescent films is of interest. This is due to the relatively large amount of energy carried by these modes as well as to the fact that their propagation is confined within a relatively narrow angular range.

Section 3.3.2 listed several configurations facilitating the detection of the SC modes. Taking into account all the advantages and disadvantages mentioned in that section, the configuration employing the frustrated cones (see Fig. 3.24) was found to provide the greatest benefit. This included both a large enhancement factor of the luminescence capture efficiency (see Fig. 3.26) and a relatively simple manufacturing process. For these reasons, it was this configuration that was tested experimentally, which is reported below.

5.2.1 Preparation of the samples

The chip was made from polystyrene whose refractive index over the range of wavelengths corresponding to the emission spectrum of the $Ru(dpp)_3$-doped sol-gel is approximately $n_s = 1.590$. The luminescent spots were made of the $Ru(dpp)_3$-doped sol-gel, which is characterised by the refractive index $n_l = 1.425$, as concluded in Sec. 5.1.3). The environment covering the spots was air ($n_a = 1.0$). Using these parameters, the critical angles θ_c^{ls} and θ_c^{as}, which play a fundamental role in the design, could be calculated. Their respective values are $\theta_c^{ls} = 63.7°$ and $\theta_c^{as} = 39.0°$. Consequently, the value of the tilt angle α, which is calculated from (3.39), was chosen to be $\alpha \approx 26°$ (see Fig. 3.24 in Sec. 3.3.2).

The configuration was designed in the axially symmetric form, as depicted in Fig. 3.27(a). The values of the dimensions w and h (see Fig. 3.24(b)) were $w = 1\,\text{mm}$ and $h = 1\,\text{mm}$. The chip incorporated a 2×4 array of frustrated cones on a single substrate. A photograph of the chip is shown in Fig. 5.7.

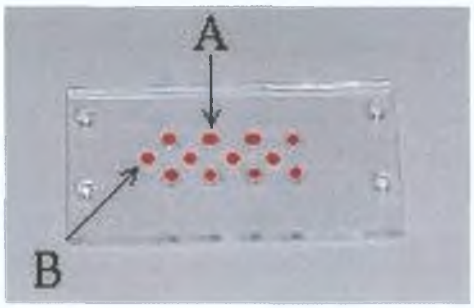

Figure 5.7: A photograph of the chip containing a 2×4 array of frustrated cones depicted in Fig. 3.24. The luminescent spots made of a $Ru(dpp)_3$-doped sol-gel were deposited by a stamping technique both at the top of each frustum (spots denoted by A) as well as on the planar (unmodified) substrate (spots denoted by B).

The thin luminescent spots were deposited onto the substrate using a stamp fabricated from poly-dimethylsiloxane (PDMS, see Sec. 5.3 for detail of the PDMS preparation). This was done both at the top of each of the frustrated cones (spots A) as well as on the planar (unmodified) substrate (spots B) in order to enable a direct comparison between the efficiencies of the conventional and improved techniques of the luminescence capture. Although the stamping method was cheap, fast to implement and easy to use, it did not facilitate the deposition of spots with equal volume of sol-gel. Nevertheless, it was sufficient for the purpose of this experiment as the discrepancies between the dimensions of the spots could be taken into account during data processing. The diameter of the spots B was found to be approximately 2 times greater than the diameter of the spots A, which was determined by the imperfection of the stamping technique.

5.2.2 Experimental apparatus

A simple experiment for measuring the intensity radiated by the luminescent spots was set up as shown in Fig. 5.8. The chip containing the luminescent spots (LS) was held in a fixed position by a holder. The excitation light was provided by a blue LED, which was placed above the chip so as to provide approximately uniform illumination of luminescent spots. The LED was slightly misaligned with respect to the detector axis (dash-dotted line) in order to prevent direct illumination of the detector array by the excitation light which could not be eliminated completely even with the use of a high quality red filter. The detector (either a CCD or CMOS camera) was placed at the back side of the chip. The lens of the camera was adjusted so as to provide focused image of the luminescence emitted from the spots.

5.2.3 Experimental results

Two independent experiments using two independently prepared samples were carried out in order to measure the improvement of the luminescence capture efficiency provided by the configuration employing frustrated cones. The first experiment employed a CCD camera, and the second one used an in-house developed detection system based on a CMOS-camera [4]. Typical examples of images obtained by the CCD and CMOS camera are shown in Fig. 5.9(a) and 5.9(b), respectively.

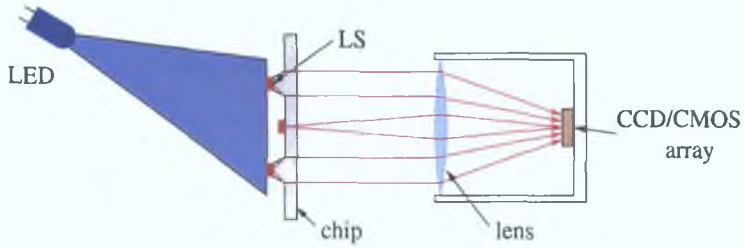

Figure 5.8: A schematic diagram of the experimental apparatus for the measurement of luminescence radiated by luminescence spots (LS) deposited onto a chip containing structures providing improved luminescence capture efficiency. See text for further details.

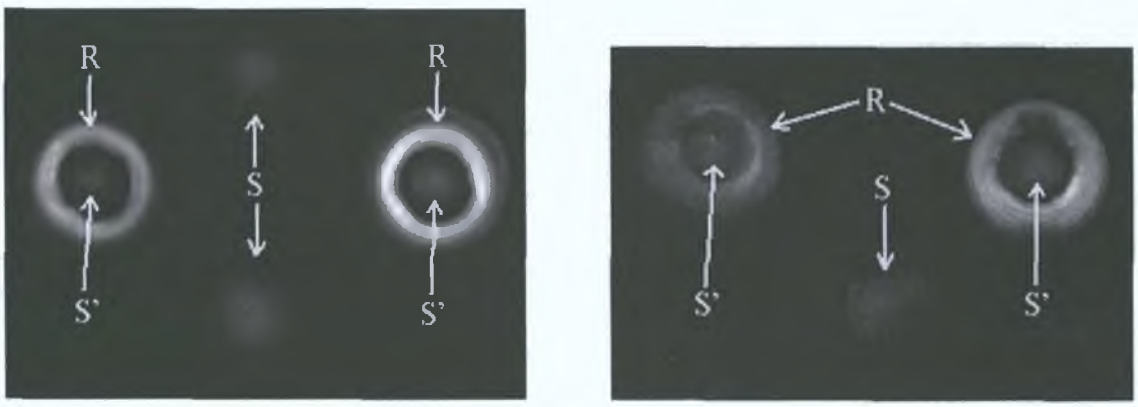

(a) (b)

Figure 5.9: Typical examples of the images of the luminescence detected from 4 spots deposited onto the polystyrene chip depicted in Fig. 5.7. The bright ring-like intensity profiles denoted by **R** and the less intense spots denoted by **S'** correspond to the SC and ST modes of the luminescence emitted by the spots deposited at the top of the frustrated cones, respectively (see Fig. 3.24). The spots denoted by **S** are produced by the luminescent spots deposited onto an unmodified (planar) substrate, i.e., they represent the images obtained by the conventional detection technique. The images (a) and (b) were obtained by two independent measurements using a CCD and CMOS cameras, respectively.

It can be seen that there are two distinct intensity profiles visible in both images. The ring-like profiles correspond to the luminescence produced by the spots which were deposited at the top of the frustrated cones. In particular, the light impinging the detector array at the area of the bright **ring** (**R**) corresponds to the **SC modes** of the luminescence radiated by the spot. On the other hand, the less evident grey spots (**S**) correspond to the **ST modes** of the light produced by the luminescent spots deposited onto an unmodified planar substrate, i.e., they correspond to the images of the luminescence intensity obtained by the conventional detection technique. The intensity corresponding to the ST modes radiated from the spots deposited at the top of the frustrated cones is also visible, namely in the inner area of the rings (spots denoted by **S'**).

It can be seen that there is some non-uniformity in the intensity distribution across the image. For example, using the image in Fig. 5.9(a), the right ring appears to be brighter than the left one and the top spot seems to be less bright than that at the bottom. Similar features can be observed from the image in Fig. 5.9(b). This is due to non-uniformity of

the intensity profile of the blue excitation light illuminating the luminescent spots, which could not be avoided due to an inherently divergent and spatially anisotropic character of the light produced by a LED. Furthermore, the spots **S** appear to be greater in size than the spots **S'**. This is due to a greater physical size of the luminescent spots deposited onto the planar substrate than those deposited at the top of the frustrated cones, which was caused solely by the stamping method, as mentioned above.

To estimate the improvement of the luminescence capture efficiency, the images, such as those shown in Fig. 5.9, were analysed. In the analysis, the effects of both the non-uniformity of excitation and the size of the luminescent spots were taken into account. Details of this analysis are summarised below for both independently obtained experimental data.

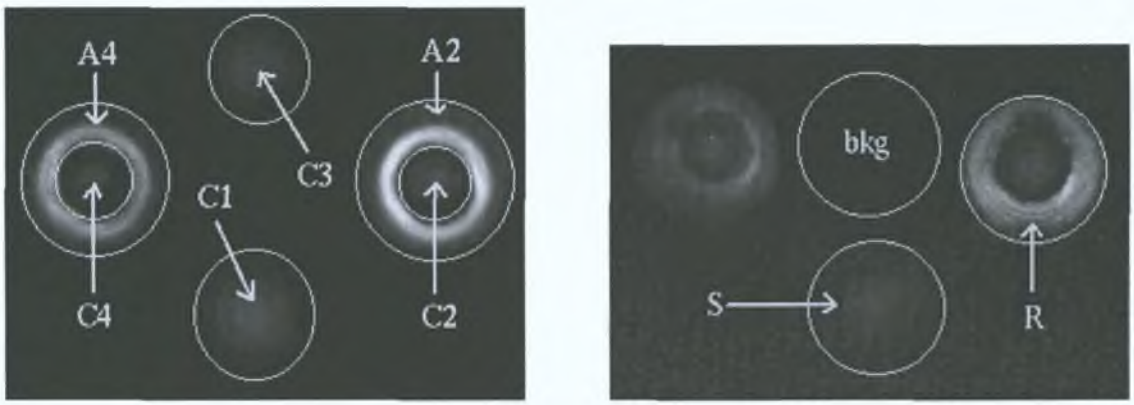

(a) (b)

Figure 5.10: Images based on which the analysis of the luminescence emitted from the chip shown in Fig. 5.7 was performed. The images (a) and (b) correspond to the experiments employing CCD and CMOS cameras, respectively. See text for further details.

CCD-based experiment

The analysis of the experiment employing the CCD camera is based on the image shown in Fig. 5.10(a). In the first step of the analysis, the total intensities detected in the areas denoted by C1–C4, A2 and A4 were obtained. The circular areas C1 and C3 represent the intensity profiles of the ST modes emitted by the luminescent spots deposited onto the unmodified (planar) substrate and detected by the CCD camera. The circular areas C2 and C4 represent the same but for the spots deposited at the top of the frustrated cones. The annulus areas A2 and A4 represent the intensity profiles of the SC modes which are emitted by the luminescent spots deposited at the top of the frustrated cones and redirected towards the detector, as discussed in Sec. 3.3.2. The corresponding total intensities are listed in Table 5.2, step 1.

In the next step of the analysis, the non-uniformity of the illumination by the blue light was taken into account. This was done by requiring that the intensity in the *centre* of the circular areas C1–C4 be the same for each circular area. This was based on the assumption that all the spots deposited either at the top of the frustrated cones or onto the unmodified (planar) substrate have equal thickness. Indeed, in that case, the intensities of the luminescence radiated at an angle $\theta = 0°$ should be equal, as follows from the theory in Sec. 3.1. The intensities corresponding to the centre of the circular areas C1–C4 are listed in

	total intensity [norm. units]							
step	C1	C2	C3	C4	A2	A4	C2 + A2	C4 + A4
1	1.15	0.438	0.528	0.257	4.30	2.87	4.74	3.13
2	0.010	0.010	0.091	0.072	—	—	—	—
3	1.15	0.438	0.589	0.359	4.30	4.01	4.74	4.37
4	0.289	0.438	0.239	0.359	4.30	4.01	4.74	4.37
5^1	**1.00**	1.52	0.830	1.24	14.9	13.9	**16.4**	**15.1**
5^2	0.660	**1.00**	0.550	0.82	**9.82**	9.16	**10.8**	9.98
5^3	1.21	1.83	**1.00**	1.50	18.0	16.8	**19.8**	**18.3**
5^4	0.805	1.22	0.666	**1.00**	12.0	**11.2**	13.2	**12.2**

Table 5.2: Analysis of the data provided by the image in Fig. 5.10(a). See text for further details.

Table 5.2, step 2. The intensities corresponding to all considered areas and obtained by this renormalisation step are listen in Table 5.2, step 3.

In the next step of the analysis, physical dimensions of the luminescent spots was taken into account. This was done by measuring the diameter d of the circular areas C1–C4 which corresponded to the diameter of the physical spots. The following values of the diameters were found:[1] $d_{C1} = 140$, $d_{C2} = 70$, $d_{C3} = 110$, $d_{C4} = 70$. The intensities obtained after this renormalisation step are listed in Table 5.2, step 4.

In order to write the values in a form which would be more convenient for further comparison, the values obtained in the step 4 were renormalised so that the intensities corresponding to the circular areas C1–C4 would be unity. These final values are listed in Table 5.2, steps 5^1–5^4, respectively.

It is important to mention that although the background intensity needed to be considered in these calculations, it was found to be zero and thus did not affect the final numerical values listed in Table 5.2. On the other hand, as can be seen from the image in Fig. 5.9(b), the background signal was quite substantial in the experiments using the CMOS camera and thus had to be considered in the calculations.

CMOS-based experiments

The analysis of the experiment employing the CMOS camera is based on the image shown in Fig. 5.10(b). As mentioned above, the background signal has to be considered in the analysis of the image shown in Fig. 5.9(b). Three regions of the same area are defined in the image, namely a ring-like region (R) which corresponds to the intensity of the luminescence emitted from the spot deposited at the top of the frustrated cone, a circular spot (S) which corresponds to the same but originating from the spot deposited onto the unmodified (planar) substrate, and a circular region "bkg" which provides a measure for the background signal. All the regions are of the same area and so the total intensities obtained in the following calculations are *directly* comparable. The total intensities measured in these regions are listed in Table 5.3, step 1.

To enable direct comparison between the intensities emitted from the spot deposited

[1] The values are given in arbitrary units.

	total intensity [norm. units]		
step	S	R	bkg
1	0.946	2.12	0.837
2	0.109	1.28	0.000
3	**1.00**	**11.8**	**0.000**

Table 5.3: Analysis of the data provided by the image in Fig. 5.10(b). See text for further details.

at the top of the frustrated cone (area R) and that deposited on the planar (unmodified) substrate (area S), the intensity of the background (area "bkg") had to be subtracted. The values of the intensities after this renormalisation step are listed in Table 5.3, step 2.

In order to write the values in a form which would be more convenient for further comparison, the values obtained in the step 2 were renormalised so that the intensity corresponding to the area S would be unity. These final values are listed in Table 5.3, steps 3.

Enhancement of the luminescence capture efficiency—summary

It can be seen from Tables 5.2 and 5.3 that the enhancement of the detected intensity provided by the configuration employing frustrated cones (see Fig. 3.24) is substantial. In particular, when the total intensity detected from a spot deposited at the top of the frustrated cone is compared to the intensity emitted by means of the ST modes, an enhancement by a factor of approximately **11–12** is obtained (see the values in columns C2 + A2 and C4 + A4 and the values in columns C2 and C4 in Table 5.2 at lines 5^2 and 5^4, respectively). When the total luminescence intensity detected from a spot deposited at the top of the frustrated cone is compared to the total intensity detected from a spot deposited on an unmodified (planar) substrate, an enhancement of approximately **15–20** is found (see the values in columns C2 + A2 and C4 + A4 and the values in columns C1 and C3 in Table 5.2 at lines 5^1 and 5^3, respectively). This factor is slightly lower (approximately **12**) when the data in Table 5.3 is used. This difference is attributed to possible discrepancies in the thickness of the spots deposited at the top of the frustrated cones and those deposited onto the unmodified (planar) substrate, the latter being approximately 1.5 times thinner than the former, due to the imperfection of the stamping method used.

These results are the first experimental evidence of the level of improvement of the luminescence capture efficiency that can be achieved by employing the structure with frustrated cones in comparison to the efficiency provided by the conventional detection technique. Even though the improvement does not reach as high values as those corresponding to the ideal situation described in Sec. 3.3.2, the 10–12-fold increase in the detected intensity clearly demonstrates how attractive the improved configuration is. It is believed that this improvement factor could be further increased by providing better quality (in terms of the surface roughness) of the reflecting surface A (see Fig. 3.24).

5.3 Thin layer vs bulk contribution to the radiated luminescence

In this section, preliminary experimental data is presented which demonstrates the capability of distinguishing between surface and bulk-generated luminescence by the method proposed in Sec. 3.4. Firstly, preparation of the samples that were used in the experiments is briefly described. Then, the experimental apparatus is characterised. Finally, the experimental data is presented and discussed in detail.

5.3.1 Preparation of the samples

Each studied sample comprised a standard glass microscope slide coated with a thin sol-gel layer. The sol was prepared in two forms: a sol doped with fluorescent ruthenium complex, $Ru(dpp)_3$, which will be denoted by D, and an undoped sol, which will be denoted by UD. The recipe for the preparation of the sol was reported in the literature [1, 2] and the details are listed in Table 5.4 for both the D and UD sol. After the sol was prepared, it was deposited onto one side of a glass microscope slide by dip-coating at a dipping speed of 2.5 mm/s. The final step involved aging overnight at 20°C.

(a)	dissolve 12 mg of $Ru(dpp)_3$ in 1 ml of ethanol add 1.45 ml of 0.1 M HCl and stir for 30 minutes add 4ml of MTEOS and stir for 2 hours at 20°C
(b)	mix 1 ml of ethanol and 1.45 ml of 0.1 M HCl and stir for 30 minutes add 4ml of MTEOS and stir for 2 hours at 20°C

Table 5.4: Recipes for the preparation of the doped (a) and undoped (b) samples. See Appendix A for the explanation of abbreviations used.

The theoretical background for the experiments described below was presented in Sec. 3.2.5. In the context of that section, the samples coated with the undoped sol-gel (UD-samples) correspond to the multilayer structure depicted in Fig. 5.11(a) (reproduction of Fig. 3.10(a)), while the samples coated with the $Ru(dpp)_3$-doped sol-gel (D-samples) correspond to the multilayer structure shown in Fig. 5.11(b) (reproduction of Fig. 3.10(b)).

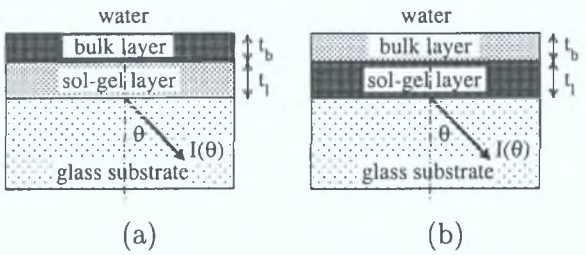

Figure 5.11: Schematic diagrams of two-layer systems consisting of a glass substrate, sol-gel layer and a bulk layer. To facilitate the easy viewing of the diagrams, they have been reproduced here. For a more detailed description, see Fig. 3.10.

The purpose of this experiment was to distinguish between the contributions to the emitted luminescence originating from a thin layer and from the bulk above the thin layer. There-

fore, it was necessary to facilitate a flow of a solution above the thin sol-gel layer, where the solution could either be undoped (UD-solution) or doped with the luminescent molecules (D-solution). In the experiments, ethanol doped with the ruthenium complex was used as the D-solution due to a very good solubility of the Ruthenium complex in ethanol. Pure ethanol was used as the UD-solution.

Initially, deionised water was used as the UD-solution. However, problems related to the non-deterministic mixing of water and $Ru(dpp)_3$-doped ethanol were encountered during the initial stage of the experiments. These problems were caused by different values of the refractive index of water and ethanol. Therefore, it was decided to change the UD-solution from water to ethanol. Nevertheless, the initial experimental data using water will also be presented as they demonstrate certain features important for the subsequent interpretation procedure.

As discussed in Sec. 5.1.1, the fluorescent ruthenium complex emits light in the spectral region from approximately 550 nm to 650 nm. For this spectral region, the refractive index of the D and UD sol-gel films was taken to be $n_l = 1.425$ (see the results of the fit of the experimental data in Fig. 5.6) and the refractive index of the glass substrate and the semi-cylindrical prism was considered to be $n_s = 1.515$. The refractive index of the $Ru(dpp)_3$-doped and undoped ethanol was of $n_e = 1.362$ while the refractive index of water was taken to be $n_w = 1.332$. Using these values, the values of the critical angles, which play an important role in the analysis of the experimental results, were determined. They are listed in Table 5.5.

interface	critical angle
air/glass substrate	$\theta_c^{as} = 41.30°$
water/glass substrate	$\theta_c^{ws} = 61.55°$
(D/UD)-ethanol/glass substrate	$\theta_c^{es} = 64.03°$
sol-gel film/glass substrate	$\theta_c^{ls} = 70.15°$

Table 5.5: Values of the critical angle corresponding to various interfaces.

5.3.2 Experimental apparatus

As described in Sec. 3.4, one possible configuration for an experimental set-up suitable for distinguishing between the thin layer and bulk contributions to the radiated luminescence is based on the measurement of the angular distribution of the luminescence radiated into a higher refractive index substrate. Although such a set-up was devised and successfully implemented in the experiments described in Sec. 5.1, it could not be employed in these experiments. The main reason for this was that this experiment was designed to enable observation of real-time changes in the angular profile of the luminescence intensity. The previous set-up enabled the acquisition of the angular profile of luminescence only every 20–30 minutes, which was not sufficiently fast. Therefore, a different experimental setup was assembled.

A schematic diagram and a photograph of the experimental set-up are shown in Figs. 5.12 and 5.13, respectively. Rather than rotating the sample, the semi-cylindrical prism (SCP) with the sample attached was kept in a fixed position and the angular profile of luminescence was recorded by a linear detector array (LDA). The LDA (Hamamatsu S3904-1024Q [5])

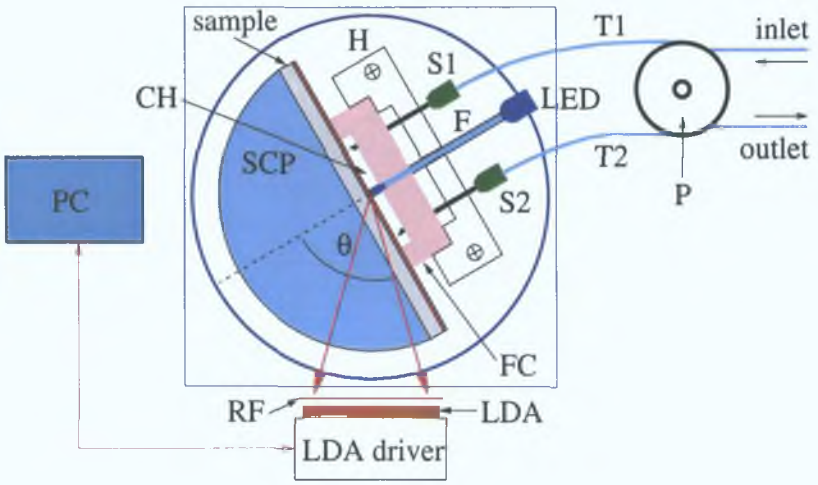

Figure 5.12: A schematic diagram of the experimental apparatus for measuring the angular distribution of luminescence intensity radiated from a sample consisting of a thin luminescent layer (LL) deposited onto a planar glass substrate (GS). In contrast to the apparatus shown in Fig. 5.2, the angular profile is obtained as a single-shot measurement using a linear detector array (LDA). See text for further details.

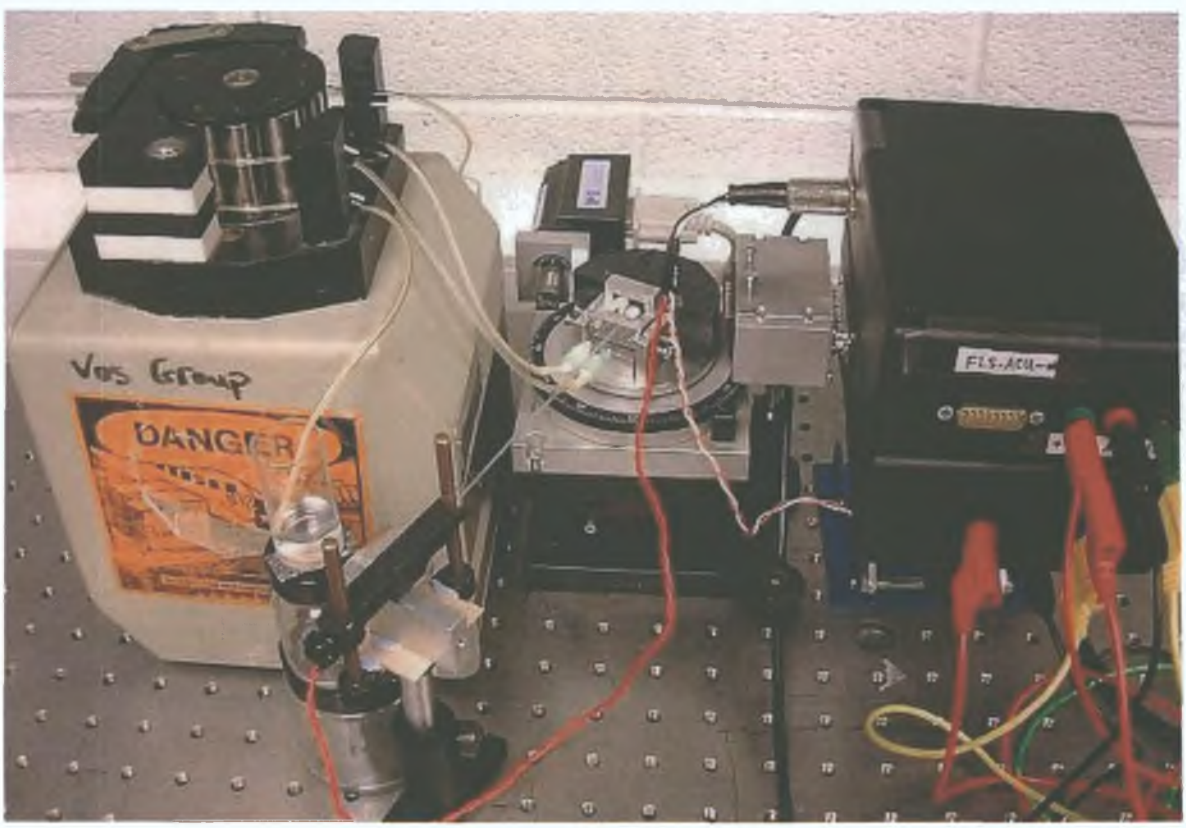

Figure 5.13: A photograph of the experimental apparatus for measuring the angular distribution of luminescence intensity in a single-shot configuration. See text and Fig. 5.12 for a detailed description.

consisted of an array of 1024 photodiodes characterised by a pitch of 25 μm and dimensions 20 μm × 2.5 mm. The total size of the array was 2.5 × 25 mm. The input window of the LDA was covered by a red filter (RF) in order to eliminate possible detection of the blue excitation light. The LDA was placed near the face of the SCP in such a way that the luminescence radiated over the angular width of approximately $\Delta\theta = 37°$ could be detected. Driver circuits (Hamamatsu C4070 and C4091), which were supplied with the LDA by the manufacturer, enabled an independent acquisition of the signal from each of the photodiodes with a repetition rate in the range of 1 Hz to 10^5 Hz, depending on the level of the light intensity. This means that the apparatus was able to acquire a single-shot angular profile of the luminescence radiated into a relatively broad range of angles every 10 μs to 1 s. Due to the very low levels of luminescence intensity provided by the samples used, the driving circuits were slightly modified so that a repetition rate of 1/12 Hz could be achieved. This value was also employed during the experiments.

The principle of operation of the LDA was as follows: The signal corresponding to the light impinging onto each photodiode was accumulated during the time between two single-shot measurements, which was equal to ≈ 12 s in this experiment. After this signal accumulation period, a train of digital pulses from the driving circuit triggered a train of analogue pulses at the video-output of the LDA chip, as shown in Fig. 5.14. The analogue value of each pulse corresponded to the total light intensity detected by the corresponding photodiode. Because the time separation of the analogue video pulses was very short (10 μs), a data acquisition card with a high acquisition rate had to be employed. For this purpose, a data acquisition card (Keithley, KPCI-3104) capable of up to 400 kS/s acquisition rate on a single analogue input channel was used.

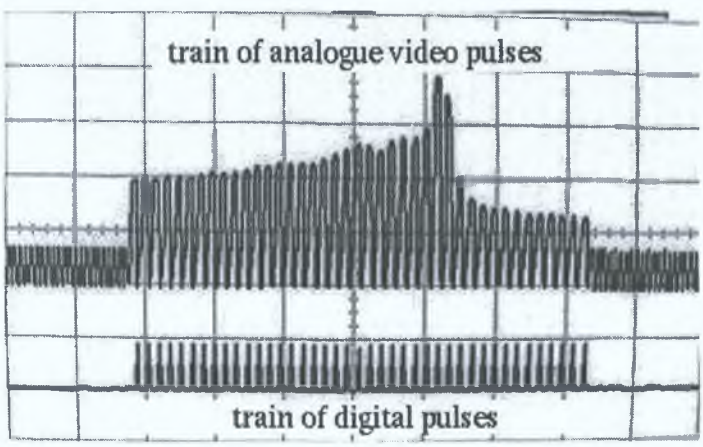

Figure 5.14: An example of a train of digital pulses produced by the LDA driving circuit which triggered a train of analogue pulses at the video output of the LDA. The image is a screenshot of the oscilloscope monitor. It is important to note that the number of pulses shown in the image does not correspond to the real number of pulses (there was a total of 1024 pulses in one train) due to the finite resolution of the oscilloscope monitor.

The flow of the solution above the thin sol-gel layer was facilitated by a flow cell (FC) attached to the glass slide. The flow cell was made of poly-dimethylsiloxane (see Table 5.6 for a brief description of the recipe) which provided good adhesion to the sol-gel film. Furthermore, the flow cell consisted of a channel (CH) with dimensions of approximately 1 × 1 × 10 mm

through which a solution could flow above the film in a controlled way.

(PDMS is commercially available as Sylgard 184 from Dow Corning [6])
mix liquid prepolymer and curing agent of Sylgard 184 in the ratio 10:1 (*volume or mass*)
pour the liquid mixture into a flow cell mould
cure at 70°C for 1 hour
detach the solidified flow cell from the mould

Table 5.6: A brief description of a recipe for the preparation of a flow cell made of polydimethylsiloxane (PDMS).

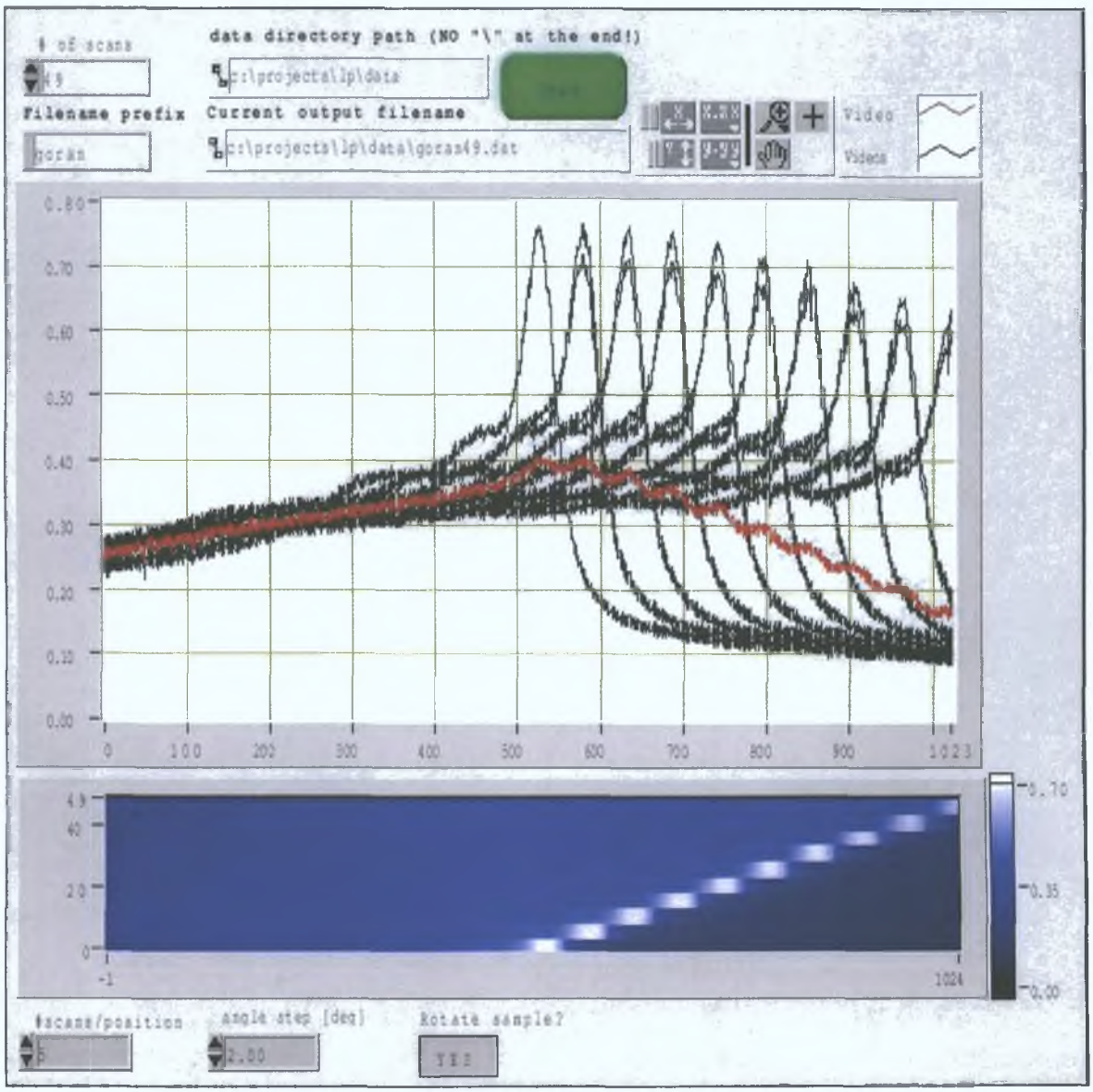

Figure 5.15: A screenshot of the LabView program facilitating acquisition and visualisation of the video-signal from the linear detector array. The program was used in conjunction with the experimental apparatus shown in Fig. 5.12.

A special holder (H) for the flow cell was designed. The holder provided a rigid support

for two syringe needles (S1 and S2), which acted as the inlet and outlet ports. The needles were attached to tubes T1 and T2, both with inner diameter of approximately 0.76 mm. A peristaltic pump (P) was used to provide a controlled flow of the solution at a constant rate.

The direct excitation of luminescence was provided by a multimode optical fibre (F) with a core diameter of 600 μm, which guided the light from a blue LED (see Fig. 5.1 for the emission spectrum) placed at the other end of the fibre. The fibre was supported by the holder (H) in such a way that the fibre tip was close to the surface of the thin layer. The distance between the fibre tip and the surface of the layer, which defined the thickness of the bulk layer t_b considered in Sec. 3.2.5, was in the order of 200–500 μm but could not be determined with greater precision.

The peristaltic pump and changing of solutions was controlled manually. The data acquisition and processing was facilitated by a personal computer (PC). The measurement program was written in `LabView`. A screenshot of the program is shown in Fig. 5.15.

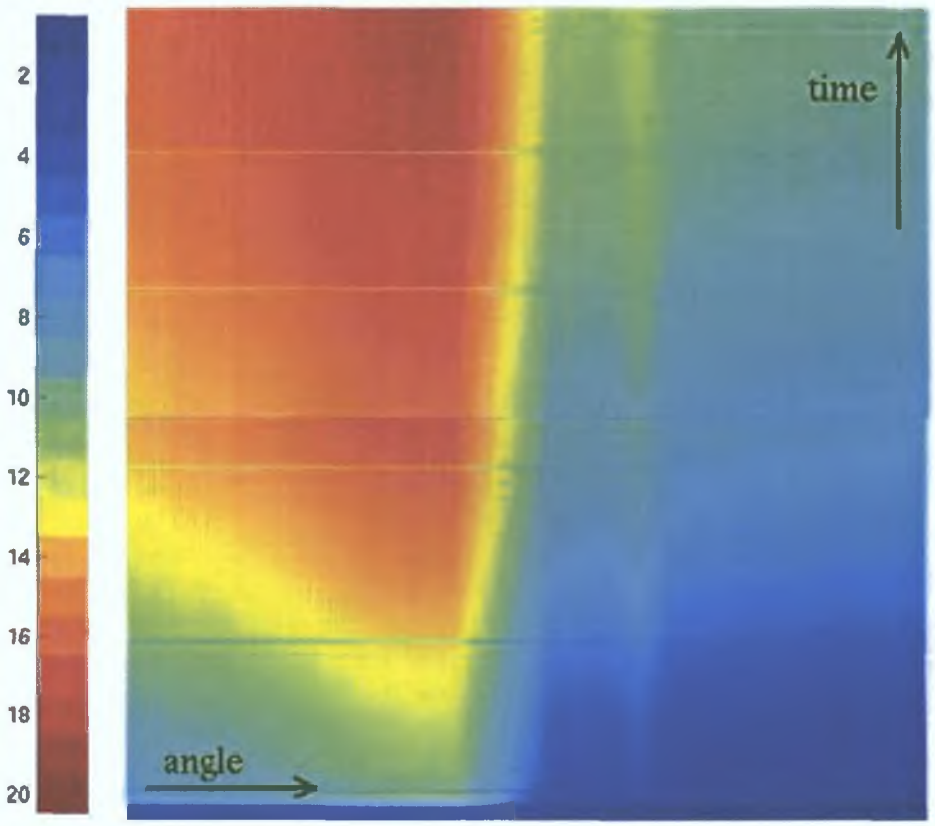

Figure 5.16: An example of a 2D intensity chart displaying the time evolution of the angular profile of luminescence. Each horizontal section of the chart represents an angular profile of the luminescence intensity at a certain time. Different colours represent different luminescence intensities, blue corresponding to the lowest and red to the highest level of intensity.

A typical experiment proceeded as follows:

1. Air was flowed over the sample in order to acquire a background signal.
2. The undoped solution was passed over the sample for several minutes and the angular

profiles of the detected luminescence (if any) were acquired every 12 seconds.

3. The doped solution was passed over the sample and the angular profiles of luminescence were recorded.

4. Steps 2 and 3 were repeated several times until a sufficient amount of data was acquired.

The angular profiles of the radiated luminescence were represented in 2D intensity charts to provide an illustrative representation of the time-evolution of the detected signal. An example of such a chart is shown in Fig. 5.16.

5.3.3 Experimental results

In this section, an example of an experiment employing the apparatus and samples described above is discussed. The experiment is described step by step, each step accompanied by a thorough discussion and, where possible, interpretation of the observed phenomena.

Calibration of the experimental apparatus

As mentioned in Sec. 5.3.2, the experimental apparatus included a linear detector array (LDA) containing a total of 1024 photodiodes. The total length of the imaged area was 2.5 cm. The signal from each photodiode represented a pixel on the acquired image. Since the linear detector was placed close to a *round* face of a semi-cylindrical prism, the distance of the photodiodes from this face differed with the position of the photodiode on the LDA chip. Therefore, at the begin of the experiment, it was necessary to calibrate the experimental set-up. In particular, it was necessary to find (i) a relation between the pixel number and the corresponding angular position and (ii) a relation between the measured intensity detected by the photodiode at a certain position and the true intensity value at the corresponding angular position.

The calibration was carried out using a sample coated with a relatively thick luminescent layer ($\approx 0.8\,\mu$m) surrounded by air. For this sample, the peak in the angular profile of the radiated luminescence was distinct and its angular position could be determined precisely. The semi-cylindrical prism with the attached sample and the fibre providing the excitation light were mounted on a rotary stage. This allowed the images to be obtained at different angular positions of the prism with respect to the LDA chip. In particular, after each image was acquired, the prism, sample and the light source were rotated by $\Delta\theta = 2°$. This was repeated 9 times and the corresponding experimental data is shown in Fig. 5.17. In the graph, the x axis corresponds to the number of the pixel, i.e., the position of the single photodiode, and the y axis represents the corresponding intensity detected by that particular photodiode.

It can be seen that the angular profile of the luminescence intensity remains unchanged as the prism with the sample is rotated. On the other hand the profile is slightly distorted at the edges of the image. This is caused by the fact that the photodiodes at the edge of the LDA chip are more distant from the face of the semi-cylindical prism than those in the centre of the chip, as mentioned previously. This is clearly demonstrated by the decrease of the intensity of the peak as the peak position approaches the edge of the image.

The variation of the angular position of the peak was found to be linear with respect to the sample rotation. Every rotation of the sample by $\Delta\theta = 2°$ corresponded to the same

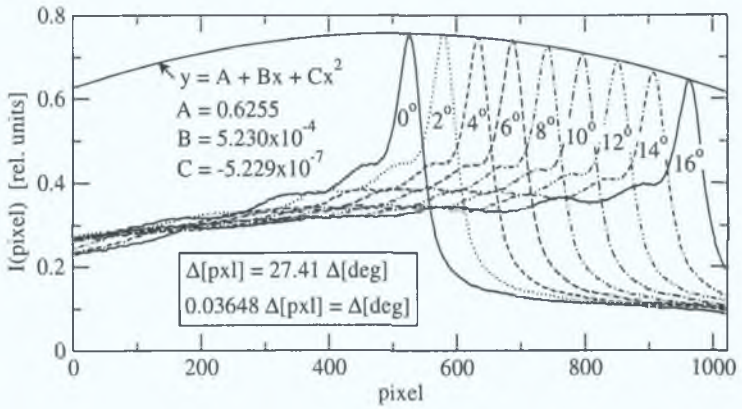

Figure 5.17: Angular distributions of the luminescence intensity obtained for 9 different orientations of the semi-cylindrical prism containing the sample. The angles of rotation are shown in the graph. Also shown are the calibration functions of the detection system employing the LDA.

change of the peak position on the image over the entire measured interval. Consequently, the relation between the difference in the angular position, represented by Δ [deg], and the difference in the pixel position, represented by Δ [pxl], was found to be

$$\begin{aligned} \Delta\,[\mathrm{pxl}] &= 27.41\,\Delta\,[\mathrm{deg}], \\ \Delta\,[\mathrm{deg}] &= 0.03648\,\Delta\,[\mathrm{pxl}]. \end{aligned} \tag{5.1}$$

The variation of the peak intensity across the image was found to be described by a quadratic function

$$y = A + Bx + Cx^2, \tag{5.2}$$

where $A = 0.6255$, $B = 5.230 \times 10^{-4}$ and $C = -5.229 \times 10^{-7}$. In this equation, y represents the detected luminescence intensity and x represents the pixel position.

Equations (5.1) and (5.2) represent the calibration functions of the LDA-based detection system. After the intensity profile is measured by the LDA chip, the values have to be divided by the intensity calibration function (5.2) in order to obtain the true intensity profile of the radiated luminescence. Subsequently, the profile is transformed to the angular profile using (5.1).

It needs to be pointed out that this procedure does *not* provide *absolute* values of angles but only the *relative* angular differences. This is caused by the experimental apparatus itself. In particular, the positioning of the semi-cylindrical prism containing the sample is not precisely defined. For example, when the samples are exchanged, the absolute value of the angular position of the new sample can differ (by up to approximately 5°) from the position of the old sample. On the other hand, once the absolute value of the angle of one particular pixel is determined, it does *not* change during the course of the experiment for the particular sample. Therefore, the angular profile of the luminescence intensity has to contain at least one feature with a known angular position during any part of the experiment in order to enable the interpretation of the observed data during the entire course of the experiment.

Ru(dpp)$_3$-doped sample

After the calibration procedure was completed, testing of different samples could proceed. Firstly, the sample coated with Ru(dpp)$_3$-doped thin sol-gel film (see Table 5.4(a)) was employed.

Curve 1 in Fig. 5.18 shows the angular profile of the luminescence intensity when the luminescent layer was initially surrounded by air. The profile exhibits features that are typical for a relatively thick luminescent layer (see Sec. 3.2.3). Using the refractive indices mentioned at the end of Sec. 5.3.1, the thickness of the sol-gel layer is estimated to be $t_l \approx 1.5\,\mu$m.

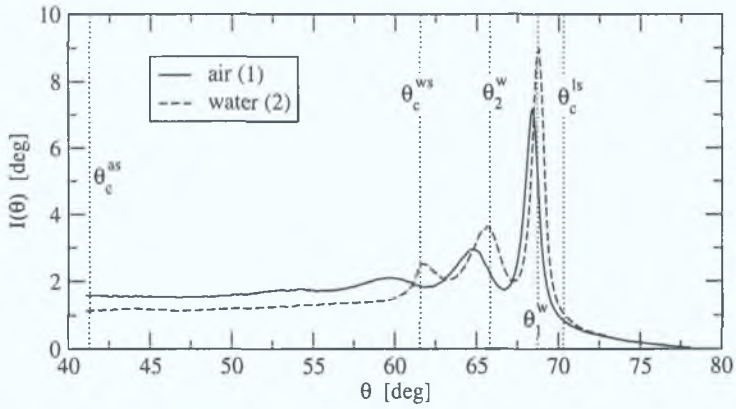

Figure 5.18: Angular distributions of the luminescence intensity radiated by a Ru(dpp)$_3$-doped sample surrounded by air (curve 1) and water (curve 2). The curves represent the stabilised profiles and they correspond to the data which was calibrated using Eqs. (5.1) and (5.2).

After the sol-gel layer was covered by water, the angular profile of the luminescence intensity changed to that depicted by curve 2 in Fig. 5.18. Again, the profile exhibits familiar features as discussed in Sec. 3.2.5. From the profile, the thickness of the sol-gel layer of $t_l \approx 1.5\,\mu$m could be estimated, in agreement with the previously obtained estimation. The most important feature of the profile is the transition between the (almost) constant intensity profile below the critical angle θ_c^{ws} and the profile with distinct peaks within the angular range $\theta \in \langle \theta_c^{ws}, \theta_c^{ls} \rangle$ (compare the graphs in Fig. 5.18 and Fig. 3.11(b)). The typical shape of this transition region could be used to determine the absolute angular position of the sample. In particular, it was deduced that this feature is located at $\theta_c^{ws} = 61.55°$, as follows from Table 5.5. All other features and their corresponding angular positions were deduced relative to this value.

Another important noticable difference between the intensity profiles corresponding to the situations where the layer is covered by air (curve 1) and water (curve 2) is that the intensity of the peaks located at θ_1^w and θ_2^w is greater when the layer is covered by water. Furthermore, the angular position of these peaks is slightly shifted towards greater angles in the case the luminescent layer is covered by water. Both of these features completely agree with the expectations following from the theory developed in Sec. 3.1.

Following exposure to water, Ru(dpp)$_3$-doped ethanol (D-solution) was passed above the sol-gel layer. During the period of time when the coverage of the sol-gel film changed from water to the D-solution, the behaviour of the angular profile of the luminescence intensity was unpredictable. However, after the water had been completely substituted by the D-solution,

the profile stabilised. This stabilised profile is shown by curve 3 in Fig. 5.19.

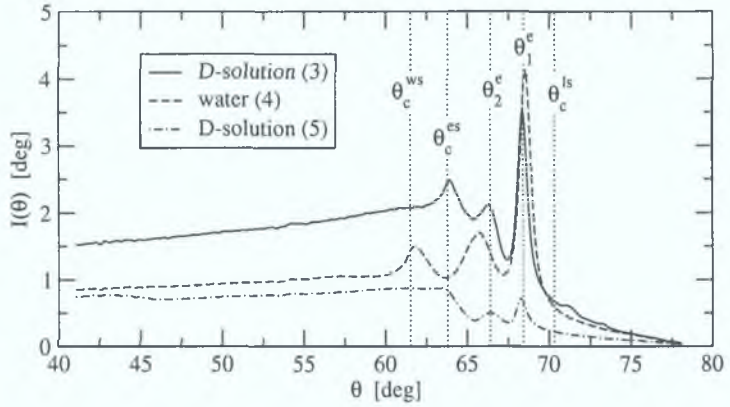

Figure 5.19: Angular distributions of the luminescence intensity radiated by a $Ru(dpp)_3$-doped sample. The curves correspond to the cycle during which the $Ru(dpp)_3$-doped layer was surrounded by the D-solution (curve 3), water (curve 4) and the D-solution (curve 5), respectively. The curves represent the stabilised profiles and are calibrated using Eqs. (5.1) and (5.2).

There are several important differences between curves 2 in Fig. 5.18 and 3 in Fig. 5.19. Firstly, the feature characterising the location of the critical angle of the substrate/environment changed its angular location from θ_c^{ws} to θ_c^{es}. When the numerical values obtained from the calibration function (5.1) were evaluated, values that are in excellent agreement with those listed in Table 5.5 were found. Therefore, it can be said that the change of the refractive index of the medium flowing above the luminescent layer could clearly be observed by this experimental method.

Referring to curve 3 in Fig. 5.19, the second important difference is that the intensity of the angular profile below the critical angle θ_c^{es} increased substantially relative to the intensity of the profile above the critical angle. This is in excellent agreement with the expectations that the main contribution to the luminescence originating from the bulk above the luminescent layer should occur below the critical angle θ_c^{es}, as follows from the numerical examples presented in Sec. 3.2.5. Furthermore, this is also the first experimental demonstration of such a phenomenon.

When the scales of the graphs in Figs. 5.18 and 5.19 are compared, it can be seen that the intensity of the angular profile depicted by curve 3 substantially decreased relative to that depicted by curve 2, especially above the critical angle θ_c^{es}. This could not be explained by the same argument as for the transition from air to water, as discussed above, because that argument would imply an opposite effect. The observed phenomenon can, however, be explained by considering that the D-solution containing luminescent molecules absorbed the blue excitation light. This is understandable since this absorption had to occur in order to generate the luminescence within the bulk region above the sol-gel layer. Due to this absorption, the intensity of the blue excitation light reaching the luminescent layer is reduced. Consequently, the contribution of the luminescent layer to the luminescence intensity is reduced, in agreement with the observed reduction of the intensity of the profile above the critical angle θ_c^{es}.

In the next step of the experiment, the D-solution was changed back to water. Again,

during the transition period, the detected signal behaved unpredictably. However, after the D-solution was completely substituted by water, the signal stabilised. This stabilised angular profile is shown by curve 4 in Fig. 5.19.

It can be seen that the angular profile of the luminescence intensity essentially returned to the profile corresponding to the case when the luminescent layer was covered by water, which is shown by curve 2 in Fig. 5.18. On the other hand, the absolute intensity of luminescence decreased by a factor of approximately 2 uniformly across the entire angular range. During the experiment, the current through the blue LED was kept constant and even though there could be some variations in the blue light intensity, they would definitely not be as large as 50 %. Therefore, the most likely and reasonable explanation for the observed decrease in the luminescence intensity was that the molecules of the ruthenium complex were either washed away from the luminescent layer or their quantum yield was somehow reduced during the previous step of the experiment. Although these processes seem to be very unlikely from the chemistry point of view, no other explanation of the observed phenomena could be found.

In the next step of the experiment, water was substituted by the D-solution. The corresponding angular profile of the luminescence intensity is shown by curve 5 in Fig. 5.19. The same features corresponding to the water→D-solution transition as those discussed above were observed. Additionally, however, a further decrease in the overall intensity of the angular profile was observed. This observation provided further evidence to support the proposed process of leaching of the molecules of the ruthenium complex from the sol-gel layer, as opposed to the idea of a systematic decrease of the excitation light intensity mentioned in the previous paragraph.

In order to eliminate the above mentioned unpredictable behaviour of the angular profile of the luminescence intensity during the period of time when the transition between water and the D-solution occurred, water was substituted by undoped ethanol (UD-solution). This removed the problems related to the fact that ethanol and water have different refractive indices and that they mix in an unpredictable way. After this substitution, the change of the solution above the sol-gel layer between the D-solution and UD-solution was accompanied by a very smooth change of the corresponding angular profile of the luminescence intensity.

Three additional cycles were carried out during which the environment covering the luminescent sol-gel layer was changed between the D and UD solutions. The angular profiles of the luminescence intensity (stabilised signals) corresponding to these three cycles are shown by curves 1–6 in Fig. 5.20.

Comparing the curves in the graphs (a) and (b), a clear difference in the angular profiles at the angles below the critical angle θ_c^{es} can be observed. This is, again, in agreement with the expectations implied by the theoretical analysis in Sec. 3.2.5. In particular, the presence of the D-solution above the thin luminescent layer results in a substantial increase of the luminescence intensity below the critical angle θ_c^{es} and a negligible influence on the profile above that angle.

A further decrease in the intensity, which was uniform across the entire observed angular range, was observed during the cycles. This supported the proposition that the luminescent molecules were washed away from the thin luminescent film, as mentioned above. However, an additional modification of the angular profile of the luminescence intenity was observed during the course of the cycles. In particular, the angular profile obtained for the last cy-

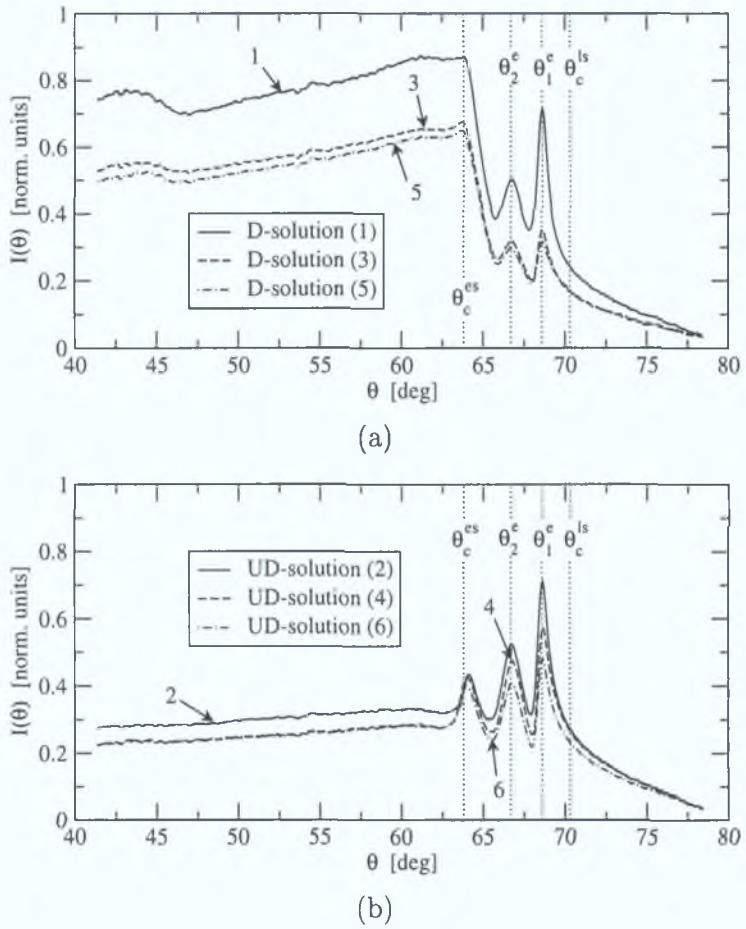

Figure 5.20: Angular distributions of the luminescence intensity radiated by the $Ru(dpp)_3$-doped sample. The curves correspond to the cycle during which the D-doped layer was surrounded by the D-solution—curves 1, 3 and 5 in the graph (a)—and by the UD-solution—curves 2, 4 and 6 in the graph (b). The curves represent the stabilised profiles and are calibrated using Eqs. (5.1) and (5.2).

cle (see curve 6 in Fig. 5.20(b)) was quite different from the profile that would be expected if a thin layer with uniformly distributed luminescent molecules was considered. Preliminary calculations revealed that the angular profile such as that depicted by curve 6 could be explained if the distribution of the *sources* of luminescence within the thin layer was *non-uniform*. More precisely, if the contribution originating from the region of the layer neighbouring the environment was greater than the contribution originating from the region close to the layer/substrate interface, then the observed phenomena could be explained. This non-uniformity could have two possible explanations. The first one would suggest that the *concentration* of the luminescent *molecules* within the region neighbouring the environment was greater than that of the region close to the layer/substrate interface. The second explanation would suggest that the cycling of the D and UD solution above the sol-gel layer resulted in a substantial *increase of absorption* (over the blue region of the spectrum) in the sol-gel layer. If this was the case, the intensity of the excitation light would change abruptly across the luminescent layer. In particular, it would be lower in the region closer to the layer/substrate interface, which would result in the observed effect on the angular profile of

the luminescence intensity. Althought both of the above-mentied explanations seem to be rather obscure and unlikely from the chemistry point of view, they cannot be completely discarded.

Undoped sample

After the cycles employing the $Ru(dpp)_3$-doped sample were completed, the sample was replaced by the undoped sample (UD-sample). Figure 5.21 shows the experimental results.

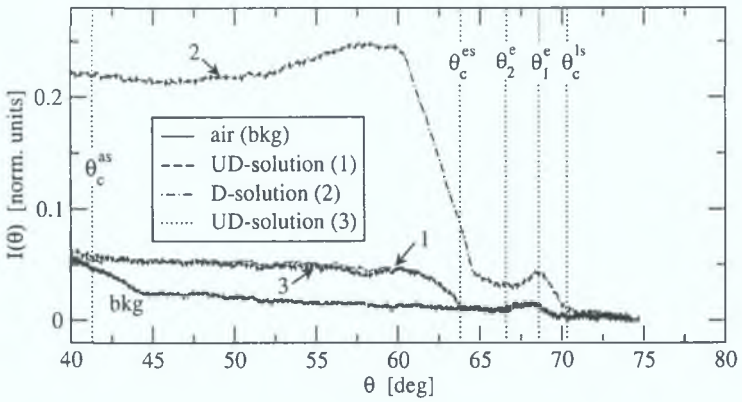

Figure 5.21: Angular distributions of the luminescence intensity radiated by the UD-sample. The curves correspond to the cycle during which the undoped sol-gel layer was surrounded by air (curve "bkg"), UD-solution (curves 1 and 3) and the D-solution (curve 2), respectively. The curves represent the stabilised profiles and are calibrated using Eqs. (5.1) and (5.2).

Initially, the UD-layer was surrounded by air. The corresponding angular profile of the luminescent intensity is shown in Fig. 5.21 by curve denoted by "bkg". This curve also represents the background signal for those parts of the experiment where the thin sol-gel layer was surrounded by air. The curve is characterised by two visible features. In particular, the slight increase of the intensity below the angle 44.3° corresponds to the blue excitation light detected within this angular region. The light, which is generated at a great distance (in comparison with the wavelength) from the UD-layer, cannot propagate within the glass substrate at angles greater than the critical angle θ_c^{as} but can be observed at angles smaller than this angle. If the divergence of the beam emerging from the tip of the fibre is considered, the increase of the background signal below θ_c^{as} could be explained. However, as follows from Table 5.5, the value of the critical angle is $\theta_c^{as} \approx 41.3°$, which is 3° less than the measured value. This is probably due to the fact that when the calibration (5.1) was extrapolated to this angular region, it did not hold exactly.

The second feature can be observed around the angle θ_1^e. It is attributed to the scattering of the blue excitation light at either the top or bottom interface of the sol-gel layer, or even within the volume of the layer. If this scattering took place, it would effectively act as a source of blue light within the sol-gel layer, which could result in a non-zero intensity within the angular range $\theta \in \langle \theta_c^{es}, \theta_c^{ls} \rangle$, as observed.

After exposure to air, the volume above the UD-layer was filled with ethanol (UD-solution). The corresponding angular profile of the luminescence intensity is shown by curve 1 in Fig. 5.21. Again, the slight increase of the measured intensity below θ_c^{es} was due to the

blue excitation light, which was allowed to propagate within this angular region by the same argument as in the case when the layer was surrounded by air. In fact, it was this feature that determined the absolute angular position of the sample.

Following the UD-solution, ethanol *doped* with the ruthenium complex (D-solution) was flowed above the thin sol-gel layer. The corresponding angular profile of the luminescence intensity is depicted by the curve 2 in Fig. 5.21. A substantial increase of the intensity below the critical angle θ_c^{es} and a slight increase of the intensity within the angular range $\theta \in \langle \theta_c^{es}, \theta_c^{ls} \rangle$ agree very well with the changes expected from the theoretical analysis in Sec. 3.2.5.

There were, however, several difficulties with the interpretation of curve 2. Firstly, the decrease of the intensity within the angles from approximately 60° to 64° was not as steep as it was expected from the theoretical analysis. Furthermore, the theory suggests that the small peak occurring within the angular region $\theta \in \langle \theta_c^{es}, \theta_c^{ls} \rangle$ should be more pronounced at $\theta = \theta_2^e$ rather than at $\theta = \theta_1^e$. These features could not be explained satisfactorily and require further investigation.

In the next step of the experiment, the UD-solution was flowed again above the sol-gel layer. The corresponding angular profile of the luminescence intensity is shown by curve 3 in Fig. 5.21. It was found that the angular profile returned back to the same level as in the previous case (depicted by curve 1). This means that no changes to the properties of the thin sol-gel layer, such as diffusion of the molecules of the ruthenium complex into the layer, could be observed.

Undoped sample—long term experiment

During the experiments described above, it was observed that the baseline of the experimental data did not remain constant during the course of the experiments but gradually increased instead. Although this increase was negligible with respect to the characteristic features of the observed experimental data, it was necessary to investigate it further in order to determine possible reasons.

Since there was no change of the properties of the UD-sample observed during the previous experiment, the same sample was used in the long-term experiment. In this experiment, the D-solution was flowed above the undoped sol-gel layer for an extended period of time, approximately 3.5 hours. The corresponding results are shown in Fig. 5.22.

As can be seen from the graph, the angular *profile* of the luminescence intensity was the same as that depicted by curve 2 in Fig. 5.21 and did not change during the course of the experiment. On the other hand, the *baseline* exhibited a substantial drift towards larger values. This drift was found to be approximately twice as large during the first 500 frames ($\approx$ 1.7 hours) as during the second 500 frames. Even though every measure was taken to ensure that the intensity of the source of the excitation light (the blue LED) was constant, the drift could not be eliminated. Furthermore, no other source of this drift could be identified. Even though the drift might seem to be caused by seepage of the luminescent molecules into the sol-gel layer, this explanation would not be acceptable as it would require a change in the angular profile of the luminescence intensity, which was not observed. Therefore, it has to be concluded that the origin of the drift is still unknown and requires further experimental investigation.

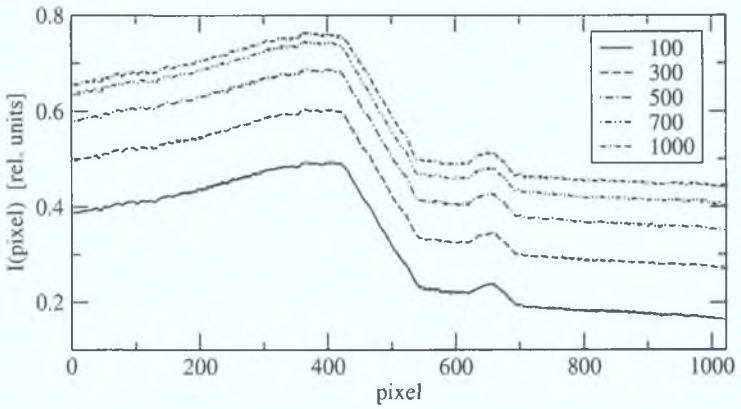

Figure 5.22: Angular distributions of the luminescence intensity obtained for the UD-sample over which the $Ru(dpp)_3$-doped ethanol flowed steadily over approximately 3.5 hours. The curves represent the raw experimental data. Different curves represent the angular distributions at different time frames which are indicated by the legend. Each frame lasted approximately 12 s, i.e., the frames number 100, 300, ..., 1000 correspond to 20, 60, ..., 200 minutes, respectively.

Summary of the experimental results

The experimental data shown in Figs. 5.18–5.21 demonstrate that the novel experimental technique, whose theoretical background and technical details were described in Sections 3.2.5–3.2.6 and 3.4, respectively, is suitable for distinguishing between the contributions to the luminescence originating from the surface layer and from the bulk above the layer. Furthermore, as can be judged from the number of conclusions drawn during the interpretation and discussion of the observed data, the capabilities of the technique extend even further than this. In particular, using this method, *in-situ* and *real-time* micro-scale variations of the properties of thin luminescent layers could be detected and assessed. For example, an inhomogeneous distribution of luminescent molecules in a thin layer could be mapped using this technique.

Another area of application of this method is the detection of luminescence emitted by molecules located within a specific distance from the surface of a substrate, while employing excitation by direct illumination. This area has not yet been fully explored and more experiments need to be conducted in order to quantify the capabilities and limitations of the experimental set-up or the method itself. Nevertheless, the preliminary experiments described above indicate that the application of this method to this area is experimentally feasible in its present configuration.

It also needs to be pointed out that the interpretation of the observed data is not trivial and requires an in-depth knowledge of the area of angular dependence of luminescence radiated from thin films or molecules located close to an interface. This is particularly true if the observed phenomena exhibit complex and unexpected behaviour and there is no independent source of information as to what factors might cause it. An example of such behaviour could be the possible leaching or seepage of the luminescent molecules from or into the thin layer, as mentioned earlier. Nevertheless, application of the theoretical model developed in Chapter 3 enables the analysis of results obtained even from such systems as those containing, for example, inhomogeneously distributed luminescent molecules.

5.4 Conclusion

The first part of this chapter presented the experimental corroboration of the angular dependence of luminescence intensity emitted from thin films. Using the experimental data, the thickness and refractive index values of a thin luminescent film were evaluated.

In the second part, a configuration providing enhanced luminescence collection efficiency, as designed in Chapter 3, was tested experimentally. It was found that the configuration employing frustrated cones exhibits approximately 11–12 fold increase in the efficiency of luminescence collection in comparison with the conventional technique employing the detection above or below a planar (unmodified) substrate.

In the last part of this chapter, an experimental set-up which enables the real-time measurement of the angular distribution of the luminescence intensity emitted by molecules located in the close vicinity of a planar substrate was reported. The preliminary experimental results demonstrated that it was possible to distinguish between the luminescence originating from the thin layer and that originating from the liquid above the layer, while employing direct illumination of molecules located in both regions. It was also pointed out that the application of this approach to the detection of luminescence emitted by molecules located within a specific distance from the surface of a substrate is feasible, in principle, but its more specific quantification requires further experimental investigation.

5.5 Bibliography for Chapter 5

[1] B. D. MacCraith, C. M. McDonagh, G. O'Keffe, A. K. McEvoy, T. Butler, and F. R. Sheridan. Sol-gel coatings for optical chemical sensors and biosensors. *Sensors and Actuators*, B 29:51–57, 1995.

[2] C. McDonagh, B.D. MacCraith, and A.K. McEvoy. Tailoring of sol-gel films for optical sensing of oxygen in gas and aqueous phase. *Anal. Chem.*, 70(1):45–50, 1998.

[3] W.Lukosz and R. E. Kunz. New method for determining refractive index and thickness of fluorescent thin films. *Optics Communications*, 31(3):251–256, December 1979.

[4] Pierre Couratier. CMOS-based detection system—user's manual. Internal report, Dublin City University, August 2001.

[5] Solid State Division Hamamatsu Photonics K.K. NMOS linear image sensor—series S3901/S3904. *http://usa.hamamatsu.com/cmp-detectors/arrays/nmos.htm*, 2001.

[6] `http://www.galindberg.se/bilder/184.pdf`. Dow Corning, SYLGARD 184—Silicone Elastomer, 2001.

Chapter 6

Conclusions

6.1 Summary of work

The aim of this dissertation was to address the issues regarding optimisation of the performance of absorption and luminescence-based optical chemical sensors and biosensors employing planar multimode platforms. In addition to theoretical development, the main focus was on the instrumentation and optical design of the sensor systems in order to optimise their performance.

With regard to the absorption-based sensors, a rigorous electromagnetic theory was developed which is particularly suitable for the description of operation of sensor systems employing multimode waveguides coated with a thin sensing film. Using the theory, conditions for which the performance of such sensor systems can be optimised were identified. Situations dealing with the so-called 'ideal' and 'real' sensing elements were analysed in detail and compared. A number of numerical examples were provided to illustrate the fundamental theoretical results. In addition, numerical simulations were used to demonstrate the superior performance of the optimised sensing configuration in comparison with the typically used evanescent-wave sensing technique.

The theoretical predictions were experimentally corroborated using a laser-based experimental set-up. Combining the experimental results and theoretical modeling, an optimised configuration of an LED-based sensor system was designed. A compact and portable prototype of such a sensor system was fabricated and employed for sensing of pH and gaseous ammonia. A resolution of 0.007 pH units and limit of detection of 10 ppb of ammonia in nitrogen were achieved with a sensor operating in a single-reflection configuration.

With regard to the luminescence-based sensors, a rigorous electromagnetic theory was developed which is suitable for the description of angular dependence of luminescence emitted by molecules embedded in arbitrary multilayer systems. A number of numerical examples were discussed to illustrate the main implications of the theory for the optimisation of luminescence-based sensor systems.

The theory was applied in two areas. Firstly, it was used to describe the spatial anisotropy of luminescence emitted from thin luminescent films. Based on this analysis, a variety of configurations were proposed which should facilitate improved efficiency of luminescence collection. One such configuration was fabricated and tested. In comparison with the conventional

detection techniques, the optimised configuration exhibited more than a 10-fold improvement in the luminescence capture efficiency.

The second application of the theory involved the detection of luminescence originating specifically from molecules located in the close vicinity of a surface. This task is of particular importance in biomedical applications in order to monitor surface-specific binding or adsorption. Based on the theoretical predictions, a novel technique has been proposed, developed and experimentally tested which facilitates the detection of surface-generated luminescence. In contrast to the conventional technique employing evanescent-wave excitation, the improvement offered by this novel technique is derived from the fact that the excitation is provided by direct illumination.

6.2 Future outlook

The results obtained in this work can be implemented in the design and fabrication of novel sensor platforms with enhanced sensitivity. This was successfully demonstrated in Chapters 4 and 5 where the experimental results obtained during the course of this research programme were presented. Although the experimental results presented in this dissertation are very promising, there are still many possibilities for further exploitation of the theoretical predictions and their practical implementation. Some of the ideas are outlined below.

The compact absorption-based sensor system with the optimised design, as described in Sec. 4.2, exhibited a very good performance which was superior or at least comparable to the more complex laboratory systems reported in the literature. Even though the sensor unit was small, compact and portable, its size could still be further decreased by employing surface-mount technology in the fabrication of the electronic circuit and by purposely designing smaller and more compact sensor chips containing the sensing chemistry. Apart from the issues of size, the generic platform could be expanded to multi-analyte sensing employing a single sensor chip. This would be of particular interest in many practical applications. Another possibility of improvement of the sensitivity would be by designing the sensor chip so as to facilitate the operation in the multiple reflection configuration.

In section 2.3, the differences between the performance of so-called 'ideal' and 'real' sensing elements operating in particular optimised configurations were analysed theoretically. Furthermore, a simple method was proposed which enables single-point recalibration of a sensor unit whose calibration function was perturbed by such effects as misalignment or replacement of the sensing element. It would be beneficial for further improvement of the sensor performance to investigate these concepts experimentally and implement them in real sensor systems.

With regard to the luminescence collection efficiency, it was demonstrated that the configuration employing frustrated cones exhibited a very promising performance, as described in Sec. 5.2. It would therefore be very beneficial if this configuration was employed directly as a generic platform for optical chemical sensors based on the measurement of luminescence intensity or lifetime. In conjunction with a miniaturised electronic circuit, it could enable the fabrication of small and compact sensor devices. If the frustrated cones were designed in a two-dimensional array, these devices could be easily expanded to multi-analyte sensing.

An important area where the research presented in this dissertation could be further

expanded is the detection of the surface generated luminescence It was successfully demonstrated in Sec 5 3 that the specially designed experimental apparatus enabled a clear distinction between the luminescence generated from a thin layer deposited on a substrate and a bulk (volume) above the layer, while exciting the luminescent molecules present in both regions by direct illumination This method could be directly employed in the real-time monitoring of adsorption or specific surface binding of molecules onto a surface By using direct illumination of the luminescent molecules, this method could provide a more efficient and sensitive alternative to the currently used technique employing evanescent-wave excitation Other advantages provided by this method include the possibility of monitoring the luminescence generated by molecules located within a specific distance above the surface or determining the distribution of luminescent molecules above the surface Although this work provided a detailed theoretical analysis and successful preliminary confirmation of these concepts, it would be desirable to conduct further and more specific experiments to provide more precise quantification of this method

Finally, further work could be done in order to expand the theoretical model developed in Sec 3 1, especially its software implementation Its current capabilities are limited to the cases covering a single luminescent molecule or a layer of uniformly distributed molecules embedded inside an arbitrary multilayer system However, the formalism implemented in the model is flexible which means that its expansion to more complex systems, such as those employing inhomogeneously distributed luminescent molecules, is rather straightforward

Appendix A

List of abbreviations of chemical compounds

BCP	Bromocresol Purple — pH sensitive dye
MTEOS	methyl-triethoxysilane — $CH_3(C_2H_5O)_3Si$
PDMS	poly-dimethylsiloxane
$Ru(dpp)_3$	Ruthenium complex — Ru(II) tris(4,7-diphenyl-1,10-phenantrolme)
TEOS	tetraethoxysilane — $(C_2H_5O)_4Si$

Publications

Peer reviewed publications

[1] Ladislav Kalvoda and Lubos Polerecky. Investigation of a planar chiral waveguide structure by a modified ATR method. *Advanced Materials for Optics and Electronics*, 8(4):195–199, July–August 1998.

[2] Lubos Polerecky, Jaroslav Hamrle, and Brian D. MacCraith. Theory of radiation of dipoles placed within a multilayer system. *Applied Optics*, 39(22):3968–3977, August 2000.

[3] Lubos Polerecky, Conor S. Burke, and Brian D. MacCraith. Optimisation of multimode waveguide platforms for absorption-based optical chemical sensors. To be published in *Applied Optics*, March 2002.

[4] J. Hamrle, M. Nývlt, Š. Višňovský, R. Urban, P. Beauvillain, R. Mégy, J. Ferré, L. Polerecký, and D. Renard. Magneto-optical properties of ferromagnetic/non-ferromagnetic interfaces: application to Co/Au(111). *Physical Review B*, 64:155405, 2001.

[5] L. Polerecky, J. Hamrle, and J. Ferré. Theory of SHG from multilayer systems based on point-dipole radiation—application to magnetic multilayers. Manuscript in preparation.

Patent applications

[1] Lubos Polerecky and Brian D. MacCraith. A luminescence-based sensor. Irish Patent Application No. S2001/0051, Filed on Jan 23 2001.

[2] Lubos Polerecky and Brian D. MacCraith. A luminescence-based sensor assembly. Irish Patent Application No. S2001/0825, Filed on Sept 11 2001.

[3] Lubos Polerecky and Brian D. MacCraith. A luminescence-based sensor. PCT Patent Application, Submitted on Jan 23 2002.

Conference presentations

[1] Lubos Polerecky. The polarization state maintenance in the chiral optical fiber waveguides. In *Proceedings of PIERS'96*, page 637, Innsbruck, Austria, 1996. Oral presentation at the Progress in Electromagnetics Research Symposium.

[2] Lubos Polerecky and Pater Neumann. Application of Monte Carlo method in solving 2D elliptic partial differential equations. In *Dresdner Schriften zur Mathematischen Stochastik*. Dresden Technical University, Dresden, Germany, October 1997.

[3] B. D. MacCraith, L. Polerecky, A. M. Doyle, C. Burke, A. K. McEvoy, and C. M. McDonagh. Optical waveguide sensing platforms based on sol-gel-derived materials. Presented at Photonics West SPIE conference No. 3943, San Jose, CA, January 2000. Private communication.

[4] B. D. MacCraith, C. von Bültzingslöwen, A. K. McEvoy, C. McDonagh, and L. Polerecky. Sol-gel waveguide fluorescence sensors for food packaging. In *Oral presentation at PITTCON 2000*, 12-17 March 2000.

[5] Lubos Polerecky, Conor S. Burke, and Brian D. MacCraith. Optimisation of waveguide platforms for absorption-based optical sensors. In *Poster presentation at the Europt(r)ode 2000 conference*, Lyon, France, April 2000.

[6] Lubos Polerecky, Jaroslav Hamrle, and Brian D. MacCraith. Fluorescence emission near an interface: Implications for optical sensor design. In *Oral presentation at the Europt(r)ode 2000 conference*, Lyon, France, April 2000.

[7] B. D. MacCraith, C. von Bültzingslöwen, A. K. McEvoy, C. McDonagh, and L. Polerecky. Sol-gel waveguide fluorescence sensors for food packaging. In *Oral presentation at Photonics East*, Boston, Massachusetts, USA, 5–8 November 2000.

[8] Lubos Polerecky, Conor S. Burke, and Brian D. MacCraith. Optical ammonia sensor employing a planar waveguide platform. In *Oral presentation at Photonics East*, Boston, Massachusetts, USA, 5–8 November 2000.

[9] J. Hamrle, S. Visnovsky, M. Nyvlt, L. Polerecky, R. Urban, J. Ferre, D. Renard, M. Galtier, and P. Beauvillain. Polar magneto-optical ellipsometry of ultrathin Au/Co/Au and Au/Co/Au/Co/Au wedges. In *abstract on ICM (International Conference on Magnetism)*, page 339, Recife, Brazil, 6–11 August 2000.

[10] J. Hamrle, J. Ferre, M. Nyvlt, L. Polerecky, and S. Visnovsky. Profil de l'aimantation en profondeur de multicouches Co/Au: mesure par effet Kerr magneto-optique. In *digest on JMC7 (7èmes Journées de la Matière Condensée)*, page 362, Poitiers, France, 29 August–1 September 2000.

[11] L. Polerecky, J. Hamrle, and J. Ferré. Theory of SHG in ultra-thin magnetic multilayers based on point-dipole radiation. In *Poster presentation at NOPTI-2001 conference*, Nijmegen, October 2001.